The Influence of Neutral Flow Rate in the Operation of Hall Thrusters

by

Bryan Michael Reid

A dissertation submitted in partial fulfillment
of the requirements for the degree of
Doctor of Philosophy
(Aerospace Engineering)
in the University of Michigan
2009

Doctoral Committee:

Professor Alec D. Gallimore, Chair
Professor James F. Driscoll
Associate Professor John E. Foster
James M. Haas, U.S. Air Force Research Laboratory
Richard R. Hofer, NASA Jet Propulsion Laboratory

"Never let your schooling interfere with your education."

--Mark Twain

© Bryan Michael Reid
2009

Acknowledgements

My nine years at the University of Michigan have been immensely rewarding and the relationships that were built on this campus will last a lifetime. These relationships, some say, are more important than the three diplomas that I have received; this is my opportunity to acknowledge many of the people that have made this journey possible, tolerable, and worthwhile.

The first "shout out" is reserved for my research advisor: Dean/Professor /Dr. Alec D. Gallimore. If you are an old Princeton alum, "tool," "slick," or "Alec" will sound more familiar. You may have even been privy to stories about "Free-Body Diagrams!!!" or witnessed spontaneous/automated pectoral gyration.

Alec completely changed the trajectory of my career through the simple act of saying "yes" when I TOLD him that I was going to join his lab; instead of pushing paper at one of the big defense contractors with a B.S., I'll now be pushing paper at a nationally-recognized FFRDC with a Ph.D. Thanks a lot! (j/k, lol, :-) , WTF?). As a member of PEPL, students are not only exposed to some of the best facilities and equipment in the nation, possibly the world, they join an elite fraternity of men and women who have demonstrated excellence in research, who have achieved in their careers, and who have built strong networks in the research community. This

network is often referred to as the "Michigan Mafia," and joining this brother/sisterhood should be taken as an honor to be upheld at the highest level.

During my time at PEPL, I have become sincere friends with many of the "Michigan Mafia." I have seen many of them defend, get married, and have kids. I have run experiments or shared office space with Dr. Richard ("Rich" or "dickbob") Hofer, Dr. Peter ("Pete") Peterson, now Professor Mitchell ("Mitch" or "Sergeant" if you've experienced an over tightened bolt) Walker, Dr. Daniel ("Hermo") Herman, now Professor Joshua ("I'm out in 4") Rovey, Dr. Allen ("Abs") Victor, and Dr. Jesse Linnell. I want to thank all of you for welcoming me to the lab, teaching me about research, or in the case of one special guy, teaching me what NOT to do on "Hot-or-Not."

To the people that I would consider to be my cohort, those that spent most of their Ph. D. at Michigan with me: Dr. David ("Floppy") Kirtley, Dr. Prashant Patel, Dan ("Oso de Noche," "Bearded," or "DB") Brown, Kristina ("Bubbles," "BHW," or "Tina") Lemmer, who spent many days and many nights, partaking in my random outbursts yelled across the lab, Robert ("LT" or "Robbie") Lobbia, Bailo Ngom, Tom Liu, the guy that was kind enough to guide me through the streets of Munich when I needed "a little help," Sonca Nguyen, and Ricky Tang. Thank you for supporting me on my journey to candidacy and accompanying me in the lab through these years.

To the newbies: Rohit(h) ("Giggles," "Tic-Tac," "Damian," or just plain old "Cursed SOB") Shastry, the originator of the "East-Side" vs. "West-Side"

terminology, Wensheng (David or "Shuffles") Huang, Michael (aka "Klutz" or "Terminally Tardy") McDonald, who is usually on Suzanne's least-favorite-PEPL person-ever list, Adam ("Shab") Shabshelowitz, Ray Liang, Laura Spencer, Kimberly Trent, and Roland Florenz. You all inherit a lab that is like no other, yet it still requires a ton of care, attention, and effort to bring it to the level that it deserves.

I have to include thanks to the dedicated support staff that has made many of my ventures possible. First, Alec's administrative assistants Karen Schaefer (2005-2006) and Colleen Root (2007-present). These two dedicated women endured the struggle of Alec's overwhelming scheduling restrictions and the frustration of dealing with his abundant stock of graduate students. Thank you! Another round of thanks goes to the administrative staff in the aerospace department: The graduate liaisons Margaret Fillion who was followed by Denise Phelps, Doris Micou who helped me on many occasions beyond acceptance into graduate school, Michelle Shepherd, and purchasing "darlings" Suzanne Smith and Cindy Collins. Thank you all! To the technical staff of the aerospace department, the outwardly surly but deep-down sensitive master machinist Terry Larrow, Dave McLean, Tom Griffin, Erik Kirk, and Chris Chartier. Thank you too!

I would be remiss if I did not acknowledge the contributions from my various graduate funding agencies that made this doctoral degree accessible to me and allowed me to stay focused on my research: NASA Harriett G. Jenkins Pre-doctoral Fellowship Program (JPFP), NASA Michigan Space Grant Consortium (MSGC), and the Rackham Merit Fellowship (RMF).

As is tradition, I have saved the most important people for last; those who were a vital part of my personal life outside campus. These people have offered support beyond measure, and this doctoral degree is as much theirs as it is mine. The largest debt of gratitude is probably reserved for Charlene Reid; the mother who made sacrifices, offered encouragement, and did everything she could to help me succeed. My extended family offered additional support through the years. When times got tough, I used their beaming expressions and awe of my work as motivation to persevere and achieve a goal that, to my knowledge, has not been met in our family's history. Although they were not related by blood, Mr. Derrick Scott and Mrs. Sheila Scott kept me aware of opportunities as they came along, and they hold a large fraction of the responsibility for me going to graduate school. I always felt like a part of the "family" with the Scotts, and I owe a huge debt of gratitude to you both. To my partner in crime Jessica Brooks, the only person who has, or ever will, read my dissertation in its entirety, I want to express sincere appreciation for your shoulder to cry on when things were going terrible (figuratively not literally…geesh) and for helping me celebrate while keeping things in perspective when they went well. Through you, I kept my sanity through this perilous journey, and for that, I thank you.

Bryan Michael Reid

Ann Arbor, MI

November 2008

Table of Contents

Acknowledgements ..... **ii**

List of Figures ..... **xi**

List of Tables ..... **xx**

List of Appendices ..... **xxii**

Nomenclature ..... **xxiii**

Abstract ..... **xxxii**

Chapter 1 Introduction **1**

1.1 Problem Statement 1
1.2 Motivation for Research 2
1.3 Contribution of Research 3
1.4 Organization 5

Chapter 2 Background **7**

2.1 Rocket Propulsion Fundamentals 7
2.2 Electric Propulsion Overview 10
2.3 Hall Thrusters 11
2.3.1 Magnetic Layer Thrusters 11
2.3.2 Anode Layer Thrusters 12
2.3.3 Hall Thruster Basics 12
2.4 Summary 18

Chapter 3 Neutral Flow Dynamics **20**

3.1 Review of Neutral Flow Research 20
3.2 Analytical Calculations 25

3.2.1 Pressure Calculations 25
3.2.2 Neutral Residence Time 30
3.2.3 Azimuthal Uniformity of Neutrals 32
3.2.4 Visual Evidence of Neutral Non-uniformities 35
3.3 Numerical Tools 37
3.3.1 FLUENT 38
3.3.2 MONACO 39
3.3.3 HPHALL-2 40
3.3.4 Comparison of the Three Simulations 41
3.4 Anode Pressure Acceptance Test 42
3.4.1 Pressure Probe 43
3.4.1.1 Pressure Transducer 43
3.4.1.2 Inlet Geometry 44
3.4.1.3 Probe Diameter 45
3.4.2 Neutral Flow Test Bed 48
3.5 Analytical, Numerical, and Experimental Comparisons 48
3.5.1 Radial Profiles 49
3.5.2 Axial Profiles 51
3.6 Flow Distributions in the Discharge Channel 52
3.6.1.1 Simulated 53
3.6.1.2 Experimental 55
3.7 Influence of Anode Boundary Conditions 59
3.7.1 Injection Method 59
3.7.2 Anode Temperature 61
3.7.3 Anode Mass Flow Rate 64
3.8 Neutral Acceleration in the Channel 66
3.9 Summary 68

Chapter 4 Experimental Apparatus 69

4.1 Large Vacuum Test Facility 69
4.2 6-kW Hall Thruster 71
4.3 Hall Thruster Support Equipment 73
4.4 Discharge Current and Discharge Voltage Monitoring 74
4.5 Linear Stages 75
4.6 HARP 75
4.7 Thrust Stand 77
4.7.1.1 Method of Operation 78
4.7.1.2 Electrical Modifications 80
4.8 Plume Diagnostics 81
4.8.1 E×B (Wien filter) 81

4.8.1.1 Probe Design and Experimental Setup 83
4.8.1.2 Data Analysis 85
4.8.1.3 Correction for Charge-Exchange 85
4.8.1.4 Plume-averaged Methodology 87
4.8.1.5 Measurement Uncertainty 89
4.8.2 Single Cylindrical Langmuir Probe 89
4.8.2.1 Probe Design and Experimental Setup 89
4.8.2.2 Data Analysis 90
4.8.3 Retarding Potential Analyzer 92
4.8.3.1 Probe Design and Experimental Setup 92
4.8.3.2 Data Analysis 95
4.8.3.3 Measurement Uncertainty 97
4.8.4 Nude Faraday Probe 98
4.8.4.1 Probe Design and Experimental Setup 98
4.8.4.2 Data Analysis 99
4.8.4.3 Measurement Uncertainty 102
4.8.5 Near-field Faraday Probe 103
4.8.5.1 Probe Design and Experimental Setup 103
4.8.5.2 Data Analysis 105
4.8.5.3 Measurement Uncertainty 109
4.9 Internal Diagnostics 111
4.9.1 Measurement Domain 111
4.9.2 Single Cylindrical Langmuir Probe (Internal) 112
4.9.2.1 Probe Design and Setup 113
4.9.2.2 Probe Operation 114
4.9.2.3 Data Analysis 117
4.9.2.4 Probe Measurement Circuit 120
4.9.3 Floating Emissive Probe 122
4.9.3.1 Probe Design and Setup 123
4.9.3.2 Data Analysis 124
4.9.3.3 Probe Measurement Circuit 126
4.10 Summary 128

Chapter 5 Plume Measurements 130

5.1 Angularly-Resolved E×B Measurements 131
5.1.1 Variation with Flow Rate 134
5.1.2 Variation with Discharge Power 137
5.1.3 Discussion 138
5.2 Far-field Langmuir Probe Measurements 140
5.3 Retarding Potential Analyzer Measurements 142

5.4 Far-field Faraday Probe Measurements 143
5.5 Near-field Faraday Probe Measurements 146
5.5.1 Near-field Ion Current Density 146
5.5.2 Centerline "Spike" 151
5.5.3 Current Density Fluctuations 157
5.5.4 Integrated Ion Beam Current 160
5.5.5 Plume Divergence 164
5.6 Summary of Plume Measurements 166

Chapter 6 Performance Measurements and Efficiency Analysis 168

6.1 Framework of Phenomenological Performance Model 169
6.2 Discharge Oscillations 171
6.3 Performance 177
6.3.1 Thrust 178
6.3.2 Total Specific Impulse 179
6.3.3 Total Efficiency 180
6.3.4 Thrust-to-Power 182
6.4 Utilization Efficiencies 183
6.5 Discussion 184
6.6 Summary of Efficiency Analysis Findings 189

Chapter 7 Internal Measurements 191

7.1 Probe-Induced Perturbations 191
7.2 Langmuir Probe 195
7.2.1 Fluctuations in Plasma Properties 195
7.2.2 Floating Potential 196
7.2.3 Electron Temperature 198
7.2.4 Ion Number Density 201
7.3 Floating Emissive Probe Results 209
7.3.1 Electron Temperature 210
7.3.2 Plasma Potential Fluctuations 213
7.3.3 Plasma Potential 217
7.3.4 Axial Electric Field 221
7.3.5 Radial Electric Field 223
7.4 Discussion 224
7.4.1 Hall Thruster Regions 224
7.4.1.1 Ionization Region 225
7.4.1.2 Acceleration Region 225
7.4.1.3 High T_e Region 226

7.4.2 Comparisons with HPHALL-2 Simulations 230
7.4.3 Plasma Potential Consistency 236
7.5 Summary of Internal Measurements 237

Chapter 8 Internal Analysis 240

8.1 Electron Equations 241
8.1.1 Electron Energy Equation 241
8.1.2 Electron Momentum Equation 243
8.1.3 Collisions 246
8.1.4 Total Hall Parameter 248
8.2 Continuity Analysis 249
8.2.1 Ion and Electron Current 252
8.2.2 Neutral Density 255
8.3 Collision Frequency 264
8.3.1 Experimental Collisions 264
8.3.2 HPHALL-2 Simulations 267
8.4 Hall Parameter 268
8.4.1 Classical Hall Parameter 269
8.4.2 Total Hall Parameter 273
8.4.3 HPHALL-2 Simulations 277
8.4.4 Discrepancy in the Near-field Plume 280
8.5 Hall Current 283
8.6 Trends with Flow Rate 286
8.6.1 Internal Regions 286
8.6.2 Electron Temperature 290
8.7 Summary of Internal Analysis 293

Chapter 9 Conclusions 296

9.1 Neutral Flow Dynamics 297
9.2 Influence of Neutral Flow Rate 297
9.3 Three-region Mobility 298
9.4 Comparisons with HPHALL-2 299
9.5 Suggestions for Future Work 299

Bibliography 334

List of Figures

Figure 2-1. Cross-section of a typical Hall thruster with a center-mounted cathode. 15

Figure 2-2. Schematic of typical Hall thruster magnetic field. 16

Figure 2-3. Schematic of Hall thruster ionization and acceleration regions. 17

Figure 2-4. Generic representation of plasma potential, ion density, and magnetic field profiles in the channel of a Hall thruster. 17

Figure 3-1. Schematic of primary Hall thruster anode configurations for neutral injection. 22

Figure 3-2. Schematic of UM/AFRL P5 Hall thruster anode. The anode uses radial injection towards channel centerline. 23

Figure 3-3. Schematic of primary Hall thruster anode configurations for neutral injection (not to scale). 29

Figure 3-4. Schematic showing temperature boundary conditions used in analytical calculations. 30

Figure 3-5. Photograph of the UM/AFRL P5 Hall thruster operating at nominal conditions of 300 V and 10 mg/s. 36

Figure 3-6. Photograph of the 6-kW Hall thruster operating at nominal conditions of 300 V and 20 mg/s. 36

Figure 3-7. Comparison of simulated neutral flux at the anode exit plane for FLUENT, MONACO, and HPHALL-2. 42

Figure 3-8. Schematic of APAT pressure probe inlet tube and inlet chamfering (not to scale). 45

Figure 3-9. Calculated probe settling time as a function of pressure for several probe diameters. Measured settling time for the Pirani gauge is also shown. 47

Figure 3-10. Comparison of radial pressure profiles for MONACO simulations and experimental measurements with and without the discharge channel. 50

Figure 3-11. Simulated and experimental neutral pressure on channel centerline for anode mass flow rate of 20 mg/s. 52

Figure 3-12. Simulated neutral properties in the discharge channel for an injected mass flow rate of 20 mg/s. FLUENT (top), MONACO (middle), and HPHALL-2 (bottom). 54

Figure 3-13. Raw experimental (left) and HPHALL-2 simulated (right) neutral pressure in the discharge channel for injected mass flow rates of 10, 20, and 27 mg/s. 57

Figure 3-14. Corrected experimental (left) and HPHALL-2 simulated (right) neutral pressure in the discharge channel for injected mass flow rates of 10, 20, and 27 mg/s. 58

Figure 3-15. FLUENT simulations of the mass flux at the anode exit for the NASA-173M and 6-kW Hall thruster. 61

Figure 3-16. FLUENT simulated axial velocity variation with anode temperature at anode centerline and average across the anode exit [31]. Square-root dependence of the axial velocity on anode temperature is shown by the dashed lines. 63

Figure 3-17. HPHALL-2 simulation results for neutral density on thruster centerline during cold flow operation (no plasma). 65

Figure 3-18. Neutral properties from HPHALL-2 simulations on channel centerline in the presence of the discharge plasma. 67

Figure 4-1. Photograph of the Large Vacuum Test Facility at the University of Michigan's Plasmadynamics and Electric Propulsion Laboratory. 70

Figure 4-2. Facility pressure as a function of total xenon mass flow rate for the LVTF. The average pressure indicates a facility pumping speed of approximately 220,000 l/s. 71

Figure 4-3. Photograph of the 6-kW Hall thruster prior to initial firing. 72

Figure 4-4. Photograph of the 6-kW Hall thruster during operation at 300 V and 20 mg/s (6 kW). 73

Figure 4-5. Schematic of the thruster and probe positioning systems used for internal plasma measurements. 76

Figure 4-6. Photograph of probe insertion into the thruster discharge channel during internal plasma measurements with the HARP. 77

Figure 4-7. Change in thrust due to change in thrust stand inclination. 79

Figure 4-8. E×B probe schematic (not to scale). 84

Figure 4-9. E×B probe electrical diagram. 84

Figure 4-10. Ion current density taken on a 1-m arc from 0 to 90°, showing E×B data collection locations. 88

Figure 4-11. Schematic of the cylindrical Langmuir probe used in the far-field plume (not to scale). 90

Figure 4-12. Sample Langmuir probe I-V characteristic illustrating the methods used to compute the plasma potential for correcting the RPA measurements. 91

Figure 4-13. Schematic of the RPA showing major internal components. 93

Figure 4-14. Electrical Schematic of the RPA. 94

Figure 4-15. Electric potential diagram showing the relationship between experimentally measured quantities (V_{RPA}, V_p, V_k, V_D), the most probable voltage (V_{mp}), and the loss voltage (V_{loss}). 96

Figure 4-16. Sample ion voltage distribution demonstrating the definitions of V_{mp} and FWHM. 97

Figure 4-17. Schematic of the JPL nude Faraday Probe. 99

Figure 4-18. Schematic of near-field Faraday probe design and construction (not to scale). 104

Figure 4-19. Measurement domain for the near- and far-field Faraday probe measurements (not to scale). 105

Figure 4-20. Schematic showing the modified 1/e integration bounds for a sweep that does not reach 1/e at the inner radius (~ 0.5 $D_{T,mean}$). 108

Figure 4-21. Schematic of internal measurement domain (not to scale). 112

Figure 4-22. Schematic of Langmuir probe construction (not to scale). 114

Figure 4-23. Schematic of Langmuir probe voltage characteristic during injection into the discharge channel. 115

Figure 4-24. Capacitive current caused by line capacitance due to the probe voltage oscillation. 116

Figure 4-25. Schematic of Langmuir probe measurement and bias circuits. 122

Figure 4-26. Schematic of probe design and construction (not to scale). 124

Figure 4-27. Schematic of emissive probe voltage measurement circuit and heater supply. 127

Figure 4-28. Emissive probe filament voltage drop along channel centerline for thruster operation at 300 V and 10 mg/s. 128

Figure 5-1. Xe^{1+} and Xe^{2+} ion current fractions for 300 V, 10, 20, and 30 mg/s ($z = 9\ D_{T,mean}$). Open markers are uncorrected data, solid markers have been corrected for CEX. 132

Figure 5-2. Xe^{3+} ion current fraction and $\Sigma(\Omega_i/Z_i)$ for 300 V, 10, 20, and 30 mg/s ($z = 9\ D_{T,mean}$). Open markers are uncorrected data, solid markers have been corrected for CEX. 133

Figure 5-3. Plume-averaged $\Sigma(\Omega_i/Z_i)$ for thruster operation at 300 V and 10, 20, and 30 mg/s. 135

Figure 5-4. $\Sigma(\Omega_i/Z_i)$ versus discharge power for plume-averaged, thruster center, and channel center quantities. 139

Figure 5-5. Far-field Langmuir probe ln(I) and dI/dV displaying plasma potential used to correct the RPA. 141

Figure 5-6. RPA ion voltage distribution for operation at 300 V and 10, 20, and 30 mg/s. 143

Figure 5-7. Far-field Faraday probe measurements for thruster operation at 300 V and 5, 10, 20, and 30 mg/s. 144

Figure 5-8. Ion current density in the near-field plume for thruster operating conditions of 300 V and 10, 20, and 30 mg/s (note exponential contour scaling). 147

Figure 5-9. Comparison of ion current density at several axial locations for thruster operation at 300 V and 20 mg/s. 149

Figure 5-10. Peak current density for thruster operation at 300 V and 10, 20, and 30 mg/s. 150

Figure 5-11. Photograph of the 6-kW Hall thruster operating at 300 V and 20 mg/s. Note the "spike" that emanates from the center of the thruster. 152

Figure 5-12. Plasma potential in the near-field plume for thruster operating conditions of 300 V at 10 and 20 mg/s (data courtesy JPL). 155

Figure 5-13. Standard deviation of the ion current density for thruster operation at 300 V and 10, 20, and 30 mg/s. 158

Figure 5-14. Integrated ion beam currents using three different integration techniques for thruster operation at 300 V and 20 mg/s. 161

Figure 5-15. Integrated ion beam current at each axial location for thruster operation at 300 V and 10, 20, and 30 mg/s. 163

Figure 5-16. Plume divergence at each axial location for thruster operation at 300 V and 10, 20, and 30 mg/s. 165

Figure 6-1. Discharge oscillation spectra for thruster operation from 150-600 V and 10 to 30 mg/s. 172

Figure 6-2. Breathing mode frequency for thruster operation from 150 to 600 V and 10 to 30 mg/s. 173

Figure 6-3. Discharge oscillation in percent of mean for thruster operation from 150 to 600 V and 10 to 30 mg/s. 174

Figure 6-4. Discharge current versus discharge voltage for anode flow rates from 5 to 30 mg/s. 176

Figure 6-5. Measured thrust for operation at 150-600 V and 5-30 mg/s. 179

Figure 6-6. Total specific impulse for operation at 150-600 V and 5-30 mg/s. 180

Figure 6-7. Total efficiency for operation at 150-600 V and 5-30 mg/s. 181

Figure 6-8. Thrust-to-power ratio for operation at 150-600 V and 5-30 mg/s. 182

Figure 6-9. Measured and computed thruster efficiency and individual utilization efficiencies for thruster operation at 300 V and 10, 20, and 30 mg/s. 183

Figure 7-1. Probe induced perturbations of discharge current and cathode potential during probe insertion at 300 V and 10 mg/s. 192

Figure 7-2. Discharge current and cathode potential perturbations throughout the measurement domain for thruster operation at 300 V and 10 mg/s. 193

Figure 7-3. Langmuir probe I-V trace, discharge current, and cathode potential at 360% L_c from the anode for thruster operation at 300 V and 10 mg/s. 196

Figure 7-4. Comparison of floating potential with respect to cathode on channel centerline for thruster operating conditions of 300 V and 10, 20, and 30 mg/s. 197

Figure 7-5. Electron temperature measured by the Langmuir probe for thruster operation at 300 V and 10, 20, and 30 mg/s. 199

Figure 7-6. Comparison of electron temperature calculated by the Langmuir probe on channel centerline for thruster operating conditions of 300 V and 10, 20, and 30 mg/s. 200

Figure 7-7. R_p/λ_D for thruster operation at 300 V and 10, 20, and 30 mg/s. ..202

Figure 7-8. Thin sheath ion density measured by the Langmuir probe for thruster operation at 300 V and 10, 20, and 30 mg/s. 203

Figure 7-9. OML ion density measured by the Langmuir probe for thruster operation at 300 V and 10, 20, and 30 mg/s. 204

Figure 7-10. Blended ion density measured by the Langmuir probe for thruster operation at 300 V and 10, 20, and 30 mg/s. 205

Figure 7-11. Centerline comparison of ion number density for thin sheath analysis at 300 V and 10, 20, and 30 mg/s. 208

Figure 7-12. Centerline comparison of ion number density for OML analysis at 300 V and 10, 20, and 30 mg/s. 208

Figure 7-13. Centerline comparison of ion number density for blended analysis at 300 V and 10, 20, and 30 mg/s. 209

Figure 7-14. Electron temperature from emissive probe for thruster operation at 300 V and 10, 20, and 30 mg/s. 212

Figure 7-15. Emissive probe electron temperature on channel centerline at 300 V and 10, 20, and 30 mg/s. 213

Figure 7-16. Time-dependent correlation between plasma potential and discharge current oscillations on channel centerline and 10% L_c from the anode during thruster operation at 300 V and 10 mg/s. 214

Figure 7-17. Plasma potential percent oscillation throughout the measurement domain for thruster operation at 300 V and 10, 20, and 30 mg/s. 216

Figure 7-18. Plasma potential contours for thruster operation at 300 V and 10, 20, and 30 mg/s 218

Figure 7-19. Comparison of pre- and post-corrected plasma potentials, including electron temperature at 300 V and 10 mg/s. 220

Figure 7-20. Comparison of plasma potential on channel centerline at 300 V and 10, 20, and 30 mg/s. 220

Figure 7-21. Axial electric field contours for thruster operation at 300 V and 10, 20, and 30 mg/s 222

Figure 7-22. Comparison of axial electric field on channel centerline at 300 V and 10, 20, and 30 mg/s. 223

Figure 7-23. Location of upstream and downstream boundaries of ionization region for thruster operation at 300 V and 10, 20, and 30 mg/s. 227

Figure 7-24. Location of upstream and downstream boundaries of acceleration region for thruster operation at 300 V and 10, 20, and 30 mg/s. 228

Figure 7-25. Location of upstream and downstream boundaries of high electron temperature region for thruster operation at 300 V and 10, 20, and 30 mg/s. 229

Figure 7-26. Comparison of plasma potential and electron temperature for HPHALL-2 simulations and experimental results on channel centerline at 300 V and 10, 20, and 30 mg/s. 233

Figure 7-27. Comparison of ion density for HPHALL-2 simulations and experimental results on channel centerline at 300 V and 10, 20, and 30 mg/s. 235

Figure 7-28. Comparison of RPA most probable voltage and plasma potential at peak ion density measured by the emissive probe for thruster operation at 300 V and 10, 20, and 30 mg/s. 237

Figure 8-1. Schematic of coordinate transformation used in electron analysis. 243

Figure 8-2. Experimental ion and electron currents at each axial location for operation at 300 V and 10, 20, and 30 mg/s. 253

Figure 8-3. Simulated ion and electron currents at each axial location for operation at 300 V and 10, 20, and 30 mg/s. 254

Figure 8-4. Centerline neutral density calculated from 1-D analysis for thruster operation at 300 V and 10, 20, and 30 mg/s (uncorrected). 256

Figure 8-5. HPHALL-2 simulated neutral density on thruster centerline during thruster operation at 300 V and 10, 20, and 30 mg/s. 257

Figure 8-6. Schematic of the geometric area definitions used in the mass correction for the 1-D mass continuity analysis. 259

Figure 8-7. HPHALL-2 simulation results for the mass flux within the experimental measurement domain at 300 V and 20 mg/s. 260

Figure 8-8. Centerline neutral density calculated from 1-D analysis for thruster operation at 300 V and 10, 20, and 30 mg/s (corrected). 261

Figure 8-9. Contours of experimental neutral density during thruster operation at 300 V and 10, 20, and 30 mg/s (corrected). 262

Figure 8-10. Contours of simulated neutral density for thruster conditions of 300 V and 20 mg/s. 264

Figure 8-11. Electron collision frequencies for thruster operation at 300 V and 10, 20, and 30 mg/s. 266

Figure 8-12. HPHALL-2 simulated collision frequencies 300 V and 20 mg/s. Values are volume-weighted averages over magnetic field lines. 268

Figure 8-13. Classical Hall parameter contours for thruster operation at 300 V and 10, 20, and 30 mg/s. 270

Figure 8-14. Radially-averaged classical Hall parameter (including wall collisions) downstream of the anode for thruster operation at 300 V and 10, 20, and 30 mg/s. 272

Figure 8-15. Radially-averaged classical Hall parameter as a function of plasma potential for thruster operation at 300 V and 10, 20, and 30 mg/s. 273

Figure 8-16. Total Hall parameter contours for thruster operation at 300 V and 10, 20, and 30 mg/s. 274

Figure 8-17. Radially-averaged total Hall parameter downstream of the anode for thruster operation at 300 V and 10, 20, and 30 mg/s. 276

Figure 8-18. Radially-averaged total Hall parameter as a function of plasma potential for thruster operation at 300 V and 10, 20, and 30 mg/s. 277

Figure 8-19. Simulated classical Hall parameter on channel centerline for thruster operating conditions of 300 V and 10, 20, and 30 mg/s..278

Figure 8-20. Simulated total Hall parameter on channel centerline for thruster operating conditions of 300 V and 10, 20, and 30 mg/s. 279

Figure 8-21. Turbulence intensity ratio along channel centerline for thruster operation at 300 V and 10, 20, and 30 mg/s. 282

Figure 8-22. Hall current contour plots for thruster operation at 300 V and 10, 20, and 30 mg/s.....285

Figure 8-23. Schematic showing the downstream displacement of the high electron temperature region with increased flow rate. 288

Figure 8-24. HPHALL-2 simulated contributions to the electron energy equation for thruster conditions of 300 V and 10, 20, and 30 mg/s. 292

Figure B-1. Thrust and discharge current variations with facility backpressure at 6 kW thruster power (300 V and 20 mg/s).....308

Figure B-2. Thrust and discharge current variations with facility backpressure at 8 kW thruster power (400 V and 20 mg/s).....309

Figure B-3. Ion current density measurements at facility pressures ranging from 1.5 to 2.0×10^{-5} torr-xe. 315

Figure B-4. Linear relationship of ion current density with facility pressure at several angular locations.....316

Figure B-5. Comparison of ion current density profiles for uncorrected forward-facing, rear-facing corrected by reverse-facing, linear extrapolation correction, and gridded Faraday probe.....318

Figure C-1. Far-field Faraday probe measurements at 150 V and 10, 20, and 30 mg/s. 320

Figure C-2. Xe^{1+} and Xe^{2+} ion current fractions for thruster operation at 150 V and 10, 20, and 30 mg/s ($z = 9\ D_{T,mean}$). Open markers are uncorrected data, solid markers have been corrected for CEX. 321

Figure C-3. Xe^{3+} ion current fraction and $\Sigma(\Omega_i/Z_i)$ for thruster operation at 150 V and 10, 20, and 30 mg/s ($z = 9\ D_{T,mean}$). Open markers are uncorrected data, solid markers have been corrected for CEX. 322

Figure C-4. Near-field Faraday probe measurements at 150 V and 10, 20, and 30 mg/s. 323

Figure C-5. Integrated beam current for thruster operation at 150 V and 10, 20, and 30 mg/s. 324

Figure C-6. Plume divergence half-angle for thruster operation at 150 V and 10, 20, and 30 mg/s....325

Figure C-7. Measured and computed thruster efficiency and individual utilization efficiencies for thruster operation at 150 V and 10, 20, and 30 mg/s. 327

Figure C-8. Plasma potential contours for thruster operation at 150 V and 10, 20, and 30 mg/s....328

Figure C-9. Axial electric field contours for thruster operation at 150 V and 10, 20, and 30 mg/s....329

Figure D-1. Near-field Faraday probe measurements with the NASA-173M Hall thruster operating at 300 V and 7, 10, and 15 mg/s. 331

Figure D-2. Integrated beam current at each axial location for the NASA-173M Hall thruster operating at 300 V and 7, 10, and 15 mg/s....332

Figure D-3. Plume divergence half-angle at each axial location for the NASA-173M Hall thruster operating at 300 V and 7, 10, and 15 mg/s...333

List of Tables

Table 2-1: Typical performance parameters for various propulsion systems. 11

Table 5-1: Maximum values of each of the terms in Eq. 5-1, derived from HPHALL-2 simulations. 137

Table 5-2: Summary of results from plume measurements for thruster operation at 300 V. 167

Table 6-1: Summary of results from discharge current oscillations analysis. ...174

Table 6-2: Summary of results from efficiency analysis. 190

Table 7-1: Summary of inputs used for HPHALL-2 simulations. 231

Table 7-2: Summary of peak ion number density, axial electric field, and electron temperature (averaged across channel). 239

Table 7-3: Summary of peak location for ion number density, axial electric field, and electron temperature (averaged across channel). 239

Table 7-4: Summary of region length for ionization, acceleration, and high electron temperature regions (averaged across channel). 239

Table A-1. 6-kW Hall thruster performance data taken at PEPL after approximately 220 hours of operation. 304

Table A-2: 6-kW Hall thruster performance data taken at PEPL after approximately 40 hours of operation. 305

Table A-3: 6-kW Hall thruster performance data taken at AFRL after approximately 40 hours of operation. 305

Table C-1: Results from plume measurements for operation at 150 V..... 326

Table C-2: Results from efficiency analysis for operation at 150 V. 327

List of Appendices

Appendix A Summary of Performance Data 303

Appendix B The Effect of Facility Neutrals on Performance and Plume Measurements 306

B.1 Performance Measurements 306
B.1.1 6-kW, 300 V Thruster Operation 307
B.1.2 8-kW, 400 V Thruster Operation 308
B.2 Analytical Method to Quantify Facility Effects on Performance Measurements 309
B.2.1 Entrained Neutral Gas 310
B.2.2 Discharge Current Correction 311
B.2.3 Thrust Correction 312
B.2.4 Pressure Criterion 314
B.3 Faraday Probe Measurements 315
B.4 Summary of Facility Effects 318

Appendix C Low Discharge Voltage Measurements 320

Appendix D Near-field Faraday Probe Measurements for the NASA-173M Hall Thruster 330

Nomenclature

Constants

e	electron charge, 1.6022×10^{-19}	[C]
g	gravitational acceleration, 9.8067	[m/s^2]
k_B	Boltzmann's constant, 1.3807×10^{-23}	[J/K]
m_e	mass of an electron, 9.1094×10^{-31}	[kg]
m_{xe}	mass of a xenon atom, 2.1801×10^{-25}	[kg]
n_o	reference density, 1×10^{18}	[m^{-3}]
ε_o	permittivity of free space, 8.8542×10^{-12}	[F/m]
μ_o	permeability of free space, $4\pi\times10^{-7}$	[H/m]

Variables (Arabic)

A_c	collector area	[m^2]
A_{ch}	discharge channel cross sectional area	[m^2]
A_{en}	neutral entrainment area	[m^2]
A_p	probe area	[m^2]
A_s	sheath area	[m^2]

b	discharge channel width	[m]
B	magnetic field	[T]
C	capacitance	[F]
d	tube diameter or E×B plate gap distance	[m]
D	diffusivity	[m^2/s]
$D_{T,mean}$	mean thruster diameter	[m]
$\hat{e}$	unit vector for coordinate transformation	[-]
E	electric field	[V/m]
E_i	ionization energy	[eV]
F	force or Lorentz force	[N]
$f(V)$	ion velocity distribution function	[-]
f_B	breathing mode frequency	[Hz]
f_{esc}	escaping particle velocity distribution function	[-]
I_B	beam current	[A]
I_{cap}	capacitive current	[A]
I_{corr}	corrected discharge current	[A]
I_D	discharge current	[A]
ID	inner diameter	[m]
I_e	electron current	[A]
I_{en}	neutral entrainment current	[A]
I_i	ion current	[A]

$I_{i,sat}$	ion saturation current	[A]
IR	inner radius	[m]
I_{sp}	specific impulse	[s]
I_{tot}	total integrated current (entire trace method)	[A]
$I_{tot,DC}$	total integrated current (DC-only method)	[A]
$I_{tot,dyn}$	total integrated current (dynamic window method)	[A]
j	ion current density	[A/m^2]
L_a	ionization region length	[m]
L_c	discharge channel length	[m]
M	Mach number	[-]
m	atomic mass of propellant	[kg]
M_f	final spacecraft mass	[kg]
m_i	ion mass	[kg]
M_o	initial spacecraft mass	[kg]
M_p	mass of propellant	[kg]
$\dot{m}_a$	anode mass flow rate	[kg/s]
$\dot{m}_b$	beam mass flow rate	[kg/s]
$\dot{m}_c$	cathode mass flow rate	[kg/s]
$\dot{m}_{en}$	entrained mass flow rate	[kg/s]
$\dot{m}_t$	total mass flow rate (anode + cathode)	[kg/s]
N	reference density for settling time calculations	[m^{-3}]

$\dot{n}_i$	ion production rate	[$m^{-3}s^{-1}$]
OD	outer diameter	[m]
OR	outer radius	[m]
OR_{beam}	outer radius of main ion beam	[m]
P	pressure	[N/m^2]
P_b	facility base pressure	[N/m^2]
P_c	facility corrected pressure	[N/m^2]
P_e	electron pressure	[N/m^2]
P_D	discharge power	[W]
P_i	facility indicated pressure	[N/m^2]
P_{jet}	jet power	[W]
P_t	total thruster power (discharge + magnets)	[W]
Q	fit coefficienct for Drawing ionization model	[-]
Q_{ei}	electron-ion cross section	[m^2]
Q_{en}	electron-neutral cross section	[m^2]
Q_{MT}	electron-neutral momentum transfer cross section	[m^2]
R	gas constant	[J/kg-K]
R	far-field Faraday probe distance from thruster	[m]
r_L	Larmor radius	[m]
R_{mean}	discharge channel mean radius	[m]
R_p	probe radius	[m]

S_i	inelastic loss term in electron energy equation	[W/m^3]
T	thrust or temperature	[N]
T_{corr}	corrected thrust	[N]
T_e	electron temperature	[eV]
u_e	exhaust or electron velocity	[m/s]
u_i	ion velocity	[m/s]
u_n	neutral velocity	[m/s]
u_{pass}	pass velociy of the E×B	[m/s]
Δu	spacecraft velocity change	[m/s]
Δu_a	velocity change across acceleration region	[m/s]
V_{accel}	ion acceleration voltage	[V]
V_D	discharge voltage	[V]
V_f	floating potential	[V]
V_K	cathode floating potential	[V]
V_L	ion acceleration voltage loss	[V]
V_{mp}	RPA most probable voltage	[V]
V_p	plasma potential	[V]
V_p^*	thermalized plasma potential	[V]
$V_{p,loc}$	local plasma potential	[V]
V_{probe}	probe voltage	[V]
V_{RPA}	ion voltage measured by RPA	[V]

z	axial location	[m]
Z	ion charge state	[-]

Variables (Greek)

α	neutral temperature accomodation factor	[-]
$\alpha(T_e)$	ionization rate parameter	[-]
α_B	Bohm coefficient	[-]
β_1, β_2	fit coefficiencts for Drawing ionization model	[-]
$\Gamma_m, \Gamma_{m,c}$	mass flux, centerline mass flux	[kg/m^2-s]
γ	ratio of specific heats	[-]
ε	electron current recylce fraction	[-]
ζ_{en}	entrainment utilization	[-]
ζ_i	species fraction of ith ion species	[-]
η_a	anode efficiency	[-]
η_b	current utilization efficiency	[-]
η_c	cathode utilization efficiency	[-]
η_d	divergence utilization efficiency	[-]
η_m	mass utilization efficiency	[-]
η_{mag}	magnet efficiency	[-]
η_q	charge utilization efficiency	[-]
η_t	total efficiency	[-]

η_v	voltage utilization efficiency	[-]
θ	beam divergence angle	[degrees]
λ_D	Debye length	[m]
Λ	plasma parameter	[-]
$\mu, \mu_\perp$	electron mobility, cross-field mobility	[C-s/kg]
ν	collision frequency	[Hz]
ξ	exchange ratio	[-]
ρ	mass density	[kg/m^3]
σ_e	electron conductivity tensor	[F/m-s]
σ_{en}	electron-neutral collision cross section	[m^2]
τ	pressure probe settling time	[s]
τ_i	ionization time	[s]
τ_{res}	neutral residence time	[s]
ϕ	coordinate transformation rotation angle	[degrees]
φ	Dugan's ionization cost factor	[-]
ω_c	electron cyclotron frequency	[Hz]
ω_e	electron plasma frequency	[Hz]
Ω_e	electron Hall parameter	[-]
Ω_i	current fraction of ith ion species	[-]
$\Omega_{i,avg}$	plume-averaged current fraction	[-]
$\Omega_{i,loc}$	local current fraction of ith ion species	[-]

Subscripts

CB	contiunnum-based
class	classical
e	electron
i	ion
KB	kinetic-based
n	neutral
r	radial
tot	total
turb	turbulent
z	axial
θ	azimuthal, or angular
$\perp$	perpendicular
$\parallel$	parallel

Acronyms

AFRL	Air Force Research Laboratory
BNC	Bayonet Neill-Concelman
CDT	Closed Drift Thruster
CEX	Charge-exchange collision
CFD	Computational Fluid Dynamics
DAQ	Data Acquisition

DSMC	Direct Simulation Monte Carlo
EEDF	Electron Energy Distribution Function
FFT	Fast Fourier Transform
FWHM	Full Width at Half Maximum
GRC	Glenn Research Center
HARP	High-speed Axial Reciprocating Probe
ITAR	International Traffic in Arms Regulation
I-V	Current-Voltage characteristic
JPL	Jet Propulsion Laboratory
LVTF	Large Vacuum Test Facility
MPD	Magnetoplasmadynamic thruster
NASA	National Aeronautics and Space Administration
OML	Orbital Motion Limited
PEPL	Plasmadynamics and Electric Propulsion Laboratory
PIT	Pulsed Inductive Thruster
PPT	Pulsed Plasma Thruster
RHS	Right Hand Side
RPA	Retarding Potential Analyzer
SEE	Secondary Electron Emission
SPT	Stationary Plasma Thruster
TAL	Thruster with Anode Layer
UM	University of Michigan

Abstract

Neutral flow dynamics in Hall thrusters are not often regarded as a critical aspect that controls thruster operation and discharge channel physics. This dissertation, combined with previous work, showed that neutral flow dynamics affect global properties including thruster performance, stability, thermal margin, and lifetime. In addition, the neutral flow rate, and more importantly, the electron-neutral collision rate in the channel have an impact on other thruster properties including the location, size, and intensity of the ionization, high electron temperature, and acceleration regions. The results of these findings are relevant to ongoing efforts to understand thruster operation, electron physics, and thruster lifetime.

Performance and plume measurements indicated that thruster efficiency remained constant from ± 50% of the nominal flow rate of 20 mg/s. Current utilization was the primary loss mechanism and it decreased with flow rate due to increased ionization losses and electron-wall losses. To compensate, the divergence and mass utilizations increased with flow rate through a more

compact ionization region and increased ionization efficiency from the increasing neutral density.

Electron collision frequencies and the electron Hall parameter were calculated from measurements of the ion density, electron temperature, and electric field inside the discharge channel. The peak Hall parameter moved downstream and decreased in magnitude as flow rate was increased, and the results confirmed that there exist at least three distinct electron mobility regions as implemented in some plasma simulations. Near the anode, the turbulence was approximated by the Bohm value. Near the channel exit, the turbulence was suppressed and electrons were most effectively trapped by the Hall current in this region. In the plume, the turbulence was an order of magnitude greater than the Bohm value, indicating large contributions to electron transport from turbulence or a currently unaccounted for anomalous transport mechanism. For most of the channel, the electron-neutral collisions were the primary contributor to electron energy loss and cross-field mobility. However, near the channel exit, electron-wall collisions increased and became the primary contributor to the measured decrease in electron temperature with increased flow rate.

Chapter 1

Introduction

This chapter was written with two primary goals in mind: 1) to summarize the motivation for this dissertation and scientific contribution of the research contained herein, and 2) to introduce the organization of the remaining chapters.

1.1 Problem Statement

Hall thrusters are typically regarded as a moderate specific impulse (1600 seconds) space propulsion device. Since their acceptance by the Western scientific community in the late 20th century, Hall thrusters have gained popularity. Recently, Hall thruster have been as the primary propulsion system for a number of missions, including Deep Space 1 [1], SMART–1 [2], and DAWN [3]. As Hall thrusters find more applications for a variety of missions, it becomes more important to understand the details of thruster operation throughout a wide range of operating conditions. The main topics of concern in Hall thruster research can be loosely grouped into four categories:

1) Magnetic field (electron mobility, ionization, acceleration, erosion)

2) Cathode physics (coupling effects, electron physics)

3) Channel effects (erosion, secondary electron emission, sheaths)

4) Plume effects (limitations to efficiency, spacecraft interaction)

5) Neutral flow dynamics (electron mobility, ionization, erosion)

Many of the listed contributions (i.e., electron mobility, erosion) are affected by several categories, and some of the categories are dependent upon each other. These general categories are not meant as a comprehensive list of Hall thruster research topics or as a strict delineation between consequences of each topic; instead this list is meant as a functional delineation for discussion purposes.

The five research categories have each been investigated and understood to varying degrees. Of the five categories, neutral flow dynamics has likely received the least attention, and remains a topic of interest to the research community. This dissertation was written to increase the understanding of the influence of neutral flow dynamics in the operation of Hall thrusters.

1.2 Motivation for Research

The neutral flow dynamics in the discharge channel of Hall thrusters have typically been underemphasized in the literature. However, several studies that focused on the topic have indicated profound consequences of altering neutral flow conditions. Often, the significance of a properly designed neutral injection manifold is not recognized until an issue causes unfavorable operation of a Hall thruster. Improper anode design or functioning can have significant consequences

including asymmetric current density profiles, decreased thruster efficiency, reduction in thermal margin, or decreased stability.

The research presented in this dissertation focused on understanding the effects of neutral flow conditions (uniformity and velocity) and highlighted the fact that neutral flow rate has as much authority over the ionization and acceleration processes as the magnetic field and discharge voltage. This research was also intended to increase understanding of Hall thruster operation over a wide range of operating conditions.

1.3 Contribution of Research

This dissertation represents several contributions to the Hall thruster research and development community. Much of this work focused on a systematic study of the effects of neutral flow rate through characterization and analysis of the internal ionization and acceleration processes. The major contributions of this dissertation include:

1) **Parametric anode design technique and methodology**. Although not presented in this dissertation due to ITAR restrictions, a new method to design the gas distributor was formulated and validated with analytical, numerical, and experimental methods.
2) **Method of accurately measuring the neutral flow distribution downstream of an anode**. A neutral flow test-bed and measurement diagnostic were

introduced that allowed accurate measurements of the neutral flow distribution during cold-flow operation (no plasma).

3) **Method to consistently determine ion beam current and plume divergence half angle**. A new diagnostic and analysis technique allowed the first known measurement of ion beam current and plume divergence that were consistent with performance model estimations.

4) **Method of determining plume-averaged ion charge state**. Measurements of local ion charge state were weighted by the local current density to improve the fidelity of single-point E×B measurements. These improvements decreased the uncertainty in the charge state and improved results from the efficiency analysis.

5) **Plasma potential fluctuations within discharge channel**. Fluctuations of the plasma potential inside the discharge channel were correlated to discharge oscillations by acquiring data at high-speed during probe measurements. These measurements allowed a detailed perturbation analysis to be performed and identified a distinct correlation between discharge current oscillations and plasma potential fluctuations.

6) **Neutral flow rate controls ionization and acceleration locations.** Internal plasma measurements indicated a direct correlation between neutral flow rate and location of the primary ionization and acceleration regions. These results combined with the electron temperature results (below) indicated

that neutral flow rate has significant authority over the internal plasma structure. This authority has the potential to improve thruster performance, stability, thermal margin, and lifetime.

7) **Electron temperature decreases with flow rate**. Internal plasma measurements indicated that the electron temperature decreased with increased neutral flow rate, primarily due to increased wall losses near the exit plane (electron-neutral collisions also contributed).

8) **Facility effects on performance and plume measurements**. Thrust and ion current density were recorded as a function of facility pressure. The results indicated that facility neutrals are ingested by the thruster to create additional thrust and that facility-induced charge-exchange ions (CEX) cause significant scattering within the plume.

1.4 Organization

The organization of this dissertation can be naturally split into three major parts: 1) background information (Chapters 2-4), 2) plume characterization and analysis (Chapters 5 & 6), and 3) internal characterization and analysis (Chapters 7 & 8). Chapters 1 and 9 are introductory and concluding chapters, respectively.

Chapters 2-4 provide the reader with background information that motivated the research contained in this dissertation. Chapter 2 describes rocket propulsion fundamentals, categories of electric propulsion devices, and basics of

Hall thrusters – the focus of this dissertation. Chapter 3 discusses the neutral flow dynamics in Hall thrusters, focusing on the computational methods that can be used to predict neutral properties. Chapter 4 is largely a documentation of the experimental apparatus and analysis techniques that were used during data collection and processing.

Chapters 5 and 6 discuss the characterization of plasma properties in the near- and far-field plume. Chapter 5 discusses the near- and far-field plume measurements that were used to determine global plasma properties that describe the overall behavior of the thruster. Chapter 6 discusses the performance measurements that were taken with a thrust stand. Efficiency-limiting mechanisms were identified through an efficiency analysis that combined information from performance and plume measurements.

Chapters 7 and 8 continue characterization and discussion of plasma properties within the discharge channel. Chapter 7 describes the results from the internal measurements and Chapter 8 uses those measurements to discuss the electron mobility and trends that were seen in the data.

Finally, in Chapter 9, the major conclusions from this dissertation are summarized and suggestions for future research of Hall thrusters are proposed.

Chapter 2

Background

This chapter was written with the primary goal of introducing the reader to the fundamentals of rocket propulsion, the critical need for electric propulsion, and the basics of Hall thruster design and operation.

2.1 Rocket Propulsion Fundamentals

In general, rocket propulsion systems can be classified according to the type of energy source (chemical, nuclear, or solar), the basic function (booster stage, station keeping, etc.), and type of vehicle (aircraft, launch vehicle, satellite, etc.) [4]. Although there are a wide variety of rocket propulsion systems, the behavior of rockets can be described by a single equation that is derived from first principles: Tsiolkovsky's rocket equation

$$\frac{M_f}{M_o} = \frac{M_f}{M_p + M_f} = e^{-\Delta V / u_e}, \tag{2-1}$$

where M_f is the final rocket mass (dry mass), M_o is the initial rocket mass (wet mass), M_p is the propellant mass, ΔV is the change in rocket velocity, and u_e is the propellant exhaust velocity. To decrease the amount of propellant, which

increases the useful spacecraft payload, the exponential term on the right hand side of Eq. 2-1 must approach unity. Since the mission requirement (ΔV) and spacecraft mass (M_f) are typically fixed, the only practical way to decrease propellant mass is through increased exhaust velocity.

Rocket performance is typically reported in terms of specific impulse, I_{sp}, which is related to the exhaust velocity by

$$I_{sp} = \frac{T}{\dot{m}\, g} = \frac{u_e}{g}, \tag{2-2}$$

where T is the thrust, g is the gravitational constant, and $\dot{m}$ is the propellant mass flow rate. The specific impulse is a figure of merit for the thrust per propellant flow rate, and is analogous to the automotive industry's measure of fuel economy: "miles per gallon" [4].

Conventional rockets operate by converting the stored chemical energy of the propellant into kinetic energy by thermodynamic expansion through a nozzle. Since the specific energy of propellants and the variety of nozzle designs do not offer significant changes in performance, the specific impulse of chemical rockets is limited to a few hundred seconds. This level of performance limits the range of applicable missions, especially those that require large ΔV or have challenging mass constraints.

In general, electric propulsion is defined as the acceleration of gases to create thrust by electric heating, electric body forces, and/or electric and magnetic body forces [5, 6]. Electric propulsion devices use an external power

source to add energy to the propellant and accelerate the working fluid to high velocities. Unlike chemical propulsion, electric propulsion systems are not limited by the working fluid, rather they are limited by the amount of power available on the spacecraft.

The thruster efficiency η, is often described by the ratio of the jet power to the discharge power (input power) by

$$\eta = \frac{P_{jet}}{P_{tot}} = \frac{\dot{m}u_e^2}{2P_D} = \frac{g}{2P_D} I_{sp} T \,, \tag{2-3}$$

where P_D is the discharge power, $\dot{m}$ is the propellant mass flow rate, and Eq. 2-2 has been used to derive the relation on the right hand side. Equation 2-3 illustrates the inherent tradeoff between specific impulse and thrust; increasing the specific impulse at constant power necessitates a decrease in thrust. The intrinsically low thrust associated with electric propulsion causes longer spacecraft trip times and must be considered in the mission design phase. Although low thrust is often cited as a potential limitation of electric propulsion, it can similarly be seen as an advantage in situations where precision control is needed.

The most common application for electric propulsion systems have been station keeping in low-Earth and geosynchronous orbits. Recently, several missions including Deep Space 1 [1], SMART–1 [2], and DAWN [3] have demonstrated the ability of electric propulsion to serve as the primary propulsion

system for attitude control and orbit transfer and capture during science missions.

2.2 Electric Propulsion Overview

A concise history of electric propulsion is provided in Ref. [7], and the myriad of electric propulsion architectures can be grouped into three major categories that are discussed in greater detail in Refs. [5, 6]:

1) **Electrothermal** thrusters operate by electrically heating the working fluid and expanding it through a conventional rocket nozzle. Examples include resistojets, arcjets, and microwave thrusters.
2) **Electromagnetic** thrusters operate by accelerating an ionized gas through the interactions of plasma driven currents and applied magnetic fields. Examples include Pulsed Plasma Thrusters (PPTs), MagnetoPlasmaDynamic thrusters (MPDs), and Pulsed Inductive Thrusters (PITs).
3) **Electrostatic** thrusters operate imposing a static electric field to accelerate an ionized gas. Examples include gridded ion thrusters, Hall thrusters, colloid thrusters, and field emission thrusters.

A comparison of the performance parameters for several electric propulsion thrusters and chemical bi-propellant thrusters is shown in Table 2-1 [4, 8].

Table 2-1: Typical performance parameters for various propulsion systems.

	Power Level, kW	Specific Impulse, s	Efficiency, %
Chemical (bi-propellant)	--	300-450	--
Resistojet	0.5-1.5	200-350	65-80
Arcjet	0.3-30	500-1,500	24-45
Hall Thruster	0.1-20	1,000-3,000	45-65
Ion Engine	0.2-10	2,000-10,000	55-80
PPT	0.001-0.2	1,000-1,500	7-13
MPD	1-4,000	2,000-5,000	30-50

2.3 Hall Thrusters

For the remainder of this dissertation, the focus will remain on Hall thrusters. Conventional Hall thrusters are typically grouped into two variants known as anode layer and magnetic layer Hall thrusters. These two architectures employ similar fundamental methods of plasma generation and acceleration, with subtle differences in the details that are attributed to variations in the geometry and material selections. The work contained in this thesis is focused on the magnetic layer Hall thruster, but a cursory treatment of the anode layer Hall thruster is included for completeness.

2.3.1 Magnetic Layer Thrusters

The magnetic layer Hall thruster is also referred to as the Stationary Plasma Thruster (SPT) or Closed Drift Thruster (CDT). The term "Hall thruster" is generally acknowledged to refer to the magnetic layer variety due to the higher rate of acceptance and hence, characterization in the electric

propulsion community. The popularity of the magnetic layer Hall thruster is mainly attributed to the higher performance and lifetime when compared to the anode layer Hall thruster. In addition, the magnetic layer thruster is preferred since the erosion products are non-metallic, making spacecraft integration easier.

2.3.2 Anode Layer Thrusters

A Hall Thruster with Anode Layer (TAL) is similar to the magnetic layer Hall thruster, except having a shorter discharge channel that is composed of metal rather than ceramic. The lower Secondary Electron Emission (SEE) of the metal discharge channel reduces the number of low energy electrons emitted by the channel walls, resulting in a higher bulk electron temperature within the channel. The shorter channel length and higher bulk electron temperature also result in a higher peak electric field for acceleration of ions.

2.3.3 Hall Thruster Basics

Although the TAL and SPT Hall thruster variants are both similar, the following discussion will focus on the SPT due to its direct relevance to the research in this dissertation. A more detailed and rigorous treatment of the operation of Hall thrusters can be found in Refs. [9, 10].

Hall thruster designs can be broken into four major components, shown in Figure 2-1:

1) **Anode/Gas Distributor**. In addition to serving as the positive electrode for the thruster, the anode also serves as the gas distributor. The anode

is designed such that the propellant enters the discharge channel with low axial velocity and high radial and azimuthal uniformity [11, 12]. Several gas injection techniques can be implemented including radial injection, axial injection, and reverse injection. These variations are considered in more detail in Section 3.1.

2) **Cathode/Neutralizer**. In addition to serving as the negative electrode for the thruster, the cathode also serves as the electron source. A portion of the cathode electrons are "trapped" in the discharge channel by the magnetic field and the remaining electrons are used to neutralize the plume to prevent the spacecraft from charging. The cathode is typically located at the outermost diameter of the thruster; however, the cathode can be mounted internally if the thruster dimensions and thermal margin allow [13-15], as is the case for the 6-kW Hall thruster used in this dissertation.

3) **Discharge Channel**. The boron nitride discharge channel confines the neutral gas and plasma flow and protects the magnetic circuit from plasma interaction. The choice of wall material strongly influences the bulk electron temperature in the channel because of SEE effects [16-18]. Each primary electron that collides with the channel walls releases a flux of low-energy secondary electrons. Due to their lower temperature, the secondary electrons effectively cool the bulk electrons,

leading to an effective electron temperature that is approximately 10% of the discharge voltage [19-21]. The magnitude of the cooling effect depends primarily on the choice of wall material. Several ceramics have been investigated, including diamond [22, 23], graphite, silicon carbide, alumina, and boron nitride-silica [18, 24]. However, boron nitride remains the material of choice, and there have been additional studies concerning the particular grade of boron nitride [25]. Grade HP boron nitride is used in the 6-kW Hall thruster in this dissertation.

4) **Magnetic Circuit**. The primary function of the magnetic circuit is to provide the magnetic field that traps electrons in the discharge channel. In most thruster designs, the magnetic circuit also serves as the mechanical support structure for the remaining thruster components. The magnetic circuit is composed of several ferromagnetic parts (front/back poles, inner/outer screens, etc) that act as a "c-core" for inner and outer electromagnets. The magnetic circuit is designed so that the magnetic field topology creates electric potential lines that focus ions towards channel centerline and peaks near the exit plane.

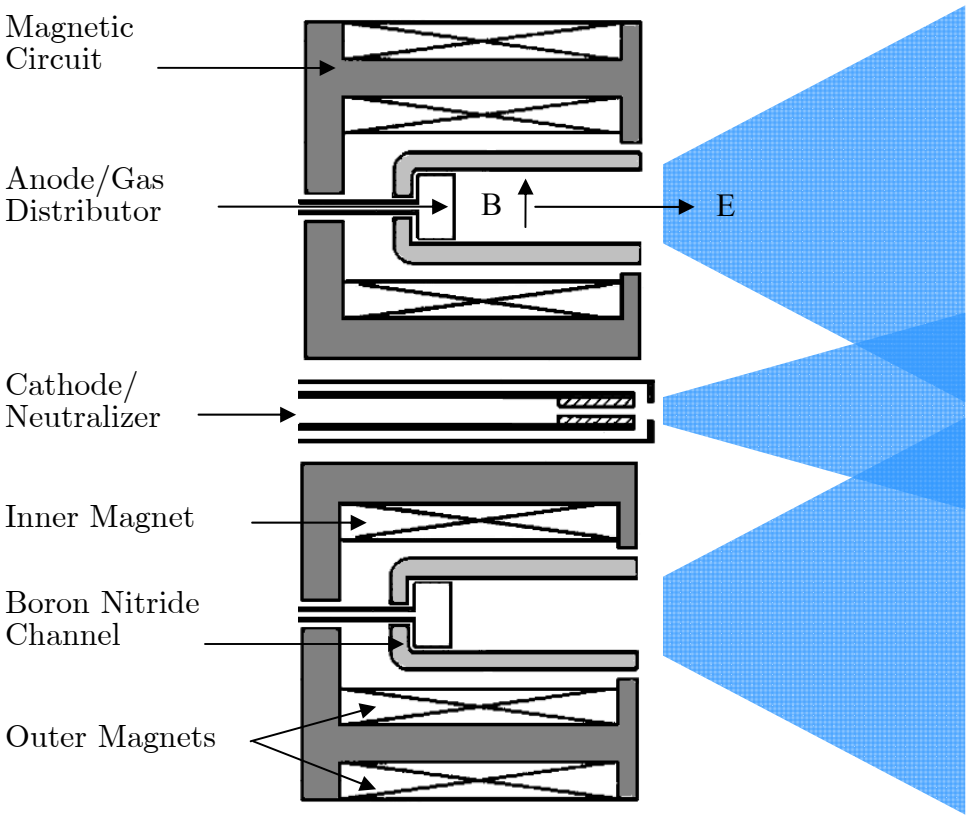

Figure 2-1. Cross-section of a typical Hall thruster with a center-mounted cathode.

The shape of the magnetic field is important in achieving high thruster efficiency. The magnetic field streamlines of the NASA-173Mv1 are shown in Figure 2-2 [26]. To first order, the electric potential lines are determined by the magnetic field lines and the curved shape inside the channel leads to the formation of a "plasma lens" that tends to focus ions towards channel centerline. This focusing effect increases the overall thruster performance by reducing thrust-vector cosine losses and increases thruster lifetime by reducing the number of ion collisions with the wall. The magnetic field also traps a portion of the electrons that are produced by the cathode, allowing them to be trapped in E×B motion so that they provide electron-impact ionization of the neutral propellant.

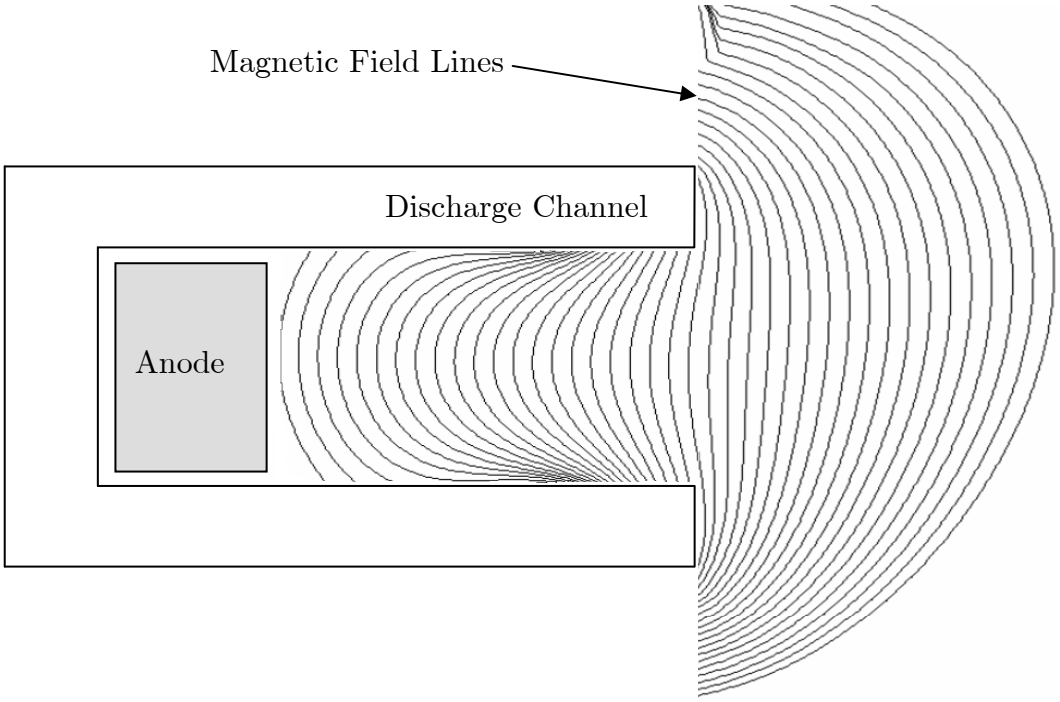

Figure 2-2. Schematic of typical Hall thruster magnetic field.

Most ionization occurs upstream of the thruster exit, while acceleration can extend outside the thruster depending on operating condition and specific design configurations. The ionization and acceleration regions overlap as shown in Figure 2-3, a characteristic that is responsible for most of the measured distribution in ion velocities in the plume. This distribution occurs because ions that are created in different parts of the acceleration region experience a different amount of total acceleration, altering the ion's terminal velocity. The cause for this ion velocity distribution is shown in Figure 2-4, which shows a generic view of the ion density (n_i), plasma potential (V_p), and magnetic field (B_r) profiles. The primary feature to note in Figure 2-4 is that not all ions are created at the same plasma potential, allowing ions to have distribution of terminal velocities.

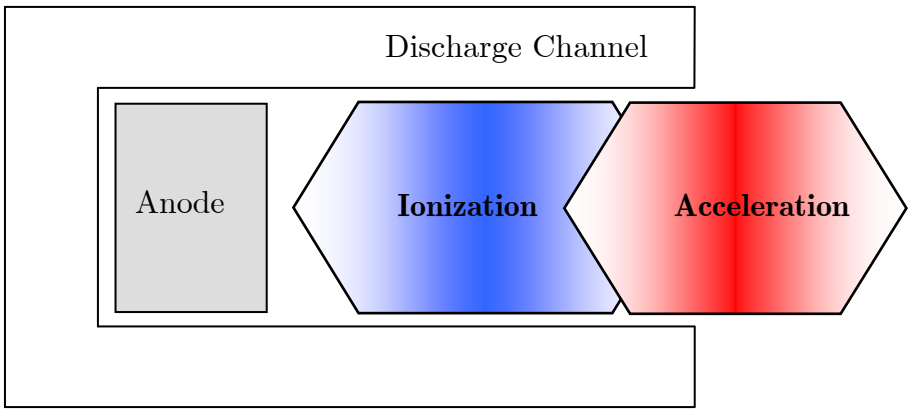

Figure 2-3. Schematic of Hall thruster ionization and acceleration regions.

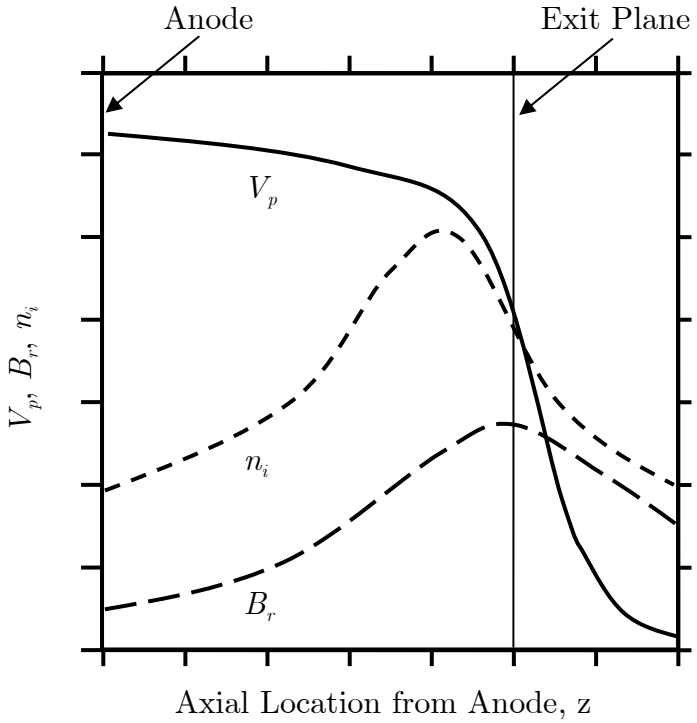

Figure 2-4. Generic representation of plasma potential, ion density, and magnetic field profiles in the channel of a Hall thruster.

Another peculiarity of Hall thruster operation is the presence of an ionization instability that is referred to as the "breathing mode" [27-30]. In summary, the breathing mode is thought to occur based on the transit time required to replenish neutrals lost to ionization. As neutrals advance to fill the

void left by ionization, they are then ionized again to repeat and sustain the process. The breathing mode frequency is typically on the order of 20 kHz, placing it well above the ion cyclotron frequency, yet well below the lower hybrid or electron cyclotron frequencies. The severity of the oscillation amplitude varies greatly between thruster designs and operating conditions. Typical amplitudes are on the order of 10-20% of the mean, but severe oscillations can reach 100% of the mean discharge current, resulting in poor thruster stability and eventual loss of thruster discharge.

2.4 Summary

This chapter discussed the fundamentals of rocket propulsion and the desire to use electric propulsion as a means of increasing the propellant exhaust velocity to achieve higher spacecraft payload mass fractions. This naturally led to an overview of the three major categories of electric propulsion: electrothermal, electromagnetic, and electrostatic. From these broad descriptions, Hall thrusters (the focus of this dissertation) were identified as a technology that is gaining popularity due to its relatively large range of demonstrated specific impulses (1000-3000 seconds). The two major Hall thruster variants were discussed: TAL and SPT, with focus on the SPT based on relevance to the thruster used in this dissertation. The basics of thruster operation were discussed along with several peculiarities of operation, including the ion velocity distribution and breathing mode instability.

The goal of this chapter was to provide the reader with the necessary background to continue with further discussions of Hall thruster physics in the remaining chapters. In particular, Chapter 3 discusses neutral flow dynamics in the channel of Hall thrusters, with a heavy emphasis on computational methods used to predict neutral properties. The remaining chapters discuss several plasma measurements that are used to understand the details of thruster operation.

Chapter 3

Neutral Flow Dynamics

The influence of neutral flow dynamics in the operation of Hall thrusters is typically underemphasized in the literature. Instead, focus is typically placed on the discharge voltage, magnetic field, and cathode behavior. This chapter discusses the motivation for neutral flow research and provides a critical review of the pre-existing research on neutral flow in Hall thrusters. This chapter also reviews the analytical, numerical, and experimental methods that were used to design, validate, and characterize the neutral flow properties downstream of a 6-kW Hall thruster. Finally, neutral flow distributions are shown in the discharge channel, serving as a generic resource for future analyses.

3.1 Review of Neutral Flow Research

Generally, the neutral flow dynamics in a Hall thruster can be described as the flow characteristics associated with the neutral density distribution and velocity, which are directly linked to plasma density and neutral residence time. It is commonly accepted that in order to enhance ionization, the neutral

distribution within the discharge channel must be azimuthally and radially uniform, while maximizing the neutral residence time.

As indicated in the Hall thruster description (Section 2.3.3), the anode serves a dual purpose as positive electrode and gas distributor. In the role of gas distributor, the anode has a strong influence over the neutral flow dynamics in the discharge channel. Several computational and experimental investigations of the influence of neutral flow dynamics on thruster performance, stability, thermal margin, and lifetime are summarized below. The conclusion that should be drawn from this brief discussion is that neutral flow dynamics have a direct influence on the operation of Hall thrusters. A more detailed review of prior neutral flow research can be found in Ref. [31].

The most practical way to alter the neutral flow dynamics in the discharge channel is to change the anode injection method. In practice, the anode injection method is limited to four primary options shown in Figure 3-1: 1) radial injection towards channel center [26, 32], 2) radial injection towards the channel walls [25, 33], 3) axial injection towards the channel exit [11, 13, 34, 35], and 4) reverse-feed injection towards the rear of the channel [36]. The schematics in Figure 3-1 are shown as block diagrams for illustrative purposes since particular geometries that produce each injection method varies greatly between thrusters, some of which are not publicly available.

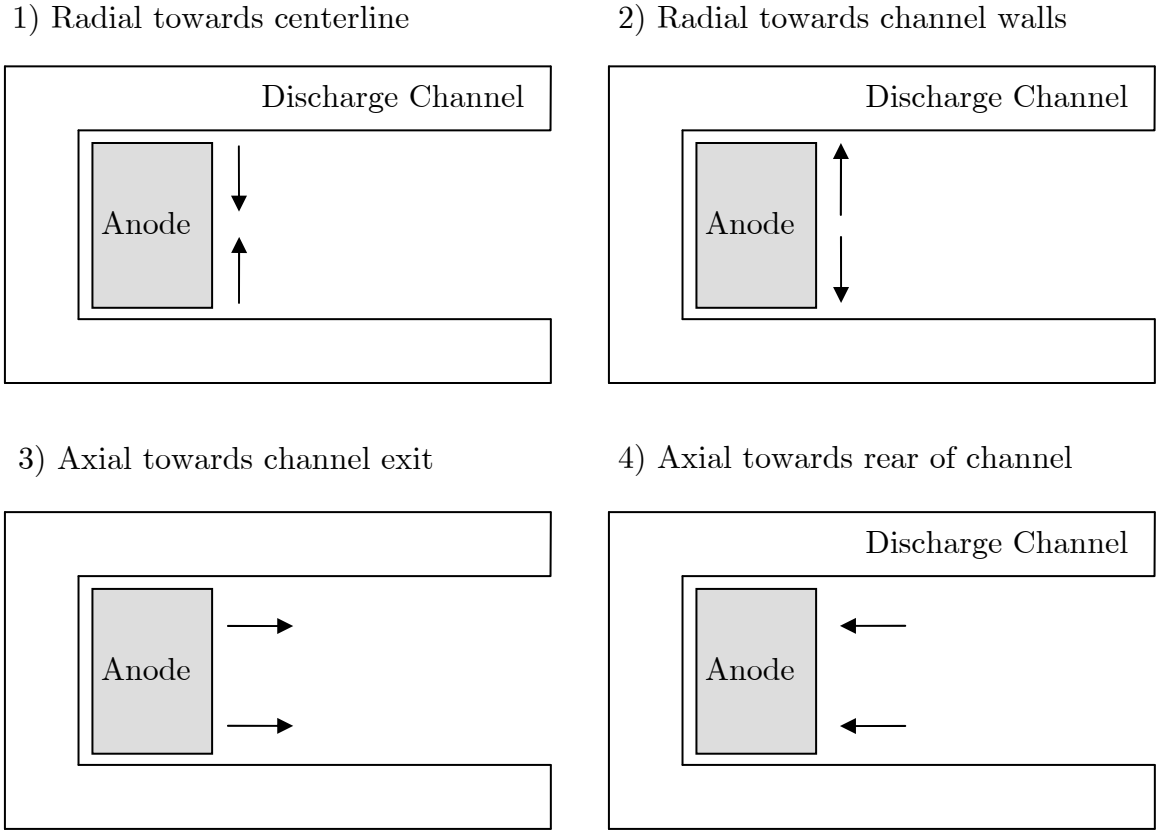

Figure 3-1. Schematic of primary Hall thruster anode configurations for neutral injection.

The majority of anode injection methods rely on a manifold of small diameter orifices to provide an azimuthally uniform distribution of neutrals in the discharge channel. A generic view of a Hall thruster anode is shown in Figure 3-2 from the publicly available schematics of the UM/AFRL P5 Hall thruster (which shares a functionally identical anode with the NASA-173M). The P5/NASA-173M anode uses a single propellant inlet that exhausts into a mixing chamber. The flow is redistributed around the anode annulus through several small-diameter orifices ($<$ 1 mm diameter). After mixing in the next chamber, the flow is then exhausted through several dozen pairs of small-diameter orifices, referred

to as the manifold, which injects neutrals radially toward channel centerline (option 1 above). The flow then mixes and exhausts into the discharge channel.

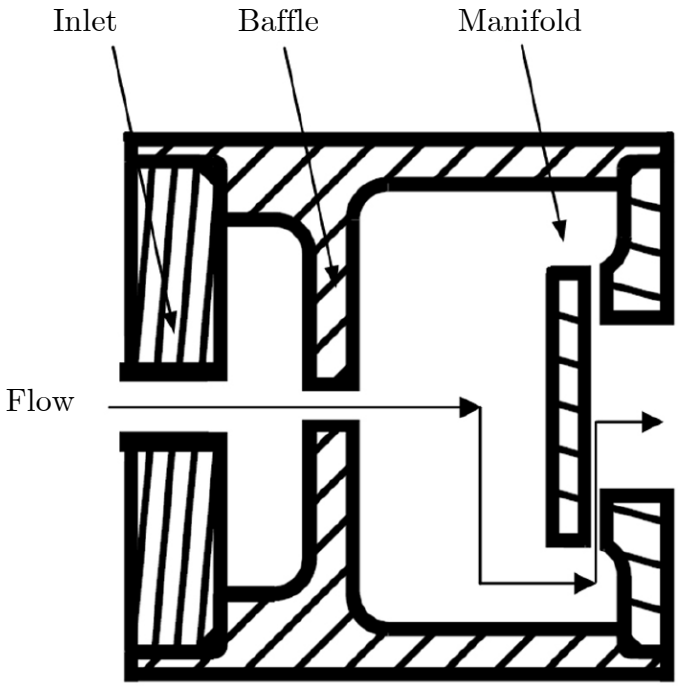

Figure 3-2. Schematic of UM/AFRL P5 Hall thruster anode. The anode uses radial injection towards channel centerline.

The anode of 6-kW Hall thruster used in this dissertation utilizes axial injection towards the channel exit (option 3 above), which is described in Ref. [11].

Through a variety of anode geometry and channel configurations, Kim *et al.* [36] and Vial *et al.* [37] indicated reduced plume divergence angle, which led to increased thruster efficiency and lifetime. The divergence was presumably decreased due to the geometry changes that increased neutral residence time and caused ionization to occur further upstream. The reduction in plume divergence is typically associated with better beam focusing within the channel and in the

near-field plume that leads to fewer wall collisions and hence, increased thruster lifetime. Computational work of Garrigues *et al.* [38] showed that injecting additional propellant between the ionization and acceleration regions led to increased propellant utilization and flattening of the plasma potential profiles in the channel. This led to increased thruster performance and lifetime. Miyasaka *et al.* [39] changed propellant temperature and anode configuration, causing changes in the neutral flow that led to decreased discharge oscillations and hence, increased thruster stability. Dorf *et al.* [35] indicated that the anode configuration and neutral flux directly influenced the anode sheath potential drop that is directly coupled to the voltage utilization (see Section 6.1). With proper neutral flow design, the onset of an electron-repelling sheath was avoided; this decreased the electron flow towards the anode (increased current utilization) and increased thruster efficiency.

Changing the profile of the discharge channel is another method that can significantly change the neutral flow. Raitses *et al.* [40] altered the discharge channel cross section by inserting tapered ceramic spacers. The spacers improved ionization and specific impulse, while efficiency was essentially unchanged. Ionization efficiency was increased by increasing the neutral density in the ionization region, which locally elevated the collision frequency. Loyan *et al.* [41] performed similar experiments, inserting flat spacers into the discharge channel. The results indicated that decreasing the neutral velocity (increasing residence

time) led to improved ionization, increased thruster efficiency, and longer lifetime.

3.2 Analytical Calculations

An analytical prediction of the neutral flow properties internal to the anode was challenging due to the large changes in pressure and flow regime from fully continuum at the anode inlet to nearly rarefied at the anode exit. Contributing to these complications, abrupt changes in cross sectional area accompanied by small diameter flow paths result in non-isentropic losses that must be accounted for by discharge coefficients (see Figure 3-2 for generic anode configuration). To address this complexity, a semi-iterative process was introduced to adapt continuum- and kinetic-based equations where appropriate. This analysis focused on creating a preliminary design that would maintain the sonic condition over the projected range of anode flow rates and was implemented to guide the computational modeling that was ultimately used to design the anode.

3.2.1 Pressure Calculations

To produce a uniform neutral flow distribution in the channel, the orifices of the anode manifold must be choked. By choking the orifices, the mass flux through each hole must be equal, thereby ensuring uniform flow downstream of the anode.

In order to ensure choked (sonic) flow of a monatomic gas, the pressure ratio across each orifice must be greater than two, which was determined by thermodynamic variables alone from

$$\frac{P_1}{P_o} = \left(\frac{2}{\gamma + 1} \right)^{\frac{\gamma}{\gamma - 1}}, \tag{3-1}$$

which is based on isentropic relations [42]. In practice, the flow across a sharp orifice is non-isentropic, which requires a pressure drop that is greater than that given by Eq. 3-1 in order to maintain sonic flow. Using discharge coefficients from results in Ref. [43], a conservative correction of two was used as a margin against subsonic flow. This increased the minimum required pressure ratio to approximately four.

To ensure that the minimum pressure ratio across each orifice location was maintained, the pressure was calculated throughout the anode. Under the assumption of continuum flow, the pressure can be determined through isentropic relations. For an isentropic flow with constant specific heats, the stagnation temperature can be written as [42, 44]

$$\frac{T_0}{T} = 1 + \frac{\gamma - 1}{2} M^2 . \tag{3-2}$$

where the subscript 0 denotes the upstream condition and the Mach number is

$$M = \frac{u}{\sqrt{\gamma R T}} . \tag{3-3}$$

The denominator is the speed of sound, and after rearranging, the velocity may be expressed as

$$u = M\sqrt{\frac{\gamma RT_0}{1+\frac{\gamma-1}{2}M^2}}. \tag{3-4}$$

Combining this relation with the mass flow per unit area

$$\frac{\dot{m}}{A} = \rho u\,, \tag{3-5}$$

ideal gas law ($P = \rho RT$), and density ratio

$$\frac{\rho_0}{\rho} = \left(1+\frac{\gamma-1}{2}M^2\right)^{1/(\gamma-1)}, \tag{3-6}$$

the mass flow rate per unit area may be written as

$$\frac{\dot{m}}{A} = P_0 M\sqrt{\frac{\gamma}{RT_0}}\left(\frac{1}{1+\frac{\gamma-1}{2}M^2}\right)^{(\gamma+1)/2(\gamma-1)}. \tag{3-7}$$

Assuming sonic conditions, the continuum-based pressure upstream of the choked orifice may be written as

$$P_{CB} = \frac{\dot{m}}{A}\sqrt{\frac{RT}{\gamma}}\left(\frac{2}{\gamma+1}\right)^{\frac{1+\gamma}{2(1-\gamma)}} \approx 1.4\frac{\dot{m}}{A}\sqrt{RT}\,. \tag{3-8}$$

The pressure was separately calculated for kinetic flow conditions following the work of King [45]. Each location within the anode is treated as a finite volume container with inlet and exit orifices. The flux of particles entering the volume much be equal to the total flux exiting the volume

$$n_n\langle u_n\rangle\big|_{in} = n_n\langle u_n\rangle\big|_{out}\,. \tag{3-9}$$

Assuming that the gas is Maxwellian, the velocity distribution of atoms escaping from the volume through the combined orifices is

$$f_{esc}(u) = n_n \left(\frac{m_{xe}}{2\pi k_B T} \right)^{3/2} e^{-m_{xe}\left(u_x^2+u_x^2+u_x^2\right)/2k_B T}, \tag{3-10}$$

where n_n is the atomic density, and u is the atomic velocity. The direction exiting the orifice is taken as the positive z direction so that the integral can be written

$$\begin{aligned} n_n \langle u_n \rangle &= \int_{-\infty}^{\infty} du_x \int_{-\infty}^{\infty} du_y \int_0^{\infty} du_z u_z f_{esc}(u) \\ &= n_n \sqrt{\frac{k_B T}{2\pi m_{xe}}} \end{aligned} . \tag{3-11}$$

Eq. 3-11 is combined this with Eq. 3-10 and the ideal gas law

$$P = n k_B T , \tag{3-12}$$

to achieve the kinetic-based pressure

$$P_{KB} = \frac{\dot{m}}{A} \sqrt{\frac{2\pi k_B T}{m_{xe}}} \approx 2.5 \frac{\dot{m}}{A} \sqrt{RT} , \tag{3-13}$$

where the mass flow was taken as

$$\dot{m} = n_n m_{xe} u_n A . \tag{3-14}$$

The transition between continuum- and kinetic-based flow behavior is known as the transitional regime. In this regime, it is inappropriate to use the equilibrium approach of the continuum-based equations or the statistical approach of the kinetic-based equations when deriving analytical solutions. The transitional pressure was assumed to be bounded by the continuum- and kinetic-based calculations, which vary by approximately 50%. Any uncertainty associated with this assumption was deemed acceptable since the analytical predictions of this section were meant as a preliminary estimate of the pressure distribution within the anode.

In order to determine the appropriate flow equation to use at each location throughout the anode, the Knudsen number (Kn) was considered. The local length scale for the Kn varied throughout the anode and was defined as the orifice diameter or the shortest dimension of a particular chamber. Based on the value of Kn, the flow regime was determined by defining continuum flow as Kn $\leq$ 0.1 and free molecular flow as Kn $\geq$ 1; transitional flow was between 0.1 and 1.

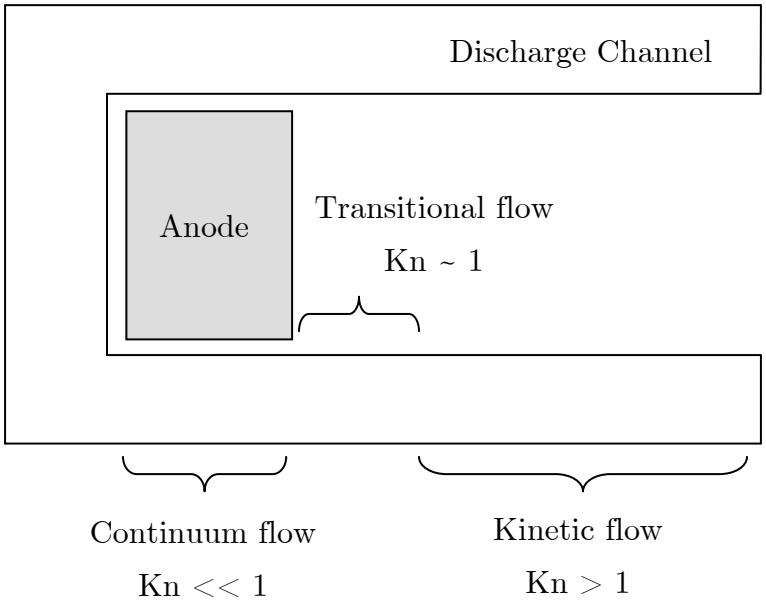

Figure 3-3. Schematic of primary Hall thruster anode configurations for neutral injection (not to scale).

The propellant was assumed to accommodate fully to the local wall temperature in the pressure calculations. Consistent with temperature measurements reported in Refs. [46-49], the wall boundary conditions at each location, shown in Figure 3-4, were taken as 300 K at the propellant inlet (upstream of the thruster), 775 K throughout the anode, and 875 K within the discharge channel. Although the entire discharge channel was taken as a constant

temperature, there is typically a temperature gradient along the channel [49] due to the elevated plasma flux to the walls near the channel exit where the Hall current is located.

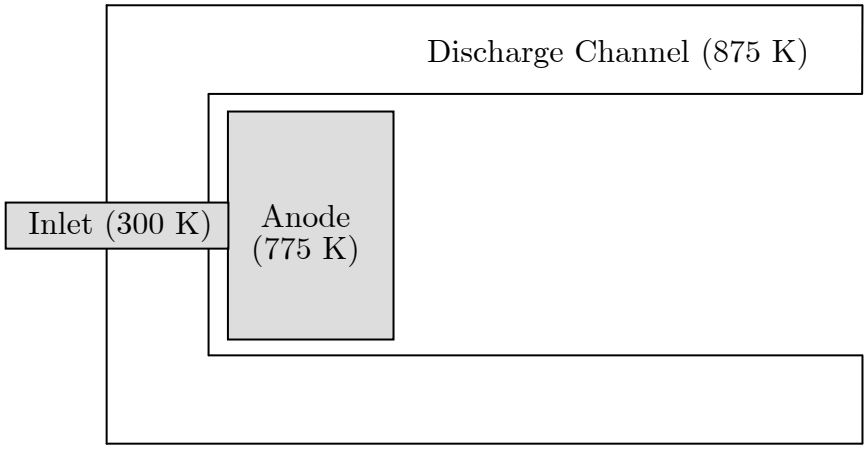

Figure 3-4. Schematic showing temperature boundary conditions used in analytical calculations.

Using the temperature definitions in Figure 3-4 and fixed mass flow, the continuum- and kinetic-based pressures were primarily governed by cross-sectional area, which defined by inlet diameter, channel width, or combined orifice area at the baffle and manifold. Since the area directly controlled the pressure at each location, it also controlled the pressure ratio across each orifice. This dependence on pressure ratio created a strong correlation between the number of orifices at each location and the ability to achieve sonic flow at the orifices.

3.2.2 Neutral Residence Time

Decreasing the axial velocity of the neutrals increases their residence time within the discharge channel, which increases the likelihood of ionization

collisions and hence, increased propellant utilization. The residence time in the discharge channel, τ_{res} was compared with the ionization time, τ_i to quantify the effect of neutral velocity. The residence time within the discharge channel is

$$\tau_{res} = \frac{L_c}{u_n}, \tag{3-15}$$

and the mean collision time for an ionizing collision between electrons and neutrals is

$$\tau_i = \frac{1}{n_n \langle \sigma_{en} u_e \rangle}. \tag{3-16}$$

In these equations, n_n is the neutral number density, u_e is the electron velocity, σ_{en} is the ionization cross section, L_c is the discharge channel length, and u_n is the neutral velocity.

To maintain a high level of propellant utilization, the neutral residence time must be much larger than the ionization time ($\tau_{res} >> \tau_i$). The neutral residence time can be increased with a longer channel; however, this leads to increased wall losses, and hence decreased efficiency. Conversely, the residence time can be increased by decreasing the neutral velocity. The neutral velocity can be controlled by changing the anode injection method or by directly cooling the anode to reduce the neutral thermal velocity. Cooling the incoming propellant may have little effect since incoming neutrals accommodate quickly to the anode temperature due to the large number of collisions prior to reaching the anode exit; for this reason, directly cooling the anode is more effective.

Combining the mean ionization time and neutral residence time, we obtain a criterion for maintaining a high level of propellant utilization

$$\frac{\tau_{res}}{\tau_i} = \frac{L_c n_n \langle \sigma_{en} u_e \rangle}{u_n} >> 1. \tag{3-17}$$

Equation 3-17 indicates that increasing electron velocity (i.e., electron temperature) or reducing neutral velocity (i.e., neutral temperature) will increase propellant utilization, which is similar to the findings of Refs. [36, 41, 50, 51] that all concluded that maximizing the residence time increased propellant utilization. For fixed channel geometry, channel material, discharge voltage, and anode mass flow rate, the variables L_c, n_n, σ_{en}, and u_e in Eq. 3-17 remain approximately constant, leaving neutral velocity as the only free parameter. Although magnetic field topology has been shown to play a significant role in the ionization and acceleration processes [26, 51], which effect neutral flow dynamics, it is not considered in this analysis.

3.2.3 Azimuthal Uniformity of Neutrals

In the Hall thruster discharge channel, electrons are impeded from reaching the anode by the primarily radial magnetic field. Electrons reach the anode through the combined effects of electron-wall, electron-ion, and electron-neutral collisions. Each collision allows the electron to migrate towards the anode with a step size on the order of a Larmor radius, which is defined as

$$r_L = \frac{u_\perp}{\omega_c}, \tag{3-18}$$

where $u_\perp$ is the electron velocity perpendicular to the magnetic field and ω_c is the cyclotron frequency

$$\omega_c = \frac{e\,B}{m_e}, \tag{3-19}$$

where e is the elementary charge, B is the magnetic field, and m_e is the electron mass. Diffusion of electrons across the magnetic field lines can be slowed by decreasing the Larmor radius (increasing the magnetic field strength) or decreasing the collision frequency (lower density). In addition, the shape of the magnetic field can have a significant impact on the electron diffusion (mobility) [26, 51].

Although the anode injection method is directly responsible for the neutral density uniformity near the anode, non-uniformities at the anode exit were expected to be significantly reduced beyond the first 50% of the channel length due to inter-atomic and wall collisions [11]. Since ionization occurs throughout the discharge channel, near-anode non-uniformities will produce a non-uniform, partially-ionized plasma upstream of the primary ionization region. The electrons in this region become magnetized and begin their azimuthal E×B drift due to the applied electric and magnetic fields. The separation of charge induces an azimuthal electric field that causes E×B drift towards the anode. The global effect is an increase in the total electron current to the anode, which is a direct loss in thruster efficiency.

Although the magnetic field is relatively weak near the anode, the electrons remain magnetized in this region (for approximate near-anode values of $B = 10$ G and $T_e = 5$ eV, $r_L \sim 10$ mm, which is approximately 2-3 times smaller than the channel width). Their mobility towards the anode is increased by the high neutral density, and hence, high collision rate. In the presence of an azimuthal non-uniformity in neutral density, electron mobility will be locally increased, increasing the electron current to the anode. Janes *et al.* [52] reported experimental data that confirmed plasma non-uniformities (typically caused by neutral non-uniformities) led to polarization, electric fields, and ultimately, anomalous electron diffusion to the anode. Electrons that are lost via anomalous diffusion present a direct decrease in thruster efficiency. Experimental observations of Hofer [26] support this discussion, indicating that an anode with a fabrication imperfection produced a localized asymmetric neutral distribution that resulted in higher electron current to the anode, lower measured thrust, and asymmetric ion current density profiles in the far-field plume. The cumulative effect of the anode asymmetry was decreased thruster efficiency, plume symmetry, and stability, indicating that small changes in neutral uniformity can significantly affect thruster operation.

The work of Baranov *et al.* [53] supports the above discussion through an analytical description of the effect of azimuthal non-uniformities in neutral number density. This analysis described how the plasma density adjusted to

minimize the azimuthal electric field to account for a neutral non-uniformity, concluding that the axial electric field became skewed near the non-uniformity and electron current to the anode was increased.

3.2.4 Visual Evidence of Neutral Non-uniformities

Figure 3-5 shows an image of the University of Michigan (UM)/Air Force Research Laboratory (AFRL) P5 Hall thruster operating at nominal conditions of 300 V and 10 mg/s that provides visual evidence of azimuthal non-uniformities of neutral density. Since the NASA-173M has the same neutral injection design as the UM/AFRL P5, the photo should be representative of the neutral and plasma non-uniformities for both thrusters. The bright spots in Figure 3-5 corresponded to the neutral injection orifices, where the neutral density was elevated. The increased light intensity was likely caused by augmented electron transport to the anode, which increased excitation-induced light emission. The overall low light level was an artifact of the relatively high shutter speed necessary to view the plasma near the anode (exposure time = 1/60 seconds, focal length = 135 mm, F/8).

A photograph of the 6-kW Hall thruster operating at nominal conditions of 300 V and 20 mg/s is shown in Figure 3-6 and it shows no visual evidence of propellant asymmetry. The photograph was taken with similar camera settings that were adjusted for the increased light intensity due to the increased discharge



Figure 3-5. Photograph of the UM/AFRL P5 Hall thruster operating at nominal conditions of 300 V and 10 mg/s.

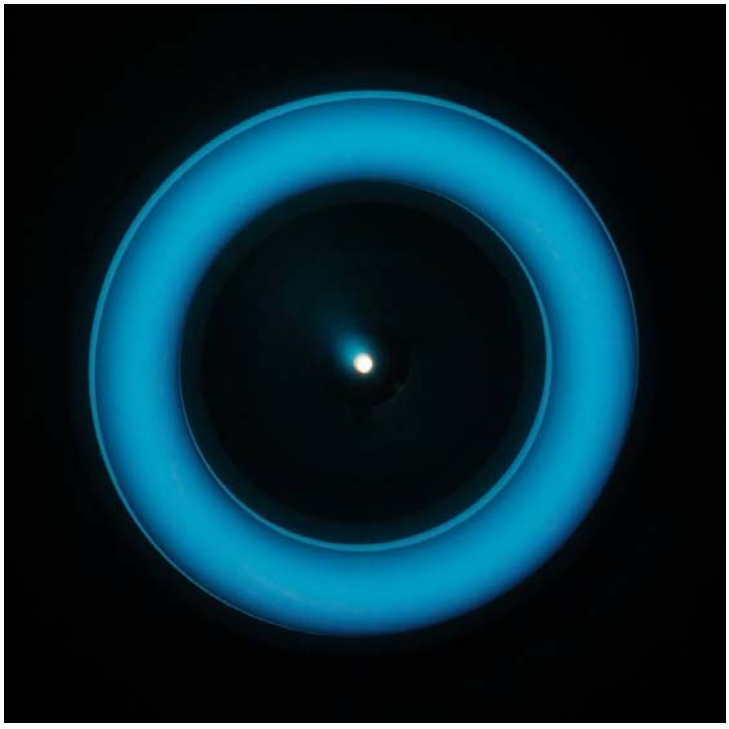

Figure 3-6. Photograph of the 6-kW Hall thruster operating at nominal conditions of 300 V and 20 mg/s.

current (exposure time = 1/400 seconds, focal length = 135 mm, F/8). The lack of visual non-uniformities indicates that the neutral flux in the channel was more uniform for the 6-kW thruster than for the UM/AFRL P5 and NASA-173M.

3.3 Numerical Tools

To capitalize on the potential benefits of increasing neutral flow uniformity and residence time, tools were required to optimize anode injection methods. This necessity was naturally suited to numerical tools that include Computational Fluid Dynamics (CFD) or Direct Simulation Monte Carlo (DSMC) computer codes. CFD codes rely on the solution of hydrodynamic equations, which limits their applicability to Kn $<$ 1. This limitation makes results from CFD loosely appropriate in the discharge channel where Kn $\geq$ 1. Conversely, DSMC codes rely on statistical approaches using the hard sphere approximation for atomic interactions. DSMC codes have been used from continuum to kinetic flow regimes; however, the high computational cost associated with the high density inside the anode makes solution in this region prohibitive. The two computational methods were used together to produce a coherent solution of the neutral flow from the anode inlet to discharge channel exit.

The ability of CFD and DSMC codes to accurately predict the flow properties downstream of a Hall thruster anode was documented in Refs. [11, 12],

where CFD was used to parametrically optimize the neutral flow uniformity, while increasing the neutral residence time.

3.3.1 FLUENT

The commercially available CFD package FLUENT [54] was used to simulate the flow of neutral xenon propellant throughout the anode interior and discharge channel. Steady-state three-dimensional simulations were used to capture the flow behavior as it progressed from the single propellant inlet tube through the anode and into the discharge channel. Three-dimensional simulations were necessary to resolve the azimuthal flow distribution that resulted from a single flow inlet and a multi-hole exhaust manifold. Simulations contained several hundred thousand elements and typically converged after several thousand iterations that required approximately eight hours to converge on a single-processor, windows-based workstation. A grid-independent solution was found based on several simulations with increasing mesh density.

Although FLUENT results outside the anode were not strictly valid due to the high Kn, a dimensionally accurate discharge channel was included beyond the anode exit to model the 6-kW Hall thruster discharge channel geometry. Including this region ensured that simulation boundary conditions did not influence results near the anode exit plane. Results in the discharge channel were used for comparisons with analytical predictions and experimental measurements in subsequent sections. Simulations were initiated with a nominal mass flow rate

of 20 mg/s at 300 K, uniformly distributed across the single 2.3-mm-inner-diameter inlet. An inlet length of 150 mm was included to adequately capture the fully-developed Poiseuille flow that exists in the propellant feed lines. The simulation stepped forward axially through the computational domain, ensuring continuity by requiring that the mass flow at each axial plane matched the inlet mass flow. The temperature of the anode and discharge channel were uniformly set throughout each surface to 775 K and 875 K, respectively, which was consistent with the temperatures used in the analytical calculations of Section 3.2.1 (see Figure 3-4 and Refs. [46-49]). All surfaces were implemented with a low-pressure slip adaptation within FLUENT to more accurately model the interaction at the wall for increasing Kn as the flow approached the discharge channel.

3.3.2 MONACO

Since the Kn approached the kinetic regime beyond the anode exit, FLUENT results were supplemented with DSMC simulations with the computer code MONACO. The version of MONACO used for this study implemented a 2-D axisymmetric computational domain. MONACO simulated particle motion and collisions to track local properties leading to calculations of macroscopic properties such as pressure and velocity. Since the computational cost of the code was directly related to the number density of the simulated flow, MONACO simulations were not practical within the entire anode. Instead, the simulation

encompassed a plane beginning at the anode manifold exit and ending approximately 10 mm downstream of the discharge channel exit. MONACO was shown to perform well across a wide range of flow conditions with some heritage within the discharge channel of Hall thrusters, making it a useful metric for comparison with analytical predictions and FLUENT simulations [55, 56].

3.3.3 HPHALL-2

HPHALL-2 is a 2-D axisymmetric computer code that treats ions and neutrals using the Particle-In-Cell (PIC) method and electrons are treated with a fluid approximation. This type of code is referred to as a "hybrid-PIC" code, and the fluid treatment for electrons significantly reduces the computational requirements of the code without negatively affecting solution accuracy. Neutrals are injected into the simulations using a half-Maxwellian distribution drifting axially at a defined Mach number. Neutral particles that impact the wall are scattered diffusely, which randomizes the reflected angle of incidence and the new velocity is found by sampling from a half-Maxwellian defined by the local wall temperature.

HPHALL was originally developed by Fife [28] and was adapted into several subsequent revisions. The version used in this dissertation HPHALL-2, was provided by the Jet Propulsion Laboratory (JPL), and a full description of modifications to the code can be found in Refs. [57-62].

For the purposes of this chapter, the code was run with the plasma turned off so that the neutral dynamics could be isolated and used in comparisons with FLUENT and MONACO simulations. Additional information on the plasma modeling can be found in Section 7.4.2. HPHALL-2 simulations with the plasma turned on were used in several comparisons with experimental data in Chapter 7, exhibiting good agreement with measured macroscopic properties including discharge current and thrust. The code also produced good agreement between measured local properties including plasma potential, plasma density, and electron temperature.

3.3.4 Comparison of the Three Simulations

The mass flux (Γ_m) profile produced by FLUENT, MONACO, and HPHALL-2 simulations are compared at the anode exit plane in Figure 3-7. The mass flux was normalized by the centerline value, $\Gamma_{m,c}$. The excellent agreement was remarkable, particularly since FLUENT was a three-dimensional, continuum-based simulation, whereas MONACO and HPHALL-2 were two-dimensional axisymmetric, kinetic-based simulations. Although the profiles had slightly different shapes, the integrated mass flux through the anode exit was within 5% of the target mass flow rate of 20 mg/s for all three simulations. The primary reason for the discrepancy between the integrated mass flux from the three simulations was due to integration errors produced by differences in grid spacing. Based on the good agreement in Figure 3-7, FLUENT simulations were

determined to be valid up to the anode exit plane, confirming its applicability for use as an anode design tool [11, 12].

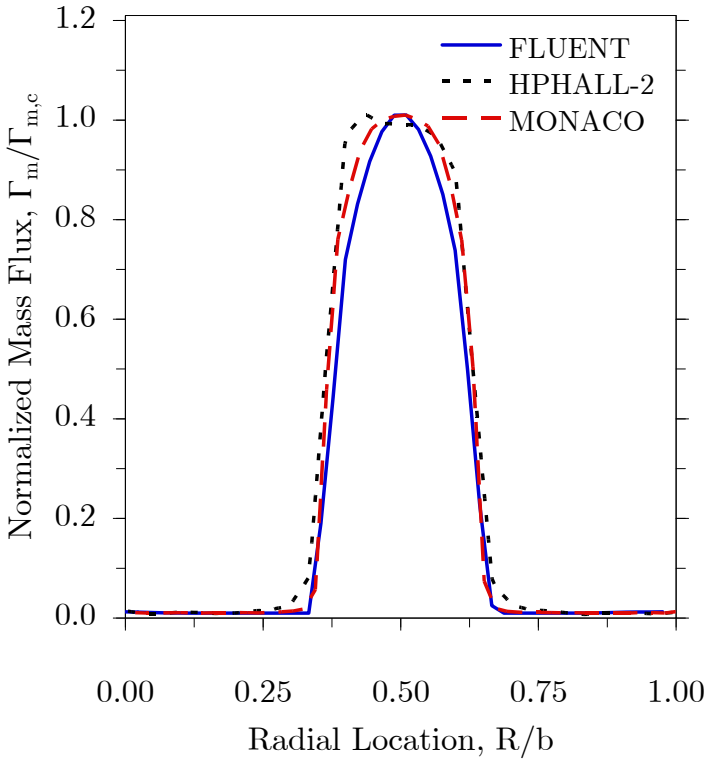

Figure 3-7. Comparison of simulated neutral flux at the anode exit plane for FLUENT, MONACO, and HPHALL-2.

3.4 Anode Pressure Acceptance Test

After an anode is designed, fabricated, and assembled the anode must undergo acceptance testing. The Anode Pressure Acceptance Test (APAT) was used to characterize the overall mass flux uniformity and agreement of measured mass flux with simulations. Each APAT consisted of dimensional and visual inspection of the anode and experimental measurement of total pressure downstream of the anode exit. Previous verification methods involved submerging the anode in a liquid, forcing a gas through it, and observing the bubble pattern

for signs of non-uniformity. The qualitative nature of the visual inspection method was less rigorous than the APAT technique that quantitatively measured the neutral pressure downstream of the anode. Additional details on the APAT can be found in Ref. [12].

3.4.1 Pressure Probe

At the outset of these APAT measurements, there was limited pre-existing literature directly related to measuring neutral flow properties downstream of a Hall thruster anode. Similar efforts employed pressure transducers, laser induced fluorescence, and electron induced fluorescence to measure or visualize the pressure distribution within the discharge channel [37, 63-65]. While these methods were marginally successful, they required extensive support equipment and set-up time. Similar work was performed with the use of pitot tubes to accurately measure pressure in low density, high Mach number flow exiting rocket nozzles using readily available laboratory equipment [66]. A more relevant approach employed an ionization gauge to measure pressure downstream of the anode [67]. Using Refs. [66] and [67] as a starting point, pressure transducers, probe diameters, and probe length were selected for the 6-kW Hall thruster APATs.

3.4.1.1 Pressure Transducer

A Pirani gauge was selected for the pressure transducer due to its low-cost, robustness, availability in most vacuum laboratory environments, and

operation range of 1×10^{-4} torr to atmosphere that was well-suited to the task. The absolute pressure uncertainty was relatively high, but since repeatability of the probe measurements was excellent, the relative uncertainty between measurements was low. Relative uncertainty was a more natural indicator of probe uncertainty for this particular application since the goal of the experiment was to measure relative changes in pressure downstream of the anode. The absolute uncertainty with respect to true pressure was accounted for by normalizing pressure results based on centerline pressure.

Anode mass flow rates of 10, 20, and 27 mg/s were investigated in the Large Vacuum Test Facility (LVTF). The mass flow meter during these tests limited the maximum flow rate at 27 mg/s but results were representative of behavior at 30 mg/s where the thruster was operated. At these flow rates, probe pressures were expected to be approximately 1×10^{-3} to 1×10^{-2} torr downstream of the anode; well within the capability of the Pirani gauge. The analog pressure signal output from the Pirani gauge was sampled at 10 Hz over one second by a data logger and 20 channel multiplexer card. The relative probe uncertainty was estimated at approximately 0.5%.

3.4.1.2 Inlet Geometry

The entrance of the probe tip was chamfered at 45° and the tube was bent at 90°. The chamfer was included on the probe tip to minimize particle reflection and maintain consistency with probe designs in the literature [66, 68]. The 90°

bend and 80 mm length of each straight portion was designed in order to keep the pressure measurement apparatus out of the anode plume as much as possible to minimize disturbances. A schematic of the probe inlet tube is shown in Figure 3-8.

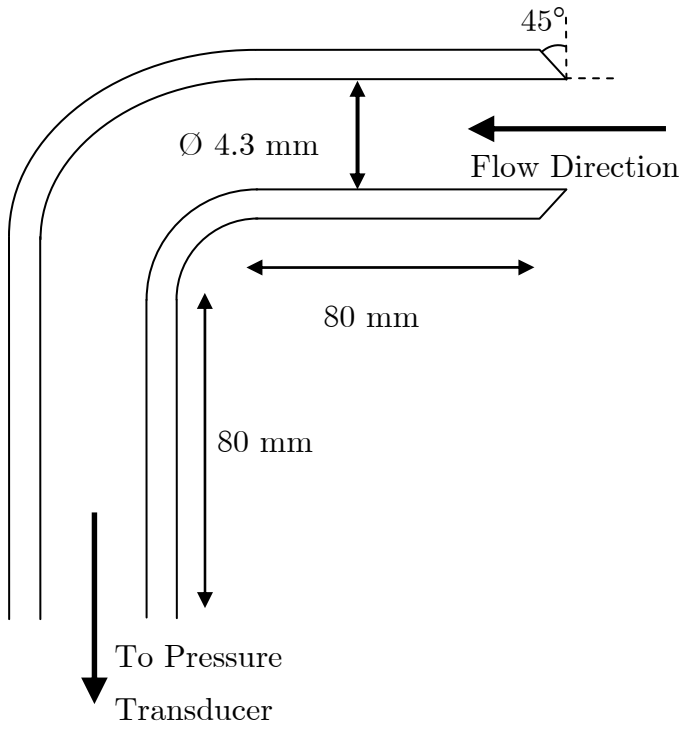

Figure 3-8. Schematic of APAT pressure probe inlet tube and inlet chamfering (not to scale).

3.4.1.3 Probe Diameter

When selecting the probe tip diameter there was a practical trade between spatial resolution and probe settling time. Spatial resolution can be increased by making the tube diameter smaller; however, the settling time increased due to the decrease in conductance. As the probe was moved through the anode plume, the pressure transducer experienced a gradient in incident flux that required a finite amount of time to reach equilibrium. Following the analysis of King [69],

the incident flux was related to the measured pressure by equating the incident and exiting fluxes

$$n\langle u_n \rangle\big|_{in} = n\langle u_n \rangle\big|_{out}, \tag{3-20}$$

which is required by continuity. Using kinetic theory, the exiting flux can be written as

$$n\langle u_n \rangle\big|_{out} = n\sqrt{\frac{k_B T}{2\pi m_{xe}}}. \tag{3-21}$$

Inserting Eq. 3-21 into Eq. 3-20 and utilizing the ideal gas law results in a relationship between the incident flux and the pressure measured by the probe

$$n\langle u_n \rangle\big|_{in} = \frac{P}{\sqrt{2\pi m_{xe} k_B T}}. \tag{3-22}$$

The settling time was found by multiplying both sides of Eq. 3-22 by the probe inlet area and inverting. The settling time, τ can be expressed as a function of local pressure and probe diameter with

$$\tau = \frac{N}{P\, d^2}\sqrt{\frac{32\; m_{xe}\; k_B\; T}{\pi}}, \tag{3-23}$$

where N is a scaling constant that is referenced to the number of particles in a 1 m^3 volume at the typical chamber operating pressure of 1×10^{-6} torr to maintain dimensional consistency.

Researchers typically choose from readily available stainless steel tube diameters of 3.2 mm (1/8”), 6.4 mm (1/4”), and 12.7 mm (1/2”). For standard wall thickness, these tubes have corresponding IDs of 2.8, 4.3, and 7.5 mm, respectively. Calculated probe settling times are shown in Figure 3-9 for these

three probe diameters. Decreasing the probe ID from 4.3 to 2.8 mm increased spatial resolution by 35%, while increasing probe settling time by 60%, making any reasonably detailed data set time-prohibited. Increasing ID from 4.3 to 7.5 mm decreased spatial resolution by 74% while decreasing settling time by 67%. Although the settling time became attractive, the probe diameter was on the order of 25% of the anode width, which was not sufficient to capture the detailed flow behavior in the channel. Using this analysis, a probe diameter of 4.3 mm was chosen for the APAT.

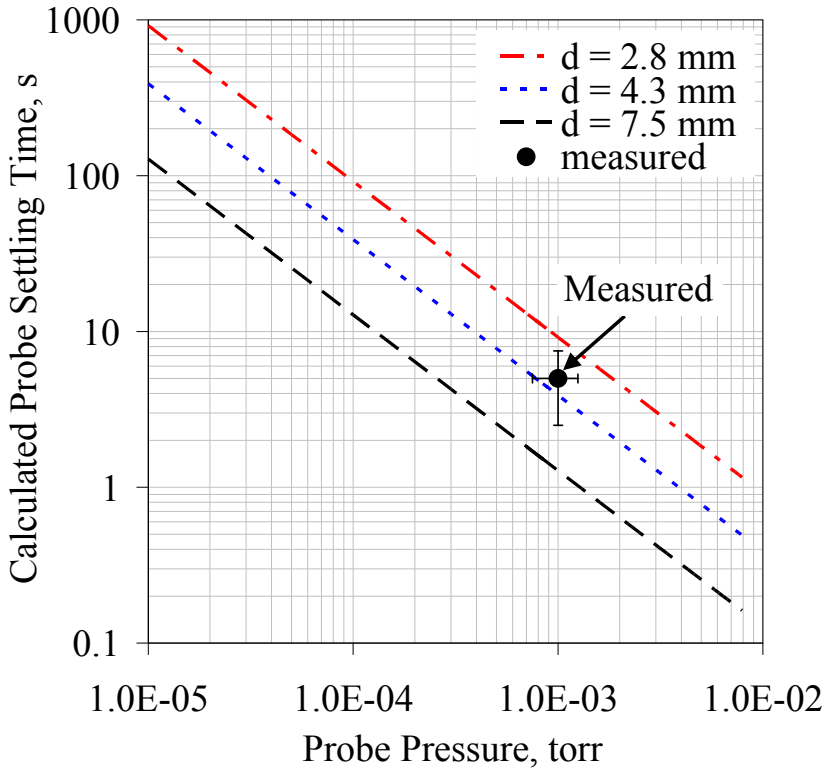

Figure 3-9. Calculated probe settling time as a function of pressure for several probe diameters. Measured settling time for the Pirani gauge is also shown.

The measured settling time is shown in Figure 3-9, displaying excellent agreement with calculated settling times for the 4.3-mm-diameter probe tip that

was used. The settling time was determined by moving the probe from an area low pressure to an area of high pressure while monitoring the pressure reading. The settling time was qualitatively chosen at the point where the pressure reading showed no appreciable change with time. The settling time varied based on the distance from the anode exit plane. To ensure that the pressure readings reached steady-state throughout the measurement domain, the longest setting time was used (measured at the furthest location from the anode).

3.4.2 Neutral Flow Test Bed

The neutral flow test bed was designed and created as a housing for the anode that could be used during neutral flow characterization in lieu of the fragile boron nitride discharge channel. The neutral flow test bed was a metallic discharge channel that matched the dimensions of the 6-kW Hall thruster used throughout this dissertation. The presence of the discharge channel allowed a more accurate cold-flow characterization to be performed during the APAT and other investigations.

3.5 Analytical, Numerical, and Experimental Comparisons

FLUENT, MONACO, and HPHALL-2 simulations were compared with analytical predictions and experimental data at the nominal anode flow rate of 20 mg/s. The simulations included the discharge channel and results were compared to experimental data taken with and without the discharge channel. Data were taken without the discharge channel during preliminary design verification when

multiple anodes were characterized in a single chamber evacuation. Data were later taken including the discharge channel allowing a direct comparison between the two measurement techniques and evaluation of the influence of the wall.

FLUENT simulations were used to complement the MONACO and HPHALL-2 simulations to fully capture the neutral flow behavior from the anode inlet (fully-continuum) to the discharge channel exit (fully rarefied). The good agreement between the various methods provided confidence in the ability of the simulations to predict true flow properties, validating their use as a future design tool. More detail on the experimental validation can be found in Ref. [12].

3.5.1 Radial Profiles

Experimental data taken with and without the discharge channel are compared to MONACO simulations in Figure 3-10. The data were taken at 20 mg/s, 180° from the anode inlet, and approximately 0.3 L_c downstream. The total pressure was normalized by the centerline pressure. The experimental data taken without the discharge channel had much lower pressure at the outer radius than the data including the channel. The axial alignment of the probe accepted primarily axially-directed particles while discriminating particles with significant radial trajectories, resulting in an artificially lowered pressure profile at the inner and outer radii. To account for this geometrical inaccuracy, raw experimental data without the channel were corrected by dividing the measured pressure by the cosine of the probe angle from centerline.

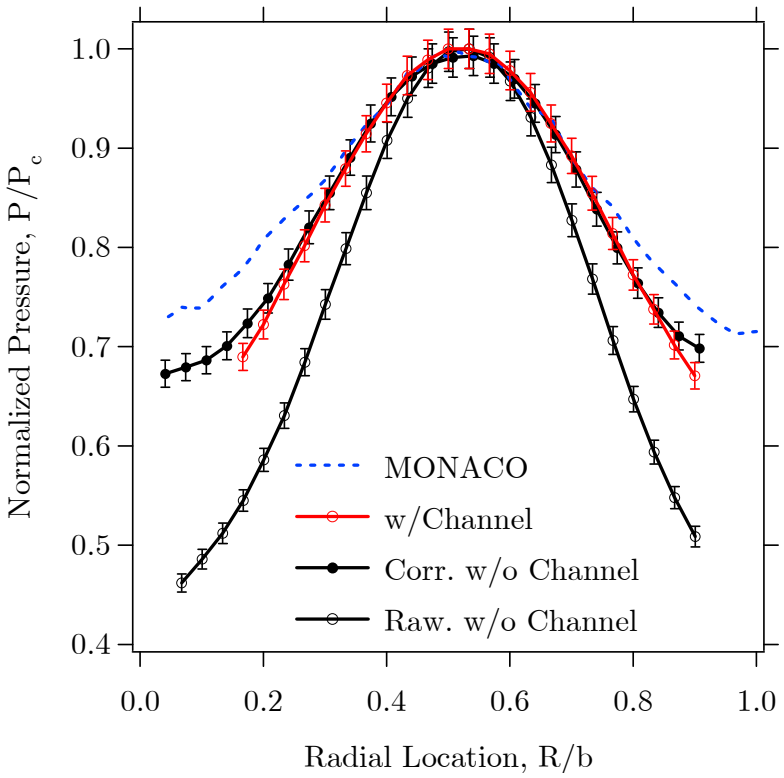

Figure 3-10. Comparison of radial pressure profiles for MONACO simulations and experimental measurements with and without the discharge channel.

Cosine correcting the data without the channel significantly increased the pressure at the inner and outer radii, resulting in excellent agreement with the simulated data and experimental data taken with the discharge channel. Although data taken with the channel were recorded with the same probe setup and orientation, these data did not need to be corrected for cosine losses since the presence of the channel wall confined the neutral flow and guided it along the axial direction.

The excellent agreement between the two experimental sets of data in Figure 3-10 indicate that the neutral flow downstream of the anode can be accurately characterized without the presence of the discharge channel wall. The

agreement will tend to be better for probe measurements taken near the anode, where the flow has experienced less expansion from centerline and hence, less flow that would be affected by the presence of the wall (or lack thereof).

It is worth noting that the pressure near the inner radius was higher than the outer radius, although the difference was subtle. This slight asymmetry occurred because the anode orifices were spaced further apart at the outer radius since the number of orifices was the same at the inner and outer radii, but the circumference was larger at the outer radius. Since the mass flow through each orifice was uniform (sonic condition) the pressure was necessarily higher in the region with closer orifice spacing.

3.5.2 Axial Profiles

The pressure from simulations in FLUENT, MONACO, and HPHALL-2, basic analytic predictions, and experimental measurements are compared on discharge channel centerline in Figure 3-11. The simulated pressure from FLUENT matched analytical predictions within the anode, but results matched poorly outside the anode. This result was expected due to the large Kn outside the anode, which exceeded the limit of FLUENT's capability. Conversely, MONACO and HPHALL-2 matched analytical results outside the anode, and matched experimental data extremely well, but could not be compared inside the anode due to prohibitively large computational requirements. The excellent

agreement between MONACO and HPHALL-2 simulations with the experimental data provides confidence in the predictive capability of the simulations.

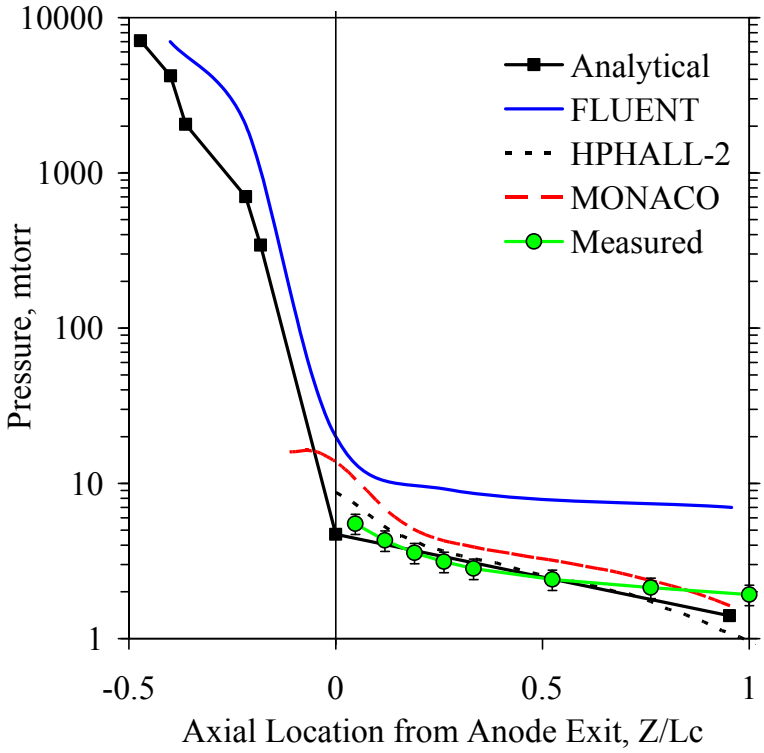

Figure 3-11. Simulated and experimental neutral pressure on channel centerline for anode mass flow rate of 20 mg/s.

3.6 Flow Distributions in the Discharge Channel

It is useful to discuss the two-dimensional neutral properties within the channel so that the results can be used as a tool for future Hall thruster research. The information may prove useful for future investigations of wall sheath, erosion, CEX phenomenon, and electron dynamics. It should be noted that although these results were presented for cold-flow operation (no plasma) they remain useful as an initial boundary condition for the initiation of a plasma discharge. In addition, the trends were consistent with the plasma-on results. The

presented results showed a self-similar characteristic with anode flow rate, presenting the opportunity for future investigations to extend these results to a wide range of flow rates and channel geometries.

3.6.1.1 Simulated

The simulated neutral flow velocity and density are shown in Figure 3-12 for FLUENT, MONACO, and HPHALL-2. The three simulations produced results that were qualitatively similar to each other in magnitude and shape. The MONACO and HPHALL-2 results were in much better agreement with each other than with the FLUENT results; however, this was expected since FLUENT was a continuum-based computer code, whereas MONACO and HPHALL-2 were kinetic-based computer codes.

All three simulated axial flow velocities exhibited a distinct peak near channel centerline. This peak extended along the length of the channel, but diminished near the thruster exit. FLUENT results exhibited less neutral acceleration towards the thruster exit than MONACO and HPHALL-2 and retained the centerline peak that existed at the anode exit. In addition, the velocity in the channel was 100-150% lower than the results from MONACO and HPHALL-2. This discrepancy in velocity was attributed to the large Kn that exceeded the capability of FLUENT's continuum-based calculations. The kinetic-based simulations of MONACO and HPHALL-2 were more appropriate in the channel and those results should be considered more accurate.

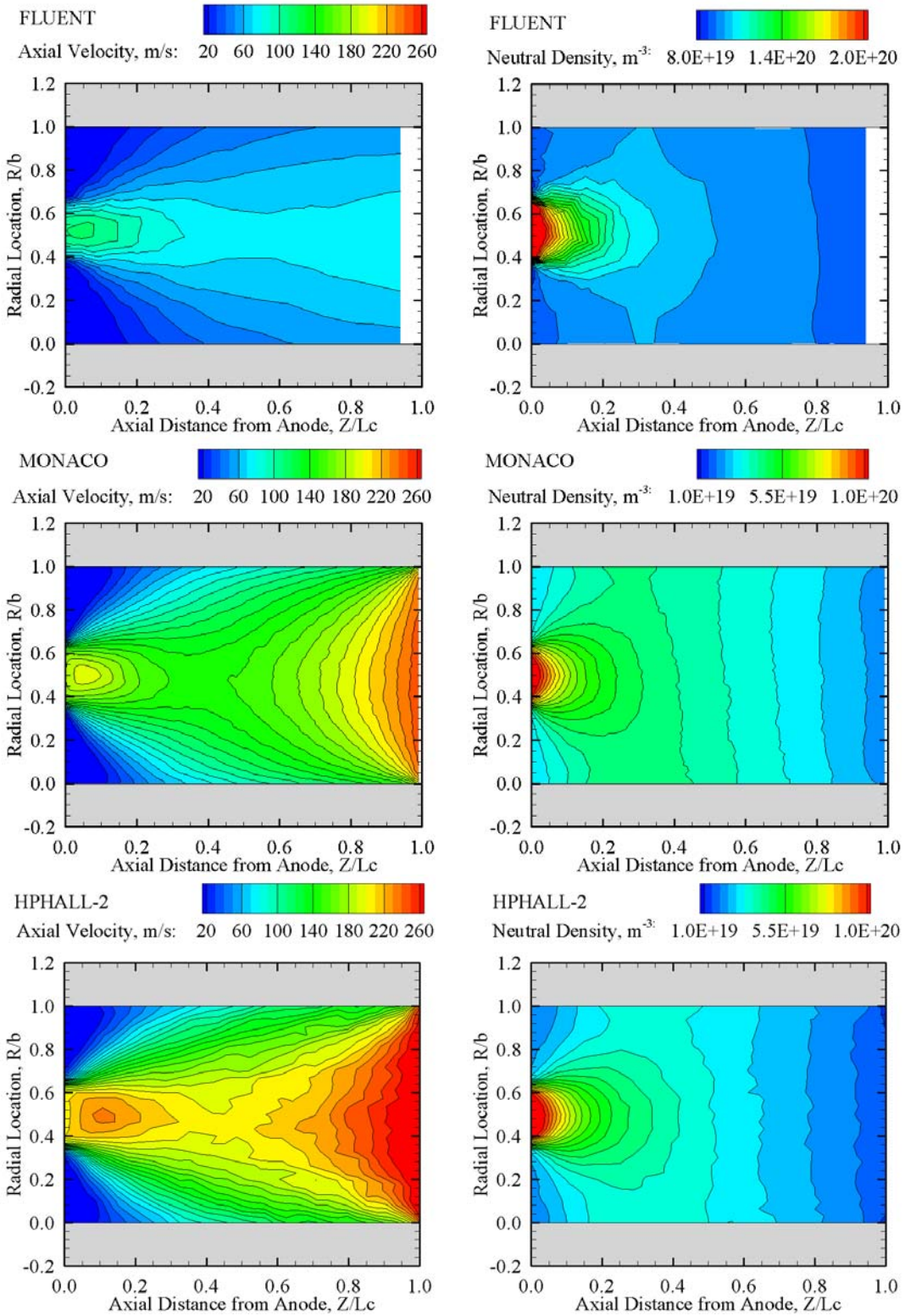

Figure 3-12. Simulated neutral properties in the discharge channel for an injected mass flow rate of 20 mg/s. FLUENT (top), MONACO (middle), and HPHALL-2 (bottom).

All three simulated neutral number densities exhibited the same characteristic quasi-Gaussian shape near the anode exit. This density profile became less peaked further downstream, eventually flattening across the channel then changing concavity. MONACO and HPHALL-2 results flattened out at approximately 0.5 L_c, whereas FLUENT flattened out at approximately 0.75 L_c. The density results from FLUENT were 100-150% higher than results from MONACO and HPHALL-2 based on the 100-150% underprediction of neutral velocity.

3.6.1.2 Experimental

The experimental flow distribution was measured in the channel using the pressure probe and neutral flow test bed described in Sections 3.4. Data were taken every 3% of the channel width (b) in the radial direction and 7% L_c in the axial direction. The uncorrected flow distributions at flow rates of 10, 20, and 27 mg/s are shown in Figure 3-13. Although data were not acquired at 30 mg/s due to limitations of the available flow meter, it was of little consequence since the data exhibited a distinctly self-similar shape. This universal flow structure presents the possibility to retrieve the pressure distribution for an arbitrary value of anode flow rate. For instance, the centerline pressure at the anode exit exhibited a highly linear relationship with flow rate

$$P = 2.4\times10^{-4}\ \dot{m}_a + 6.0\times10^{-4}, \tag{3-24}$$

where P is in units of torr, and $\dot{m}_a$ is in units of mg/s. Similar transformations can be applied at other locations to produce a full two-dimensional pressure map at an arbitrary flow rate.

The uncorrected experimental results in the presence of the channel were compared to HPHALL-2 simulations in Figure 3-13 at flow rates of 10, 20, and 27 mg/s. HPHALL-2 was chosen for this comparison since it displayed good agreement with the other simulations, was readily available, and converged faster than FLUENT and MONACO. The experimental and simulated results displayed good agreement for the first 25% L_c where the neutral flux was highly concentrated near channel centerline. Beyond 25% L_c the simulated pressure flattened and changed concavity; however, the experimental results retained their initial quasi-Gaussian shape throughout the entire channel. The discrepancy in shape and magnitude was corrected by implementing a correction for the probe cosine losses as shown in Figure 3-14, which were compared to HPHALL-2 simulations. The cosine corrected results showed better agreement with the pressure magnitude and they displayed the same pressure profile flattening and change in concavity at approximately 40% L_c that the simulations predicted. The only drawback to the cosine correction method was the unphysical profile that was produced near the anode exit. In this region, the pressure near the inner and outer wall exceeded the value at channel center since the cosine correction

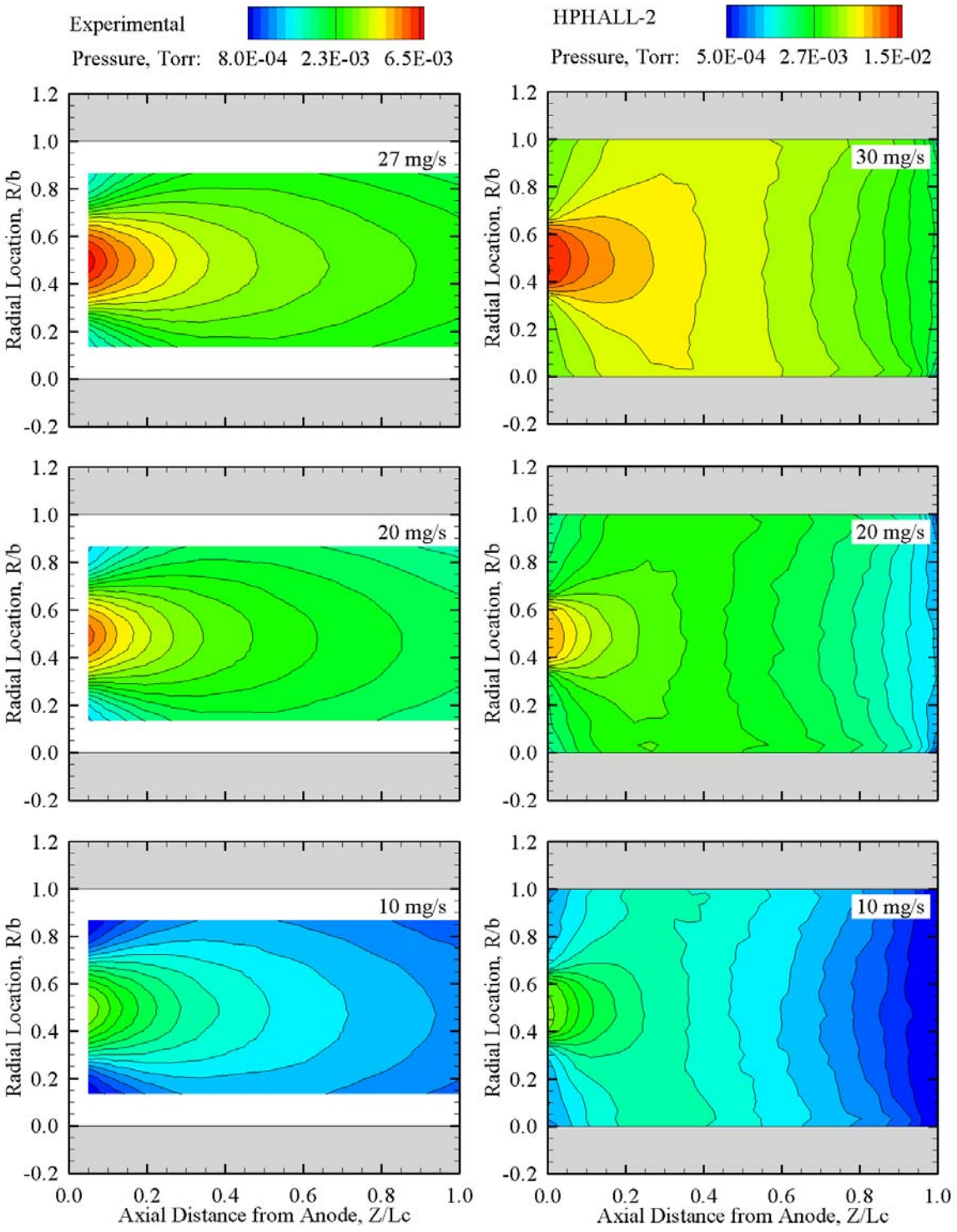

Figure 3-13. Raw experimental (left) and HPHALL-2 simulated (right) neutral pressure in the discharge channel for injected mass flow rates of 10, 20, and 27 mg/s.

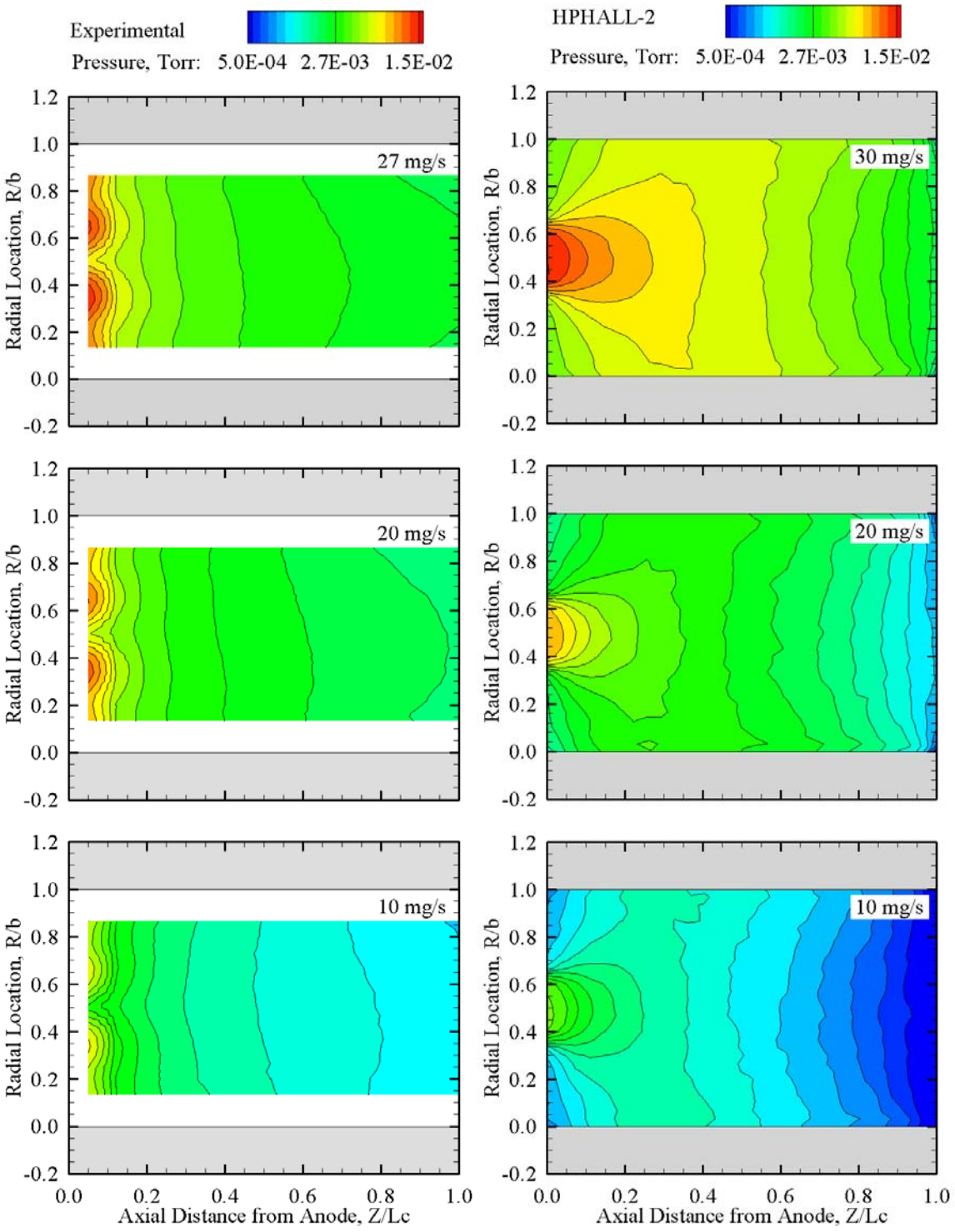

Figure 3-14. Corrected experimental (left) and HPHALL-2 simulated (right) neutral pressure in the discharge channel for injected mass flow rates of 10, 20, and 27 mg/s.

increased drastically as the axial distance was decreased and the radial distance increased. A more sophisticated correction method would reduce or remove the correction near the anode so that the quasi-Gaussian shape would remain intact. To avoid the cosine correction for the probe orientation with respect to the neutral flow, the data could be collected by aligning the probe entrance with the incoming flow. This result could be achieved by turning the probe at each location until the maximum signal strength was achieved.

3.7 Influence of Anode Boundary Conditions

Since the anode served as the primary gas distributor, changes in boundary conditions at the anode can have a large impact on the neutral flow dynamics in the discharge channel. In particular, the anode temperature and mass flow rate can have profound effects on the bulk properties downstream.

3.7.1 Injection Method

As described in Section 3.1 and Ref. [31], the flow distribution within the channel can have a significant influence on the thruster operation. One of the primary methods of altering the neutral flow is changing the neutral injection method. To highlight the influence of neutral injection changes, mass flux distributions were compared at the anode exit for the NASA-173M and the 6-kW Hall thruster. The two thrusters used different flow injection methods; the NASA-173M had radial injection towards channel centerline, and the 6-kW Hall

thruster had axial injection towards the channel exit that was combined with a diffuser [11].

FLUENT simulations of the mass flux, normalized by the maximum value on channel centerline are shown in Figure 3-15 for the NASA-173M and 6-kW Hall thruster (it should be noted that the NASA-173M shares a functionally identical anode to that of the UM/AFRL P5 Hall thruster). The mass flux downstream of the NASA-173M anode was characterized by vicinities of high mass flux that were uniformly distributed around the annulus. These areas of elevated mass flux corresponded identically with the anode injection holes that have a direct line of sight into the channel. The 6-kW Hall thruster significantly improved the azimuthal and radial uniformity. The variation from centerline to the inner and outer radii was decreased by a factor of four and the angular variation was essentially eliminated. These mass flux distributions were strikingly similar to the photographs of each thruster during operation shown in Figure 3-5 and Figure 3-6, providing additional evidence that the neutral flow uniformity has significant bearing on the plasma uniformity during operation.

This significant improvement in neutral uniformity likely increased the plasma uniformity within the channel and reduced the occurrence of azimuthal electric fields that deteriorates performance by increasing electron transport to the anode (see Section 3.1). This effect, referred to as "anomalous diffusion" was

discussed in Ref. [52] and experimental confirmation of the benefits of improved uniformity was provided in Ref. [26].

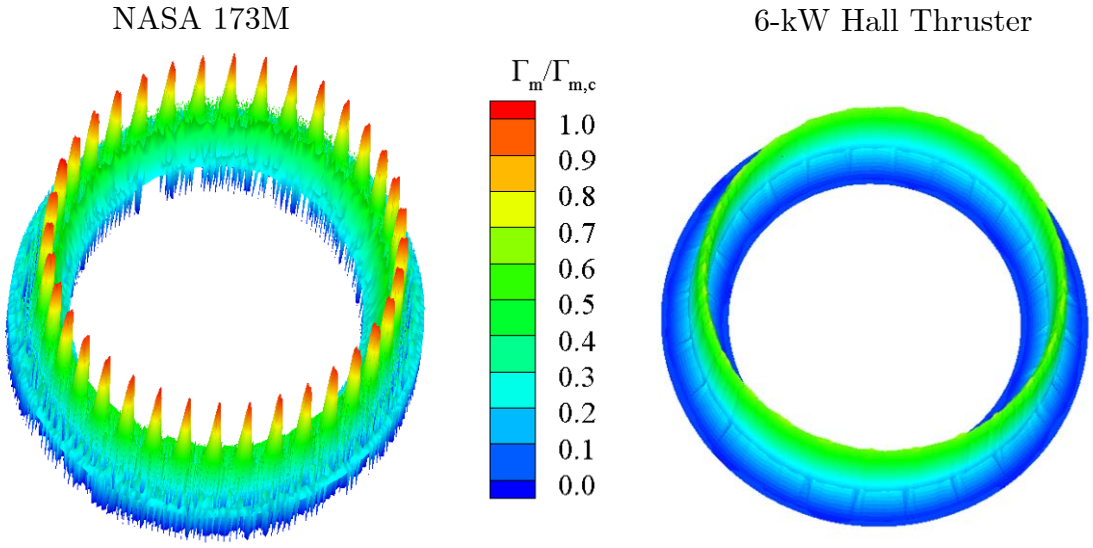

Figure 3-15. FLUENT simulations of the mass flux at the anode exit for the NASA-173M and 6-kW Hall thruster.

3.7.2 Anode Temperature

Building upon the desire to increase neutral residence time in the channel by decreasing axial velocity (see Section 3.2.2) leads to the logical suggestion of cooling the propellant to decrease the neutral thermal velocity. To adjust the temperature of neutrals entering the discharge channel, heat can be transferred to or from the neutral particles upstream of the thruster (in flow supply lines) or within the thruster (in anode or discharge channel). Due to the continuum flow and hence, large number of neutral collisions with the anode walls prior to reaching the anode exit, the neutral temperature is highly dependent on anode temperature. Hence, heat transfer upstream of the thruster has little effect. The independence of neutral velocity on inlet temperature was confirmed with

simulations in FLUENT that found less than a 1% change in axial velocity over a 100% change in anode inlet temperature.

Rather than cooling the propellant prior to reaching the thruster, the propellant can be effectively cooled by reducing the temperature of the anode. Linnell [51] attempted to actively cool the Hall thruster anode with a water-cooled chiller, but the experiment proved unsuccessful due to an electrical short. To validate the concept of this experiment, the anode flow of the NASA-173M was simulated with FLUENT. The anode surface temperature was varied from 300-1100 K, while all remaining variables in the simulation were kept constant. The results of these simulations are included in Figure 3-16 and they indicated that cooling the anode by 100% reduced the axial velocity by 30% at the anode exit. The centerline value and average value across the anode exit plane are shown, with each displaying a clear square-root dependence on anode temperature. In particular, the velocity dependence agrees well with the mean thermal speed

$$u_n = \sqrt{\frac{8k_B \alpha T}{\pi m_{xe}}}, \tag{3-25}$$

where T is the anode temperature and α is the neutral temperature accommodation factor that has a value of unity for perfect neutral accommodation to the anode temperature [31]. The relationship between neutral velocity and anode temperature is given by Eq. 3-25 and shown in Figure 3-16 as

dashed lines. Equation 3-25 closely models the centerline velocity for $\alpha = 1.0$, and the average velocity across the anode exit is modeled by $\alpha = 0.25$.

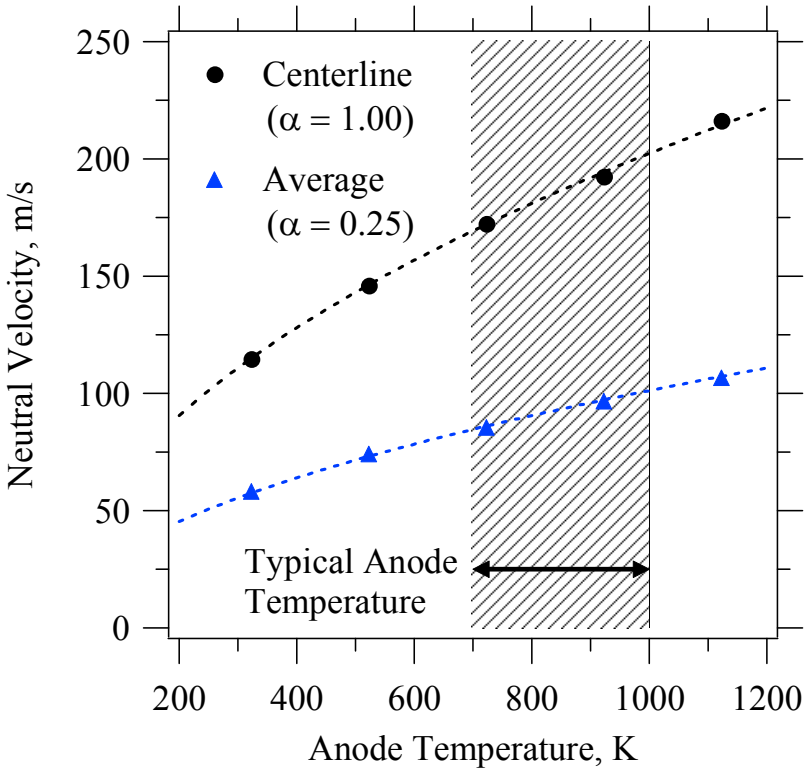

Figure 3-16. FLUENT simulated axial velocity variation with anode temperature at anode centerline and average across the anode exit [31]. Square-root dependence of the axial velocity on anode temperature is shown by the dashed lines.

The expected anode temperature ranges from 700-1000 K as shown in Figure 3-16. This range was consistent with values measured with direct-contact thermocouples [48, 70, 71]. Over this range, the centerline neutral velocity at the anode exit varied from approximately 160 to 200 m/s (25% increase). The bulk neutral velocity was well-correlated with LIF measurements in a variety of Hall thrusters [72-75].

3.7.3 Anode Mass Flow Rate

The relationship between mass flow rate and the neutral particle density and velocity in the channel is described by the mass continuity equation

$$\frac{\dot{m}}{A_{ch}} = m_{xe} n_n u_n \,. \tag{3-26}$$

The preceding section showed that the neutral velocity was heavily influenced by the anode temperature, making the mass flow directly proportional to the neutral density in the channel (assuming constant channel dimensions and propellant). In this way, the fundamental variable that changes is neutral density, not the mass flow rate. The neutral density is regarded as a fundamental property since it is directly proportional to the electron-neutral collision frequency, which ultimately controls electron cross-field diffusion (see Section 8.1). For instance, the importance of neutral density can be seen by noting that increasing the channel area for a given mass flow rate will cause a decrease in neutral density; hence, there will be fewer electron-neutral collisions and less cross-field mobility (assuming all other variables are equal, which often times they are not).

FLUENT simulations were performed at flow rates of 10, 20, and 30 mg/s to determine the average neutral velocity at the anode exit. These values were then used as initial boundary conditions for HPHALL-2 simulations that assume a half-Maxwellian velocity distribution that is injected with an axial drift velocity at a prescribed Mach number. FLUENT simulated mean axial velocities on channel centerline at the anode exit for flow rates of 10, 20, and 30 mg/s were 70,

100, and 130 m/s, respectively. Since these simulations were performed at a constant anode temperature of 700 K, the sound velocity at all conditions was 270 m/s, which resulted in injected Mach numbers of 0.26, 0.37, and 0.44 at 10, 20, and 30 mg/s, respectively.

The neutral number density produced by HPHALL-2 simulations using the computed injector Mach numbers from FLUENT are shown in Figure 3-17. The neutral density increased linearly with flow rate at the anode exit plane, and the profile throughout the channel exhibited a self-similar profile.

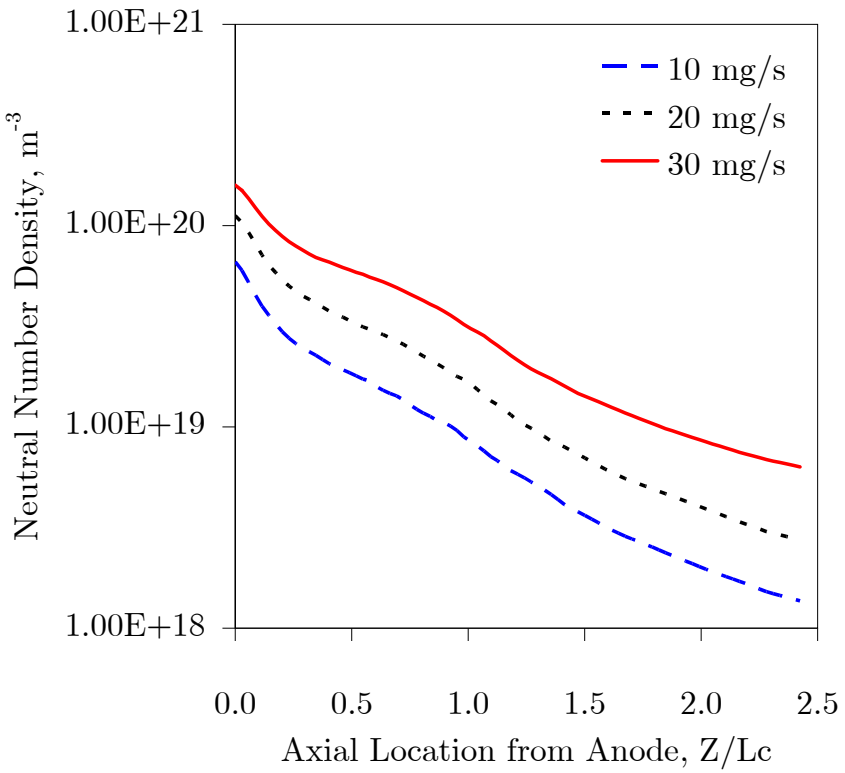

Figure 3-17. HPHALL-2 simulation results for neutral density on thruster centerline during cold flow operation (no plasma).

3.8 Neutral Acceleration in the Channel

The neutral injection method and anode boundary conditions play a significant role in the neutral flow dynamics in the rear of the channel. However, several additional contributions within the channel can alter the neutral flow dynamics by causing the neutrals to speed up as they approach the channel exit.

1) **Hydrodynamic expansion**. To maintain continuity, the flow must accelerate towards the channel exit since the density decreases as the flow expands into the vacuum chamber. Simulation results for cold flow operation (no plasma) in Figure 3-12 confirm this behavior.
2) **Depletion of slow neutrals from ionization**. The ionization cross-section is velocity-dependent, favoring collisions at the lowest relative velocity. Thus, the ionization process tends to deplete the slow-moving neutrals, causing the bulk neutral population to become faster [18, 75].
3) **CEX creation of fast neutrals**. If an ion experiences a CEX collision inside the channel, it is converted into a fast neutral and contributes to an increase in the bulk neutral velocity. However, the likelihood of CEX in the channel is relatively low since the mean free path is greater than the length of the entire discharge channel.
4) **Neutral excitation**. As neutrals travel through the discharge channel, they can gain energy through collisions with the hot walls (high neutral accommodation) and collisions with hot electrons (non-ionizing

collisions). HPHALL-2 results for neutral temperature, velocity, and density including the plasma discharge are shown in Figure 3-18. These results indicated that the neutral temperature peaked near the channel exit, while the velocity was mostly unaffected and the density dropped significantly due to ionization. Since HPHALL-2 does not solve an energy equation for the neutrals, the interaction with hot electrons did not contribute to this increased in neutral temperature. Instead, the neutral heating was entirely due to interaction with the hot wall.

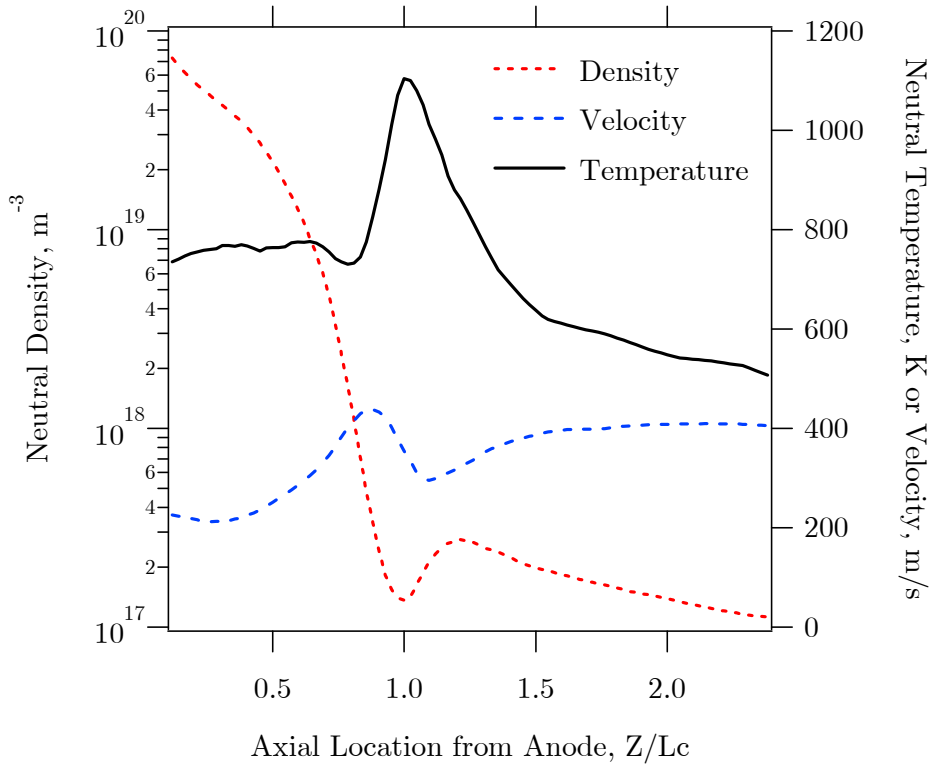

Figure 3-18. Neutral properties from HPHALL-2 simulations on channel centerline in the presence of the discharge plasma.

LIF measurements by Cedolin *et al.* [76] and Hargus *et al.* [74] indicated an increase in neutral velocity as the discharge power was increased. They concluded that the neutrals velocity increased through a combination of several of the contributions listed above. However, a large contribution to their measured increase in neutral velocity was likely due to the increased wall temperature with increased discharge power as shown in Ref. [49].

3.9 Summary

This chapter described the neutral flow dynamics that will have implications throughout the rest of the dissertation. The numerical tools described in this chapter were used to simulate the neutral flow within the discharge channel during cold-flow operation (no plasma). These same tools were used during the parametric design of the gas distributor aspect of the 6-kW Hall thruster anode. The numerical tools were verified through two-dimensional experimental measurements downstream of the anode. These measurements were achieved by using the APAT technique.

Experimental and numerical data were used to provide one- and two-dimensional flow distributions that can be used in future investigations. Additional data were presented that highlight the influence of anode boundary conditions on neutral flow distributions. Results from previous work, indicated that the neutral flow dynamics play a significant role in the operation of Hall thrusters, affecting thruster efficiency, stability, thermal margin, and lifetime.

Chapter 4

Experimental Apparatus

The facilities and apparatus described in this chapter were used to characterize the 6-kW Hall thruster to better understand the ionization and acceleration processes and to understand the competing mechanisms affecting Hall thruster performance over a wide range of operating conditions. The results, analysis, and discussion of these measurements can be found in Chapters 4-7.

4.1 Large Vacuum Test Facility

Experiments were performed in the LVTF at the University of Michigan's Plasmadynamics and Electric Propulsion Laboratory (PEPL) shown in Figure 4-1. The LVTF is a 6-m-diameter, 9-m-long, cylindrical, stainless steel vacuum chamber. Pumping was provided by seven single-stage CVI model TM-1200 cryo-pumps and liquid nitrogen shrouds, with a nominal pumping speed of 240,000 l/s on xenon.



Figure 4-1. Photograph of the Large Vacuum Test Facility at the University of Michigan's Plasmadynamics and Electric Propulsion Laboratory.

Facility pressure was monitored by a nude ionization gauge (nude gauge) and a Bayard-Alpert ionization gauge (external gauge). The base pressure was approximately 2.3×10^{-7} torr. Pressure measurements from the ionization gauges were corrected for xenon using

$$P_c = \frac{P_i - P_b}{2.87} + P_b, \tag{4-1}$$

where P_c is the corrected pressure, P_i is the indicated pressure during operation (from ionization gauges), P_b is the facility base pressure, and the coefficient of 2.87 is specific to xenon [77]. The facility pressure was reported as the average of the two ionization gauge readings, which resulted in a facility pressure during thruster operation at 22 mg/s total xenon flow rate of 1.3×10^{-5} torr. This flow

rate and pressure combination indicated a pumping speed of approximately 220,000 l/s (within 10% of the nominal pumping speed). The facility pressure that was measured by both ionization gauges is shown in Figure 4-2 as a function of total xenon flow rate. The ionization gauges were located at the center of the chamber on opposite sides of the wall.

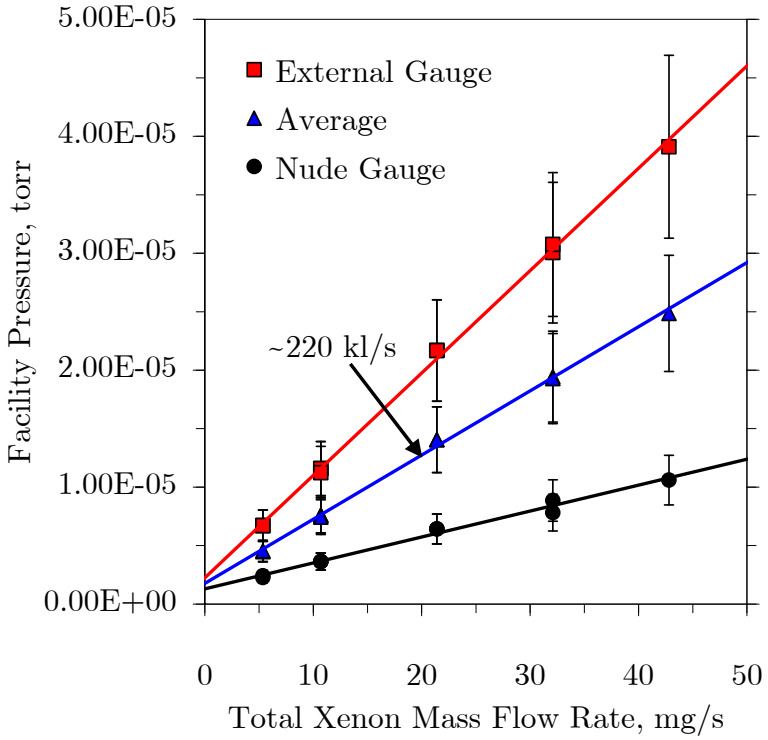

Figure 4-2. Facility pressure as a function of total xenon mass flow rate for the LVTF. The average pressure indicates a facility pumping speed of approximately 220,000 l/s.

4.2 6-kW Hall Thruster

Experiments were performed using a 6-kW laboratory model Hall thruster [13, 34, 78-80] that has a demonstrated throttling range of approximately 1-10 kW, 100-600 mN, and 1000-3000 s specific impulse (see Chapter 6). The thruster was constructed with 8 individual outer coils, a single inner coil, and an internal

trim coil. The trim coil was not used for the data presented in this dissertation. The thruster was equipped with a center-mounted LaB_6 hollow cathode that was operated at 7% of the anode mass flow rate. The thruster was positioned so that it was elevated to chamber centerline, allowing the plume to expand for approximately 4-7 m along the chamber axis depending on the experiment. A photograph of the 6-kW thruster prior to its initial firing is shown in Figure 4-3, and a photograph of the thruster during operation at its nominal condition of 300 V and 20 mg/s (6 kW) is shown in Figure 4-4.

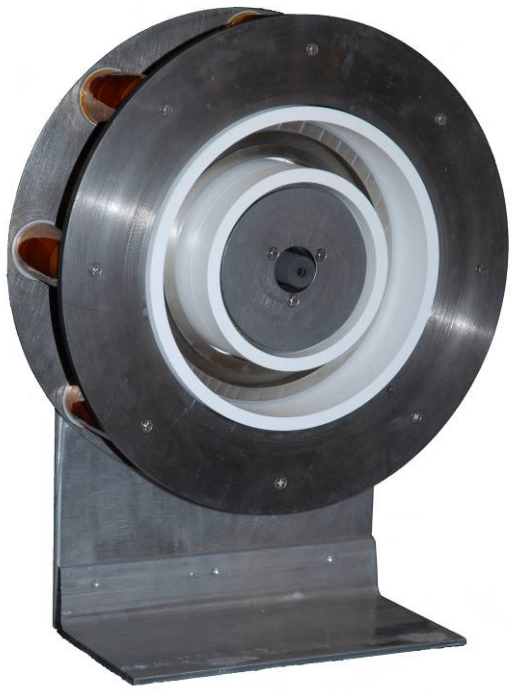

Figure 4-3. Photograph of the 6-kW Hall thruster prior to initial firing.

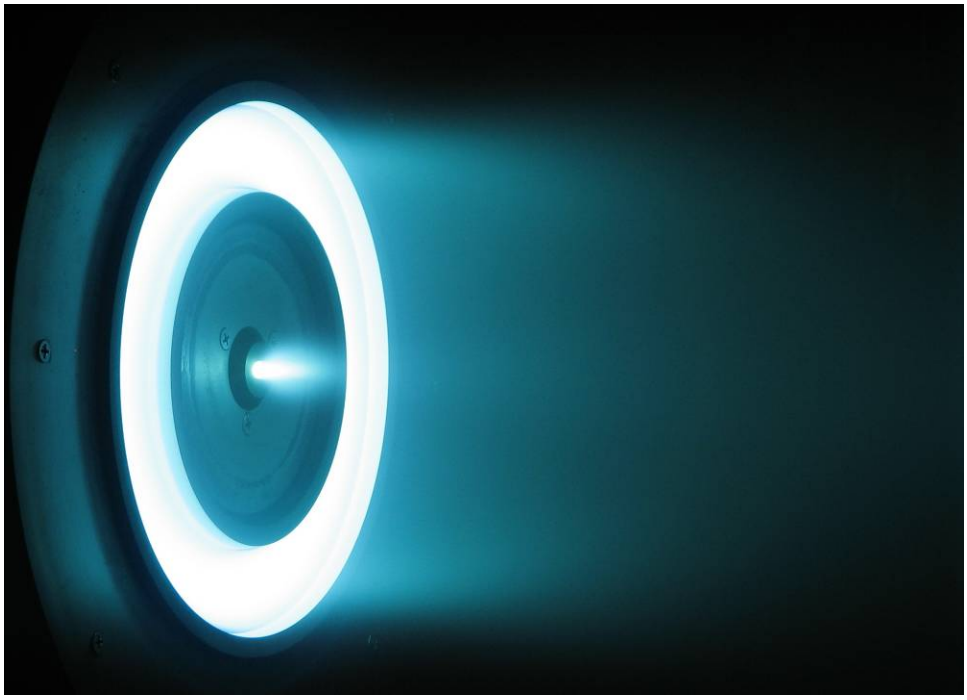

Figure 4-4. Photograph of the 6-kW Hall thruster during operation at 300 V and 20 mg/s (6 kW).

4.3 Hall Thruster Support Equipment

The thruster discharge was sustained by a 100-kW power supply that provided a maximum output of 1000 V at 100 A. Although this power supply was capable of handling the high-frequency, large-amplitude discharge oscillations from the thruster, a nominally 1-kHz RC discharge filter was used to protect the power supply. The filter consisted of a 1.3 Ω ballast resistor that was in series with the positive terminal of the power supply and a 95 μF capacitor that was installed in parallel with the power supply outputs.

Commercially-available power supplies were used to power the magnets and cathode heater and keeper. The cathode discharge was initiated at approximately 180 W (11 A and 16.5 V) of heater power and a keeper potential

of 100-150 V, current was limited to 0.5 A. The cathode was operated at the nominal 7% flow fraction ($\dot{m}_c = 0.07\ \dot{m}_a$) whenever the thruster was operated at anode mass flow rate of 10 mg/s or above. At 5 mg/s, the discharge became unstable, requiring a flow fraction of 14%.

Research-grade xenon propellant (99.999% pure) was supplied to the anode and cathode by separate commercially-available flow meters and controllers, having an accuracy of ± 1% of full scale (approximately 50 mg/s for the anode, and 5 mg/s for the cathode). The system was calibrated using a constant volume method including the effects of compressibility [81].

4.4 Discharge Current and Discharge Voltage Monitoring

The *time-averaged* discharge current of the thruster was monitored using the main discharge power supply readout that exhibited excellent correlation with a high-precision calibrated current shunt and a calibrated multimeter. The *time-varying* thruster discharge current was monitored using a commercially-available, magneto-resistive, high-speed (100 kHz) current shunt placed in series with the cathode return line between the thruster and the RC filter. In future studies, the discharge current should be monitored on the anode and cathode return lines since these signals carry distinctly different information about the discharge oscillations. These measurements may offer additional insight into the physics of cathode coupling with the main discharge.

The *time-averaged* discharge voltage of the thruster was monitored using a calibrated multimeter. The discharge voltage was measured downstream of the RC filter, at the vacuum chamber feed through. The *time-varying* discharge voltage was monitored using a commercially-available voltage probe (1000:1).

4.5 Linear Stages

The LVTF was equipped with two fixed linear stages; a 0.9-m-long stage that was aligned with the vacuum chamber centerline (thruster axial direction), and a 1.5-m-long stage that was oriented perpendicular to chamber centerline (thruster radial direction). A third 1.5-m-long linear stage was used in some experiments for additional large-range motion of thrusters and probes. Additional 0.2 to 0.4-m-long linear stages were used for small-range motion of cathodes and probes. Each linear stage was driven by commercially-available stepper motors and controllers, having a specified positioning accuracy of $< \pm 0.1$ mm.

4.6 HARP

Probes were inserted and removed from the thruster discharge channel using the High-speed Axial Reciprocating Probe (HARP) at PEPL. The HARP has an acceleration and velocity capability of approximately 70 m/s^2 (~7 g's) and 2.5 m/s, respectively [82]. For these experiments, the HARP was operated at 0.75 or 1.5 m/s, resulting in a residence time within the discharge channel of approximately 80-120 ms. The residence time was minimized to reduce the

amplitude of probe-induced discharge perturbations and to reduce the heat load on the probe, potentially extending its operational lifetime.

To reduce the effects of the vacuum chamber compression during initial evacuation (probe-thruster shifts on the order of 1 mm were hypothesized in previous experiments [51]), the HARP and thruster translation stage were connected by a steel support structure. The HARP was fixed to the support structure downstream of the thruster to dampen oscillations that were produced by the actuation of the probe arm. The thruster was mounted to a 1.5-m-long translation stage that adjusted the radial location of the probe within the discharge channel. A schematic of the relative positions and orientations of the 6-kW Hall thruster and HARP are shown in Figure 4-5 and a photograph of the probe insertion is shown in Figure 4-6.

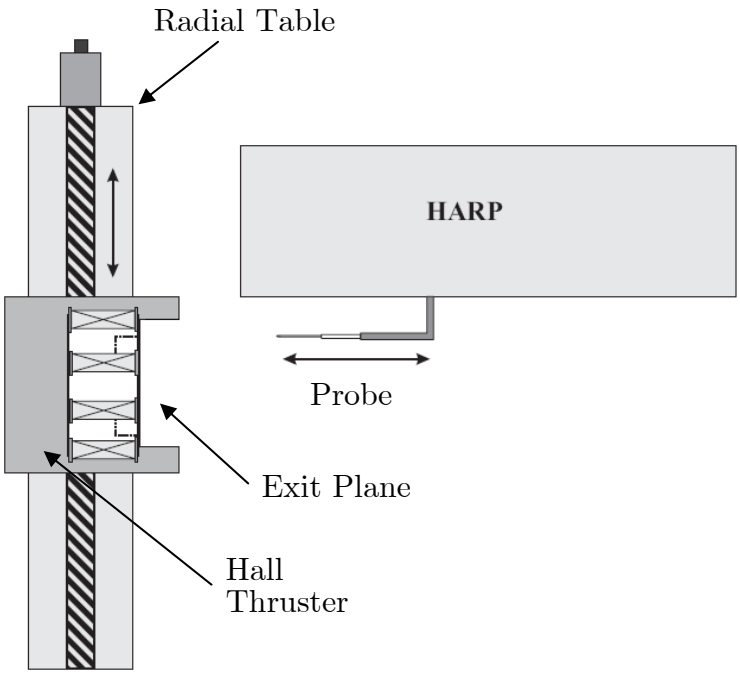

Figure 4-5. Schematic of the thruster and probe positioning systems used for internal plasma measurements.

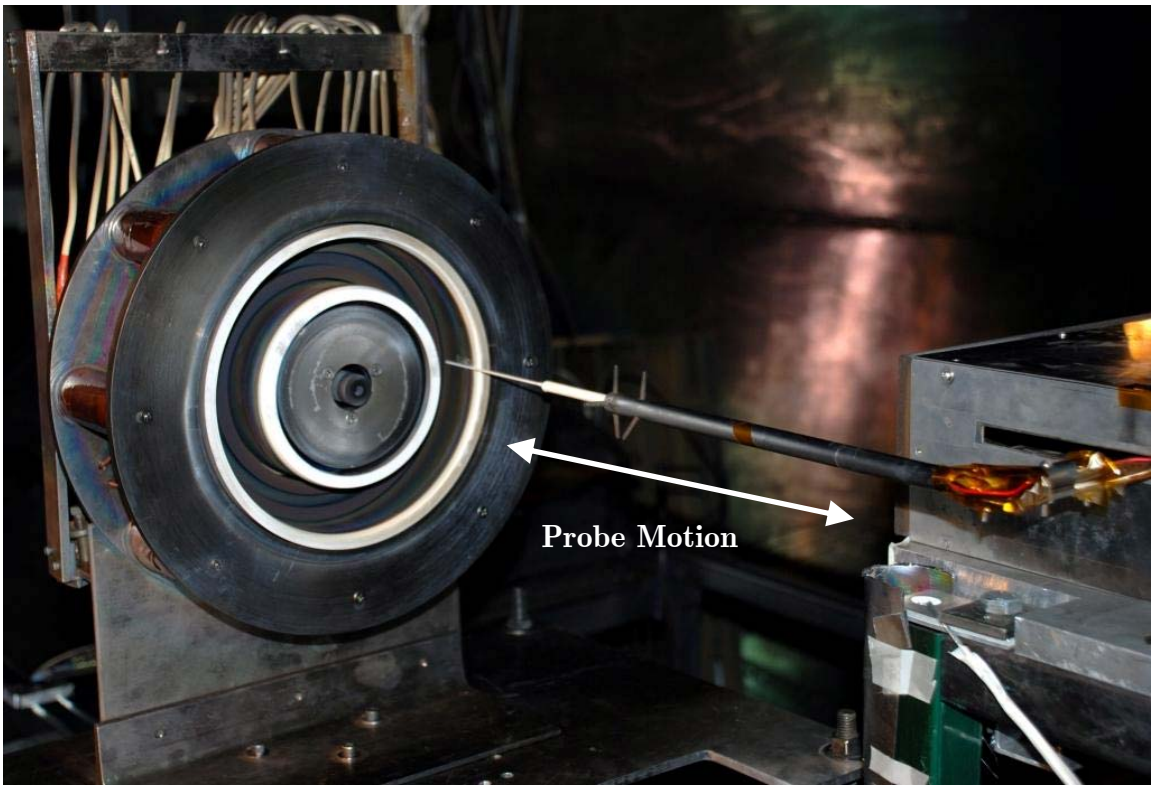

Figure 4-6. Photograph of probe insertion into the thruster discharge channel during internal plasma measurements with the HARP.

4.7 Thrust Stand

Thrust measurements were taken with a NASA GRC-designed inverted-pendulum thrust stand design. The null-type thrust stand was maintained at a constant temperature by cooling the shroud, control coils, and thruster mount with a closed-loop refrigerated glycol system. The thruster body was connected to facility ground through the thruster mount. The thrust readout was recorded using a 12-bit digital multimeter and a mechanical plotter to monitor time-varying thrust fluctuations. The typical sources of thrust stand uncertainty were associated with the null-coil output, inclination, zero position, and calibration slope and linearity. The cumulative uncertainty in thrust due to each of these

sources was conservatively estimated as ± 2 mN (typically $< 1\%$ of full-scale). Additional details on the thrust stand design and construction can be found in Ref. [83].

4.7.1.1 Method of Operation

During thruster operation, the position of the thrust stand relative to its rest position was monitored with a high-sensitivity Linear Voltage Displacement Transducer (LVDT). As thrust was produced, the thruster pushed on the stand causing a measureable displacement. The thrust stand responded by increasing current to the null-coil to keep the stand at its initial rest position. The coil current required to maintain the rest position was proportional to the applied force and a calibration was performed by applying a set of known masses and recording the null-coil response. The calibration masses were connected to the thruster and fed horizontally over a low-friction wheel that allowed each mass to hang freely in the vertical direction. Each of the four masses were 28.800 ± 0.007 grams, providing a calibration up to 1120 mN. The calibration sequence was a five minute process that included a forward calibration during addition of the four masses, and a reverse calibration during removal of each mass. This two-way data collection provided a measure of the hysteresis in the system. The null output had a 0.5 mN/mV relationship to thrust.

Generally, the slope of thrust calibrations remained constant throughout testing, even under changing thruster conditions and thermal loads. Thermal

drift of the system caused shifts in the thrust stand zero position throughout testing, but this effect was repeatable, predictable, and easily accounted for by pausing thruster operation to obtain the present zero position or to perform a calibration. In addition to thermal drift of the zero position, inclination of the thrust stand changed with variations in thermal load. To reduce this effect, the inclination was manually zeroed throughout data collection and the effect was highly repeatable, predictable, and easily accounted for. The inclination had a 0.7 mN/mV linear relationship with the measured thrust, as shown in Figure 4-7. Since the measurement accuracy of the inclination was ± 1 mV, the uncertainty in thrust due to inclination was approximately ± 0.7 mN. The effect of inclination

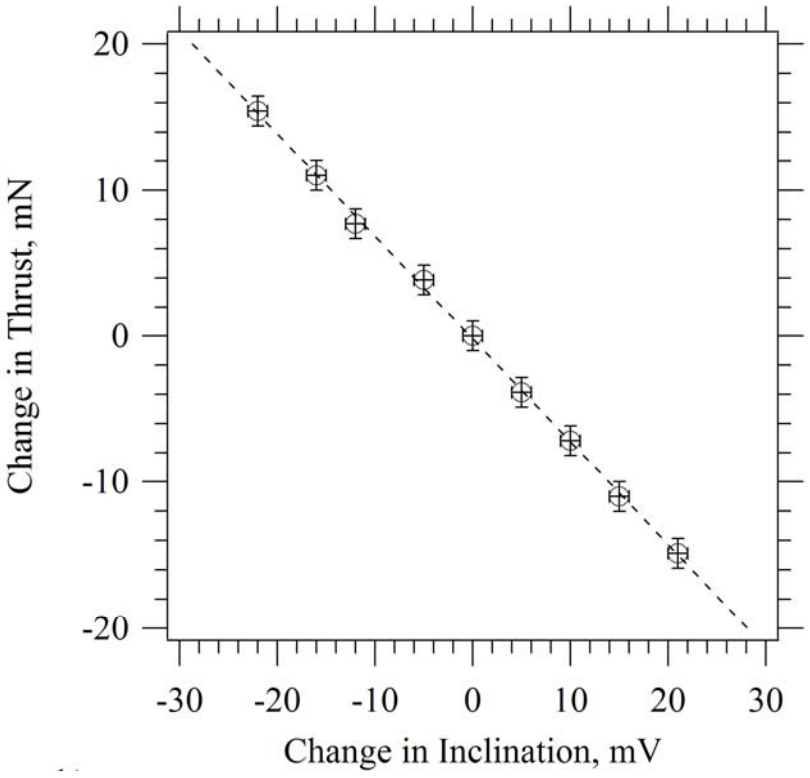

Figure 4-7. Change in thrust due to change in thrust stand inclination.

can be ignored if the thrust stand zero position is obtained for each thrust measurement; however, for long-duration comparisons of thrust, the inclination must be maintained at a constant level.

4.7.1.2 Electrical Modifications

The thrust stand used four main components to maintain stability and provide thrust measurements; LVDT, control electronics, linear amplifier, and electromagnet. The control electronics of the thrust stand were significantly improved by replacing the custom made "breadboard" control logic with a commercially-available Proportional Integral Differential (PID) circuit. The existing amplifier was also replaced with a low-noise linear amplifier that had a 5 kHz bandwidth. These electrical modifications greatly improved the thrust stand stability, functionality, flexibility, and resolution. The primary impact of the new electronics was the ability of the system to operate using a single control coil. In the previous design, high-frequency damping control (10^3 Hz) and low-frequency null control (10^0 Hz) were provided by individual coils operated by autonomous portions of the control circuit. By using two coils, the system would often deteriorate into an unstable, uncontrollable oscillation as the coil actions opposed each other. A consequence of controlling the thrust stand with a single coil was the high-frequency damping signal was superimposed upon the low-frequency null signal. This caused the DC value of the null signal to have an additional oscillatory component associated with it. Under most circumstances, the

amplitude of the damping signal was small with respect to the null signal and the additional uncertainty was small (< 0.1 mN).

4.8 Plume Diagnostics

In this dissertation, plume diagnostics refer to any electrostatic measurement device that was used within the plume of the thruster rather than inside the discharge channel. These diagnostics were used to measure a variety of plasma properties that relate to thruster performance and operation.

4.8.1 E×B (Wien filter)

An E×B probe, or Wien filter, is a band-pass ion filter that selects ions according to their velocities through the application of crossed electric and magnetic fields [84-86]. Most probes establish a constant magnetic field with permanent magnets, while the electric field is established between two parallel plates separated by a gap distance d and biased to a potential V_{probe}. Sweeping the plate voltage while monitoring the ion current that passes through the probe yields a current-voltage characteristic that is related to the ion velocity distribution function. Because the velocity of multiply-charged ions in Hall thrusters is proportional to the square root of their charge state, an E×B probe can be used to discriminate between ion species. Analysis of the ion current from the probe characteristic can then be used to compute the ion species fractions.

The E×B probe was comprised of three main sections: the entrance collimator, E×B test section, and exit collimator. Ions passing through the

entrance collimator must travel through the test section undeflected to reach the collector. The motion of an ion through the test section is described by the Lorentz force equation given by

$$\vec{F} = eZ\left(\vec{E} + \vec{u} \times \vec{B}\right), \tag{4-2}$$

where $\vec{F}$ is the force on each particle, e is the elementary charge, Z is the ion charge state, $\vec{E}$ is the electric field, $\vec{u}$ is the particle velocity, and $\vec{B}$ is the magnetic field. The velocity of an incoming ion can be accurately described by

$$u_i = \sqrt{\frac{2eZ_i V_{accel,i}}{m_{xe}}}, \tag{4-3}$$

where Z_i is the ion's charge state and $V_{accel,i}$ is the ion's acceleration voltage. The test section filters particles with a particular velocity by balancing the electric and magnetic fields so that there is no net force acting on those particles. Setting the force equal to zero in Eq. 4-2, the velocity of an undeflected ion passing through the test section is

$$u_{pass} = \frac{E}{B} = \frac{V_{probe}}{B\,d}, \tag{4-4}$$

where d is the E×B gap distance. Since the gap distance and magnetic field are fixed, the ion velocity is proportional to the probe voltage. Thus, the probe voltage can be swept across an appropriate range to capture the current from various charge states. The current collected at any given voltage can be written as:

$$I_i = eZ_i n_i u_i A_c = eZ_i n_i A_c \sqrt{\frac{2eZ_i V_{accel,i}}{m_{xe}}}, \tag{4-5}$$

where n_i is the ion number density, A_c is the probe collection area, and u_i is described by Eq. 4-3.

4.8.1.1 Probe Design and Experimental Setup

The E×B used in this study was designed by the NASA Glenn Research Center (GRC) based on a set of incremental improvements upon the probe used in Ref. [86]. A schematic of the probe is shown in Figure 4-8. The test section was 150 mm long and the inlet and outlet collimators were 75 mm long. The two collimating orifices and the inlet orifice had diameters of 1.6 mm. To reduce the effects of SEE due to impacts of high-energy ions on the collector, the collector was shaped as a high aspect ratio tube with a conical end and spray coated with tungsten (see Figure 4-8). Tungsten has a relatively low-yield of secondary electrons under xenon bombardment and the collector geometry ensured that any secondary electrons that were emitted were re-collected. The collected current was sent to a picoammeter using a 50 Ω BNC cable and feed through.

The fixed magnetic field was supplied by two permanent magnets, reaching a peak of 0.16 T in the center of the probe test section. The magnets were made from a sintered hard ferrite with a Curie temperature of 730 K and a rated operating temperature of 530 K. The bias plates were separated by a 9.7-mm gap and the voltage was applied with a programmable voltage source. The voltage was split between the two plates using the circuit in Figure 4-9 such that

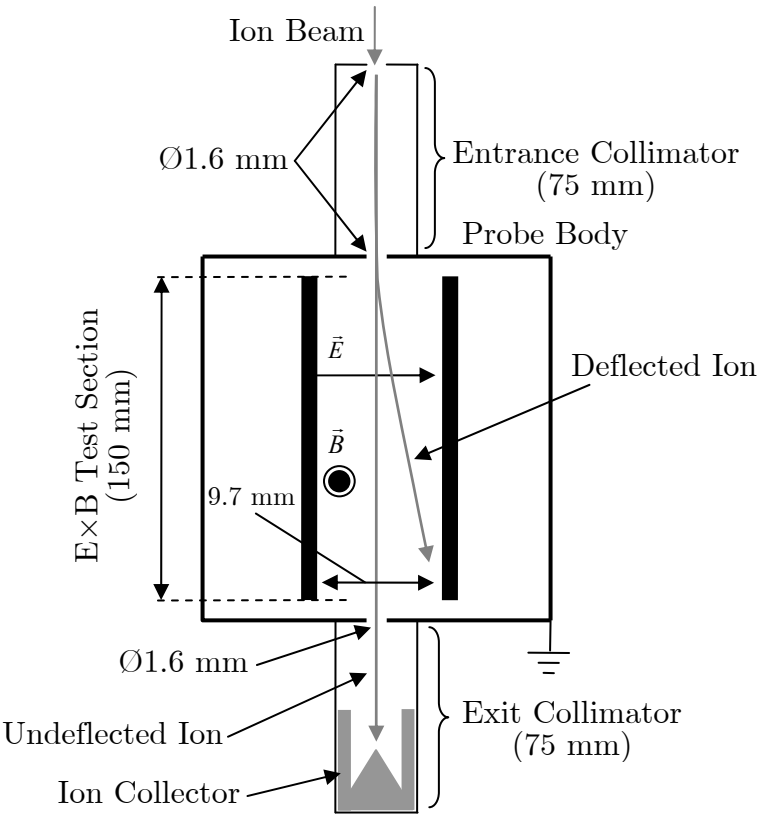

Figure 4-8. E×B probe schematic (not to scale).

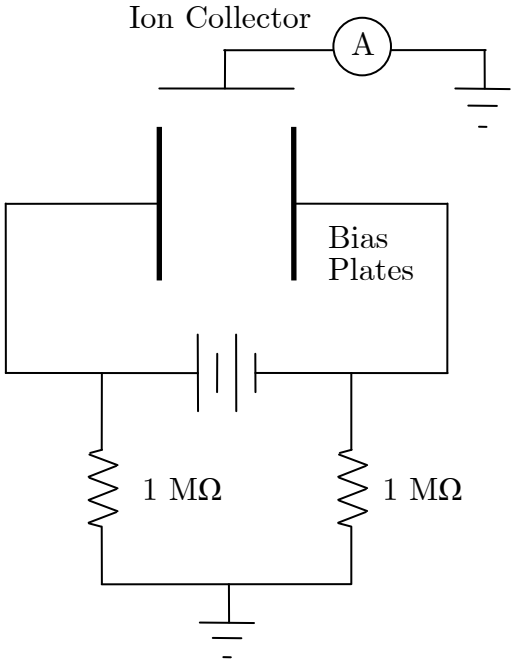

Figure 4-9. E×B probe electrical diagram.

the potential at the center of the probe was held constant and remained within a few volts of facility ground. Additional details on probe operation, orifice selection, probe heating, and neutral filling, can be found in Ref. [87].

4.8.1.2 Data Analysis

The primary function of an E×B probe is to measure the current collected due to each individual ion species within the plume. Analysis of the probe spectra yields the ion current fractions of each ion species given by

$$\Omega_i = \frac{I_i}{\sum I_i} = \frac{n_i Z_i^{3/2}}{\sum n_i Z_i^{3/2}}. \tag{4-6}$$

This dissertation focuses on the ion current fractions; however, it should be noted that in the Hall thruster literature the most commonly cited figure of merit is the ion species fractions [84, 88, 89] given by

$$\zeta_i = \frac{n_i}{\sum n_i} = \frac{\Omega_i / Z_i^{3/2}}{\sum \Omega_i / Z_i^{3/2}}. \tag{4-7}$$

The ion current fractions were used here since they are based directly on the measured currents and the current fractions are typically used in performance models (see Section 6.1). Equations 4-6 and 4-7 can be used to convert between the two representations of the data that are described in more detail in Ref. [90].

4.8.1.3 Correction for Charge-Exchange

CEX collisions in the plume have the undesirable effect of redistributing ion current away from thruster centerline. This causes an underprediction of ion

current that becomes more severe with increasing distance from the thruster exit plane. The decay in centerline ion current density due to CEX collisions can be written as [91]

$$\frac{j_z}{j_o} = \exp\left(-n_b \sigma_{CEX} z\right) \tag{4-8}$$

where j_z is the current density at a downstream location, z, j_o is the current density at the exit plane, n_b is the background gas density, and σ_{CEX} is the CEX collision cross section. Equation 4-8 describes the downstream evolution of the beam and can be used to estimate and correct for the effects of CEX collisions. Equation 4-8 can be used to correct the current density of each species in the plume by using the appropriate CEX cross section given by

$$\begin{aligned} \sigma_{CEX,Xe^{1+}} &= 87.3 - 13.6\log\left(V_D\right) \\ \sigma_{CEX,Xe^{2+}} &= 45.7 - 8.9\log\left(2V_D\right). \\ \sigma_{CEX,Xe^{3+}} &= 16.9 - 3.0\log\left(3V_D\right) \end{aligned} \tag{4-9}$$

Since the cross sections are insensitive to the ion energy, the discharge voltage can be used in place of the acceleration potential for convenience. This analysis only accounts for symmetric reactions between each ion species and a uniform neutral background density that was determined by the facility pressure. Corrections were not made for Xe4+ since it typically comprises much less than 1% of the beam.

4.8.1.4 Plume-averaged Methodology

Ion current density measurements were recorded with the Faraday probe axially aligned (face parallel to the thruster exit plane) in order to determine the *plume-averaged* ion current fractions. After analyzing the E×B probe spectra to yield the local ion current fraction of each species, the local current density was used to weight the current fraction so that a plume-averaged value could be determined according to

$$\Omega_{i,avg} = \frac{\int_0^R \Omega_{i,loc} j(R) R dR}{\int_0^R j(R) R dR}. \tag{4-10}$$

The radial integration was necessary since E×B data were taken along a radial path.

The 6-kW thruster used in this study had a plume-divergence half angle that was less than 20° for most operating conditions (see Section 5.5). Ideally, E×B data would be captured from 0 to 90°, but translation stage limitations only allowed measurements to 30°. Although data were not collected throughout the entire plume, the species fraction variations captured within the 30° cone were sufficient to adequately characterize the plume-averaged current fractions. This is shown by the current density plot in Figure 4-10 that highlights the locations where E×B data were taken. These Faraday probe data were taken from 0 to 90° on a 1-m probe arm with a rotational stage that was centered on the thruster exit plane. This comparison indicates that the current density decreases by

approximately two orders of magnitude from centerline to 30°. Additional species fraction data beyond 30° would be useful for this analysis, but their contribution to the plume-averaged current fractions was negligible.

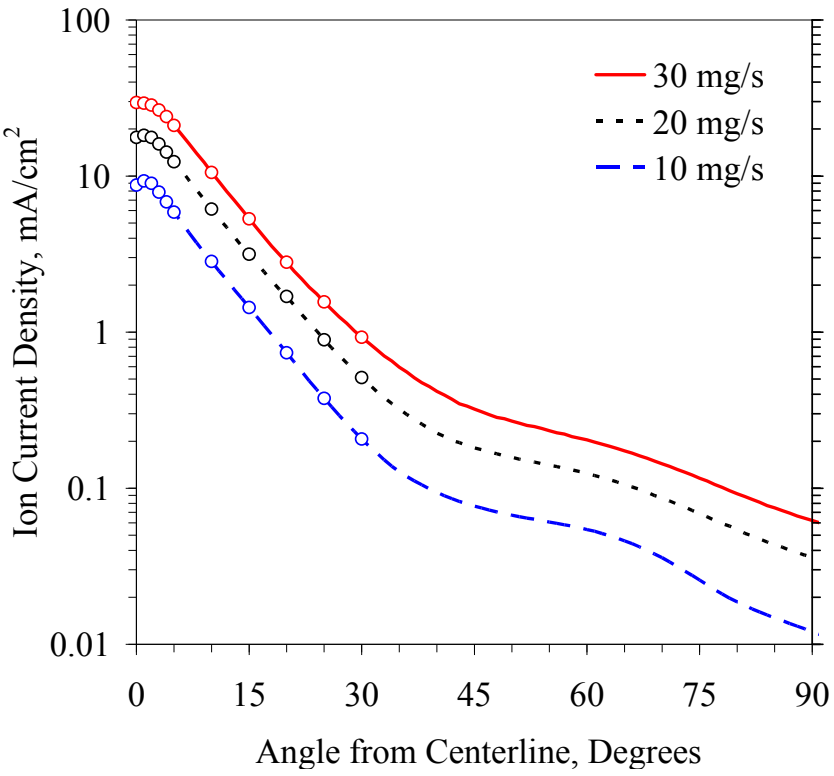

Figure 4-10. Ion current density taken on a 1-m arc from 0 to 90°, showing E×B data collection locations.

Ion current density profiles in the far-field plume for each operating condition are shown in Section 5.4. When normalized (not shown) the profiles showed a self-similar characteristic for each discharge voltage. In particular, the normalized current density measurements at 10, 20, and 30 mg/s collapsed onto a single curve at 150 and 300 V indicating that the plume structure (i.e., divergence) remained approximately constant as power was increased at constant discharge voltage. This characteristic was important for the CEX corrections

since it ensured that facility effects were not dominating the plume-averaging technique at higher flow rates. The data in Section 5.4 also indicated that the plume divergence decreased with increasing discharge voltage.

4.8.1.5 Measurement Uncertainty

Using the methods outlined by Kim [84], the probe energy resolution was estimated as 1%, which contributes to overall uncertainty of less than 0.5%. The primary sources of measurement uncertainty for the E×B probe were identified as beam loss to CEX prior to reaching the probe and loss of ion current introduced by the method of triangle fitting [87, 90]. Several other analysis methods were considered (peak heights, variable exponential fitting, Gaussian fitting, etc), consistently producing larger uncertainties. The cumulative uncertainty in ion current fractions was approximately 2%.

4.8.2 Single Cylindrical Langmuir Probe

A single cylindrical Langmuir probe was used to measure the plasma potential in the vicinity of the RPA during data collection in order to correct the measured voltage distribution.

4.8.2.1 Probe Design and Experimental Setup

The Langmuir probe electrode was composed of a 0.38-mm-diameter tungsten wire that was enclosed in a 0.76-mm-diameter alumina tube. The length of the tungsten electrode was 8.25 mm, resulting in a length-to-diameter ratio of approximately 22, well above the recommended value of 10. A schematic of the

probe construction is shown in Figure 4-11. The length of the probe was aligned parallel with the ion flow with the mid-point located 200 ± 1 cm downstream of the thruster exit plane and 10° away from thruster centerline (consistent with RPA location).

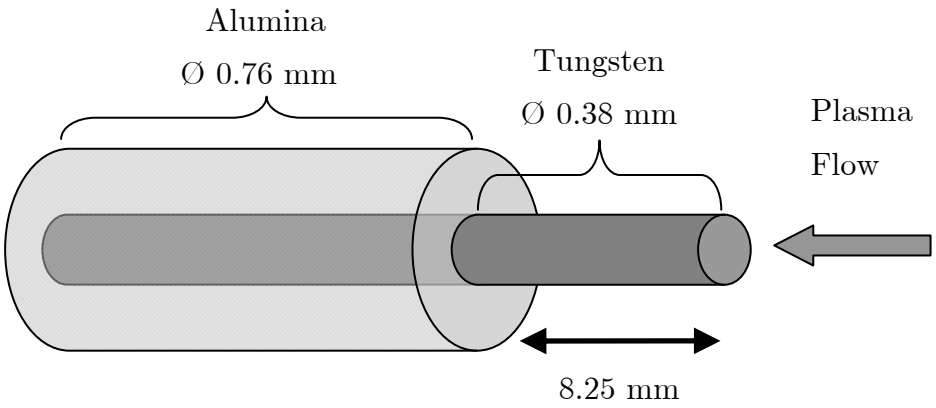

Figure 4-11. Schematic of the cylindrical Langmuir probe used in the far-field plume (not to scale).

The Langmuir probe was operated using a function generator, bi-polar power supply, and measurement circuit that was described in Section 4.9.2.4. The voltage was swept between ± 50 V from facility ground at 15 Hz, allowing approximately 30 I-V traces to be collected within one second. Data were collected at 250 kHz, resulting in more than 8000 individual I-V measurements in each trace. The combination of high time resolution and large number of samples offered a significant reduction in the plasma potential uncertainty.

4.8.2.2 Data Analysis

A typical I-V trace (thruster operating at 300 V and 20 mg/s) and its first derivative are shown in Figure 4-12 to illustrate the method used to determine

the plasma potential [92]. The plasma potential was also calculated using the graphical method that relies on subjective intersection of the electron retarding and electron saturation regions. The two plasma potential analysis techniques produced reasonably good agreement for the cases investigated. The derivative method consistently produced a plasma potential that was approximately 1 V greater than the graphical method. Both techniques were automated since hundreds of I-V traces were recorded at each operating condition and the average of the two results was reported as the local plasma potential for correcting the RPA. Considering all the sources of uncertainty described above, the uncertainty in the plasma potential was estimated as ± 1 V.

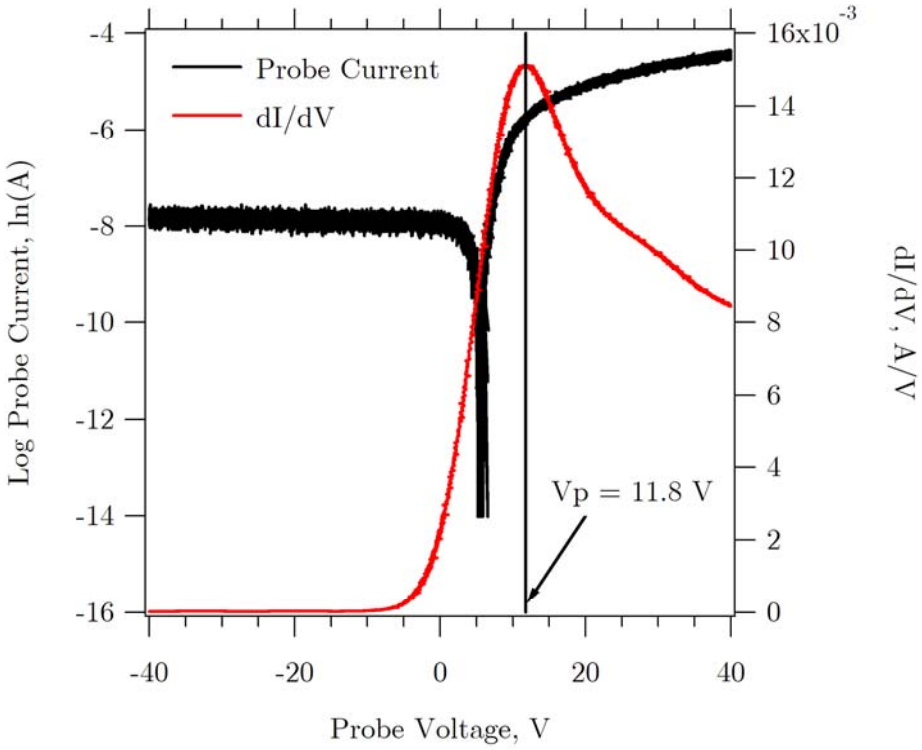

Figure 4-12. Sample Langmuir probe I-V characteristic illustrating the methods used to compute the plasma potential for correcting the RPA measurements.

The effect of sheath growth and end effects are typically accounted for in Langmuir probe analysis (see Section 4.9.2.3). However, these effects are not explicitly accounted for in this context since the ion/electron saturation currents were not directly used in the analysis.

4.8.3 Retarding Potential Analyzer

A Retarding Potential Analyzer (RPA) uses a series of biased grids to selectively filter ions across a wide range of energies. The probe characteristic is related to the ion energy distribution function, and from this distribution, the most probable ion energy is extracted.

4.8.3.1 Probe Design and Experimental Setup

The RPA used in this experiment was described in further detail in Refs. [26, 93]. For these experiments, the phenolic sleeve was replaced with Macor, offering a substantial increase in grid isolation from the probe body and decrease in probe failure due to overheating. A schematic of the updated RPA is shown in Figure 4-13.

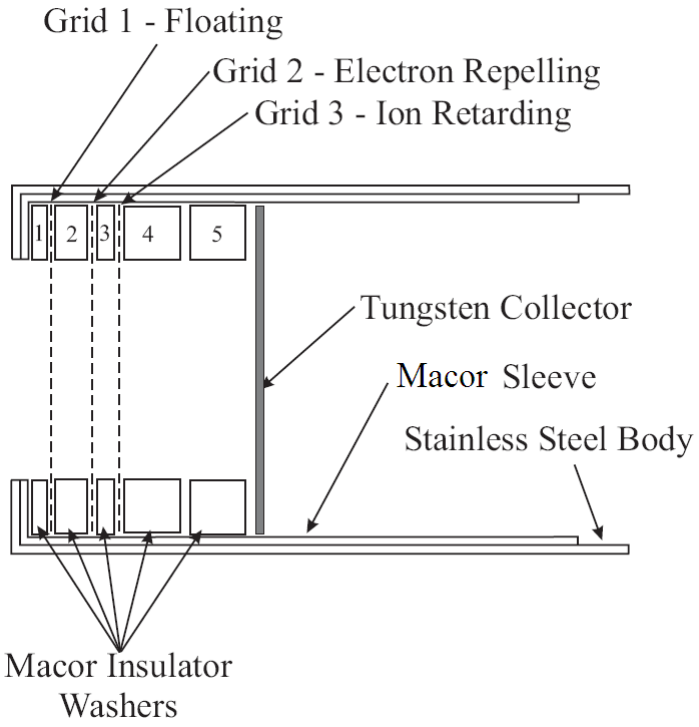

Figure 4-13. Schematic of the RPA showing major internal components.

The first grid was allowed to float at the local plasma floating potential to minimize perturbations to the plasma flow. The second grid was biased to -30 V with respect to facility ground in order to repel electrons from entering the device. The third and final grid was biased through a wide range of positive potentials (0-1100 V) acting as a high-pass filter by allowing only ions with voltages (i.e., energy-to-charge ratios) greater than the grid voltage to reach the collector. The ion current to the collector was measured with a picoammeter. An electrical schematic of the RPA is shown in Figure 4-14.

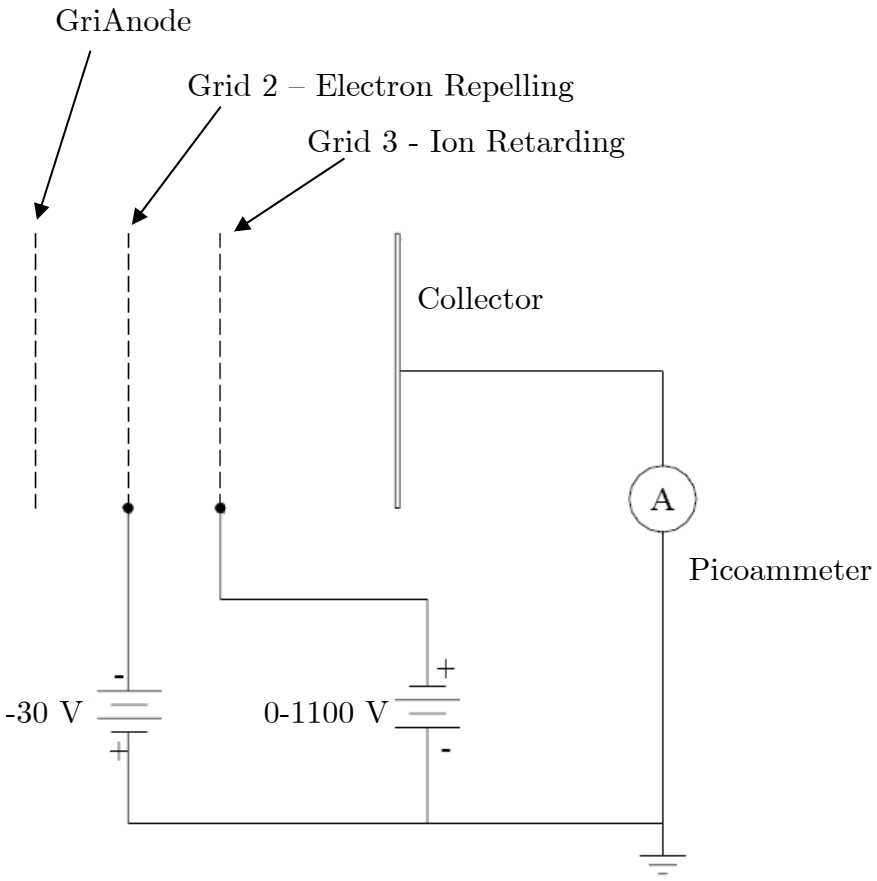

Figure 4-14. Electrical Schematic of the RPA.

The RPA was located 2 m downstream of the thruster exit plane at 10° from thruster centerline. The RPA grids were angled towards the discharge channel centerline within an accuracy of approximately 2°, which was an acceptable uncertainty due to the 45° acceptance angle of the probe [26]. When not in use, the RPA was turned 90° so that it was behind a graphite plate, protecting it from the flow of plasma.

The single-point measurement technique used in these experiments provided a reasonably good approximation of the bulk ion voltage distribution. However, a more rigorous approach is outlined in Ref. [94] involving angularly-

resolved RPA measurements that extended from 0 to 90° from thruster centerline. Based on these measurements, taking a single measurement near thruster centerline added less than 1% to the uncertainty in the ion voltage distribution.

4.8.3.2 Data Analysis

The derivative of the current-voltage characteristic produced by the RPA is proportional to the ion energy distribution function, *f(V)* and can be written as [95]

$$\frac{dI_p}{dV_{probe}} = \frac{-Z_i^2 e^2 n_i A_c}{m_{xe}} f(V). \tag{4-11}$$

The RPA measures the ion energy distribution function only if the plasma is composed of ions of the same mass and charge (as pointed out by King [95]). Hall thruster plumes are typically composed of several percent Xe^{2+} and Xe^{3+} [84, 87, 88, 95]. In particular, the Hall thruster used in this investigation had multiply-charged ion current fractions that ranged from 15 to 40 % as the thruster was operated at 300 V from 10 to 30 mg/s, respectively (see Section 5.1). Based on the multiply-charged ion content in the plume, the RPA measures the ion *voltage* distribution function.

Since the RPA filtering potential was referenced to facility ground, it was necessary to correct the voltage distribution for the presence of a local plasma potential using the potential diagram shown in Figure 4-15. The "true ion

voltage," referred to as the most probable voltage, V_{mp} was obtained by subtracting the plasma potential from the measured value, V_{RPA} by

$$V_{mp} = V_{RPA} - V_p \,. \tag{4-12}$$

The local plasma potential was measured by a cylindrical Langmuir probe that was located 2 cm from the RPA center, as described in Section 4.8.2. Once V_{mp} was calculated, the loss voltage

$$V_{loss} = V_D - V_{mp} \,, \tag{4-13}$$

was calculated and used in the efficiency analysis presented in Section 6.1.

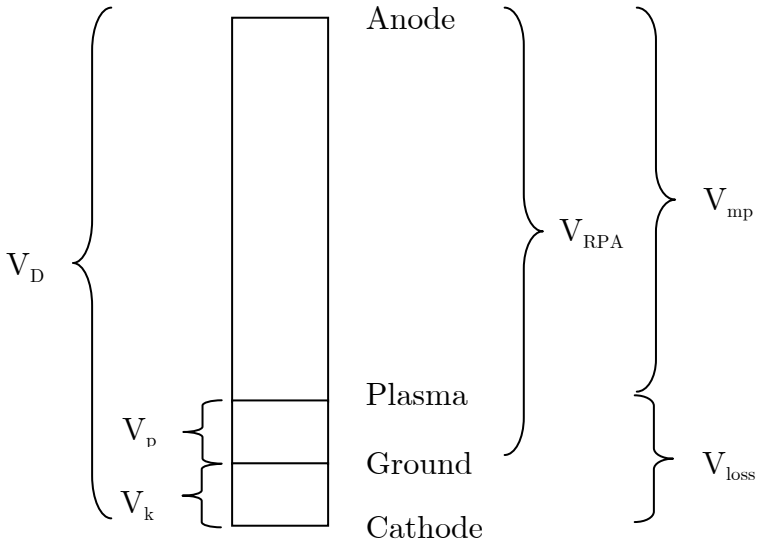

Figure 4-15. Electric potential diagram showing the relationship between experimentally measured quantities (V_{RPA}, V_p, V_k, V_D), the most probable voltage (V_{mp}), and the loss voltage (V_{loss}).

Due to probe noise, the voltage distribution function was not easily integrated. Instead, the distribution was used to identify V_{mp} and the Full-Width at Half-Maximum (FWHM) as shown in Figure 4-16. The most probable voltage was located at the peak of the voltage distribution and it represented an estimate

of the average ion kinetic energy, represented in units of electron volts. The FWHM provided a figure of merit for the spread in ion energies; however, its usefulness was often overshadowed by the effects of facility-induced collisions and CEX that caused broadening of the spectrum.

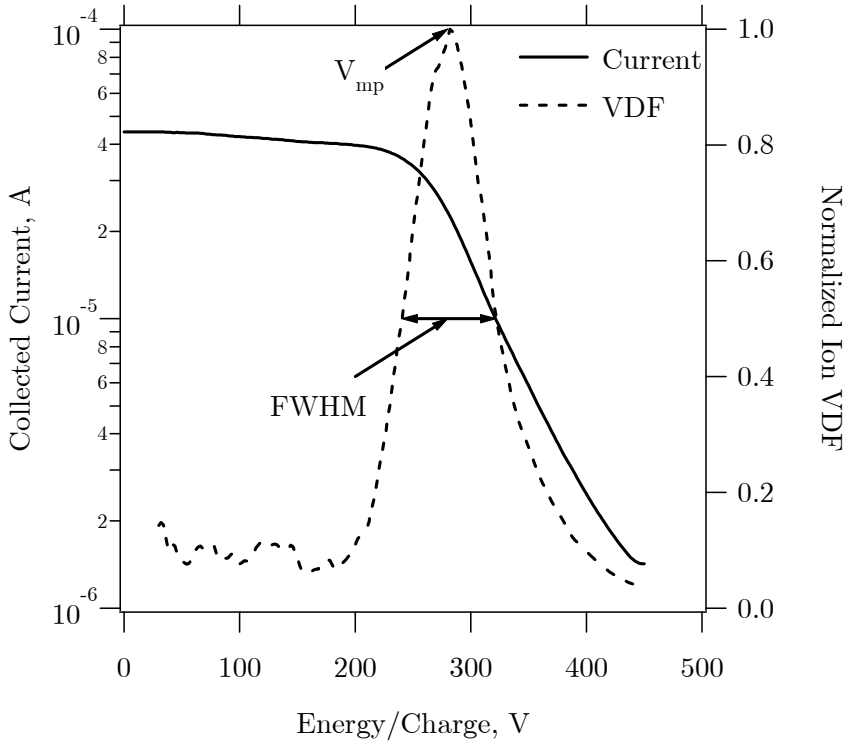

Figure 4-16. Sample ion voltage distribution demonstrating the definitions of V_{mp} and FWHM.

4.8.3.3 Measurement Uncertainty

The voltage resolution of the probe was limited by the 1-V step-size used during data acquisition. However, the measurement uncertainty in V_{mp} and FWHM are estimated in Refs. [26, 96] as ± 10 V and +0/-20 V, respectively. Further uncertainty can be introduced by taking measurements at large angles from centerline, indicated by measurements in Refs. [94, 96].

4.8.4 Nude Faraday Probe

The ion current density (ion charge flux or current per unit area) was measured using a Faraday probe. Several probe designs have been used in previous experiments, including a magnetically-filtered [97], gridded [98, 99], collimated [100, 101], and nude Faraday probes. The nude Faraday probe is the most straightforward to deploy and analyze, making it is the most commonly used design. The major weakness of the nude Faraday probe is the lack of active correction for the effects of facility-induced CEX. This weakness can be mitigated with a systematic characterization of the probe measurement as a function of facility pressure that is summarized in Appendix B using a similar method as reported by Azziz *et al.* [99]. The nude Faraday probe was used exclusively in the far-field plume throughout this dissertation, unless otherwise noted.

4.8.4.1 Probe Design and Experimental Setup

The collector of the JPL nude Faraday probe is a 23.1-mm-diameter tungsten-coated aluminum disk. The tungsten coating reduces the secondary electron emission due to high-energy impacting ions. To reduce edge effects, the collector was surrounded by a guard ring that was biased to the same potential as the collector to repel plasma electrons and to minimize edge effects by creating a flat, uniform sheath over the collection area. The collector and guard ring were biased at -15 V with respect to ground and the current collected at the probe was

measured across a 107.1 Ω current shunt. A schematic of the probe design is shown in Figure 4-17.

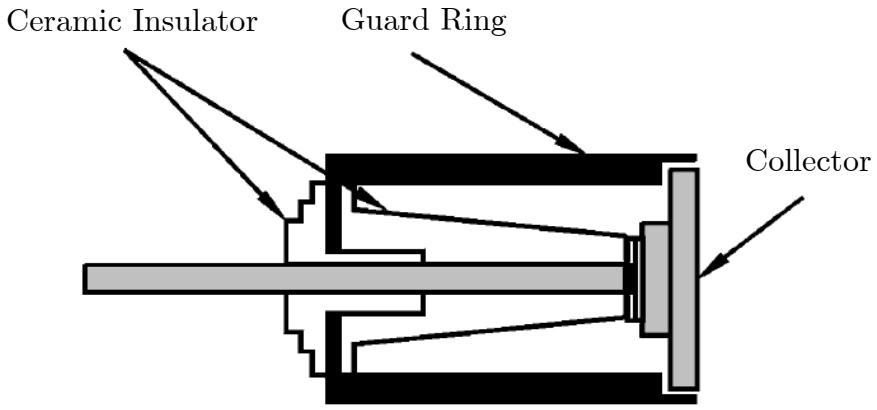

Figure 4-17. Schematic of the JPL nude Faraday Probe.

The gap between the collector and guard ring was less than 0.5 mm, which was much smaller than the typical Debye length in the far-field plume that was approximately 1-3 mm [102]. This feature ensured that the collector and guard ring sheaths overlapped to produce a smooth sheath over the collector surface.

The face of the nude Faraday probe was located at 100 ± 0.5 cm downstream of the thruster exit plane, with the axis of rotation located on thruster centerline at the exit plane. The angular coordinate system was defined such that thruster centerline was 0°. When viewed from above, probe traces were acquired in a clockwise direction from -180° to +180° in 1° increments.

4.8.4.2 Data Analysis

The current density was integrated from ± 90° using a spherical coordinate system to obtain the total ion beam current, I_B

$$I_B = \pi \cdot R^2 \int_{-\pi/2}^{+\pi/2} j(\theta)\sin(\theta)d\theta\,, \tag{4-14}$$

where R is the probe distance from the thruster exit and $j(\theta)$ is the ion current density at each angular location θ.

Ideally, the plume divergence angle is determined by the ratio of axial-to-total ion momentum. However, this information is rarely available since it requires knowledge of the local ion velocity vector throughout the measurement domain (entire plume!). LIF measurements are an excellent way to accurately measure the velocity field in the plume; however, these measurements typically require extensive setup and data collection times that reduce their applicability. The velocity field in the plume can also be determined by recording ion current density measurements throughout the plume with a rotatable Faraday probe that is aligned with the local ion velocity vector. Again, this measurement technique is time consuming and difficult to implement, making it impractical in most cases.

Without knowledge of the ion velocity field, standard Hall thruster analysis calculates the plume divergence half-angle by determining the location from thruster centerline over which the ion current density integrates to 90% or 95% of the total integrated current (integrated from ± 90°). This analysis idealizes the thruster plume as a jet issuing from a single point-source located at the thruster center, which is a valid assumption as long as the probe distance is several thruster diameters downstream of the thruster exit plane (not valid within 1 mean thruster diameter). The integration boundaries are somewhat

arbitrary and do not relate to ion momentum in any way. An incremental improvement on this method is to consider the ratio of the axial current to the total integrated current by multiplying the local ion current density by the cosine of the angle from centerline [103]:

$$\cos\theta = \frac{\text{Axial Current}}{\text{Total Current}} = \frac{\int_0^r 2\pi r\, j(r)\, \cos\theta(r)\, dr}{\int_0^r 2\pi r\, j(r)\, dr}. \tag{4-15}$$

This measurement reduces the gross overprediction of plume divergence half-angle, however results are still much greater than the values suggested by efficiency analyses. Equation 4-15 is used throughout this dissertation to determine the plume divergence half-angle for far-field Faraday probe measurements.

It should be noted that the plume divergence is truly an effective value that characterizes the collective behavior of all ions. In truth, each ion has an individual plume divergence.

Far-field Faraday probe measurements are severely corrupted by thruster- and facility-induced collisions that alter the charge flux distribution [91, 104]. These collisions cause the beam current to be overestimated by as much as 20-30% and the far-field plume divergence to be overestimated by as much as 200%. For these reasons, measurements should be taken as close to the thruster exit plane as possible to reduce effects of plume collisions.

4.8.4.3 Measurement Uncertainty

The primary sources of uncertainty in the measured ion current density were area definition, current measurement, alignment, and pointing. Of these sources, the dominant factor was area definition. Plasma that enters the gap between the collector and guard ring can be collected along the width of the collector disk, adding uncertainty to the collection area. However, the small gap between the collector and guard ring, coupled with the large diameter of the collector with respect to its width ensured that the contribution of plasma entering the gap remained below 1%.

Unfortunately, the typical sources of *measurement* uncertainties were overshadowed by the effects of facility-induced CEX and gas entrainment into the thruster annulus. Facility-induced CEX was caused by the interaction of plume ions with background neutrals that existed due to the finite pumping speed of the facility. The CEX collisions in the plume resulted in a redistribution of the primary beam ions towards the plume periphery leading to a gross overprediction of the beam divergence. Facility-induced gas entrainment was caused by the random thermal motion of background neutrals that intersect the thruster discharge channel and near-field plume. As a result, background neutrals were ionized and accelerated into the plume causing an increase in discharge current and hence, integrated beam current (see Appendix B). Considering the contributions listed above, a conservative estimate of the uncertainty in integrated beam current and divergence angle was +0/-50%.

4.8.5 Near-field Faraday Probe

To reduce the effect of facility-induced CEX, current density measurements were taken close to the exit plane of the thruster to reduce the probability that a main beam ion will encounter a CEX collision prior to reaching the probe. These measurements were taken within approximately one thruster diameter downstream of the thruster, a region often referred to as the near-field plume. A similar experiment was performed by Hofer *et al.* [105] and Jameson *et al.* [106]. The following measurements used these previous measurements as guidance and improved the data collection methodology and analysis technique.

4.8.5.1 Probe Design and Experimental Setup

The collecting surface of the near-field ion current density probe was made of a 4.85-mm-diameter molybdenum disk that was fastened to a tungsten rod through an interference fit (often referred to as "press fit"). This connection method offered a sound mechanical and electrical connection that did not require bonding materials or welding, which would alter the collecting surface. Molybdenum was chosen for the collecting surface due to its high operating temperature and relatively low SEE coefficient at the ion energies expected in the plume (approximately 1.2 at 300 eV). The downstream surface of the probe (facing away from main ion flow) was covered with a thin layer of alumina paste, and the tungsten rod was housed in an alumina tube. The probe did not incorporate a guard ring, primarily due to the very small Debye length that

required an impractical gap width of < 0.1 mm. A schematic of the probe construction is shown in Figure 4-18.

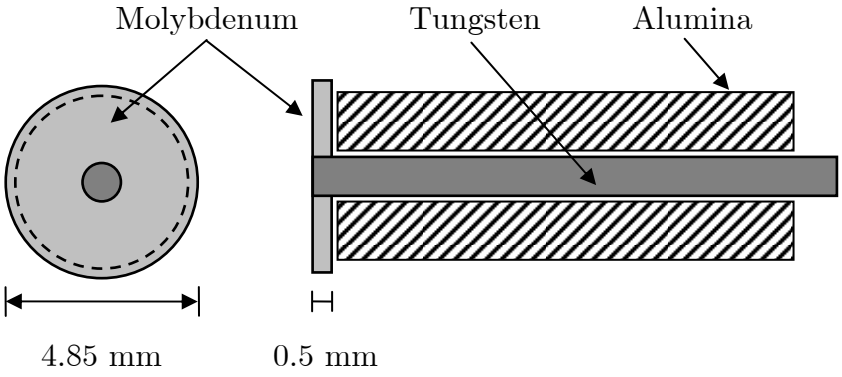

Figure 4-18. Schematic of near-field Faraday probe design and construction (not to scale).

The probe was biased at -60 V with respect to facility ground (typically 70-80 V below plasma potential) and the current was measured across a 56 Ω thin-film resistor (121 Ω at 30 mg/s). Using the Boltzmann relation, this probe bias was selected in order to repel >99% of 10 eV electrons that potentially exist close to the thruster exit. This probe bias was consistent with the results in Ref. [105] that indicated saturation of the collected ion current at approximately -50 V with respect to ground. The data acquisition (DAQ) system recorded the probe position, ion current density, thruster discharge current, and thruster cathode potential at 100 kHz per channel. This resulted in a distinct measurement of each signal every 0.1 mm in the radial direction and adequately resolved the fluctuation in collected current due to discharge current oscillations.

Data were taken along radial paths that extended from 2.35 to -1.25 mean thruster diameters ($D_{T,mean}$) from thruster centerline. Radial sweeps began at an

axial location of 5.25 $D_{T,mean}$ and ended at 0.06 $D_{T,mean}$ from the thruster exit plane. Data were taken in two separate batches; the first in 10 mm increments from 5.25 to 3.25 $D_{T,mean}$ and the second in 5 mm increments from 3.25 to 0.06 $D_{T,mean}$.

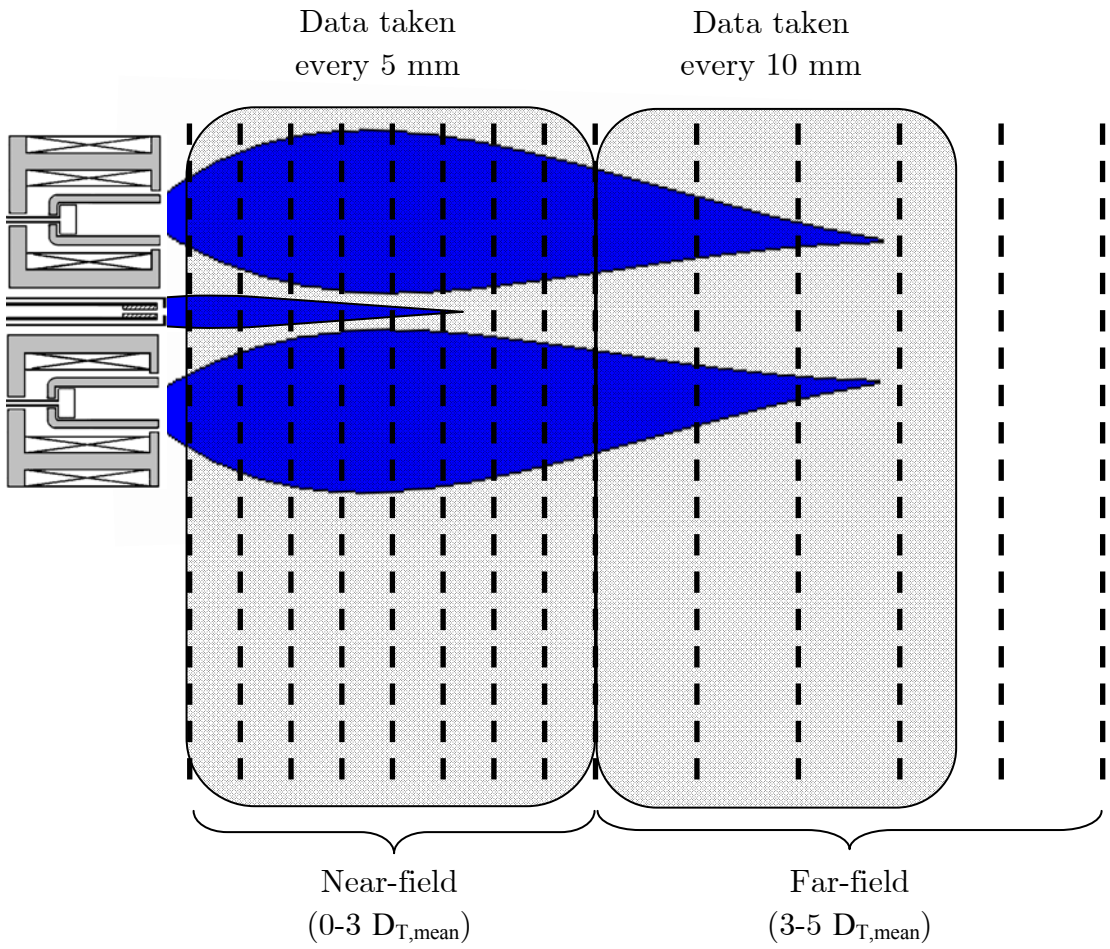

Figure 4-19. Measurement domain for the near- and far-field Faraday probe measurements (not to scale).

4.8.5.2 Data Analysis

The ion beam current was calculated in a manner consistent with the far-field Faraday probe measurements. The current density was integrated at each

axial location with the two-dimensional integral using cylindrical coordinates given by

$$I_B = 2\pi \int_{IR}^{OR} j(r) r dr \,, \tag{4-16}$$

where $j(r)$ is the axial current density at each radial location r and the plume was assumed axisymmetric. The integration limits in the radial direction (IR and OR) are chosen based on one of three analysis methods:

1) **Total beam integration ($\mathbf{I_{tot}}$)**. Integrate the ion flux from thruster centerline to the maximum radial location (0-3.25 $D_{T,mean}$). This method is analogous to the hemispherical integration method in Eq. 4-14 and the method used in Ref. [105].

2) **Discharge channel integration ($\mathbf{I_{tot,DC}}$)**. Integrate only the ion flux that exists directly downstream of the thruster exit plane between the discharge channel inner and outer radii (R_{CL} ± b/2). This method enforces the discharge channel exit plane boundary condition that requires all ions to exit the channel. This method is similar to the one in Ref. [106] and its usefulness diminishes as the axial distance from the exit plane is increased.

3) **Dynamic window integration ($\mathbf{I_{tot,dyn}}$)**. Integrate the flux that exists within a window around the ion flux peak, defined as the location where flux drops to 1/e of its maximum value. This method creates an integration width that is consistent with the exit plane near the

thruster (also consistent with option 2 above), yet adapts with the axial evolution of the current density distribution to capture the ions in the main beam.

As discussed in Section 5.5.4, the three options above produce drastically different results beyond 0.5 $D_{T,mean}$, with option 3 producing the best results. The 1/e cutoff criterion is not a standard definition in Hall thruster literature; however, it is supported by similar conventions in collision theory, theoretical physics, and finance (the generic topic is referred to as e-folding). In collision theory, the mean free path for decay of a beam is defined as the distance over which the uncollided flux decreases by 1/e from its initial value (see Chapter 3 of Ref. [107] and Chapter 5 of Ref. [108]). This application of e-folding is the most applicable to the discussion of thruster plume characteristics, and the cutoff criterion is well suited since the profile of the main ion beam is exponential.

One weakness of the dynamic window technique is encountered at approximately 0.5 $D_{T,mean}$ where the cathode and main ion beams begin to interact. At this point, the current density at the inner radius does not reach 1/e cutoff. In this case, the local minimum between the cathode and main ion beam is used as the inner radius boundary for integration as shown in Figure 4-20. Further downstream the beam crosses thruster centerline and the integration extends from thruster centerline to the 1/e location at the outer radius.

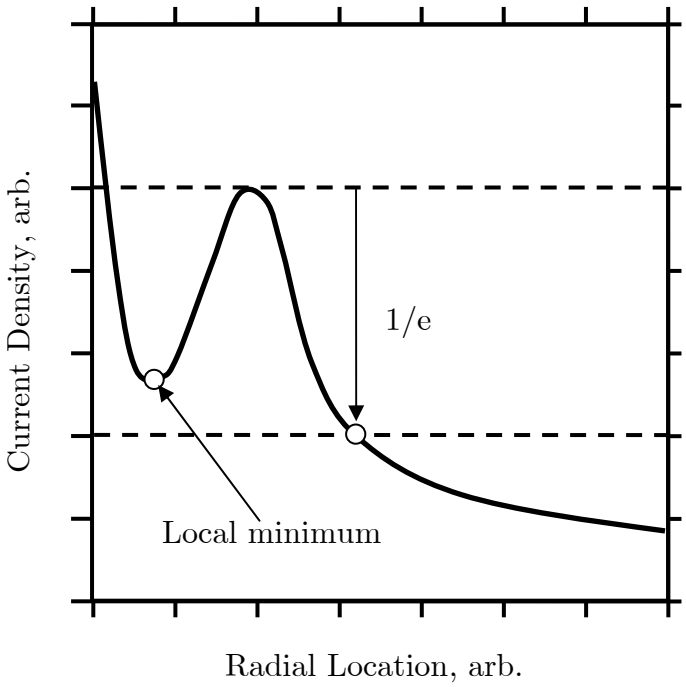

Figure 4-20. Schematic showing the modified 1/e integration bounds for a sweep that does not reach 1/e at the inner radius (~ 0.5 $D_{T,mean}$).

Without knowledge of the ion velocity field in the plume, the plume divergence angle must be defined based on the location of the ion beam. Far-field Faraday probe analysis uses this principle when determining the 90% or 95% plume divergence half angle (see Section 4.8.4.2), which are somewhat arbitrarily defined. For the near-field Faraday probe measurements, the plume divergence half-angle is defined as the angle from channel centerline that encloses the calculated beam current. Based on the beam current definition for the dynamic window technique, this beam divergence definition is equivalent to finding the angle at the 1/e location of the current density profile. In this way, the beam divergence angle provides information *about* the ion beam momentum, but it is not calculated directly *from* on the ion beam momentum.

At each axial location, the plume divergence is calculated using

$$\theta_z = \tan^{-1}\left(\frac{OR_{beam}}{z}\right), \tag{4-17}$$

where θ_z is the divergence angle at a particular axial location, z is the axial distance from the thruster exit, and OR_{beam} is the outer radius that encloses the entire integrated beam current. This beam divergence definition assumes that the ion beam can be approximated as a point source located at the center of the channel exit plane. Since the ion beam was concentrated towards channel centerline and the ion density peaked near the thruster exit [51, 109, 110], this was a reasonably good approximation, especially in the far-field plume (see also Section 5.5); however, this approximation was not valid within the first few mm from the exit plane, resulting in unphysical calculated beam divergences, even for a beam width that was a few percent of the channel width.

This new definition of beam current (using dynamic window technique) and plume divergence represents a drastic change from the standard Hall thruster data analysis methods. As shown in the next two chapters, the results from these calculations produce superior results when compared to standard analysis techniques.

4.8.5.3 Measurement Uncertainty

The primary sources of uncertainty in the measured ion current density were the area definition, measurement of current, and probe alignment. These sources were the same as the nude Faraday probe and the dominant factor

remained the area definition. Similar to the plasma collection within the guard ring gap for the nude Faraday probe, the near-field Faraday probe can collect ions along the width of the disk, artificially augmenting the probe collection area. Based on the dimensions of the probe, the collection area could be augmented by as much as 40%. To reduce the potential uncertainty in the area determination, it is recommended that future studies increase the probe radius-to-thickness ratio to greater than 10 (ratio is currently 5) to reduce the possible area augmentation below 10%. The high density in the very-near-field plume resulted in small sheath sizes ($<$ 0.5 mm) and the large axial kinetic energy of the ions (~300 eV) tended to prevent them from being drawn to the side of the probe.

Although not explicitly accounted for in the analysis, there are potential uncertainties introduced by the effect of SEE, sheath expansion, and cosine losses. Since the probe was constructed of refractory materials, and the bulk ion energy was relatively low ($<$ 300 eV), the correction for SEE was estimated to be less than 1%. Since the probe was operated in the near-field plume where the plasma density was relatively high and the ions had very large axial velocities, the correction for sheath expansion was estimated to be less than 1%. The cosine correction due to the axially aligned probe was not included in the analysis since it had very little effect on the main ion beam near the thruster where the data are most important. The integrated beam current and plume divergence changed

by less than 3% and 5%, respectively, when the cosine correction was incorporated.

To justify the omission of corrections, the measured ion current density near the thruster exit was compared to the calculated current density at the exit plane (discharge current divided by thruster exit area). These values agreed to within 5% for all operating conditions investigated, providing a relatively high level of confidence in the measurements. The combined effect of each contribution to uncertainty resulted in a conservative estimate of ± 10% uncertainty in the integrated beam current and plume divergence half-angle.

4.9 Internal Diagnostics

A large portion of this dissertation focuses on the ionization and acceleration processes that are primarily confined within the discharge channel. To record these "internal" measurements, probes were attached to the HARP (see Section 4.6) and rapidly injected into the thruster. This section covers the details of the measurement domain that was characterized, the probes that were used, and the techniques that were used to analyze the data.

4.9.1 Measurement Domain

The measurement domain was normalized in the axial direction by the channel length, L_c and in the radial direction by the channel width, b. The anode was located at 0% L_c, the channel exit was at 100% L_c, the inner wall was located at 0% b, and the outer wall was located at 100% b. Data were taken at nine

radial locations spaced 8% b apart, as shown in Figure 4-21. Since the Langmuir probe I-V traces were sampled every 2.5% L_c, the results were considered time-averaged; hence, unable to resolve variations in the plasma properties due to high-frequency oscillations (10^4 Hz) that are characteristic of Hall thruster discharges. However, the emissive probe data were sampled at 83 kHz, offering a time-resolved measurement of the plasma potential.

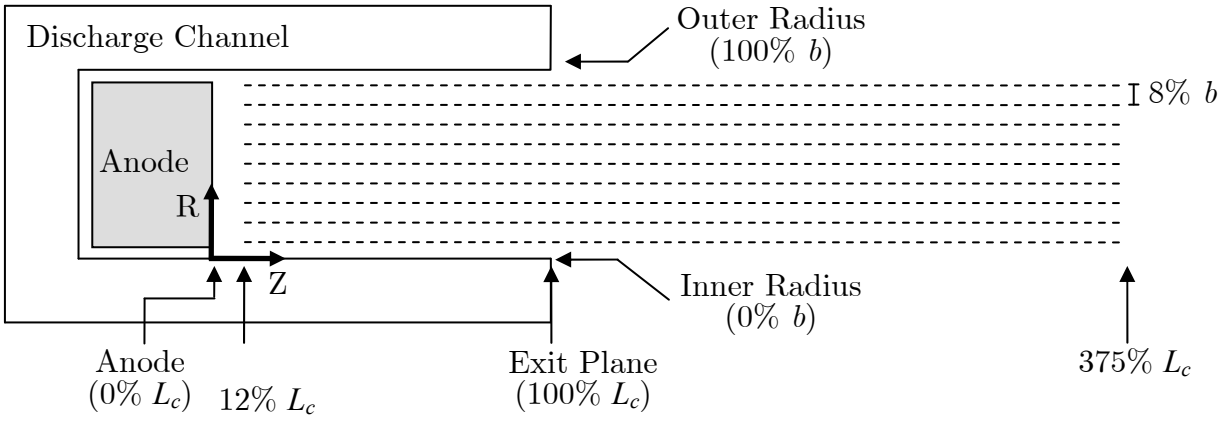

Figure 4-21. Schematic of internal measurement domain (not to scale).

4.9.2 Single Cylindrical Langmuir Probe (Internal)

The cylindrical Langmuir probe has significant heritage in the discharge channel of Hall thrusters and is a widely used electrostatic device that provides a comprehensive set of plasma parameters with a single diagnostic technique. A single electrode is exposed to the plasma and subjected to a range of applied electric potentials. The plasma's response to the probe voltage is measured by the collected current, resulting in an I-V characteristic that can be used to extract the plasma potential, floating potential, electron temperature, and plasma density. Although the probe construction and implementation are both

straightforward, the interpretation of the I-V characteristic is complicated by several effects including collisions, magnetic field, anisotropy of the Electron Energy Distribution Function (EEDF), end effects, sheath expansion, and thermionic emission [51, 109, 111-113].

4.9.2.1 Probe Design and Setup

The single Langmuir probe implemented in these experiments was based on the methodology outlined in Refs. [51, 109, 110]. The Langmuir probe was used to measure the plasma properties in the thruster discharge channel from approximately 1.5 to 9.9 kW. As the discharge power increased, the heat load to the probe increased, ultimately leading to probe failure when the ceramic surface temperature reached a significant fraction of its melting temperature. This critical power limit was reached at 6 kW (300 V, 20 mg/s) for an alumina probe body based on the design introduced in Ref. [109]. To alleviate the probe failure mechanism associated with elevated thruster discharge power, the portion of the probe that entered the discharge channel was covered with a boron nitride shroud, described in detail in Ref. [114].

The Langmuir probe was constructed using three major components for the body; a 1.5-mm-diameter, double-bore, alumina tube, telescoped inside a 6.4-mm-diameter alumina tube, capped by a graduated boron nitride shroud as shown in Figure 4-22. The boron nitride shroud was machined from a single rod into three sections with diameters of 3, 5, and 6.4 mm each of which was 35, 8,

and 8 mm long, respectively. The probe tip was created by a 0.25-mm-diameter tungsten wire that extended beyond the alumina tube by 2 mm.

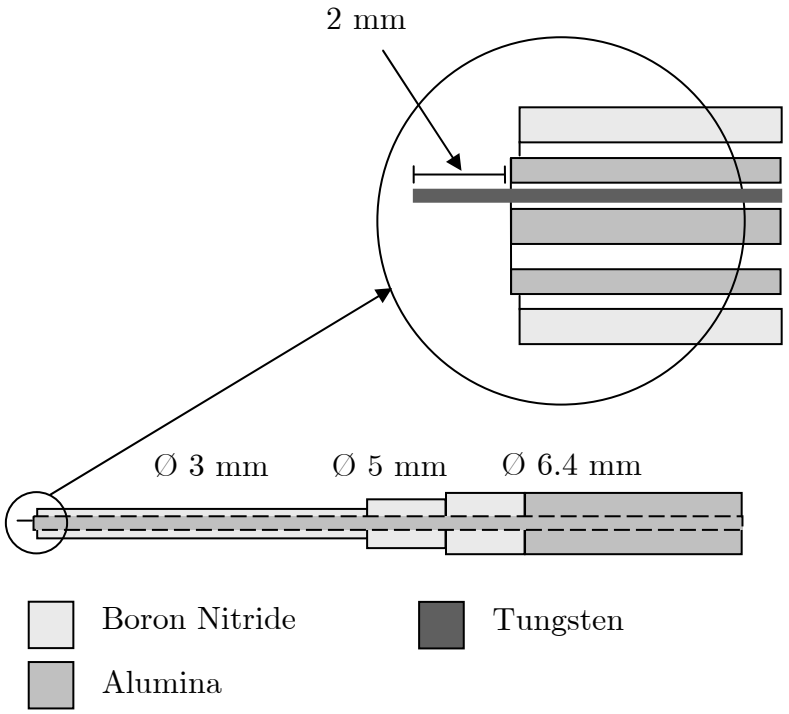

Figure 4-22. Schematic of Langmuir probe construction (not to scale).

4.9.2.2 Probe Operation

Following the work of Linnell [51], continuous I-V traces were achieved for the single Langmuir probe by varying the probe bias using a 380 Hz triangle wave. As the probe was injected into the thruster, the floating potential (and plasma potential) increased by several hundred volts. In order to capture measurements in the ion saturation and electron retarding regimes of the I-V trace, the probe voltage sweep must oscillate around the floating potential. To satisfy this requirement, the floating potential was measured on channel centerline with an unbiased probe and the profile was sent to a programmable

waveform generator. The floating potential profile was then summed with a triangle wave and sent to the input of a bipolar power supply, which amplified the signal to produce the probe bias shown in Figure 4-23. This method reduced the need for multiple pulses as implemented by Linnell [51]; however, in limited cases large differences between the floating and plasma potentials near the peak electron temperature location still required two pulses to capture the ion saturation and a significant portion of the electron retarding regime of the I-V curve. This incremental improvement in the probe bias method reduced data collection time, increased probe lifetime, and increased the ease of data reduction and post-processing.

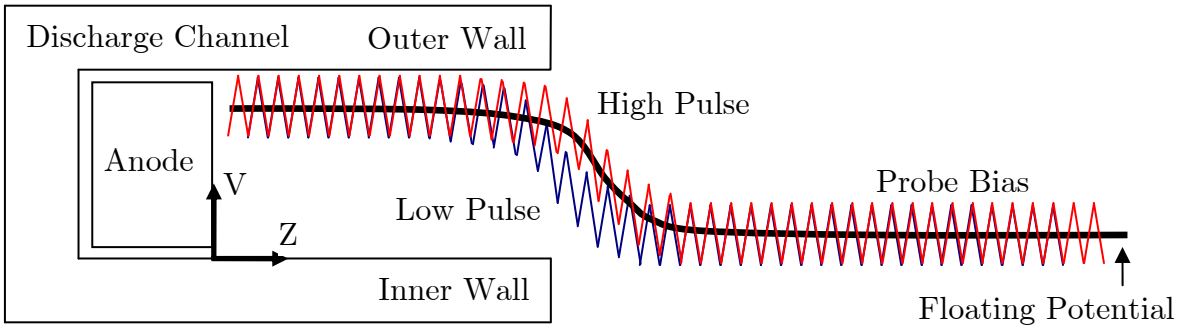

Figure 4-23. Schematic of Langmuir probe voltage characteristic during injection into the discharge channel.

To minimize thruster perturbations, the probe size should be minimized and the HARP should be operated near its upper velocity limit to decrease the probe residence time. However, increasing the HARP velocity directly increases the necessary probe bias oscillation frequency, which increases the effect of line capacitance. The line capacitance during this experiment was estimated at 500 pF by monitoring the capacitive current drawn during probe bias oscillation with

no plasma as shown in Figure 4-24. These results closely matched the theoretical trend where the capacitive current, I_{cap} follows

$$I_{cap} = C\frac{dV}{dt}, \tag{4-18}$$

where C is the line capacitance and dV/dt is the time derivative of the probe voltage. More than 90% of the total line capacitance was due to the cable length from the HARP carriage to the probe tip where the signal wire had a small physical separation from electrical ground. This near-probe capacitance was unavoidable and prevented all attempts to further reduce line capacitance. The competing factors of thruster perturbation and line capacitance are what led to the selection of HARP velocity of 0.75 m/s and triangle wave oscillation frequency of 380 Hz.

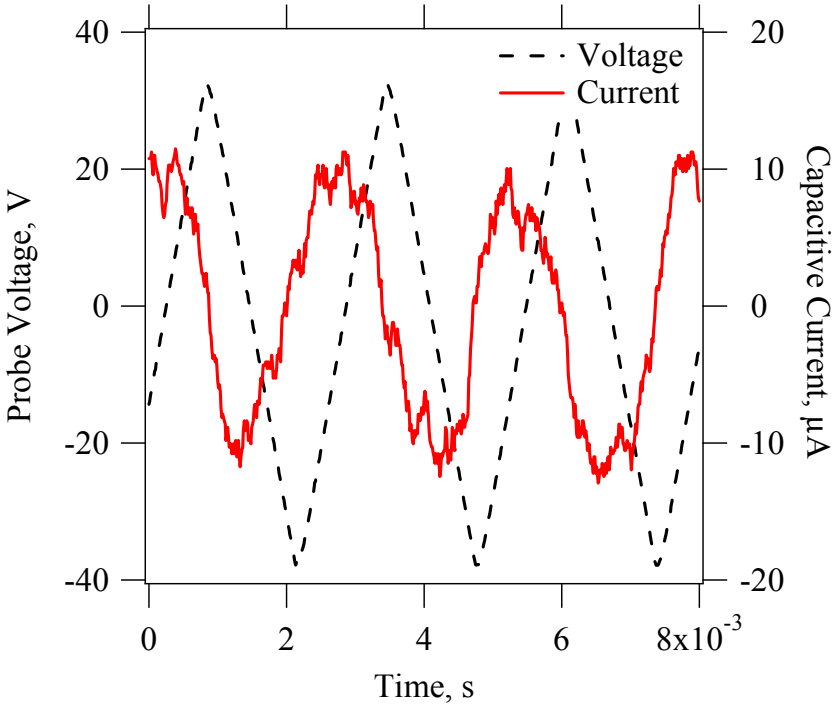

Figure 4-24. Capacitive current caused by line capacitance due to the probe voltage oscillation.

During data collection, the probe current was on the order of 10 mA, which was always much greater than the typical capacitive current of 10 μA. This ensured that the effect of capacitance had little effect on the probe I-V characteristics.

To prevent excessive heating of the tungsten electrode that can lead to thermionic emission of electrons, the probe bias was kept within 100 V of the floating potential. In addition, the probe was allowed to cool for 15 seconds between each probe injection. If the probe was heated to the point of thermionic emission, the measured current would be offset towards ion saturation. This artificial offset results in an overprediction of the ion density during analysis.

4.9.2.3 Data Analysis

The electron mean free path to probe radius was much greater than one placing the probe operation in the collisionless regime. The magnetic field effects were determined to be small for these measurements since the probe was perpendicular to the primarily radial magnetic field lines and the electron gyroradius was nearly an order of magnitude greater than the probe radius. Near the channel walls the magnetic field lines can have an appreciable axial component, which may reduce the validity of this assumption; however, the effect of magnetic field was still expected to be small based on the work of Shastry [115] that confirmed that the angle of the magnetic field had little influence on

the interpretation of Langmuir probe I-V characteristics under similar plasma conditions.

The uncertainty in the electron temperature measurement due to the EEDF anisotropy was expected to be small since the magnetic field to neutral pressure ratio (B/P_o) ranged from 1 to 4×10^4 G/torr, well below the 2.5×10^6 G/torr limit recommended in the work of Aikawa [116]. However, the electron temperature is thought to have a perpendicular and parallel component in the Hall thruster discharge channel. Simulations with HPHALL-2 found that the component of the electron temperature perpendicular to the magnetic field lines ($T_{e\perp}$) was larger than the parallel component ($T_{e\parallel}$). A ratio of $T_{e\parallel}/T_{e\perp} = 0.86$ was necessary to match the electron temperature and global parameters like discharge current and thrust from experimental measurements [61]. If this level of anisotropy existed during the experimental measurements that are presented in Chapter 7, then the probe primarily measured the parallel component since the axis of the probe was generally perpendicular to the magnetic field lines (field lines have some axial component near the wall). This probe orientation would tend to preferentially accept radially directed electrons that streamed along (parallel) the magnetic field lines.

End effects due to ion flux to the tip of the probe were accounted for by subtracting the product of the ion density and ion velocity (calculated from the plasma potential measurements) from the ion saturation current. The ion density

was updated and the process was repeated until reaching convergence of the ion density. At the same time, and using the same methodology, a correction for the sheath expansion was used for the thin sheath analysis. The sheath size was used to update the effective probe area and the new ion density was calculated until convergence was achieved. The combined corrections due to end effects and sheath size ranged from 30 to 70% depending on axial location, and the tip correction was typically an order of magnitude less than the sheath size correction.

Although the uncertainty in ion density is typically ± 50%, considering the ion flux produced by the product of ion density and ion velocity (taken from plasma potential) a 1-D current continuity analysis indicated that the ion density may have been overpredicted by as much as 2-300% (see Section 8.2.1). The source of uncertainty that could account for this level of overprediction is unknown at this time, and is a topic that must be considered in future experiments.

Each Langmuir probe I-V characteristic was analyzed by an automated script that divided each axial probe injection into individual I-V traces based on the probe voltage. The script then located the floating potential by finding the location where the probe current crossed zero. The electron temperature was calculated based on the inverse slope of the electron-retarding region. The boundary of the electron-retarding region was determined by taking several

points on either side of the location of maximum slope of the I-V curve. Finally, the ion saturation current was calculated based on the mean of all points from 5 to 50 V below the floating potential. The ion number density was calculated from the ion saturation current using thin sheath [107] analysis given by

$$n_{i,thin} = \frac{I_{i,sat}}{0.61 A_s e}\sqrt{\frac{m_i}{k_B T_e}}, \tag{4-19}$$

where A_s is the sheath area, and OML analysis (thick sheath) [107, 117] given by

$$n_{i,OML} = \frac{1}{A_p}\sqrt{\frac{2\pi m_i}{1.27 e^3}\left(-\frac{d(I_i)^2}{dV}\right)}, \tag{4-20}$$

where A_p is the physical probe area. The ion density was also calculated using a combination of Eqs. 4-19 and 4-20 where thin sheath analysis was adopted for probe radius to Debye length ratios (R_p/λ_D) $\geq$ 10 and OML analysis was adopted for $R_p/\lambda_D \leq 3$. Between these two regimes, an R_p/λ_D weighted average was employed. Analysis can also be performed for an arbitrary value of R_p/λ_D by parametrizing the results of Laframboise [117] as described by Refs. [118-121]; however, implementation of this method in these experiments did not provide consistent results. Since the blended ion density was the most rigorous analysis technique available, it was used throughout this dissertation except where explicitly noted.

4.9.2.4 Probe Measurement Circuit

The data acquisition (DAQ) system recorded the probe position, probe voltage, probe current, thruster discharge current, and cathode potential at 83

kHz per channel. The measurement frequency combined with the voltage oscillation frequency resulted in approximately 100 points per I-V trace. The limited measurement frequency of the DAQ contributed to the decision to decrease the HARP velocity and voltage oscillation frequency.

The Langmuir probe measurement I-V traces were measured with separate voltage and current measurement circuits. The voltage-measurement circuit was composed of two high-impedance thin-film resistors and the voltage drop across the minor resistor to ground was measured with a voltage following operational amplifier with isolated inputs. The current-measurement circuit was composed of a single 100 Ω thin-film resistor placed in series with the probe so that the voltage drop could be measured with an operational amplifier. The operational amplifiers were rated for a minimum bandwidth of 20 kHz (well above the 380 Hz sweep frequency) making them capable of measuring fluctuations resulting from the breathing mode discharge oscillation. The current-measuring circuit had a pair of blocking diodes in parallel with the resistor to protect the amplifier in the event of a spontaneous inrush of current from the plasma. A schematic of the probe bias and measurement circuits are shown in Figure 4-25.

The voltage and current measurement circuits were enclosed in a grounded case and located inside the chamber to reduce line losses, as shown in Figure 4-25. The output signal was connected to the DAQ by 50 Ω BNC cables and feed throughs. The dynamic response of the circuit was characterized from DC to

approximately 2 kHz, displaying a similar response to that in Figure 4-24. The measurement circuit and bipolar power supply displayed excellent linearity and negligible attenuation up to 2 kHz, well above the required operation frequency of 380 Hz. The excellent behavior of the circuit and power supply across a wide range of oscillation frequencies confirmed that the effect of line capacitance was essentially negligible for measurements taken at 380 Hz.

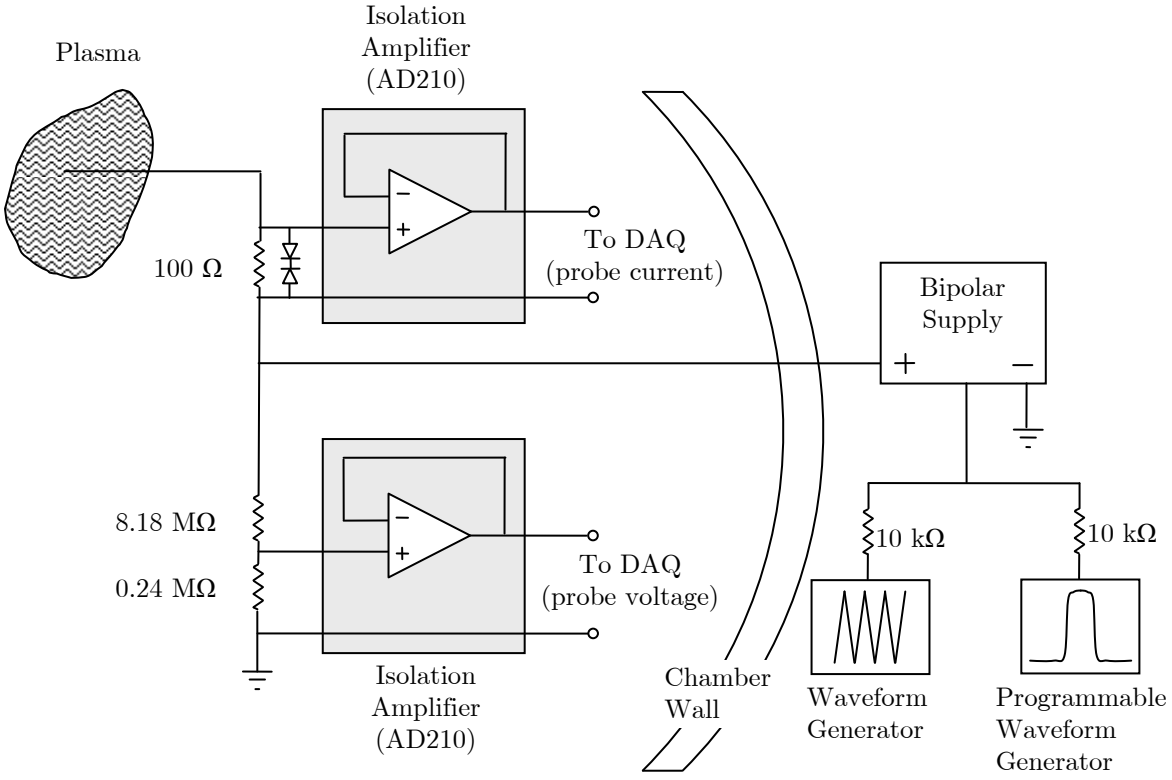

Figure 4-25. Schematic of Langmuir probe measurement and bias circuits.

4.9.3 Floating Emissive Probe

The floating emissive probe has significant heritage for measuring the plasma potential in the discharge channel of Hall thrusters [51, 75, 109, 114, 122,

123]. The probe design, operation, and analysis methods were based on the work of Haas [109].

The floating emissive probe relies on a hot filament that produces thermionic emission of electrons. At low emission currents, the probe potential is negative with respect to the local plasma potential and electrons escape to the plasma and appear as an effective ion current. At high emission currents, the probe potential is more positive than the local plasma potential and electrons emitted from the probe surface are reflected back to the probe. When the critical emission level is reached, the probe potential approaches the local plasma potential and the probe is considered to be "floating" at the local plasma potential.

4.9.3.1 Probe Design and Setup

Similar to the Langmuir probe, the emissive probe was constructed using three major components for the body; a 1.5-mm-diameter double-bore alumina tube telescoped inside a 6.4-mm-diameter alumina tube and capped by a graduated boron nitride shroud as shown in Figure 4-26. The boron nitride shroud was split into three sections with diameters of 3, 5, and 6.4 mm, each of which was 35, 8, and 8 mm long, respectively. The filament loop was based on the design of Haas [124], and was composed of 0.127-mm-diameter 1% thoriated tungsten wire bent with a radius of curvature of 0.5 mm. The total exposed

length of the filament wire was approximately 3.5 mm, resulting in an emission surface area of approximately 1.5×10^{-7} m^2.

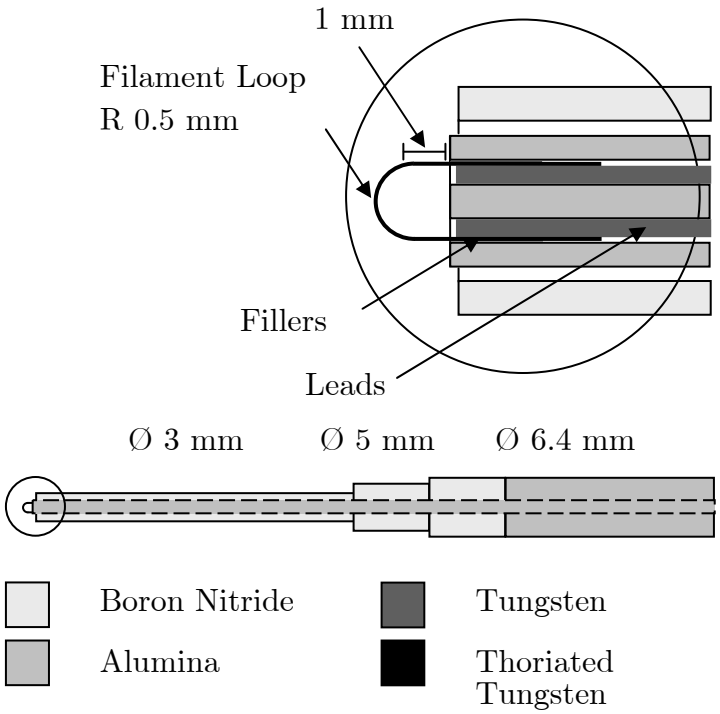

Figure 4-26. Schematic of probe design and construction (not to scale).

4.9.3.2 Data Analysis

The ideal behavior of an emissive probe is complicated by the presence of space-charge limited emission, which leads to a double sheath near the probe surface. The double sheath creates a potential well that reflects some of the emitted electrons to the probe. Since these electrons are not reflected by the *plasma*, the probe will tend to float below the plasma potential. This effect is only alleviated when the emitted electron temperature is equal to the plasma electron temperature, leading to a symmetric double sheath [111]. This condition is rarely achieved in the Hall thruster plume and discharge channel since the

emitted electrons are typically < 1 eV, whereas the plasma electrons range from 5 to 30 eV at nominal conditions.

To account for the uncertainty introduced by the double sheath, space-charge limited emission, and electron temperature mismatch, the plasma potential measured by the emissive probe must be corrected by 0.6 T_e [125, 126] using

$$V_p = V_{p,raw} + 0.6T_e, \tag{4-21}$$

where $V_{p,raw}$ is the raw (uncorrected) plasma potential. The uncertainty associated with the plasma potential correction was estimated as 0.9 T_e [126, 127], which is added to the uncertainty introduced by the voltage drop across the filament (typically 2-5 V). To reduce magnetic field effects, the probe was oriented so that the plane of the filament loop was normal to the thruster radial direction. Since the effect was expected to be relatively small, the effect of magnetic field was not explicitly accounted for in the probe analysis.

The electron temperature can also be calculated from the difference between the plasma and floating potentials, given by

$$V_p - V_f = -\frac{k_B T_e}{e} \ln\left(0.605\sqrt{\frac{2\pi m_e}{m_i}}\right), \tag{4-22}$$

where V_p is the plasma potential and V_f is the floating potential. This equation was derived based on the assumption that the plasma was quiescent and characterized by Maxwellian electrons with a temperature much greater than the ion temperature and negligible effects due to orbital motion [113]. The

uncertainty in this temperature calculation was estimated as ± 17% [122]. An excellent treatment of the uncertainties associated with emissive probes used in the channel of Hall thrusters is given in Refs. [51, 128].

4.9.3.3 Probe Measurement Circuit

The DAQ system recorded the probe position, filament high-potential, filament low-potential, thruster discharge current, and thruster cathode potential at 83 kHz per channel. This resulted in a distinct plasma potential measurement every 0.04% L_c. The sampling frequency was sufficiently high to capture the breathing mode oscillations that can range from 10 to 40 kHz.

The floating emissive probe circuit consisted of the emissive probe, a floating DC power supply capable of supplying enough current to heat the filament (3-5 A), and two voltage divider circuits. Each voltage divider circuit was composed of two high-impedance thin-film resistors and the voltage drop across the minor resistor was measured with a voltage following operational amplifier that had a minimum bandwidth of 20 kHz. The voltage measurement circuits were enclosed in a grounded case and located inside the vacuum chamber. The output signal was connected to the DAQ by 50 Ω BNC cables and feed throughs, and the entire system was calibrated at DC, displaying excellent linearity. A schematic of the probe circuit is shown in Figure 4-27.

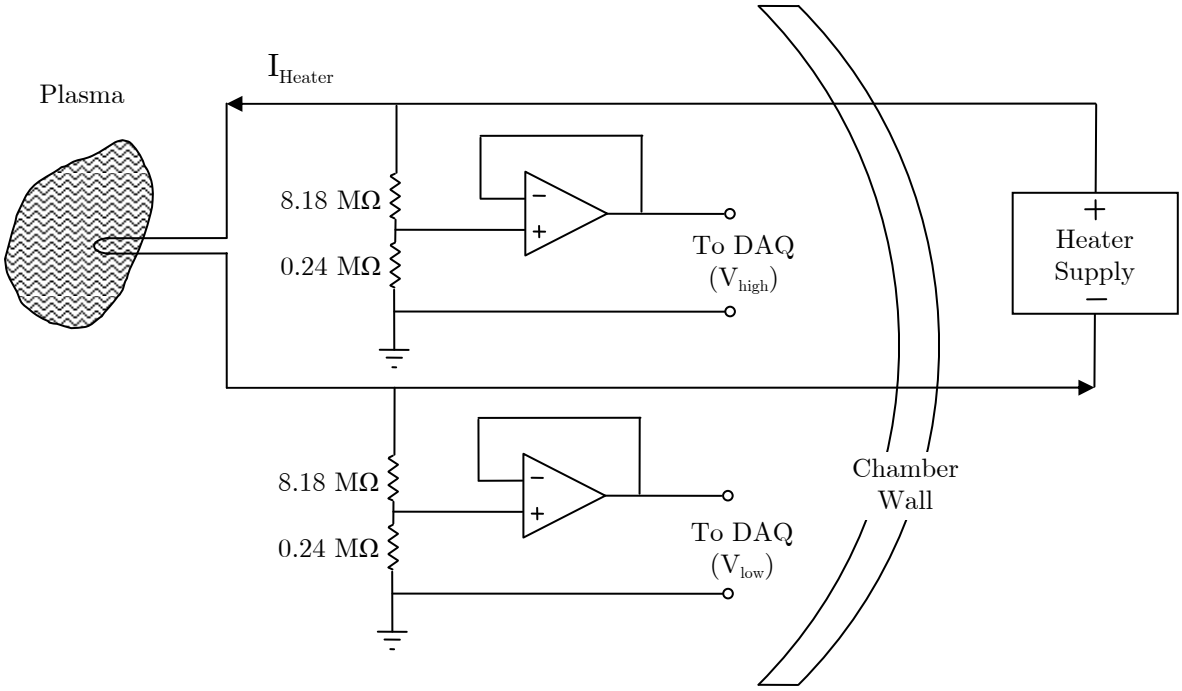

Figure 4-27. Schematic of emissive probe voltage measurement circuit and heater supply.

Previous measurements [51, 109] reported the potential on the high side of the probe, reduced by one-half of the voltage drop across the filament. This was a good approximation since the voltage drop across the filament in those experiments did not vary by more than 5 V. However, a more rigorous measurement was achieved by recording the voltage on both sides of the filament. In addition to providing a more accurate measurement of the local plasma potential, measuring both sides of the filament also provides a diagnostic tool to monitor the emissive probe emission saturation. For a properly saturated emissive probe, the voltage drop will remain approximately constant as the probe is inserted and removed from the thruster. The nearly constant voltage drop results in a percent voltage drop, $(V_{high}\text{-}V_{low})/V_p$ that monotonically decreases

until reaching the anode due to the monotonic increase in plasma potential. Hence, if the percent voltage drop had a significant increase near the location of the Hall current, then the probe was not properly saturated since it required additional heating from the impact of high-energy electrons to float at the local plasma potential. A comparison of the percent voltage drop for a fully saturated and partially saturated emissive probe is shown in Figure 4-28 along channel centerline at 300 V and 10 mg/s.

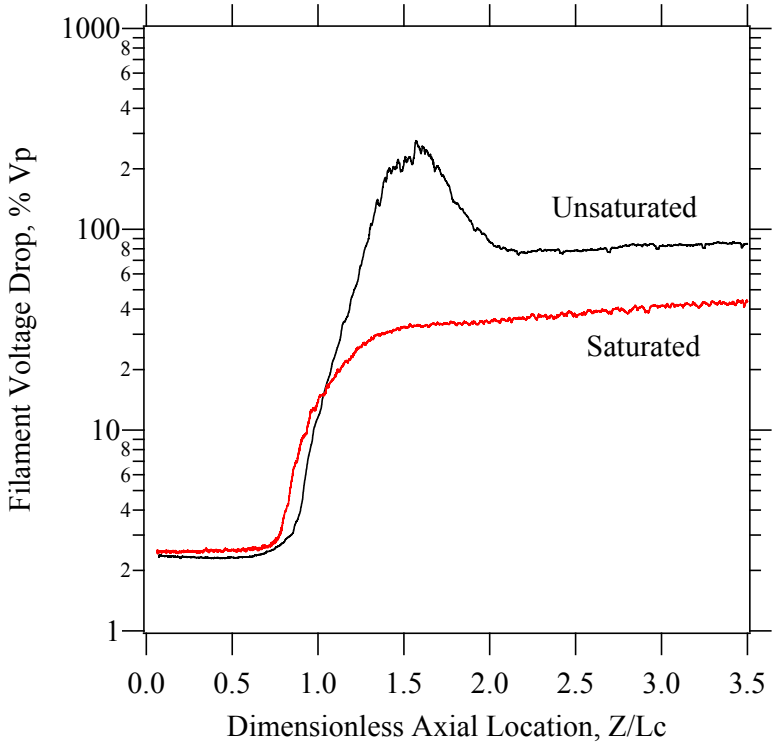

Figure 4-28. Emissive probe filament voltage drop along channel centerline for thruster operation at 300 V and 10 mg/s.

4.10 Summary

This chapter described the vacuum facilities, support equipment, and plasma diagnostics used during experiments that characterized the plasma

properties and performance of the 6-kW Hall thruster. Results from the plume and performance measurements are reported in Chapter 5 and combined into an efficiency analysis in Chapter 6. The internal measurements are reported in Chapter 7 and further analysis and discussion is included in Chapter 8.

Chapter 5

Plume Measurements

A comprehensive characterization of the plume was achieved by taking electrostatic probe measurements with an E×B, RPA, and near- and far-field Faraday probes. Detailed descriptions of the probes were discussed in Chapter 4, and results for each measurement are treated individually in the following sections. Plume measurements are presented for thruster operation at 300 V and 10, 20, and 30 mg/s. Measurements were taken at a constant cathode flow fraction of 7% and the magnetic field strength was optimized for maximum efficiency at each operating condition, while the shape was constrained to a predetermined vacuum magnetic field that was symmetric about channel centerline. A summary of the plasma parameters derived from these measurements is included in Table 5-2, and additional measurements taken at 150 V and 10, 20, and 30 mg/s are located in Appendix C.

5.1 Angularly-Resolved E×B Measurements

To account for the angular distribution of ions within the plume and the loss of main beam ions due to interaction with facility neutrals prior to reaching the probe, E×B measurements were taken at several angular locations and corrected for the effects of CEX. Uncorrected (open marker) and CEX corrected (solid marker) current fraction data are shown in Figure 5-1 and Figure 5-2 from 0 to 30° for thruster operation at 300 V and 10, 20, and 30 mg/s. These measurements were taken at 9 $D_{T,mean}$ downstream of the exit plane. The current fraction of Xe^{3+} remained approximately constant at all angles, with values of 3, 7, and 8% at 10, 20, and 30 mg/s, respectively. These data indicated that the plume was characterized by a monotonically increasing fraction of Xe^{2+} with increased angle from thruster centerline that was consistent with the monotonic decrease in Xe^{1+} fraction. This plume structure and the drastic decrease of the Xe^{1+} fraction at 25° was consistent with results reported in Refs. [85, 89]. The existence of a higher fraction of Xe^{2+} at large angles from centerline was consistent with the hypothesis that Xe^{2+} were created further downstream than Xe^{1+}. Ions created further downstream were expected to be accelerated in a electric potential field that was defocused, leading to larger divergence. The higher divergence angle of Xe^{2+} was reproduced in HPHALL-2 plasma simulations of the SPT-100 and BPT-4000 Hall thrusters [62].

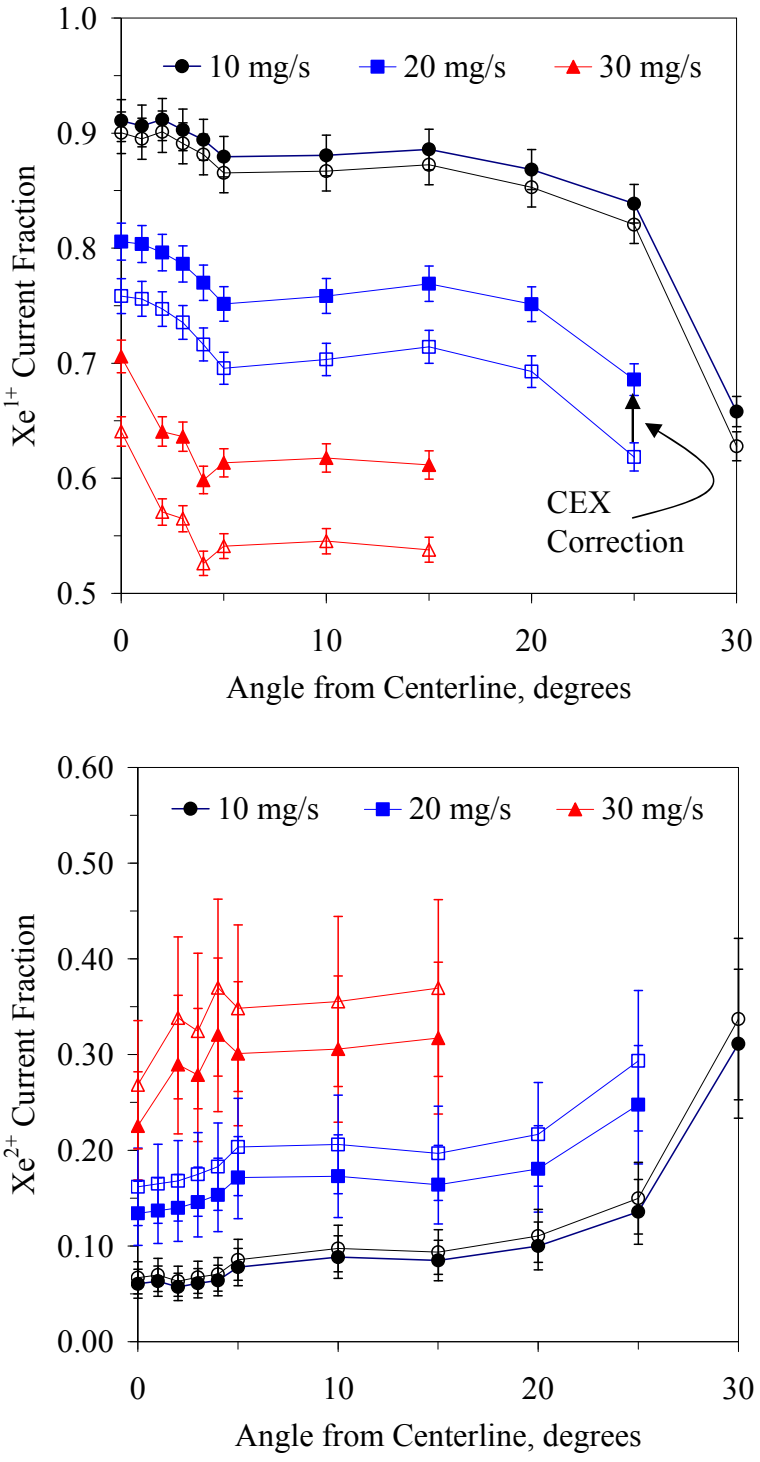

Figure 5-1. **Xe^{1+} and Xe^{2+} ion current fractions for 300 V, 10, 20, and 30 mg/s ($z = 9\ D_{T,mean}$). Open markers are uncorrected data, solid markers have been corrected for CEX.**

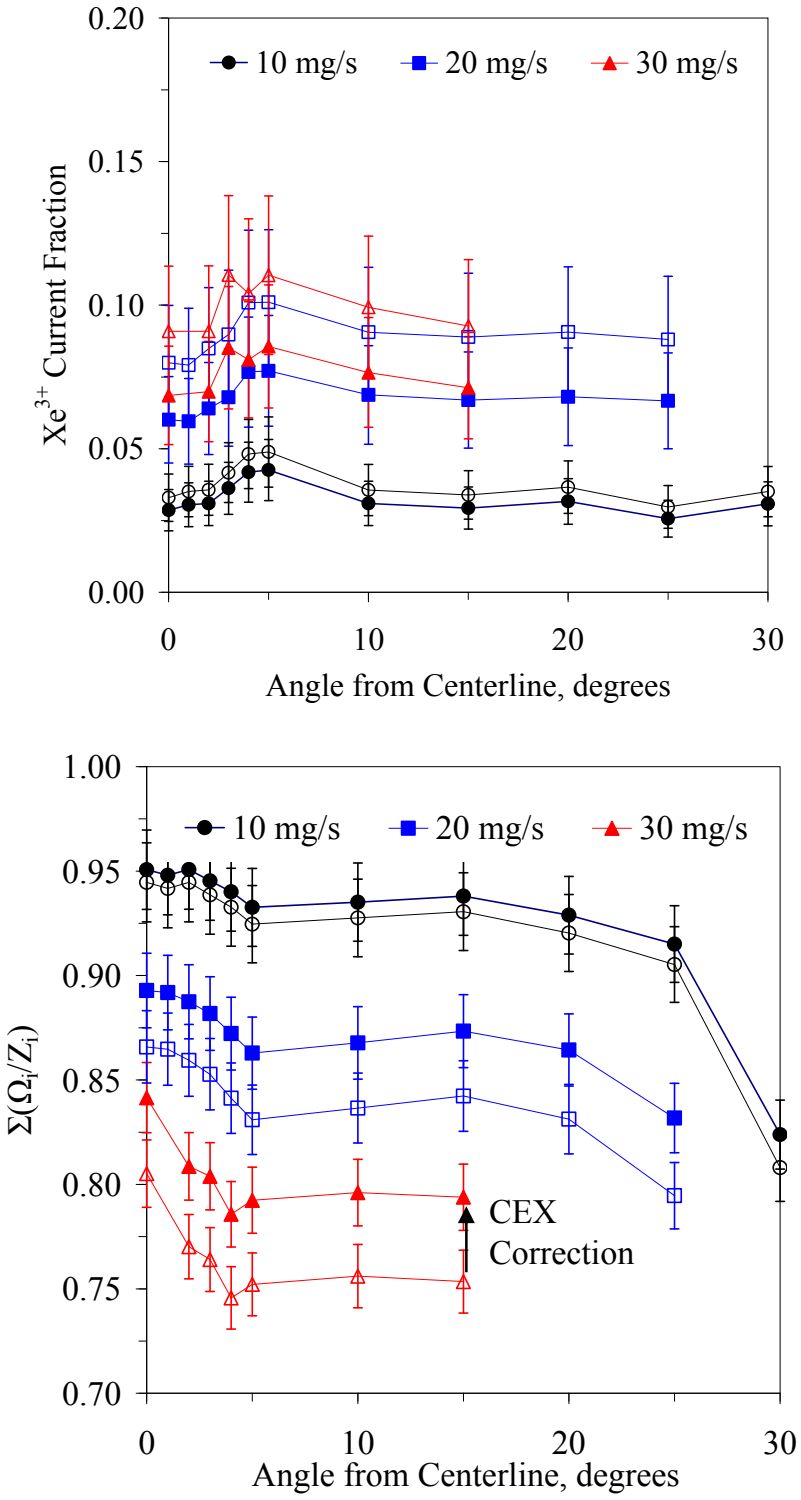

Figure 5-2. **Xe^{3+} ion current fraction and $\Sigma(\Omega_i/Z_i)$ for 300 V, 10, 20, and 30 mg/s ($z = 9\ D_{T,mean}$). Open markers are uncorrected data, solid markers have been corrected for CEX.**

After the current fractions were corrected for the effects of CEX collisions, the local mass utilization correction factor, $\Sigma(\Omega_i/Z_i)$ was calculated at each location so that the effects of multiply-charged ions could be examined in a single parameter (see Section 6.1 for formulation). The uncorrected (open marker) and CEX corrected (solid marker) values of $\Sigma(\Omega_i/Z_i)$ from 0 to 30° are shown in Figure 5-2. $\Sigma(\Omega_i/Z_i)$ decreased from 0 to 5° (thruster center to discharge channel center), remained approximately constant from 5 to 15°, then decreased from 15 to 30°. These trends were consistent with the data reported in Refs. [85, 89]. The relative change between the uncorrected and CEX corrected $\Sigma(\Omega_i/Z_i)$ was 1, 4, and 5% at 10, 20, and 30 mg/s, respectively. The increased CEX correction at higher flow rates was directly related to the increased facility pressure and hence, probability of CEX collisions.

5.1.1 Variation with Flow Rate

The variation of $\Sigma(\Omega_i/Z_i)$ with anode flow rate is shown in Figure 5-3., displaying a linear relationship. Although not shown here, $\Sigma(\Omega_i/Z_i)$ showed the same linear relationship at 150 V and decreased monotonically with increased discharge voltage [87]. The increasing fraction of multiply-charged ions (decreased $\Sigma(\Omega_i/Z_i)$) with discharge voltage was related to the increase in the electron temperature due to Joule heating. Numerous Hall thruster experiments have shown that the maximum electron temperature is approximately 7-14% of the discharge voltage [20, 114, 127, 129, 130]. Increases similar to those reported here

of the multiply-charged ion population with discharge voltage were reported by Hofer *et al.* [86, 88] for discharge voltages ranging from 300 to 900 V. The uncorrected data at 300 V are also shown in Figure 5-3 to confirming that the CEX correction method was a primary cause for the highly linear results.

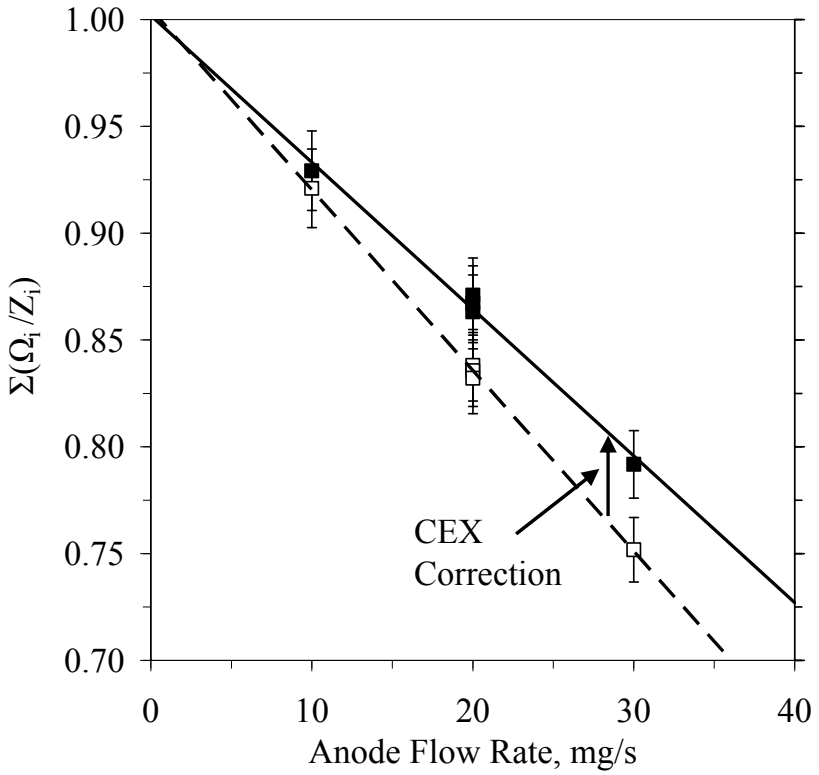

Figure 5-3. Plume-averaged $\Sigma(\Omega_i/Z_i)$ for thruster operation at 300 V and 10, 20, and 30 mg/s.

The increased fraction of multiply-charged ions (decreased $\Sigma(\Omega_i/Z_i)$) with anode mass flow rate was explained by considering the ion production rates that were produced by HPHALL-2. Considering only singly- and doubly-charged ions (since these species dominate the total ion generation rate), the Xe^{2+} -to- Xe^{1+} ion production rate ratio is given by

$$\frac{\dot{n}_i^{2+}}{\dot{n}_i^{+}} = \frac{\dot{n}_i^{0\to 2+} + \dot{n}_i^{1\to 2+}}{\dot{n}_i^{0\to 1+}} = \frac{\alpha(T_e)^{0\to 2+} n_n n_e}{\alpha(T_e)^{0\to 1+} n_n n_e} + \frac{\alpha(T_e)^{1+\to 2+} n_i^{+} n_e}{\alpha(T_e)^{0\to 1+} n_n n_e}, \qquad (5\text{-}1)$$

where n_n is the neutral density, n_e is the plasma density, and the terms $\alpha(T_e)^{0\to 1+}$, $\alpha(T_e)^{0\to 2+}$, and $\alpha(T_e)^{1+\to 2+}$ are the electron temperature dependent ionization rate parameters for the creation of singly- and doubly-charged ions from neutrals and singly-charged ions, respectively [131]. To analyze the dependency of Eq. 5-1, results from HPHALL-2 plasma simulations were used and tabulated in Table 5-1. These simulations captured the experimentally measured increase in the fraction of Xe^{2+} ions with anode flow rate. The variation in Eq. 5-1 with anode flow rate was due to the increase of the second term on the right-hand-side (RHS) of Eq. 5-1. This term is the ratio of the ionization of Xe^{1+} to the ionization of neutral Xe. Further analysis of the second term shows that changes in this ratio were driven by the increased fraction of Xe^{1+} ions relative to neutrals (shown as the last row in Table 5-1). These results indicated that as the anode flow rate increased, the increase in the density of singly-charged ions increased the ionization of Xe^{1+} such that the fraction of Xe^{2+} comprising the total ion current increased with anode flow rate.

Table 5-1: Maximum values of each of the terms in Eq. 5-1, derived from HPHALL-2 simulations.

	10 mg/s	20 mg/s	30 mg/s
$Xe^0 \rightarrow Xe^{1+}$ ionization rate ($1/m^3/s$)	2.9×10^{23}	8.6×10^{23}	2.8×10^{24}
$Xe^{1+} \rightarrow Xe^{2+}$ ionization rate ($1/m^3/s$)	2.1×10^{22}	9.0×10^{22}	3.9×10^{23}
$Xe^0 \rightarrow Xe^{2+}$ ionization rate ($1/m^3/s$)	9.5×10^{21}	5.0×10^{22}	2.3×10^{23}
1st term on RHS of Eq. 5-1	0.03	0.06	0.08
2nd term on RHS of Eq. 5-1	0.07	0.11	0.14
n_i^+/n_n	0.01	0.02	0.04

5.1.2 Variation with Discharge Power

The increased $\Sigma(\Omega_i/Z_i)$ due to higher discharge voltage and anode flow rate was combined into a single variable by examining its dependency with discharge power, as shown in Figure 5-4. In order to examine the relationship over a wide range of operating conditions, data are shown for thruster operation at 150 V and 10, 20, and 30 mg/s and 600 V and 10 mg/s. $\Sigma(\Omega_i/Z_i)$ closely followed a linearly decreasing trend with power that was consistent with the observed trends with voltage and flow rate in Figure 5-3. Since $\Sigma(\Omega_i/Z_i)$ directly affects the mass utilization efficiency (see Section 6.1), if CEX corrections were not made to the data, additional uncertainty of 1-5% would result. This uncertainty was larger than uncertainties in other parameters used in the performance model (see Section 6.1) and could lead to misinterpretations of thruster physics with operating condition.

5.1.3 Discussion

In addition to measuring the charge state throughout the plume, these measurements were also used to determine whether single-point measurements of the charge state were sufficiently accurate to gauge the plume-averaged value. To evaluate the uncertainty introduced by single point measurements, the local $\Sigma(\Omega_i/Z_i)$ at thruster centerline (0°) and channel centerline (3°) were compared to the plume-averaged value for all operating conditions in Figure 5-4. The thruster centerline and channel centerline measurements both followed a highly linear trend with discharge power, similar to the plume-averaged value. When compared to the plume-averaged $\Sigma(\Omega_i/Z_i)$, the average uncertainty (mean across all powers) introduced by taking a single point measurement was approximately 3.5% and 1.5% when taken from thruster centerline and channel centerline, respectively. The uncertainty at thruster centerline ranged from 1% at the low discharge powers to nearly 8% at the highest powers. The uncertainty at discharge channel centerline ranged from < 0.1% to 2%, with a single outlier at 5% at 600 V and 10 mg/s. Therefore, the channel centerline measurement resulted in less deviation from the plume-averaged values and exhibited a smaller spread in the deviation as a function of discharge power.

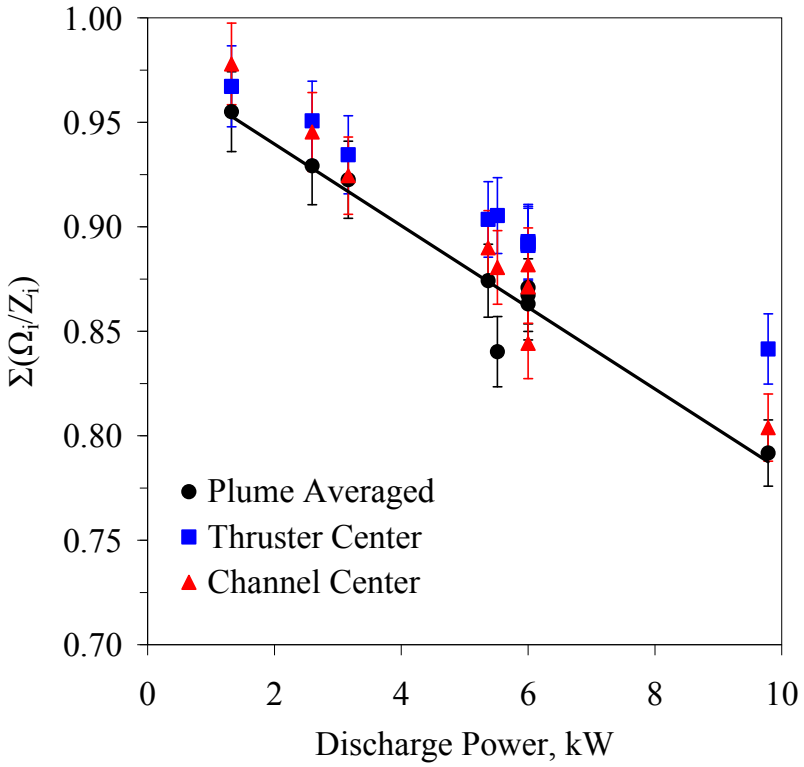

Figure 5-4. $\Sigma(\Omega_i/Z_i)$ versus discharge power for plume-averaged, thruster center, and channel center quantities.

Based on these data, a single measurement at channel centerline added less than 2% uncertainty to the charge state over a wide range of discharge powers. However, this was in addition to the uncertainty in $\Sigma(\Omega_i/Z_i)$ due to the analysis of the probe spectra, which was estimated to be approximately 2%. Thus, the total uncertainty of a single-point measurement was between 3-4%, which was on the order of the uncertainty in the anode efficiency derived from thrust stand measurements, which were typically 2-4%. Given that there were significant uncertainties in the other plasma measurements used in the performance models (e.g., ion energy, plume divergence), plume-averaged values for the multiply-charged ions are recommended when fine changes in the thruster

operating condition are being studied (e.g., magnetic field effects for a given operating condition). If the experiment is focused on understanding thruster physics over large throttling ranges of voltage and current, single-point measurements on channel centerline may be sufficient.

5.2 Far-field Langmuir Probe Measurements

The far-field Langmuir probe was used to measure the plasma potential near the RPA during data collection so that a correction could be performed on the ion voltage distribution. The results of these measurements are shown in Figure 5-5, highlighting the plasma potential that was calculated from these data. The plasma potential with respect to ground was 9.8, 11.8, and 12.4 V at 300 V and 10, 20, and 30 mg/s. The results of far-field Langmuir probe measurements are summarized in Table 5-2.

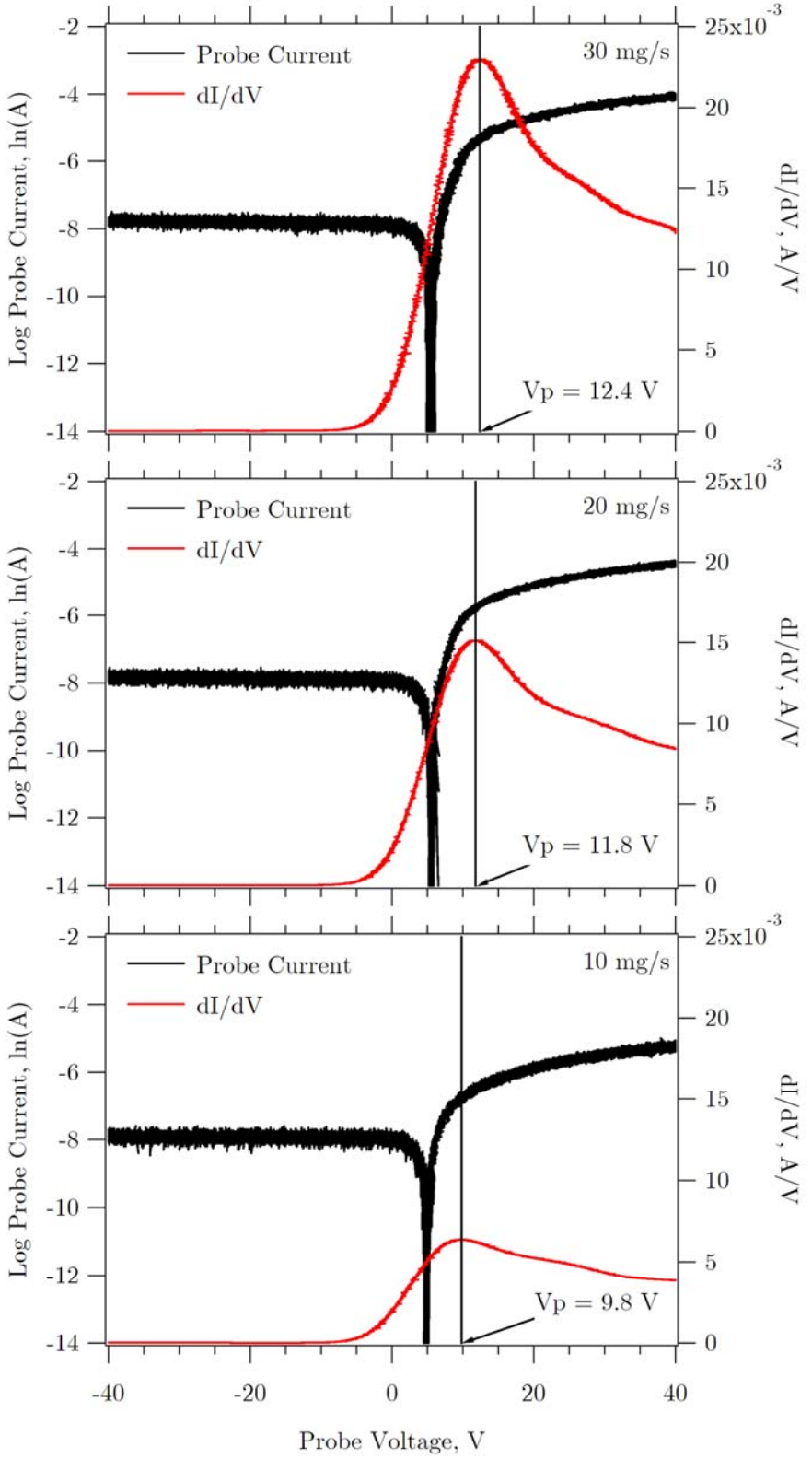

Figure 5-5. Far-field Langmuir probe ln(I) and dI/dV displaying plasma potential used to correct the RPA.

5.3 Retarding Potential Analyzer Measurements

RPA measurements were taken in the far-field plume at 10° from thruster centerline and 2 m from the exit plane. The RPA was pointed at the thruster center and two I-V characteristics were taken at each operating condition using a 1 V step size. Results for the ion voltage distribution are shown in Figure 5-6 for operation at 300 V and 10, 20, and 30 mg/s. The results indicated that the most probable voltage was approximately constant at 283 ± 1 V with respect to cathode potential after being corrected for the local plasma potential. The FWHM was larger at higher flow rates due to increased facility- or thruster-induced collisions. The effect of increased facility-induced collision was evaluated by calculating the CEX beam attenuation (see Section 4.8.1.3) that indicated only 82, 68, and 60% of the exit plane beam current reached the RPA for 10, 20, and 30 mg/s, respectively. A longer acceleration region can contribute to increased FWHM (see Section 2.3.3); however, internal plasma measurements in Chapter 7 showed that the primary acceleration occurred over a smaller region as flow rate was increased. This behavior would result in decreased FWHM with increased flow rate if the effects of facility-induced CEX were not present.

The results of RPA measurements are summarized in Table 5-2, and their consistency with internal plasma measurements is discussed in Section 7.4.3.

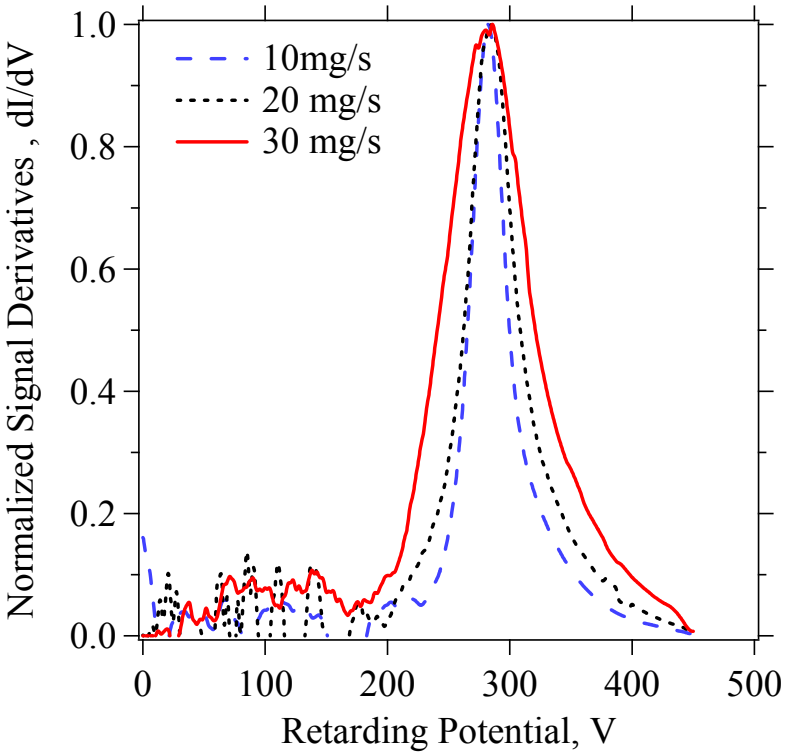

Figure 5-6. RPA ion voltage distribution for operation at 300 V and 10, 20, and 30 mg/s.

5.4 Far-field Faraday Probe Measurements

Results for the far-field Faraday probe measurements are shown in Figure 5-7 for thruster operation at 300 V and 5, 10, 20, and 30 mg/s. Measurements were taken on a 1-m circle that extended from ± 180° from thruster centerline. The data were highly symmetric about thruster centerline and indicated a consistent increase in the current density measured in the wings of the profile ($|\theta| > 90°$). This increase in current density confirmed the linear dependence of CEX collisions on facility pressure that was observed and predicted in previous work [91, 132]. These data also showed a distinct "double peak" at thruster centerline that was produced by the annular discharge channel. The "double peak" was

significantly more apparent at lower flow rates. This result was consistent with the expectation that there were more CEX collisions and hence, more beam spreading at higher flow rates due to the elevated facility pressure.

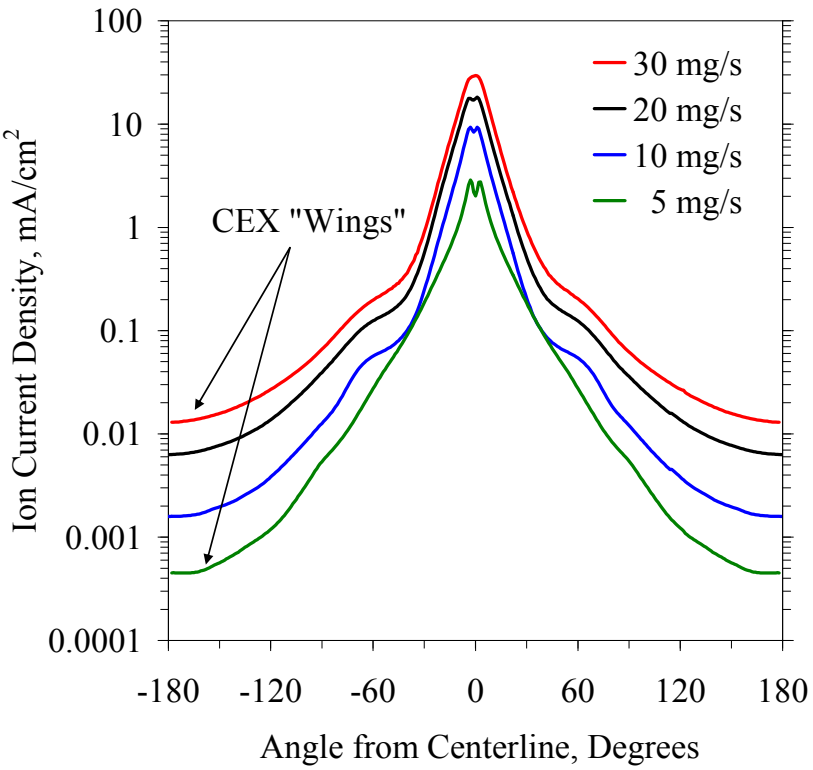

Figure 5-7. Far-field Faraday probe measurements for thruster operation at 300 V and 5, 10, 20, and 30 mg/s.

The data in Figure 5-7 indicated that the current density profile shape remained approximately constant for flow rates of 10, 20, and 30 mg/s. This caused the computed plume divergence to remain approximately constant, likely attributed to the consistency of the flat plasma potential structure that existed in the discharge channel and near-field plume at all mass flow rates (see Section 7.3.3). The flat potential structure caused ions to be accelerated primarily in the axial direction leading to relatively low plume divergence.

The far-field integrated ion beam current and plume divergence half-angle were calculated using the methods outlined in Section 4.8.4.2 and the results are summarized in Table 5-2. The fraction of discharge current composed of integrated ion beam current (referred to as current utilization, $\eta_b = I_B/I_D$, see Section 6.1) increased from 5 to 10 mg/s and decreased with flow rate from 10 to 30 mg/s: I_B/I_D = 1.05, 1.06, 1.05, and 1.02 at 5, 10, 20, and 30 mg/s, respectively. The plume divergence angle was 30º at 5 mg/s and constant at 27º from 10 to 30 mg/s.

The ion beam current trend was consistent with the near-field Faraday probe measurements in Section 5.5; however, the magnitude for the far-field measurements was larger than the discharge current. The far-field results can be improved by recalculating the beam current as the axial component: I_B/I_D = 0.91, 0.95, 0.93, and 0.91 at 5, 10, 20, and 30 mg/s, respectively. Even after reducing the total ion beam current to the axial component, the magnitude of the current utilization is still too high by approximately 20%. The plume divergence trend was also consistent with the near-field Faraday probe measurements at 20 and 30 mg/s (constant angle). At 10 mg/s the near-field measurements showed an increase in divergence, while the far-field angle remained constant. When including the angle at 5 mg/s in the far-field data, both sets of data indicate a trend of decreased divergence angle with increased flow rate.

Far-field Faraday probe measurements for thruster operation at 150 V and 10, 20, and 30 mg/s are included in Appendix C. In addition, a method to correct Faraday probe measurements for the presence of facility effects by extrapolation of the wings is included in Appendix B.

5.5 Near-field Faraday Probe Measurements

Results from the near-field Faraday probe measurements are presented in this section for thruster operating conditions of 300 V and 10, 20, and 30 mg/s. Fluctuations in the ion current density were correlated to discharge oscillations through frequency and amplitude comparisons made possible by data acquisition at 100 kHz. As mentioned in Section 4.8.5.2, the presented results were not corrected for sheath growth, SEE, or cosine losses. The beam current and plume divergence were calculated over a wide range of axial locations and a global average was determined.

5.5.1 Near-field Ion Current Density

Contours of the near-field ion current density for thruster operation at 300 V and 10, 20, and 30 mg/s are shown in Figure 5-8. Each contour represents more than 64,000 individual measurements of the local current density. All three contours showed that the ion beam exited the thruster channel and remained highly collimated for the first thruster diameter. Beyond the first thruster diameter, the main ion beam broadened and eventually coalesced near thruster

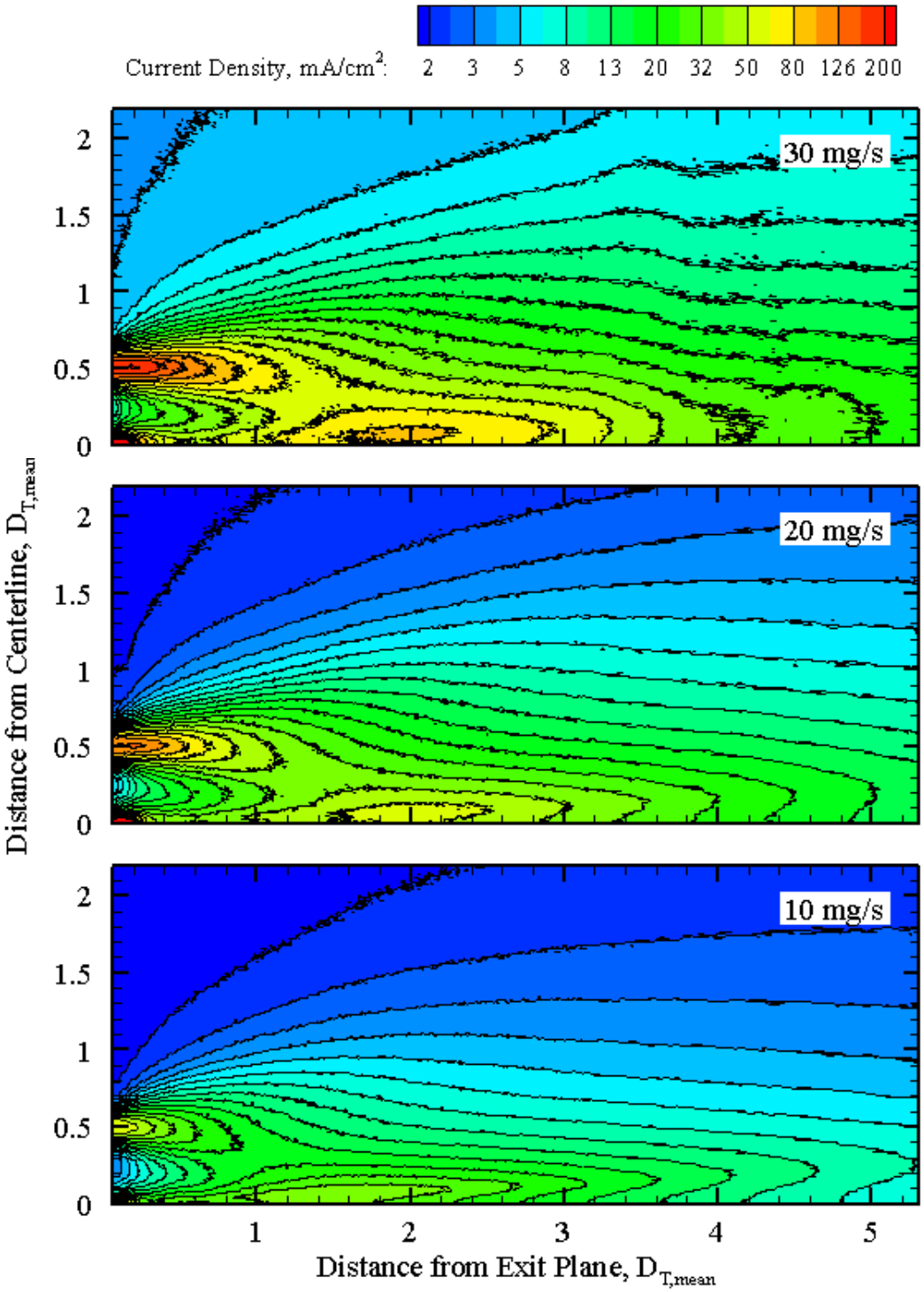

Figure 5-8. **Ion current density in the near-field plume for thruster operating conditions of 300 V and 10, 20, and 30 mg/s (note exponential contour scaling).**

centerline. The location of coalescence moved downstream with increased anode mass flow rate. This was consistent with the emissive probe results of Section 7.3.3 that indicated ionization and acceleration occurred further downstream with increased flow rate.

The change in the characteristic shape of the ion current density shown in Figure 5-8 can be more clearly seen by examining radial traces at several axial locations on a single plot, as shown in Figure 5-9 for thruster operation at 300 V and 20 mg/s. Near the thruster exit, the current density had three peaks; the two outer peaks represented each side of the thruster annulus and the center peak represented the cathode. Further downstream, the center peak decreased and then disappeared entirely. Even further downstream, the two channel peaks came together, producing the familiar shape of a far-field Faraday probe trace (see Section 5.4).

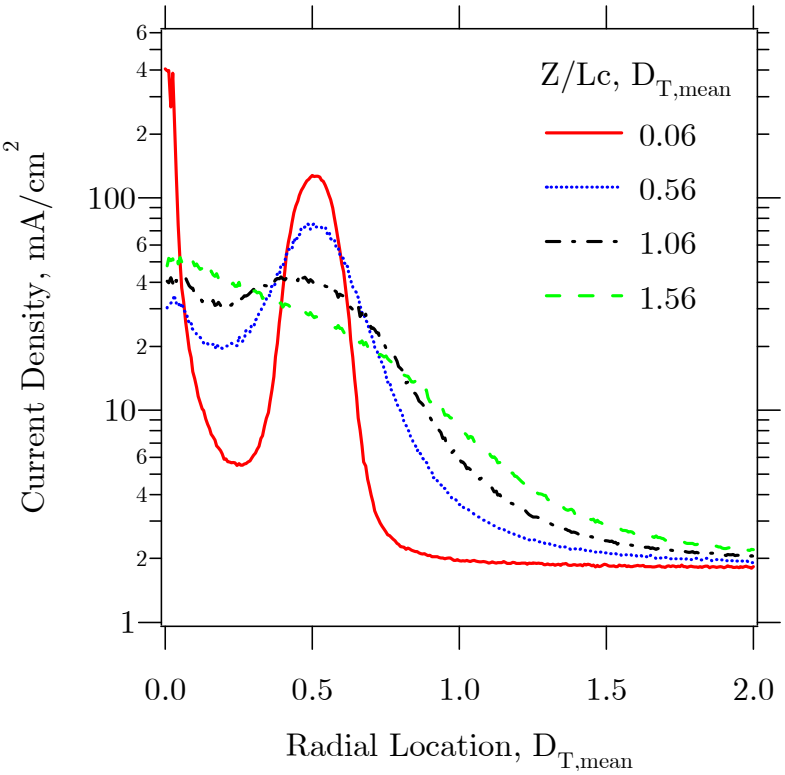

Figure 5-9. Comparison of ion current density at several axial locations for thruster operation at 300 V and 20 mg/s.

For increased clarity, the peak current density as a function of axial distance from the thruster is shown in Figure 5-10, indicating a modest peak downstream of the thruster exit at 20 and 30 mg/s. The difference between the peak current density and the exit plane current density was larger at 30 mg/s than at 20 mg/s, indicating a dependence on flow rate that may have been attributed to increased collection of CEX ions. Since the probe was biased 70-80 V below the plasma potential, CEX ions may have been drawn into the probe. The contribution of CEX ions would have a larger impact at higher flow rates due to elevated facility-induced collisions (higher facility pressure), which is

consistent with the increased severity of the peaks with flow rate as shown in Figure 5-10.

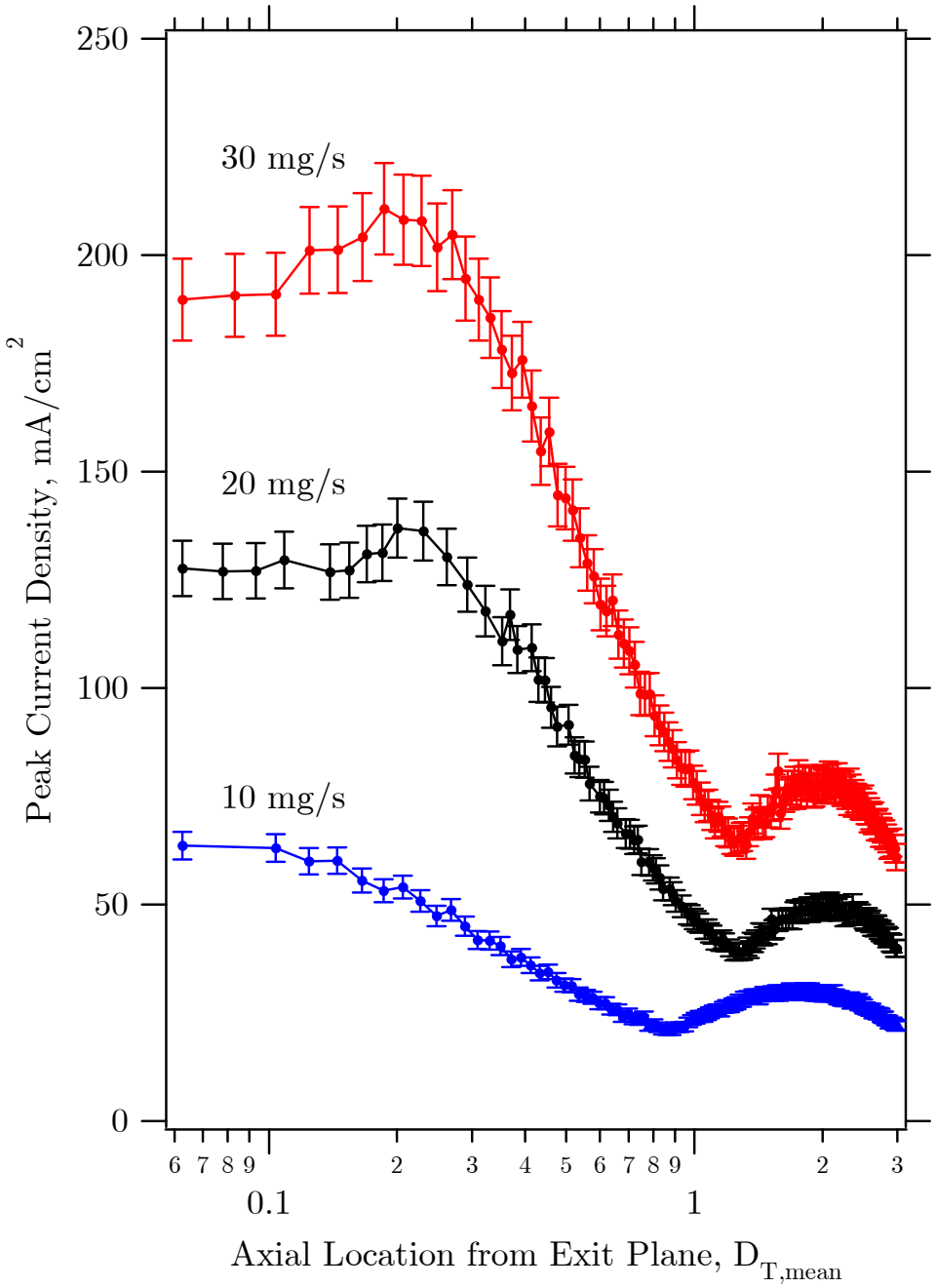

Figure 5-10. Peak current density for thruster operation at 300 V and 10, 20, and 30 mg/s.

Another potential contribution to the downstream peak in maximum current density may have been insufficient probe bias; however results in Section 7.2.3 indicated that the electron temperature was too low to contribute in this way ($T_e < 5$ eV). Another contribution may have been additional ion acceleration in the near-field plume that was shown in near-field plasma potential measurements (see Section 7.3) and LIF measurements [133, 134]. The end of the acceleration region occurred at approximately 0.02, 0.03, and 0.07 $D_{T,mean}$ for thruster operation at 10, 20, and 30 mg/s, respectively (see Figure 7-24 of Section 7.4.1.2). Since these are well upstream of the peak ion current density location of approximately 0.2 $D_{T,mean}$ for 20 and 30 mg/s, the effect of incomplete ion acceleration likely had a relatively small effect.

Although the exact cause for the peak in maximum current density downstream of the thruster exit is not known at this time, its existence is the primary reason that calculating the beam current at the exit plane alone is not strictly valid (as suggested in Ref. [106]).

5.5.2 Centerline "Spike"

The current density contours provided experimental evidence of the visual "spike" (sometimes referred to as "cone" or "dovetail") near thruster centerline that is often seen during thruster operation, as shown in Figure 5-11. These near-field measurements indicated that the "spike" was due to increased plasma density rather than excited ion or neutral species. Although the "spike" appeared

to emanate from the center-mounted cathode, it is characteristic of most efficient Hall thrusters, even those with externally-mounted cathodes. Several supporting discussions and photographs can be found in Refs. [135-138].

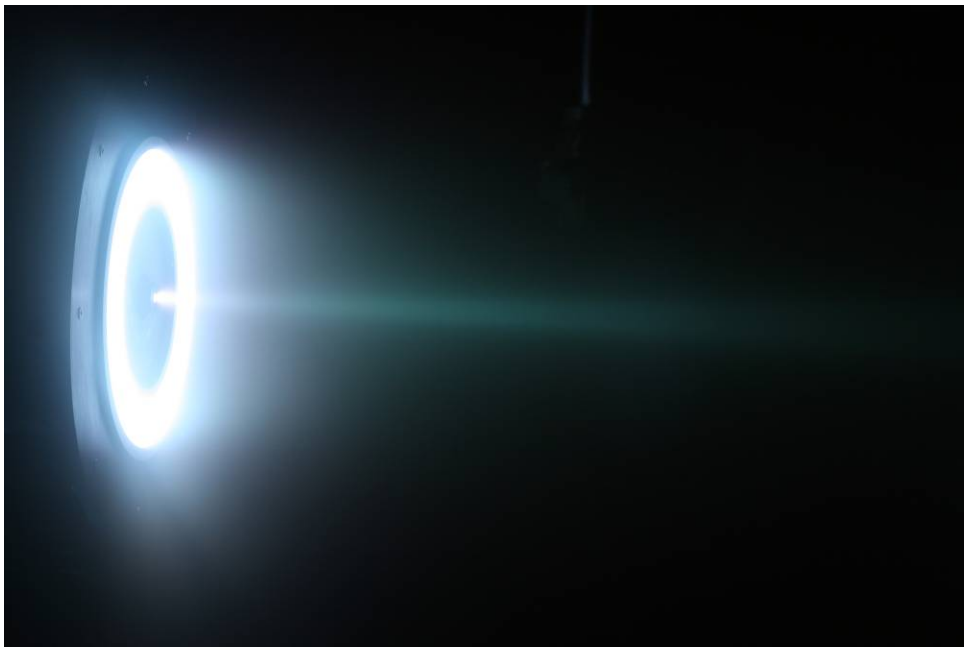

Figure 5-11. Photograph of the 6-kW Hall thruster operating at 300 V and 20 mg/s. Note the "spike" that emanates from the center of the thruster.

A large contribution to the ion beam coalescence at thruster centerline was due to the natural beam "crossover" that would occur in the absence of collisions or electric or magnetic fields (i.e., isotropic expansion). Three-axis LIF measurements in the near-field of the UM/AFRL P5 Hall thruster indicated that ions at the discharge channel exit had non-zero radial velocities, leading to ion beam "crossover" at the thruster centerline that resulted from the intersection of the thruster annulus [139]. Additional LIF measurements in the near-field of the UM/AFRL P5 Hall thruster confirmed the ion beam "crossover" was due to

divergent ions, and also identified a significant fraction of ions at thruster centerline that had zero or near-zero radial velocity [133]. Those same measurements showed that further downstream the radial velocity decreased significantly (peak of approximately 8 km/s at 10 cm versus 2 km/s at 50 cm), while the axial velocity increased (mean of approximately 15 km/s at 10 cm and 18 km/s at 50 cm). Measurements with a 600 W thruster showed the same trends [136]. These data indicated that ions were focused towards thruster centerline within the plume. Ions that emanate from the discharge channel can not reach thruster centerline having zero (or near-zero) radial velocity without an additional mechanism or force acting in the radial direction.

A potential contribution to the near-field plume focusing was a radial electric field that turned ions towards thruster centerline by increasing their initial radial velocity. The work of Hofer *et al.* [140] indicated that electric fields on the order of 0.1 V/mm could explain differences in plume divergence observed between internally and externally mounted cathodes.

Assuming ions depart the channel (0.5 $D_{T,mean}$) with primarily axial velocity, as supported by the data in Figure 5-8, we can estimate the radial field necessary to cause ions to reach thruster centerline at approximately 1 $D_{T,mean}$ downstream.

In order to reach thruster centerline at approximately 1 $D_{T,mean}$ ions must exit the thruster at an angle of approximately 27° from the axial direction.

Assuming an acceleration voltage of 280 V (consistent with RPA measurements in Section 5.3), the radial velocity must be 9 km/s and axial velocity 18 km/s. A total acceleration potential of 55 V is necessary to achieve 9 km/s of radial velocity, which is consistent with the change in potential from channel exit to thruster centerline measured in near-field plasma potential measurements performed by JPL with a 6-kW Hall thruster at 300 V and 10 and 20 mg/s, as shown in Figure 5-12. These measurements were recorded with a floating emissive probe, and the results indicated a modest radial electric field on the order of 1 V/mm that pointed towards thruster centerline and persisted downstream for the first 0.5 $D_{T,mean}$ [141]. Although the electric field is relatively weak, the cumulative effect over the first thruster diameter downstream is substantial enough to produce realizable changes in the near-field ion beam trajectory.

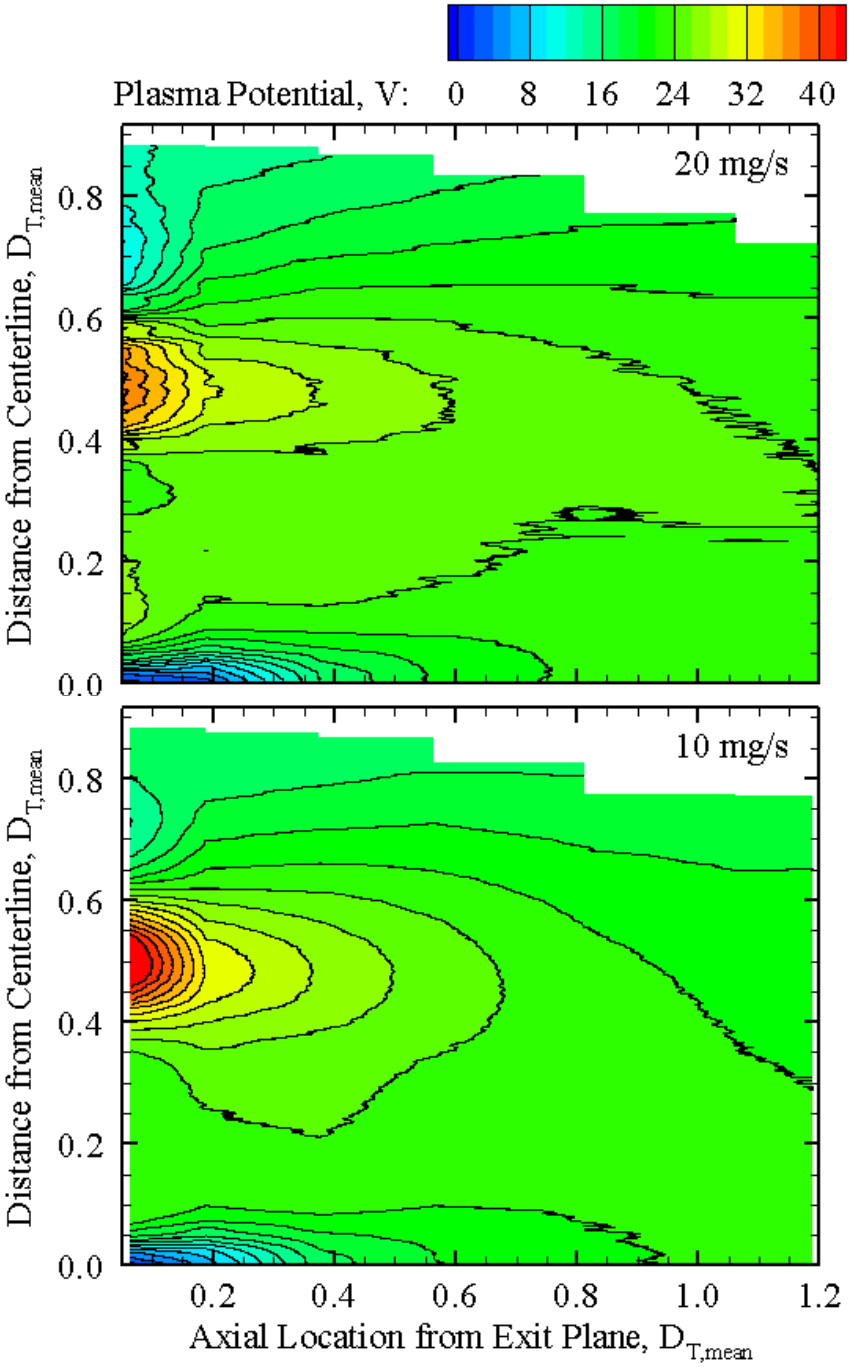

Figure 5-12. Plasma potential in the near-field plume for thruster operating conditions of 300 V at 10 and 20 mg/s (data courtesy JPL).

The creation of the near-field "spike" in Figure 5-8 and Figure 5-11 may have also been influenced by radial electric fields. To evaluate this potential contribution, we note that the "spike" was angled at approximately 5° from

thruster centerline, requiring a radial velocity of approximately 2 km/s (axial velocity of 20 km/s). If the spike was created by ions from the channel, the radial field would need to reduce the radial velocity from 9 km/s to 2 km/s. This change in velocity is equivalent to approximately 35 V, which is not supported by the data in Figure 5-12 that indicate a change in potential of a few volts beyond 1 $D_{T,mean}$. Thus, radial electric fields are not likely a factor in production of the centerline "spike" in Figure 5-8. It should be noted that unlike the main ion beam considered in the previous discussions, CEX ions in the plume can be turned by weak electric fields. Focusing of CEX ions could be a contribution to the "spike," but there is currently no evidence to support this argument.

LIF measurements support the notion that the ions turn via radial electric fields, indicating ion vectors that point in the direction of the plasma potential [136]. These measurements also indicated that the cathode produced a potential well in its vicinity, causing low energy CEX ions to be turned in the direction of the cathode. In addition to changing ion trajectories, this near-cathode potential-well may contribute to accelerated keeper erosion due to high-energy ions returning to the cathode, although no erosion measurements have been recorded.

Other contributions to the presence of the centerline "spike" could be neutral excitation or electrostatic shocks as suggested in Refs. [136, 137, 142]; however, evaluation of these contributions was not included in the scope of this research. Although the measurements presented in this section were recorded

with a center-mounted cathode, the same visual structure, current density profile shape, and plasma potential characteristics exist with an externally-mounted cathode; however, the "spike" is typically less pronounced and the plasma potential gradient is weaker in the near-field plume [141]. The universality of the "spike" indicates that its presence is inherently linked to efficient operation of Hall thrusters, and as such, should be investigated in further detail.

5.5.3 Current Density Fluctuations

Since near-field Faraday probe data were acquired at 100 kHz, the influence of discharge oscillations on ion current density was resolved. The discharge current and ion current density fluctuations were highly correlated at approximately 16, 23, and 26 kHz at 300 V and 10, 20, and 30 mg/s, respectively (see Section 6.2 for discharge oscillation information). The discharge current and cathode potential did not change appreciably as the probe traversed through the plume.

The standard deviation of the current density about the local mean is shown in Figure 5-13 for operation at 300 V and 10, 20, and 30 mg/s. Far from thruster centerline, the amplitude of the discharge current and ion current density were in good agreement (oscillation amplitude of approximately 10%). The ion current density oscillations were concentrated near the thruster centerline at approximately one thruster diameter downstream. This location was

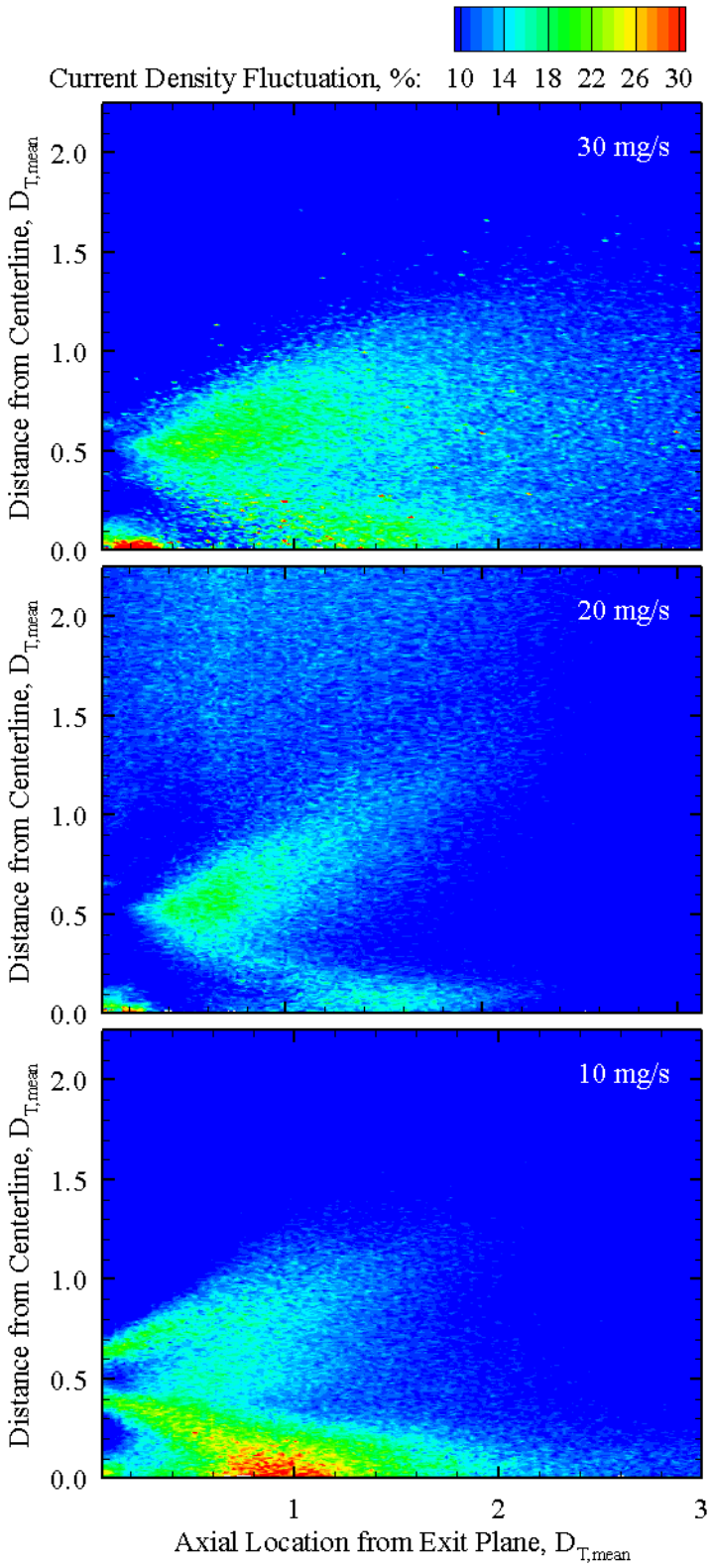

Figure 5-13. Standard deviation of the ion current density for thruster operation at 300 V and 10, 20, and 30 mg/s.

coincident with the visual "cross-over" of the beam, possibly indicating increased instability due to ion-ion two-stream instability as suggested in Refs. [137, 142]. This effect may have been due to the probe support-arm intersecting the main ion beam causing a disruption in the ion acceleration process in the plume. However, this did not appear to be the case since the discharge and cathode oscillations remained constant as the probe intersected the plume.

The elevated oscillation amplitude near the cathode exit was likely due to the interaction between the large ion current and neutral densities that were ejected from the cathode orifice. At 10 mg/s there was another interesting feature near the inner and outer radius of the channel where two "jets" of elevated oscillation appeared to emanate from either side of the channel. These features were likely associated with the increased neutral density in these regions that were predicted by HPHALL-2 simulations (see Section 8.2.2). These "jets" of increased current density oscillation were not as apparent at 20 and 30 mg/s.

The data in Figure 5-13 indicated that the global ion current density fluctuations were lower at 20 mg/s than at 10 and 30 mg/s. This was consistent with the trend exhibited by the discharge oscillation data that are shown in Section 6.2. The correlation between discharge oscillation and ion current density fluctuation provided evidence that the breathing mode produces ions in packets, which are transported into the plume. In this way, the breathing mode is not a localized ionization instability, rather a global characteristic of the bulk plasma.

To further investigate the origin of the current density oscillations, a dedicated study of the effect of propellant utilization and cathode operation is needed. Propellant utilization can be changed by operating the thruster at off-nominal magnetic field or discharge voltage/current settings. The cathode operation can be modified through additional cathode flow, heater current, or keeper current, which have been shown to affect electron dynamics [143].

5.5.4 Integrated Ion Beam Current

The beam current was calculated using all three methods outlined in Section 4.8.5.2, and the results are shown in Figure 5-14 as a function of axial distance. The beam current was used in the efficiency analysis of Chapter 6, and the results are summarized in Table 5-2.

Integrating the entire current density profile from centerline to the maximum radial location (I_{tot}) resulted in calculated beam currents that were well above the discharge current, similar to the gross over-prediction observed in the far-field beam current calculations (see Section 5.4). The beam current was also calculated by integrating the portion of the signal that existed directly downstream of the discharge channel ($0.5\ D_{T,mean} \pm b/2$) as described in Section 4.8.5. Integrating the current density with this method ($I_{tot,DC}$) produced calculated beam currents that were approximately 20% below the discharge current near the thruster exit plane; however, the beam current drastically

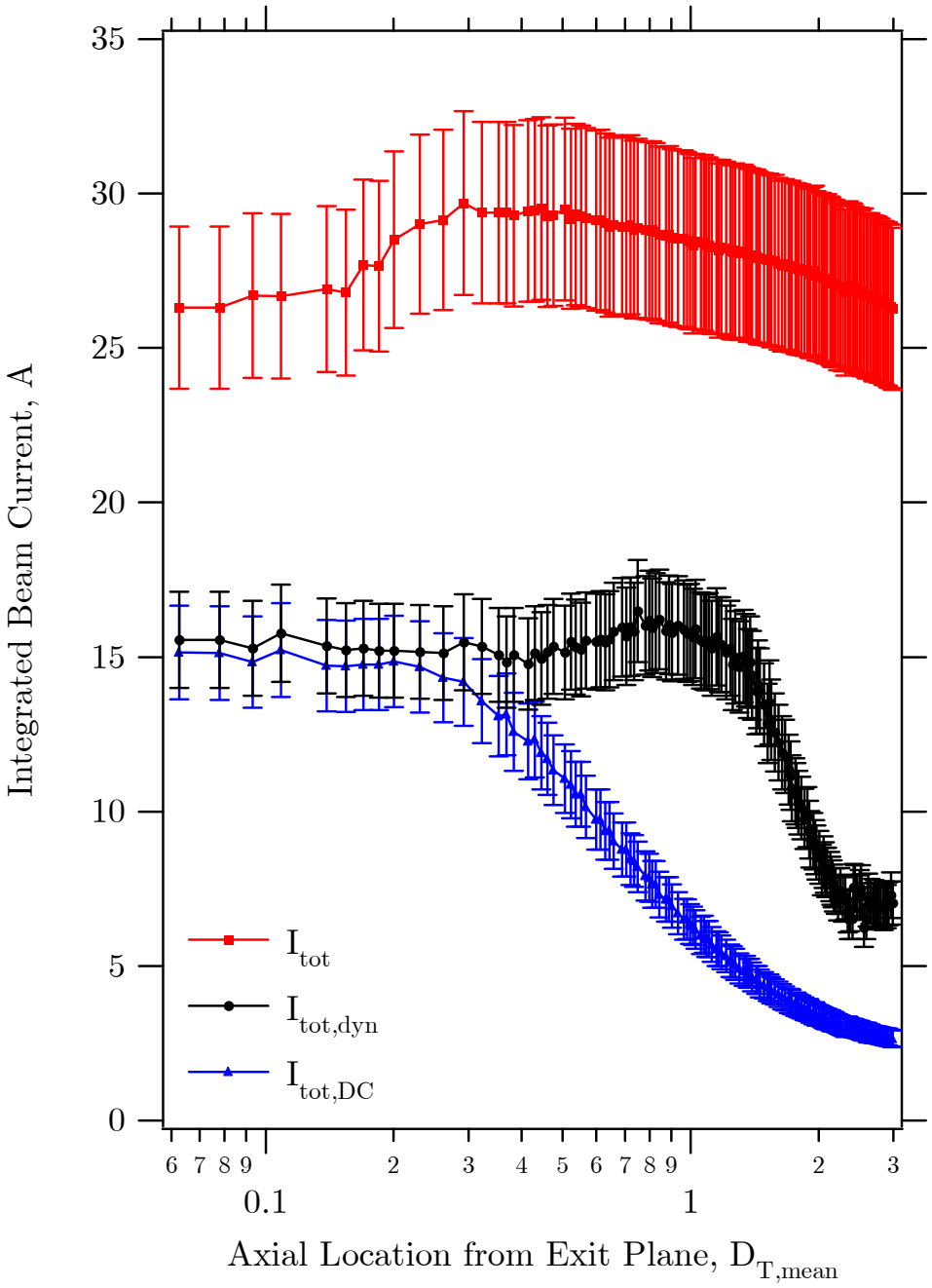

Figure 5-14. Integrated ion beam currents using three different integration techniques for thruster operation at 300 V and 20 mg/s.

decreased after approximately 0.3 $D_{T,mean}$, restricting the usefulness of the calculation. This limitation was caused by the beam crossing at approximately 1 $D_{T,mean}$ shown in Figure 5-8. The beam crossing caused the peak current density

to be shifted away from channel centerline, resulting in a drastic decrease in the flux of ions located within the static integration domain

The dynamic window integration technique ($I_{tot,dyn}$) integrated the portion of the current density that was enclosed within 1/e on either side of the peak current density at each axial location (see Section 4.8.5). This method was introduced because it produced a beam width that was approximately equal to the discharge channel exit width at the channel exit plane, while providing a dynamic integration domain that accounted for the effects of beam broadening further downstream. This integration method produced reasonable beam currents (approximately 20% below the discharge current) that were consistent with the DC-only integration near the thruster. The integrated current from the dynamic technique extended the region of acceptable beam currents from 0.3 to greater than 1 $D_{T,mean}$.

All reported beam current values were calculated from the dynamic window integration method by taking the mean beam current from 0.5 to 1.0 $D_{T,mean}$. The beam current calculated at each axial location is shown in Figure 5-15 for thruster operation at 300 V and 10, 20, and 30 mg/s (results for 150 V can be found in Appendix C). The mean calculated beam current was 7.35, 15.8, and 25.9 A at 300 V and 10, 20, and 30 mg/s, respectively. The current utilizations were 0.812, 0.777, and 0.766, respectively, and the results are summarized in Table 5-2.

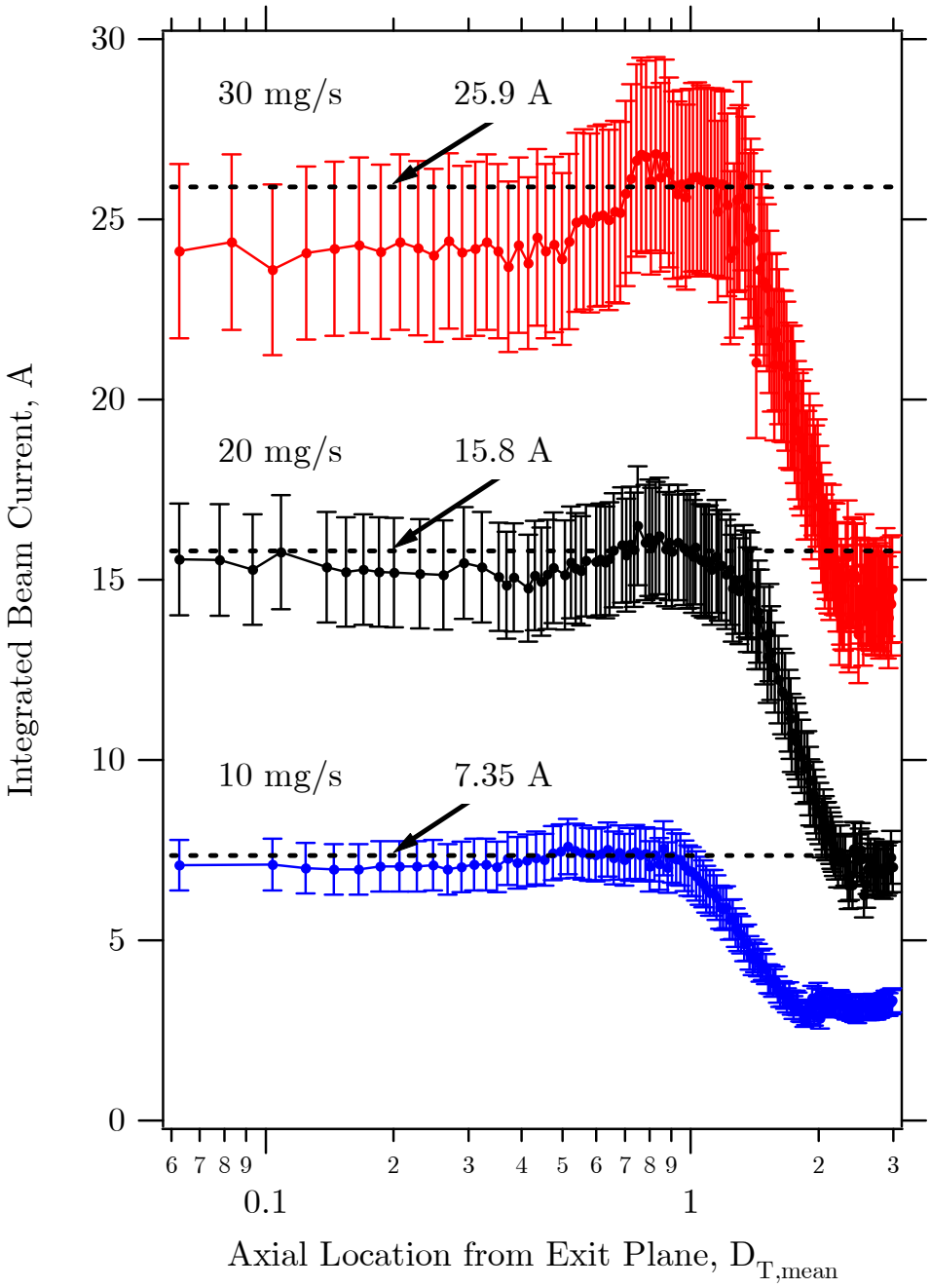

Figure 5-15. Integrated ion beam current at each axial location for thruster operation at 300 V and 10, 20, and 30 mg/s.

5.5.5 Plume Divergence

The plume divergence was calculated using Eq. 4-17, and the results are shown in Figure 5-16 for thruster operation at 300 V and 10, 20, and 30 mg/s (results for 150 V can be found in Appendix C). The plume divergence definition assumed that the ion beam could be approximated as a point source located at the center of the channel exit plane. Since the beam had a finite width, even at the channel exit, this caused an unreasonably high calculated plume divergence near the thruster. After 0.4 $D_{T,mean}$ downstream (approximately two channel widths), the calculated divergence angle leveled off and remained constant until approximately 1 $D_{T,mean}$. Beyond that point, the calculated divergence angle decreased since the entire plume was not captured because of the limited radial data collection domain.

The plume divergence for each operating condition was calculated by taking the average from 0.5 to 1.0 $D_{T,mean}$ and the results are summarized in Table 5-2. The plume divergence was 20º, 16º, and 16º at 10, 20, and 30 mg/s, respectively. The results at 20 and 30 mg/s were consistent with the far-field Faraday probe measurements that indicated constant plume divergence from 10 to 30 mg/s. These results were unexpected since the internal measurements indicated that the ionization and acceleration occurred further downstream as flow rate was increased (see Sections 7.2 and 7.3). This downstream displacement is typically associated with higher plume divergence since the plasma potential tends to be defocused outside the channel. However, the 6-kW thruster in this

study did not have a defocused potential structure, offering a wide range of acceleration locations that maintained excellent beam collimation.

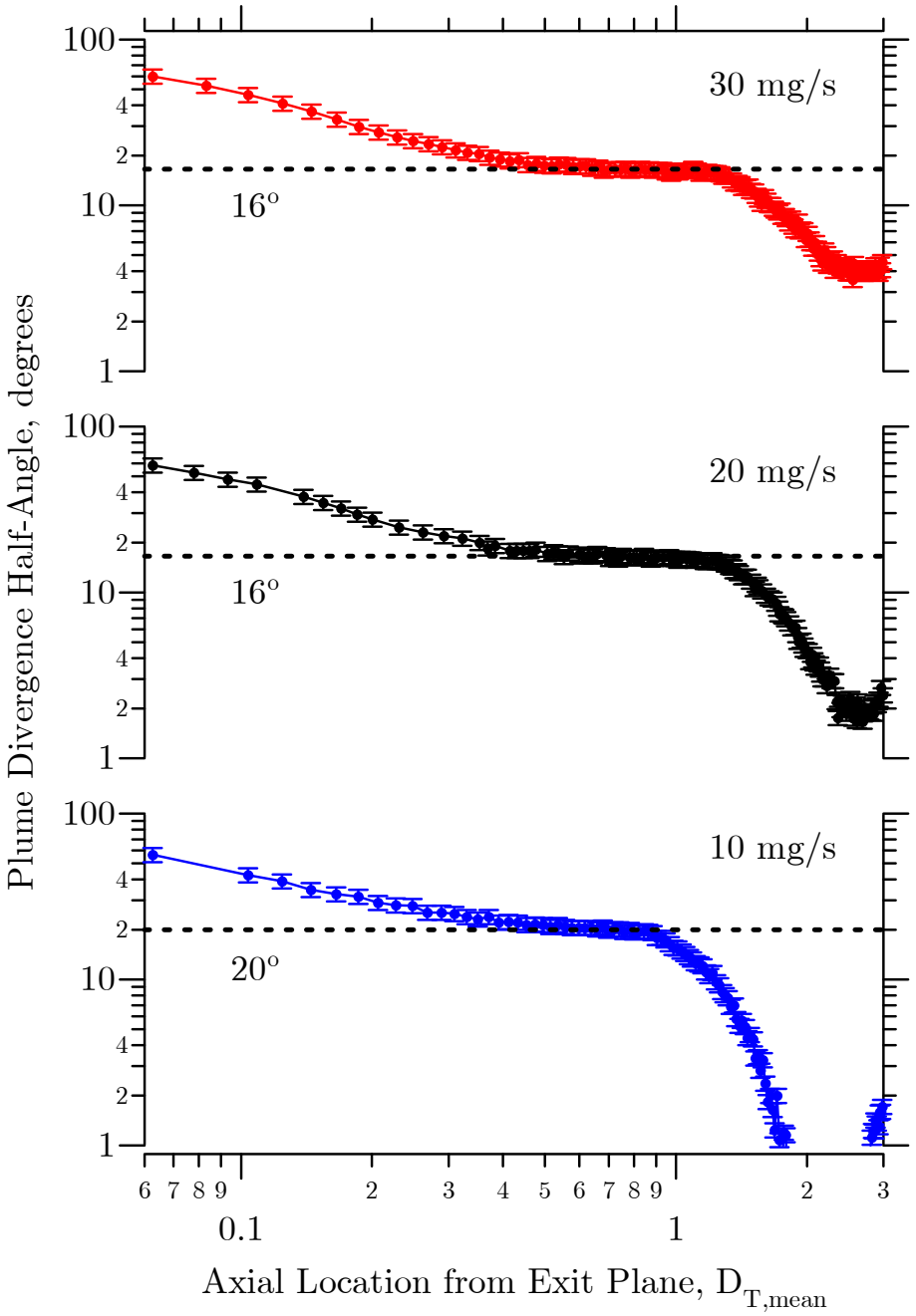

Figure 5-16. Plume divergence at each axial location for thruster operation at 300 V and 10, 20, and 30 mg/s.

5.6 Summary of Plume Measurements

Results from the variety of plume measurements described in this chapter are shown in Table 5-2. These results will be used in Chapter 6 to perform an efficiency analysis so that individual loss mechanisms can be identified as a function of injected mass flow rate.

E×B measurements indicated a higher fraction of multiply-charged ions in the plume as flow rate was increased. These results also indicated a distinct linear relationship between $\Sigma(\Omega_i/Z_i)$ and discharge power. RPA measurements indicated a constant acceleration potential at all three flow rates of approximately 284 V with respect to cathode.

Far-field and near-field Faraday probe measurements indicated that the plume divergence and beam current fraction decreased with flow rate. The near-field current density measurements offered additional fidelity to the plume divergence and beam current calculations, resulting in values that were consistent with the efficiency analysis that is reported in Chapter 6. The near-field results were consistent from the exit plane to approximately 1 $D_{T,mean}$. Beyond that point, thruster- and facility-induced collisions altered the plume and the resulting calculations of beam current and beam divergence.

Table 5-2: Summary of results from plume measurements for thruster operation at 300 V.

	10 mg/s	20 mg/s	30 mg/s
Xe^{1+} Current Fraction, Ω_1	0.869	0.749	0.596
Xe^{2+} Current Fraction, Ω_2	0.099	0.182	0.327
Xe^{3+} Current Fraction, Ω_3	0.032	0.069	0.076
RPA V_{mp}, V	282	284	286
RPA $V_{p,loc}$, V	9.8	11.8	12.4
RPA V_{accel}, V	285	283	284
RPA FWHM, V	34	46	80
Far-field Plume Div., θ	27	27	27
Far-field Total Beam Current, A	9.23	21.0	34.3
Far-field Axial Beam Current, A	8.25	18.6	30.4
Near-field Plume Div., θ	20	16	16
Near-field Beam Current, A	7.35	15.8	25.9

Chapter 6

Performance Measurements and Efficiency Analysis

This chapter begins with a brief documentation of the performance model that was used with experimental plume measurements. Next, data are presented on measurements of the discharge oscillations and overall thruster performance. Finally, results from the plume measurements of Chapter 5 are combined with a phenomenological performance model to decompose the primary contributing factors that affect Hall thruster efficiency.

Thruster performance is presented from 1.5 to 9.9 kW, 150 to 600 V, and 5 to 30 mg/s. The measurements were taken at a constant cathode flow fraction of 7% and the magnetic field strength was optimized for maximum efficiency at each operating condition, while the shape was constrained to a pre-determined vacuum magnetic field that was symmetric about channel centerline.

6.1 Framework of Phenomenological Performance Model

Excluding the electrical efficiency of the systems that provide power to a Hall thruster, the total thrust efficiency can be written as the ratio of jet power in the plume to the total input power (as in Eq. 2-3)

$$\eta_t = \frac{P_{jet}}{P_t} = \frac{T^2}{2\dot{m}_a P_D}\frac{P_D}{P_t}\frac{\dot{m}_a}{\dot{m}_t} = \eta_a \eta_{mag} \eta_c \,, \tag{6-1}$$

where P_t is the total thruster power including discharge and magnet powers, $\dot{m}_t$ is the total thruster mass flow rate including anode and cathode flows, η_a is the anode efficiency,

$$\eta_a = \frac{T^2}{2\dot{m}_a P_D}, \tag{6-2}$$

η_{mag} is the electromagnet utilization efficiency

$$\eta_{mag} = \frac{P_D}{P_D + P_{mag}}, \tag{6-3}$$

and η_c is the cathode utilization efficiency

$$\eta_c = \frac{\dot{m}_a}{\dot{m}_a + \dot{m}_c}. \tag{6-4}$$

The electromagnet and cathode utilization efficiencies account for the cathode flow rate and the power supplied to the electromagnet coils, respectively. Since these losses are not directly related to the production of useful thrust, the focus will be directed at the anode efficiency.

Following the framework of Hofer *et al.* [26, 61], the anode efficiency can be decomposed as the product of five utilization efficiencies given by

$$\eta_a = \frac{T^2}{2\dot{m}_a P_D} = \eta_q \eta_v \eta_d \eta_b \eta_m \,. \tag{6-5}$$

The individual utilization efficiencies are charge utilization efficiency

$$\eta_q = \frac{\left(\sum {\Omega_i}/{\sqrt{Z_i}} \right)^2}{\sum {\Omega_i}/{Z_i}}, \tag{6-6}$$

voltage utilization efficiency

$$\eta_v = \frac{V_{accel}}{V_D} = 1 - \frac{V_L}{V_D}, \tag{6-7}$$

divergence utilization efficiency

$$\eta_d = \left(\cos\theta \right)^2, \tag{6-8}$$

current utilization efficiency

$$\eta_b = \frac{I_B}{I_D} = 1 - \varepsilon, \tag{6-9}$$

where ε is the electron current recycle fraction (I_e/I_D), and mass utilization efficiency

$$\eta_m = \frac{\dot{m}_b}{\dot{m}_a} = \xi \eta_b \sum \frac{\Omega_i}{Z_i}, \tag{6-10}$$

where ξ is the exchange ratio defined as

$$\xi = \frac{m_{xe} I_D}{\dot{m}_a e} \,. \tag{6-11}$$

Using this methodology, the thrust, thrust-to-power ratio, and anode specific impulse can be written as

$$T = \sum \dot{m}_i \left\langle v_i \right\rangle = \eta_b I_D \sqrt{\frac{2 m_{xe} \eta_v V_D}{e}} \sum \frac{\Omega_i}{\sqrt{Z_i}} \cos\theta \,, \tag{6-12}$$

$$\frac{T}{P} = \sum \dot{m}_i \langle v_i \rangle = \eta_b \sqrt{\frac{2 m_{xe} \eta_v}{e V_D}} \sum \frac{\Omega_i}{\sqrt{Z_i}} \cos\theta \,, \tag{6-13}$$

$$I_{sp,a} = \frac{T}{\dot{m}_a g} = \frac{\eta_m}{g} \sqrt{\frac{2 e \eta_v V_D}{m_{xe}}} \frac{\sum \frac{\Omega_i}{\sqrt{Z_i}}}{\sum \frac{\Omega_i}{Z_i}} \cos\theta \,. \tag{6-14}$$

This framework will be used in conjunction with several plume diagnostics to identify the primary loss mechanisms that affect Hall thruster operation. The charge utilization was measured with the E×B probe, voltage utilization was measured with the RPA, and divergence and current utilizations were measured with the near-field Faraday probe.

Other analogous versions of this performance model are available in previous literature [144-146]. Other performance models offer the possibility of a more detailed description of some individual efficiency or energy losses. However, the model described in Eqs. 6-1 to 6-14 offers a realizable method to measure the major loss mechanisms using standardized plasma diagnostics.

6.2 Discharge Oscillations

Discharge oscillations were measured at 250 kHz over the span of one second. These data were then analyzed via Fast-Fourier Transform (FFT) analysis to produce an appropriate estimate of the primary breathing mode oscillation frequency. The power spectrum for each operating condition is shown in Figure 6-1. Measurement noise was removed from the spectrum through a

"parse and average" method; however, the application of commercially-available smoothing algorithms produced the same result.

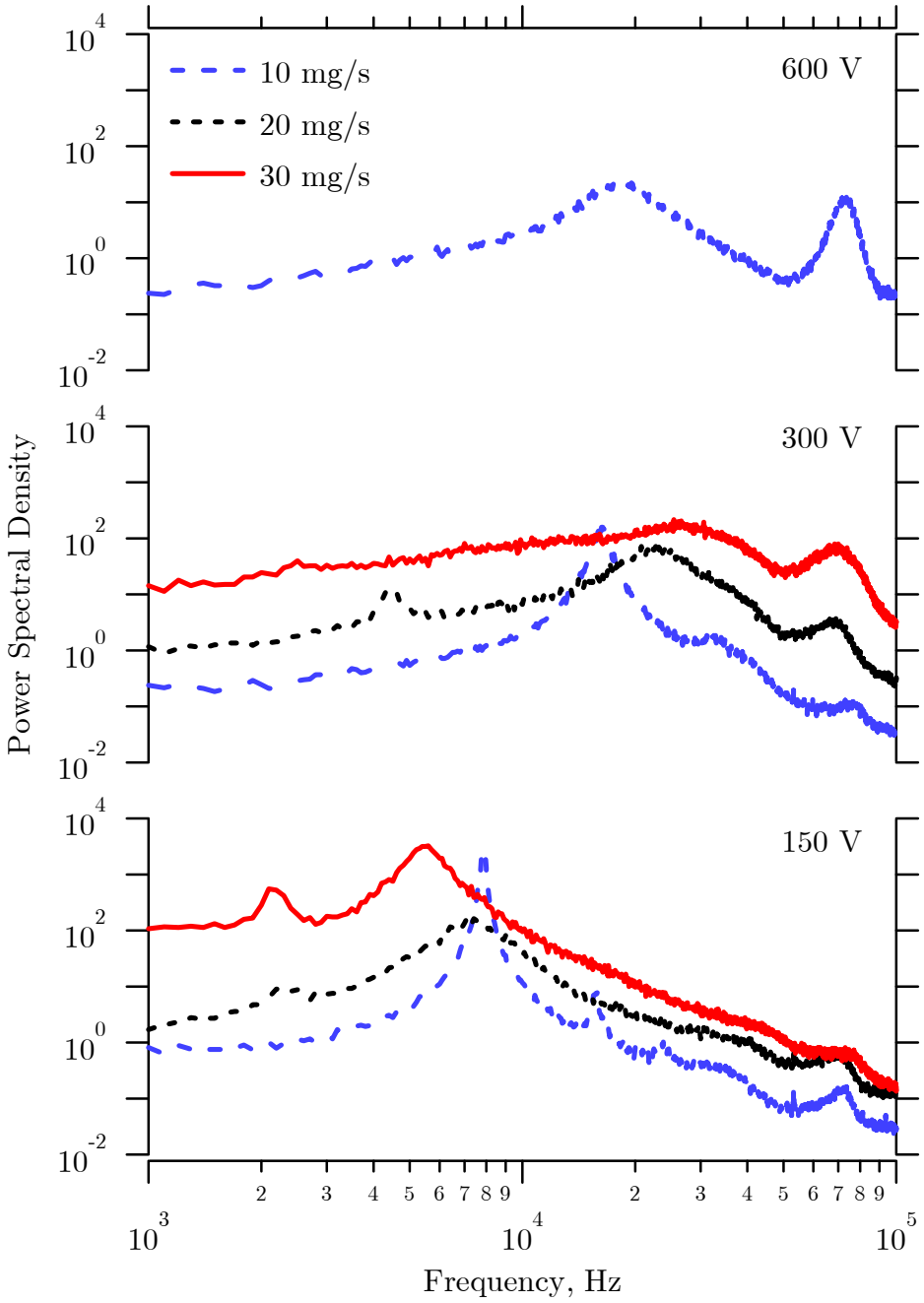

Figure 6-1. Discharge oscillation spectra for thruster operation from 150-600 V and 10 to 30 mg/s.

The primary oscillation frequency is referred to as the breathing mode (see Section 2.3.3). The breathing mode oscillation frequency indicated a trend of increased frequency with increased discharge voltage or anode flow rate. A quantitative view of these data is shown in Figure 6-2 and Figure 6-3 for the variation of the breathing mode oscillation frequency and amplitude with operating condition, respectively (summarized in Table 6-1). At 300 V, the breathing mode frequency varied from approximately 15 to 25 kHz for thruster operation from 10 to 30 mg/s.

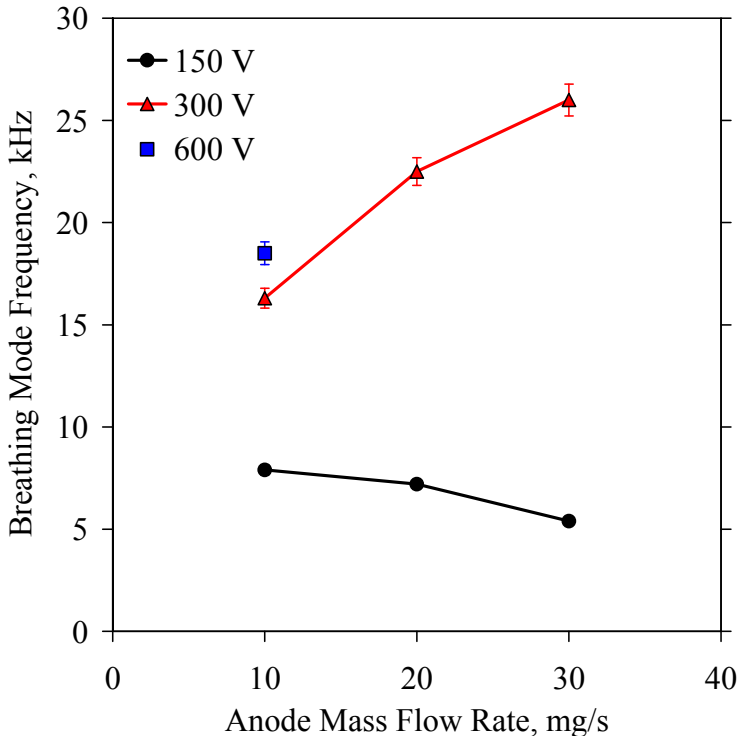

Figure 6-2. Breathing mode frequency for thruster operation from 150 to 600 V and 10 to 30 mg/s.

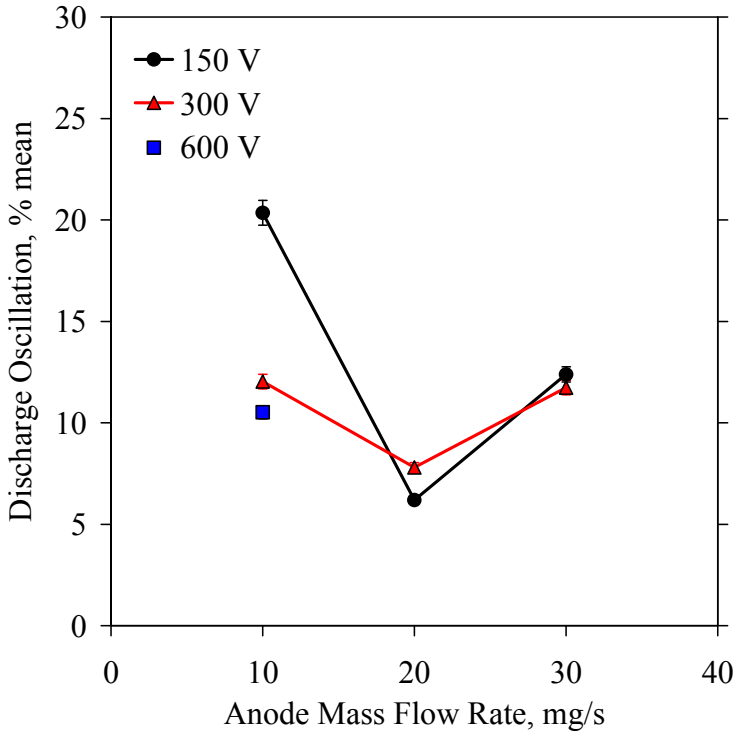

Figure 6-3. Discharge oscillation in percent of mean for thruster operation from 150 to 600 V and 10 to 30 mg/s.

Table 6-1: Summary of results from discharge current oscillations analysis.

V_D, V	$\dot{m}_a$, mg/s	Discharge Oscillation Amplitude, % $I_{D,\,mean}$	Breathing Mode Frequency, kHz
150	10	20	7.9
	20	6.2	7.2
	30	12	5.4
300	10	12	16
	20	7.8	23
	30	12	26
600	10	11	19

The variation of the discharge oscillation with operating condition can be estimated using the "predator-prey" model presented by Fife *et al.* [29]

$$f_B = \frac{\sqrt{\Delta u_a u_n}}{2\pi L_a}, \tag{6-15}$$

where u_n is the neutral velocity, Δu_a is the ion velocity change across the acceleration region, and L_a is the length of the acceleration region. The breathing mode oscillation frequency increased with discharge voltage at constant mass flow rate with $\sqrt{V_D}$ dependence. This trend was consistent with Eq. 6-15 since the discharge voltage was directly proportional to Δu_a. The breathing mode frequency increased with anode mass flow rate at 300 V with $\sqrt{\dot{m}_a}$ dependence. This trend was consistent with Eq. 6-15 since the neutral velocity increased with mass flow rate (see Section 3.7.3). Furthermore, results in Section 7.3 indicated that the acceleration region became more compact as anode flow rate was increased; hence, L_a decreased, leading to higher oscillation frequency.

The oscillation frequency decreased with flow rate at 150 V, which directly opposed the trend at 300 V and the scaling in Eq. 6-15. This deviation likely occurred since the thruster did not operate as well at 150 V as it did at 300 V. The mechanisms responsible for the deviation from the scaling in Eq. 6-15 are not yet well understood and require further study.

The standard deviation of the discharge oscillations at each operating condition is shown in Figure 6-3 as a percentage of the mean discharge current. These data indicated that the oscillation amplitude fraction decreased with increased discharge voltage at constant mass flow rate. In addition, the oscillation amplitude reached a minimum at the nominal mass flow rate of 20 mg/s for 150

and 300 V. This trend was consistent with the measured ion current density fluctuations reported in Section 5.5.3.

The dependence of the discharge current on the discharge voltage is shown in Figure 6-4 for anode flow rates of 5, 10, 20, and 30 mg/s with dashed lines that represent boundaries of constant power from 1.5 to 9.0 kW. The discharge current consistently decreased as discharge voltage was increased from 150 to 300 V at all flow rates. As the discharge voltage increased from 300 to 600 V, the discharge current increased.

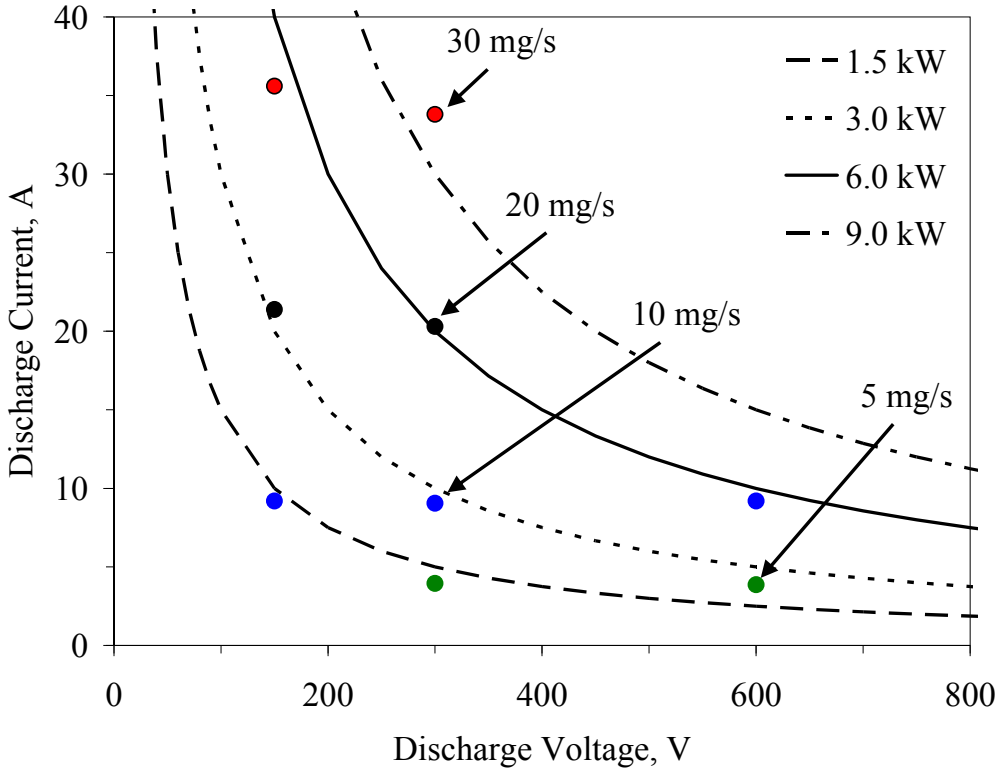

Figure 6-4. Discharge current versus discharge voltage for anode flow rates from 5 to 30 mg/s.

6.3 Performance

Results are presented for discharge voltages of 150, 300, and 600 V and anode flow rates of 5, 10, 20, and 30 mg/s. Measurements were recorded without the internal trim coil energized and the magnet settings were optimized for optimum efficiency for a constant vacuum magnetic field shape that was symmetric about channel centerline. The trim coil was not energized so that results could be directly compared to simulations in HPHALL-2, which can not model magnetic field topologies produced by the trim coil. The constant magnetic field shape was chosen as a means of controlling variables with the added benefit of streamlining comparisons with results from HPHALL-2. Omitting the inner trim coil and maintaining constant magnetic field shape each contributed to a loss of approximately 1% in total efficiency (total loss of 2% efficiency in absolute terms).

The performance measurements in this chapter were limited to measurements that were taken after approximately 220 hours of thruster operation. Additional performance data taken at the beginning of life ($<$ 40 hours of runtime) from 150 to 400 V at 20 mg/s are included in Appendix A. The erosion and performance parameters change with thruster lifetime; volumetric erosion rates decrease within the first several hundred hours of operation [147] and total efficiency tends to decrease by a 1-2% in absolute terms [148, 149].

A systematic characterization of the facility effects (neutral entrainment and CEX collisions) on performance parameters is reported in Appendix B; using this methodology the "vacuum"-corrected discharge current was lower than the measured discharge current by 2-3% and the "vacuum"-corrected thrust dropped by approximately 1%. The combined effect of the "vacuum" corrections produced a net change in anode efficiency of less than 0.5% (in absolute terms). The relative change was less than 0.1%, which was insufficient to appreciably change the magnitude or trends of the data. Based on these results, the performance parameters were not corrected for facility effects.

6.3.1 Thrust

Results for measured thrust are shown in Figure 6-5 for thruster operation from 150 to 600 V and 5 to 30 mg/s. The uncertainty in thrust was approximately ± 2 mN. The thrust increased linearly with flow rate, a result that was expected from the dependence in Eq. 6-12. At constant flow rate, the thrust increased with discharge voltage, which was expected since the ion acceleration was proportional to $\sqrt{V_D}$ as shown in Eq. 6-12.

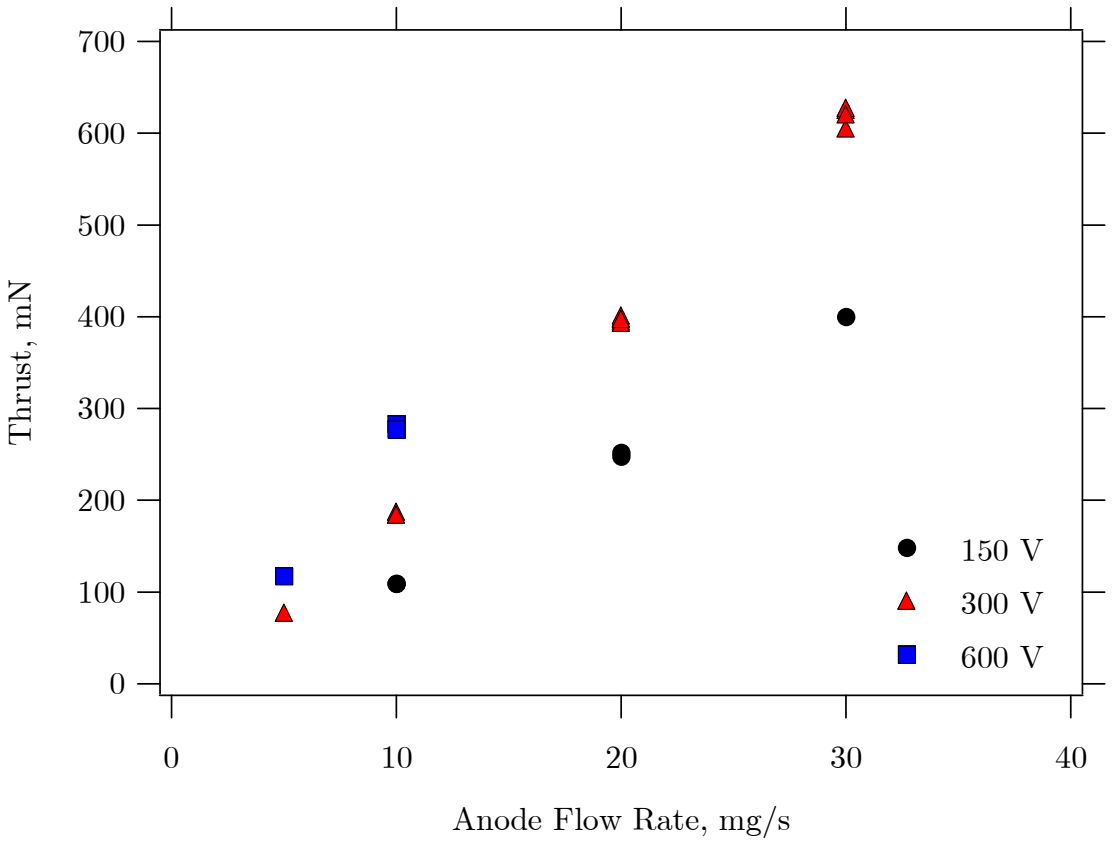

Figure 6-5. Measured thrust for operation at 150-600 V and 5-30 mg/s.

6.3.2 Total Specific Impulse

Results for the total specific impulse are shown in Figure 6-6. At a fixed mass flow rate the specific impulse increased with discharge voltage. This result was expected since the specific impulse was proportional to the exhaust velocity ($u_e \sim \sqrt{V_D}$) as shown in Eq. 6-14. The specific impulse also increased with anode mass flow rate at all voltages, although the increase was less pronounced. This behavior is somewhat universal in the operation of Hall thrusters, following the same trend for a host of Hall thrusters that were designed for high voltage (SPT-1 [150]) or high power operation (NASA 400M [147]) with the result extending to

include TALs (D80 [151]). Typically, this behavior is attributed to increased propellant utilization [26] since the ion production rate is proportional to the neutral density ($\dot{n}_i \sim n_n$, see Section 8.1.1).

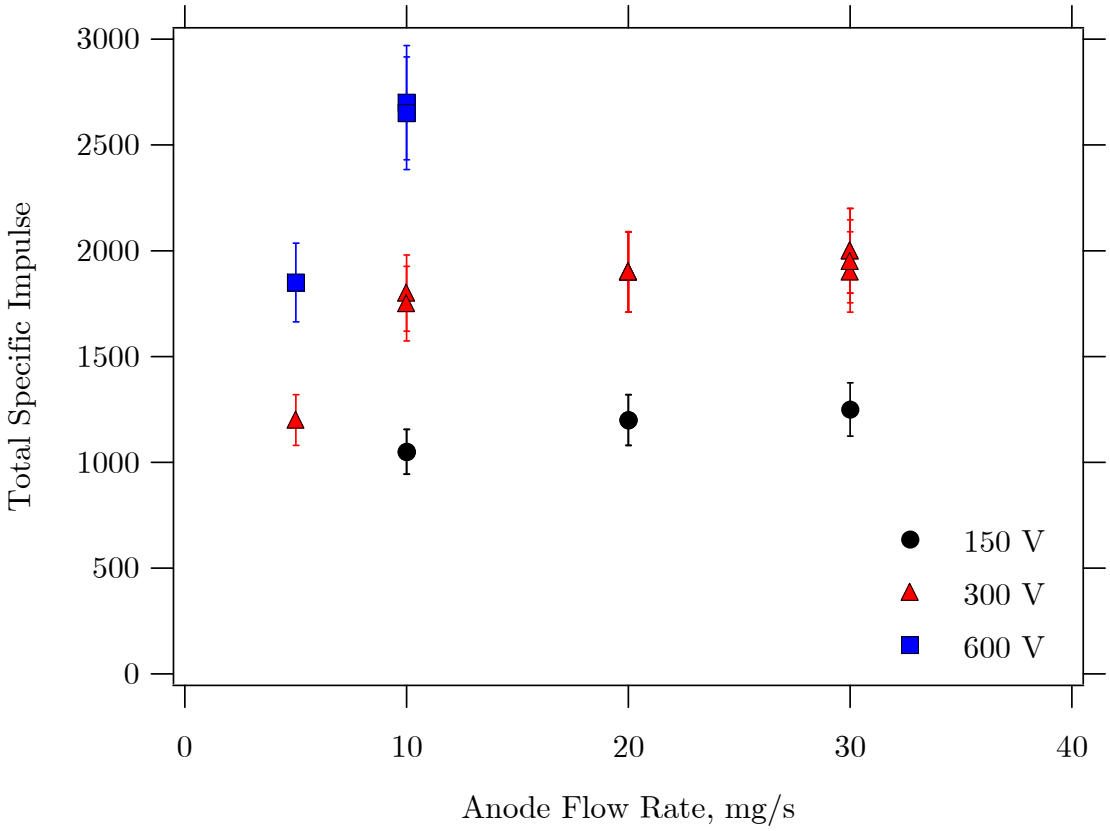

Figure 6-6. Total specific impulse for operation at 150-600 V and 5-30 mg/s.

6.3.3 Total Efficiency

Results for the total efficiency as a function of flow rate are shown in Figure 6-7. For a fixed flow rate, the efficiency consistently increased with discharge voltage; a result that was noted in previous performance measurements in the literature [152]. The primary reason for increased efficiency with discharge voltage is was due to improved beam collimation. At 300 V, the efficiency was constant from 10 to 30 mg/s. This result was unexpected since efficiency typically

increases with flow rate [152], similar to the trend shown at 150 V and 10, 20, and 30 mg/s. As flow rate is increased, the propellant utilization typically increases since the ion production rate is directly proportional to the neutral density, which is proportionally to mass flow rate ($\dot{n}_i \sim n_n \sim \dot{m}$, see Section 8.1.1). As discussed in Section 6.4, the propellant utilization remained constant and decreases in current utilization were balanced by increased divergence utilization. A large contribution to the drastic decrease in total efficiency at 5 mg/s for both 300 and 600 V was the 14% cathode flow fraction (nominal is 7%) that was needed to maintain stable cathode operation without the aid of heater or keeper currents.

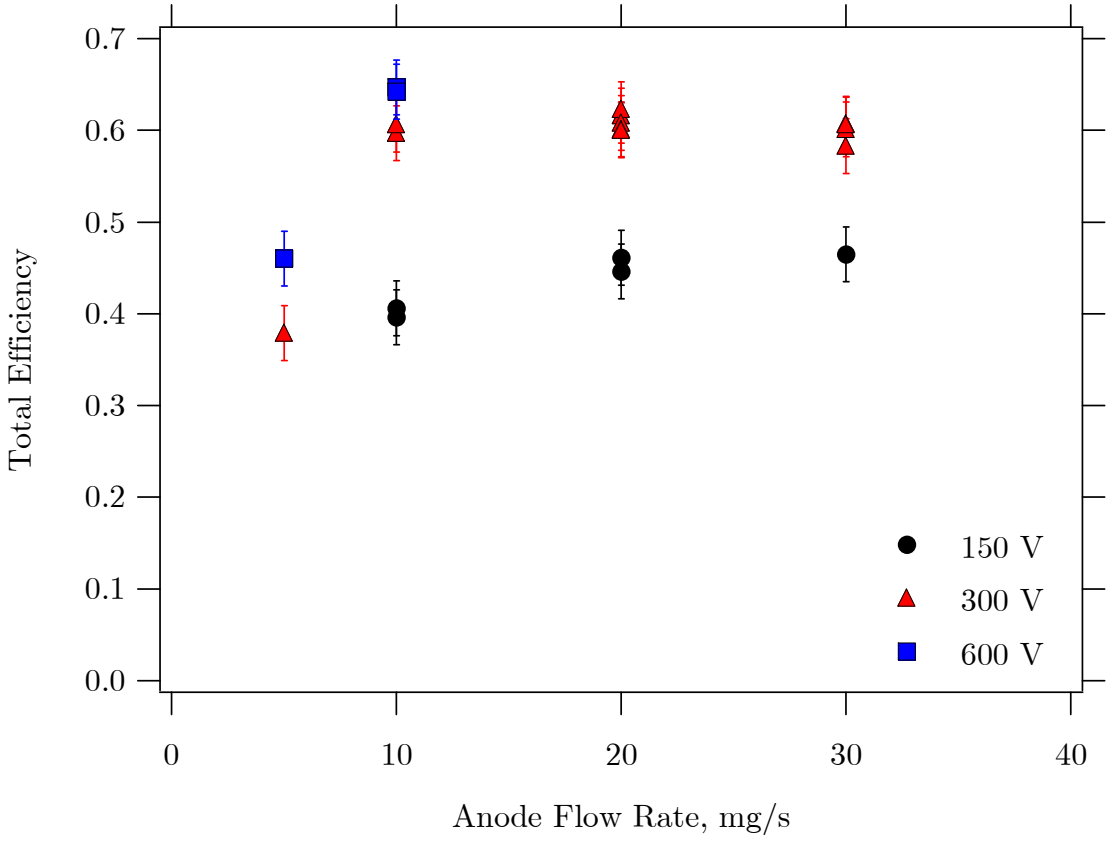

Figure 6-7. Total efficiency for operation at 150-600 V and 5-30 mg/s.

6.3.4 Thrust-to-Power

The thrust-to-power ratio is typically considered in the spacecraft design stage, allowing trajectory simulations to optimize the mission plan based on the available power and resultant thrust produced by the propulsion subsystem. Results for the total thrust-to-power ratio are shown in Figure 6-8. The thrust-to-power ratio appeared to peak at approximately 10 mg/s at 300 V. This was consistent with previous work that noted thrust-to-power maximized at low current densities [144, 145, 153]. The lack of data at 150 and 600 V prevented a similar conclusion at these operating conditions.

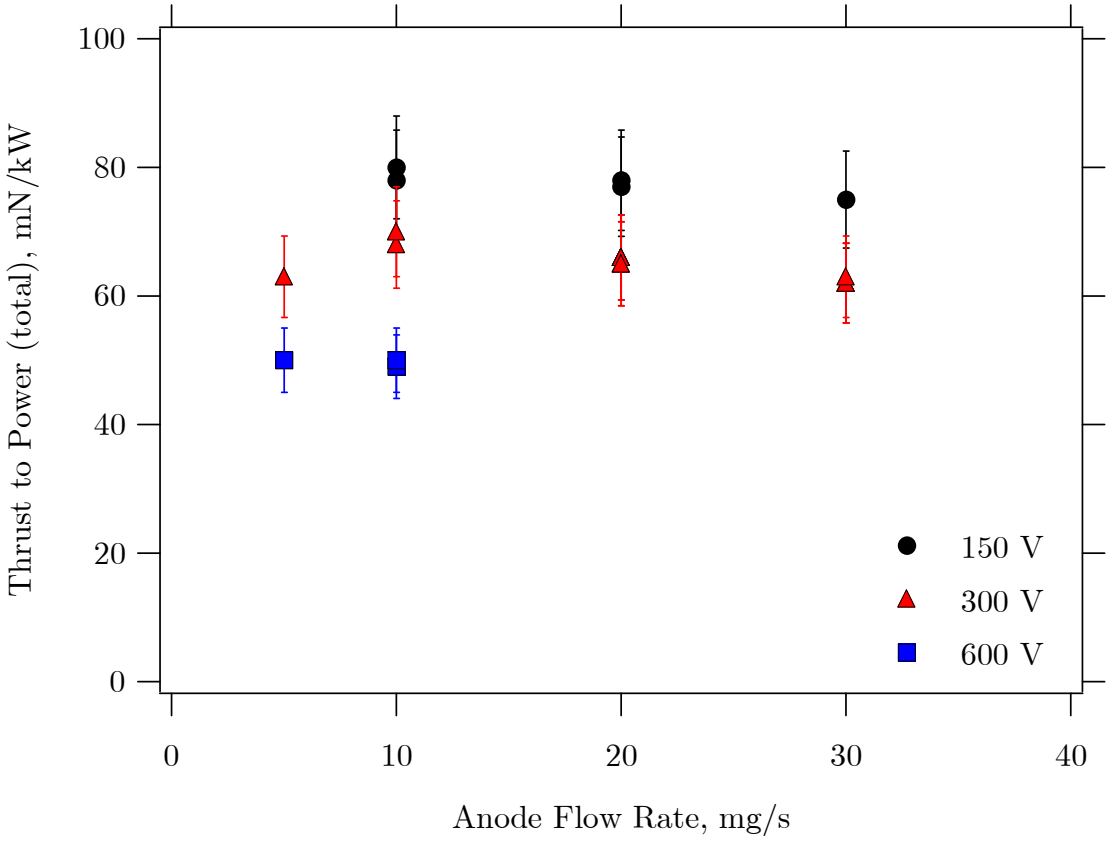

Figure 6-8. Thrust-to-power ratio for operation at 150-600 V and 5-30 mg/s.

6.4 Utilization Efficiencies

The individual utilization efficiencies were calculated using the plume-measured plasma properties summarized in Table 5-2. The results of the efficiency analysis for thruster operation at 300 V and 10, 20, and 30 mg/s are shown in Figure 6-9 and the individual utilizations are summarized in Table 6-2. There was exceptional agreement between the measured and calculated efficiencies, especially considering the uncertainties of ± 3 and ± 10%, respectively. The uncertainties in individual utilizations were omitted from the figure for clarity. The relatively large uncertainty in the calculated efficiency was due to the compounded uncertainties from each of the plasma measurements.

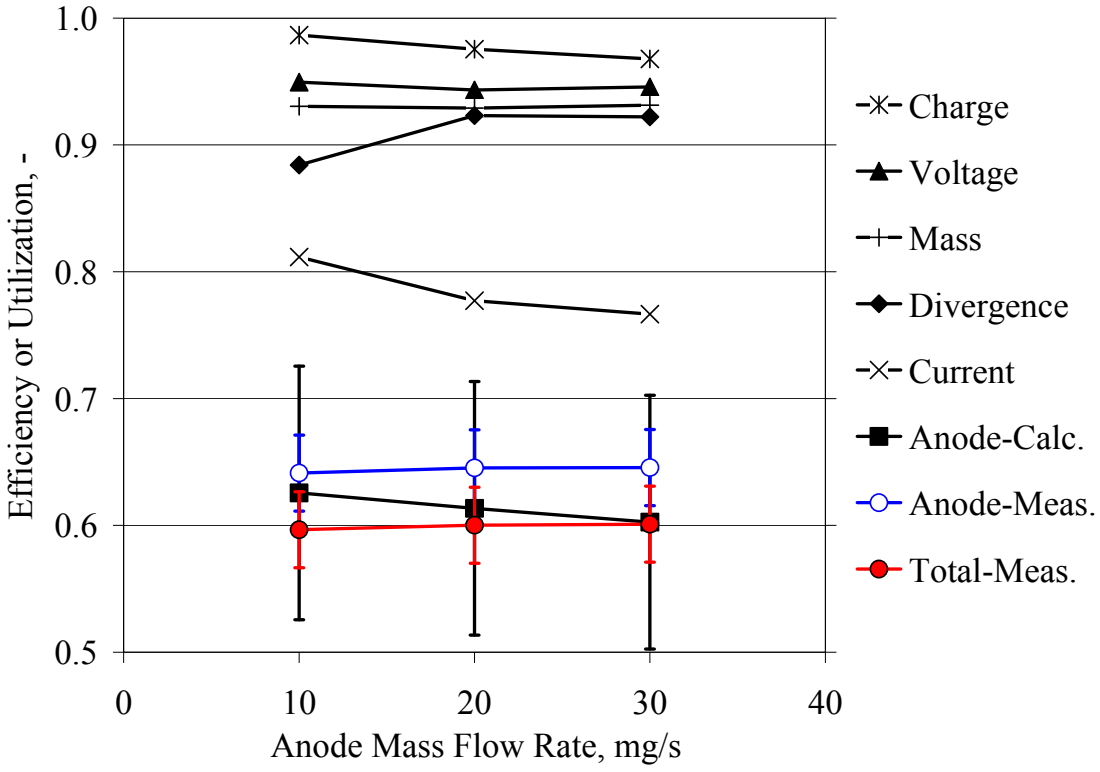

Figure 6-9. Measured and computed thruster efficiency and individual utilization efficiencies for thruster operation at 300 V and 10, 20, and 30 mg/s.

6.5 Discussion

Overall, the performance of the 6-kW Hall thruster meets or exceeds that of comparable high-performance Hall thrusters. Several preliminary hypotheses for this excellent performance are listed in order of expected influence:

1) **Centrally Mounted Cathode**. Placing the cathode on thruster centerline was shown to decrease the cathode coupling voltage and decrease divergence losses [106, 140]. The combined effect was an increase in thruster efficiency of approximately 2-3% (absolute).

2) **High-Performance Anode**. When compared to the NASA-173M and P5 Hall thrusters, the 6-kW Hall thruster anode significantly improved the radial and azimuthal uniformity, while decreasing the axial velocity by greater than 42%. These improvements are expected to increase thruster efficiency, stability, and thermal margin [26, 35-39].

3) **Increased Channel Width**. The 6 kW Hall thruster has a discharge channel that is approximately 20% wider than the P5 or NASA-173M, which decreases the influence of the walls [14]. This effect is expected to be small compared to the anode and cathode contributions.

4) **Increased Magnetic Field Uniformity**. The magnetic field has been shown to significantly affect thruster performance [26]. Although the magnetic field topography is not significantly different from previous designs, several

minor improvements were implemented [13]. This effect is expected to be small compared to anode and cathode contributions.

The constant efficiency from 10 to 30 mg/s shown in Figure 6-9 was produced by a combination of utilizations that were constant at all flows and others that opposed each other. In particular, the voltage and mass utilizations were constant from 10 to 30 mg/s, and the divergence utilization increased in direct opposition to the decreased charge and current utilizations.

The constancy of the voltage utilization from 10 to 30 mg/s was consistent with several important parameters during operation. First, the cathode operated nearly the same for each operating condition (same flow rate fraction and floating potential). This behavior was likely due to the constant flow fraction of 7%, which resulted in cathode potentials that varied by less than 1 V between operating conditions. Second, the anode sheath maintained a consistent anode fall direction and magnitude. This conjecture is supported by RPA measurements that indicated ions achieved the same acceleration potential (see Section 5.3 where the most-probable voltage varied by less than 2 V from 10 to 30 mg/s). In addition, plasma potential measurements showed that the plasma potential near the ion density peak was approximately constant across all three flow rates (see Section 7.3.3).

The constancy of the mass utilization was produced by the combination of increased discharge current per unit flow rate (referred to as the exchange ratio,

$\xi \sim I_D / \dot{m}_a$) and decreased charge utilization. The discharge current per unit flow rate increased due to decreased current utilization (i.e., increased electron current recycle fraction). The current utilization decreased with flow rate due to higher electron mobility within the channel due to increased electron-neutral and electron-wall collisions (see Chapter 8 for further discussion of electron mobility). As flow rate was increased, the electron-wall collision frequency also increased, contributing to higher near-wall conductivity and electron current to the anode. Further discussion of classical collision rates and total Hall parameter are included in Chapter 8. The charge utilization decreased due to an increased fraction of multiply-charged ions that were created by an increased ion-to-neutral density ratio (see Section 5.1).

The current utilization can be estimated based on thrust stand, RPA, and E×B measurements using

$$I_B = T\sqrt{\frac{Ze}{2m_{xe}V_{accel}}}, \tag{6-16}$$

which was derived by combining a modified form of Newton's second law ($T = \dot{m}u$) with an equation for charge flux ($I_i = n_i Z e u_i A$). A similar analysis was proposed in Ref. [26]. The current utilization produced by this calculation was 0.76, 0.74, and 0.73 at 300 V and 10, 20, and 30 mg/s, respectively. This followed the same trend as the values measured by the near-field Faraday probe; however, the magnitude was approximately 0.04 lower than the measured values, and the difference between each flow rate was smaller than the measured decrease. The

difference in current utilization magnitude is not as important as the change between each flow rate, which changes the trend in mass utilization. Using the beam current derived from Eq. 6-16 caused the mass utilization trend to change from constant with flow rate (η_m = 0.93 from 10 to 30 mg/s) to increasing with flow rate (η_m = 0.87, 0.89, and 0.88 at 10, 20, and 30 mg/s, respectively). Although the beam current calculated with Eq. 6-16 is merely an estimate of the true beam current, this comparison may indicate that the beam current was underestimated by the near-field Faraday probe measurements by a larger amount as flow rate was increased.

The increased divergence utilization (beam collimation) with flow rate was unexpected, but confirmed by two separate Faraday probe measurement techniques (see Sections 5.4 and 5.5). Internal plasma measurements (see Sections 7.2 Langmuir Probe and 7.3 Floating Emissive Probe) indicated that as flow rate was increased, the primary ionization and acceleration occurred further downstream. This behavior is typically associated with *increased* plume divergence losses since ions are expected to be created in a defocused electric potential that causes ion to be accelerated away from the axial direction (primary force direction). However, the plasma potential results in Section 7.3 indicated an expansive region of very flat plasma potential that allowed ions to be accelerated with primarily axial trajectories over a wide range of axial locations. A potential cause for the decrease in plume divergence is creation of ions closer to channel

centerline. Near the inner and outer radii, the potential profiles tend to sharply turn towards the radial direction as shown in Figure 5-12. By concentrating the ions towards channel center where the profiles exhibited a smaller radial component, the ions were effectively focused along channel centerline. The concentration of ions towards centerline was loosely supported by internal ion density measurements in Section 7.2.4. These measurements indicated an increase in peak density that was larger than the difference in flow rate, especially at 30 mg/s. This slightly non-linear relationship between peak ion density and flow rate was consistent with the suggestion of increased ion concentration towards channel centerline.

The values of electron recycle fraction, beam divergence, and voltage utilization shown in Figure 6-9 were consistent with the values that were reported in Ref. [154]. Those values were determined based on qualitative graphical analysis of performance parameters including thrust-to-power and specific impulse. The good agreement between the methods indicates that many of the individual utilizations can be accurately estimated using graphical analysis of performance data. This method can offer a wealth of insight into the details of thruster operation without the expense of deploying a full suite of diagnostics. This method could be particularly useful in examining published data for a wide range of thrusters, many of which do not have corresponding plume measurements.

In Section 6.3.2 the specific impulse increased monotonically with anode flow rate, a result that was consistent with several previous sets of data [26, 153]. However, the suggestion that the increase was due to increased mass utilization was not consistent with the results in Figure 6-9 that indicated mass utilization remained constant from 10 to 30 mg/s. In this case, the increase in specific impulse was entirely due to the decrease in charge utilization. As the charge utilization decreased, the fraction of multiply-charged ions increased. As shown in Eq. 6-14, the specific impulse is directly proportional to the ion charge state and hence, specific impulse increased.

The calculated efficiency at 5 mg/s (not shown) fell off drastically due to decreased mass, current, and divergence utilizations. The elevated cathode flow fraction (14% rather than 7% nominal) was partially responsible for the decreased efficiency since most of the cathode flow is not ionized and accelerated to produce thrust. The current utilization likely dropped due to increased bulk electron temperature that was achieved due to a lack of electron-neutral collisions. These hot electrons were more likely to collide with the channel walls and migrate towards the anode, while producing additional SEE that further contributed to the increased electron current.

6.6 Summary of Efficiency Analysis Findings

By combining the plasma properties that were measured in the plume, the mechanisms that contributed to efficiency losses were identified. The measured

and computed anode efficiencies were in good agreement and the thruster maintained a total efficiency of 60% from 10 to 30 mg/s (± 50% of its nominal operating condition, ranging in discharge power from 3 to 10 kW). The primary efficiency loss mechanism at each operating condition was due to current utilization (electron current lost to the anode). The current utilization dropped monotonically from 0.81 at 10 mg/s to 0.77 at 30 mg/s. To maintain constant total efficiency, the loss in current utilization was compensated for by an increase in divergence utilization.

Although thruster efficiency remained constant from 10 to 30 mg/s, the efficiency dropped off significantly at 5 mg/s. A portion of this deficit was due to decreased mass utilization owing to the increased cathode flow fraction (14% instead of nominal 7%); however, the primary reasons were due to decreased current and divergence utilizations.

Table 6-2: Summary of results from efficiency analysis.

300 V	10 mg/s	20 mg/s	30 mg/s
Charge Utilization	0.99	0.98	0.97
Voltage Utilization	0.95	0.94	0.95
Divergence Utilization	0.88	0.92	0.92
Current Utilization	0.81	0.78	0.77
Mass Utilization	0.93	0.93	0.93
Anode Efficiency – Calculated	0.626	0.613	0.603
Anode Efficiency – Measured	0.641	0.645	0.646
Total Efficiency – Measured	0.597	0.600	0.601

Chapter 7

Internal Measurements

To complement the comprehensive plume measurements of Chapter 5 that were used in the phenomenological performance model in Chapter 6, plasma properties were measured inside the discharge channel. The goal of these measurements was to characterize the ionization and acceleration processes inside the thruster to gain additional insight into the mechanisms that affect thruster operation as a function of injected mass flow rate.

7.1 Probe-Induced Perturbations

Probe-induced thruster perturbations were characterized by examining the discharge current and cathode potential during probe insertion and removal from the discharge channel. The probe position, discharge voltage, and discharge current are shown in Figure 7-1 for thruster operation at 300 V and 10 mg/s. The nominal discharge current oscillation amplitude was approximately ± 20% of the mean, reaching a maximum of ± 40% at the channel exit and a minimum of approximately ± 5% when the probe was inside the channel. The data in Figure

7-1 were similar to the probe-induced perturbations at 20 and 30 mg/s and were consistent with previous work [51, 109, 122].

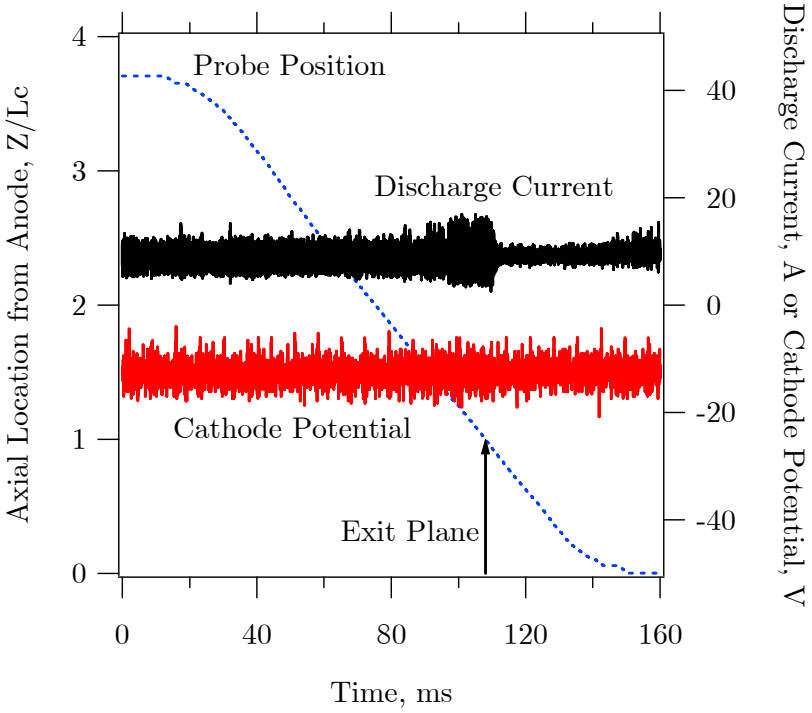

Figure 7-1. Probe induced perturbations of discharge current and cathode potential during probe insertion at 300 V and 10 mg/s.

The magnitude of the perturbations was not only a function of axial location within the thruster but also of radial location. The R-Z dependence of the discharge current and cathode potential perturbations are shown in Figure 7-2 for thruster operation at 300 V and 10 mg/s. The perturbations represent the macroscopic response of the thruster when the probe is at a particular location in the channel or near-field plume. Perturbations are shown as percent fluctuation about the mean (100 × amplitude/mean) during emissive probe measurements. The results were remarkably similar for Langmuir probe results and thus, are not repeated here.

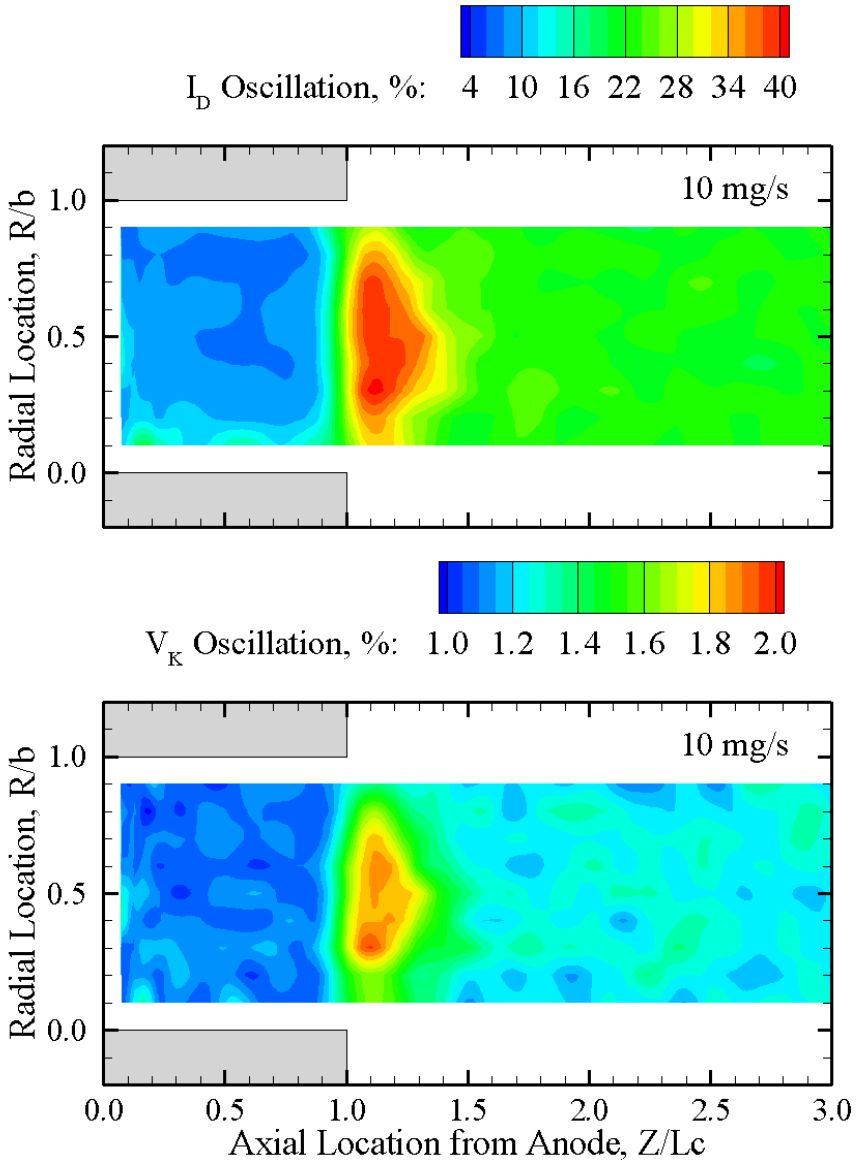

Figure 7-2. Discharge current and cathode potential perturbations throughout the measurement domain for thruster operation at 300 V and 10 mg/s.

The magnitude of the discharge perturbations was highest downstream of the channel exit. The high electric field in this region was caused an effective "short" of the plasma across the emissive probe loop. This same behavior was observed for the Langmuir probe measurements and the overall results were consistent with those of Haas [109] and Linnell [51]. The cathode potential

oscillations were highly correlated with the discharge current oscillations. However, the 1-2% variation in the magnitude of the potential oscillations was significantly lower than the 4-40% variation for the discharge current.

The magnitude of the discharge current perturbations decreased drastically inside the channel, eventually dropping below the unperturbed value. The primary cause for this behavior was attributed to the release of secondary electrons due to collisions of the Hall-current electrons with the probe surface. The probe surface effectively releases electrons that are trapped in E×B motion, allowing them to migrate across magnetic field lines at a higher rate than at nominal conditions. A similar explanation of the variation in discharge oscillations due to plasma-probe interactions was presented in Ref. [109].

The contribution of collisions of Hall-current electrons with the probe surface was estimated by calculating the flux of azimuthal electrons to the probe surface. The results indicated that approximately 2-4 A could be released from the Hall current. The amount of emission was strongly dependent on the radial location, primarily due to the ion density variation with radial location (see Section 7.2.4), which was consistent with the radial variation in the discharge current fluctuations in Figure 7-2.

The effect of SEE from the probe surface can be reduced by using low SEE materials like carbon graphite [155]. Since graphite is a conductive material, it causes excessive discharge perturbations if not configured as alternating ringlets

with a ceramic material. This configuration breaks the conductive path that leads back to facility ground. The construction of these probes is not highly repeatable and a previous investigation indicated the inability of this material to withstand the harsh environment within a Hall thruster [51].

7.2 Langmuir Probe

The Langmuir probe used in this study was described in Section 4.9.2. The primary goal of the Langmuir probe measurements was to determine the ion density and electron temperature throughout the measurement domain. The floating potential was also determined from the probe characteristics and the results were used in conjunction with the emissive probe results in Section 7.3.

7.2.1 Fluctuations in Plasma Properties

The fluctuation of collected current due to thruster discharge oscillations is shown in the raw I-V trace in Figure 7-3. The probe was located approximately 360% L_c downstream from the anode (well beyond primary acceleration region) for thruster operating conditions of 300 V and 10 mg/s. The I-V trace in Figure 7-3 is accompanied by the discharge current and cathode potential, which are correlated with the fluctuation in the collected current of the I-V trace. This I-V trace was analyzed as three distinct I-V characteristics; the upper bound of the I-V fluctuations, lower bound of the I-V fluctuations, and smoothed (mean) characteristics. When analyzed separately, the floating potential and ion saturation remained constant, while the plasma potential and electron

temperature varied by less than 2 V and 1 eV, respectively. Since the electron temperature was approximately 5 eV at this location, the variation can range from 20-50%. This level of variation was consistent across operating condition and location within the domain. Additional uncertainty was encountered for traces near the Hall current where I-V traces become more difficult to interpret due to signal noise. Those data sets are not readily analyzed as three distinct I-V traces; instead, they are only analyzed using the mean of the I-V trace.

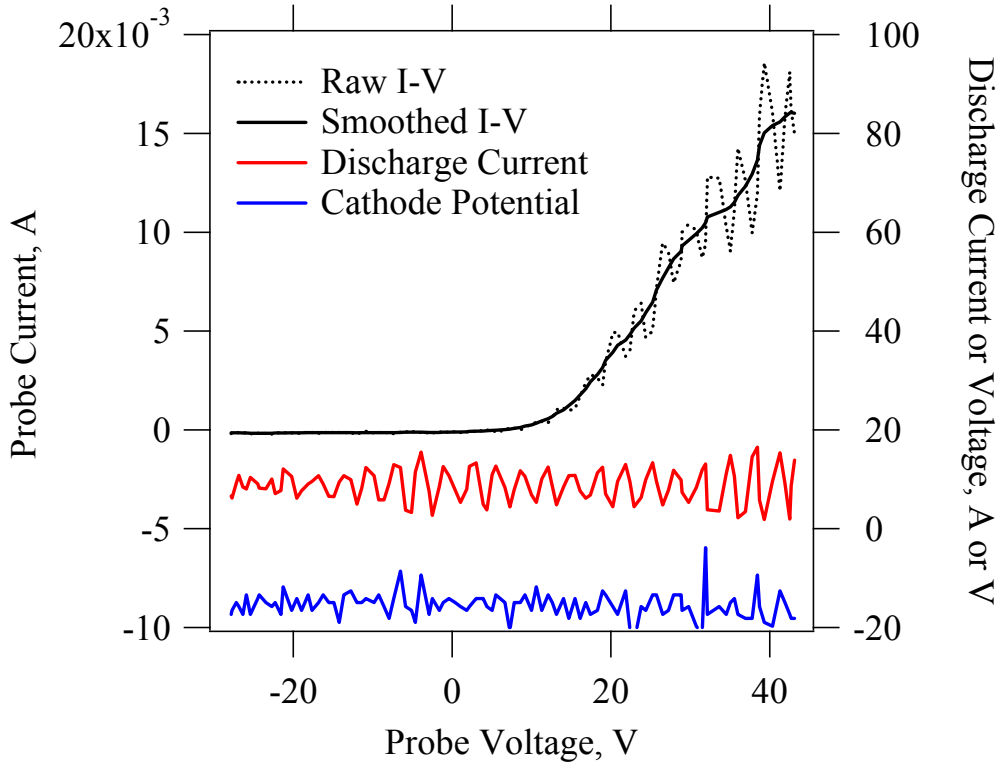

Figure 7-3. Langmuir probe I-V trace, discharge current, and cathode potential at 360% L_c from the anode for thruster operation at 300 V and 10 mg/s.

7.2.2 Floating Potential

The floating potential was similar in shape to the plasma potential and its location of maximum slope occurred 10-20% L_c upstream of the maximum slope

of the plasma potential (Section 7.3.3). The spatial separation of the plasma potential and floating potential was consistent with the increased electron temperature inside the channel. A comparison of the floating potential with respect to cathode on channel centerline is shown in Figure 7-4 for operation at 300 V and 10, 20, and 30 mg/s. The three profiles were similar in shape; however, the floating potential inside the channel at 30 mg/s was 10-20 V below the potential at 10 and 20 mg/s. This deficit in floating potential was attributed to additional noise at 30 mg/s that caused increased uncertainty in the analysis.

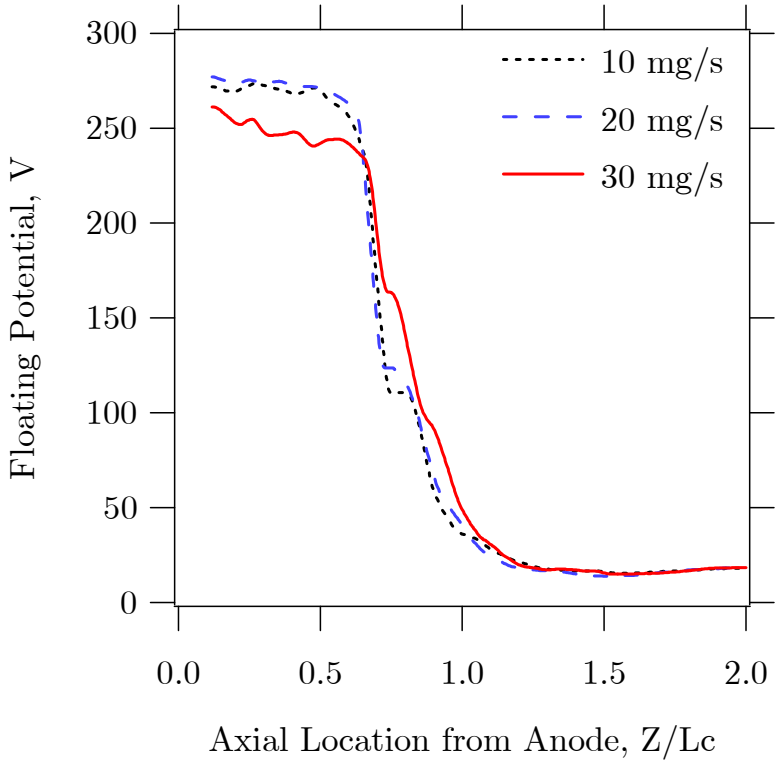

Figure 7-4. Comparison of floating potential with respect to cathode on channel centerline for thruster operating conditions of 300 V and 10, 20, and 30 mg/s.

7.2.3 Electron Temperature

Results for the electron temperature throughout the measurement domain are shown in Figure 7-5 for thruster operation at 300 V and 10, 20, and 30 mg/s. The electron temperature was somewhat variable across the channel, which accounts for most of the irregularity in the ion density calculations that are presented in Section 7.2.4. The electron temperature peaked at approximately 38, 35, and 25 eV at 10, 20, and 30 mg/s, respectively. The trend of decreased electron temperature with flow rate was consistent with results from Haas [109] that showed a peak electron temperature of 40 and 30 eV at 300 V and 5 and 10 mg/s, respectively. Experimental measurements by Fife [28] also agree with this trend, showing peak electron temperatures in the near-field plume ($<$ 20 mm from exit plane) of approximately 8.3, 8.0, and 7.8 eV at thruster operating conditions of 300 V and 1.17, 1.76, and 2.34, mg/s, respectively.

Although stated without proof for now, the reason for the trend of decreased electron temperature with flow rate was primarily due to increased electron impacts with the channel wall (wall losses), with inelastic (electron-neutral) collision playing a secondary role (see Section 8.6.2).

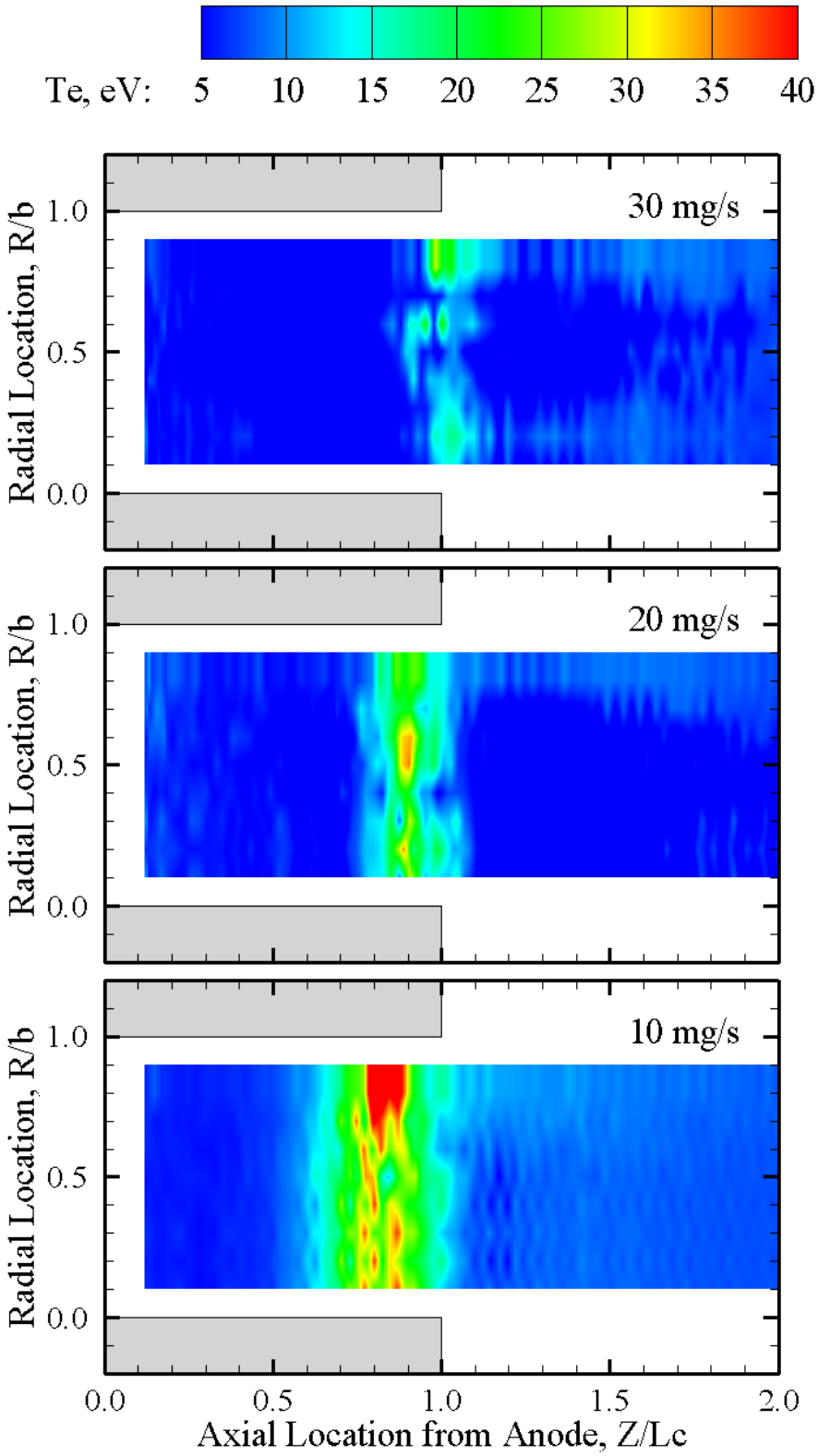

Figure 7-5. Electron temperature measured by the Langmuir probe for thruster operation at 300 V and 10, 20, and 30 mg/s.

The peak electron temperature moved downstream with each addition of anode flow rate, occurring at approximately 86, 90, and 98% L_c, at 10, 20, and 30 mg/s, respectively. This result was due to increased electron-neutral collisions within the channel that is discussed further in Sections 7.4 and 8.3. For added clarity, a comparison of the electron temperature on channel centerline is shown in Figure 7-6. The data were somewhat irregular, but the trend with flow rate was apparent; the peak electron temperature decreased and the peak location moved downstream as flow rate was increased. The centerline comparison in Figure 7-6 is loosely representative of the entire channel since the electron temperature was approximately isothermal across the channel (see Figure 7-5).

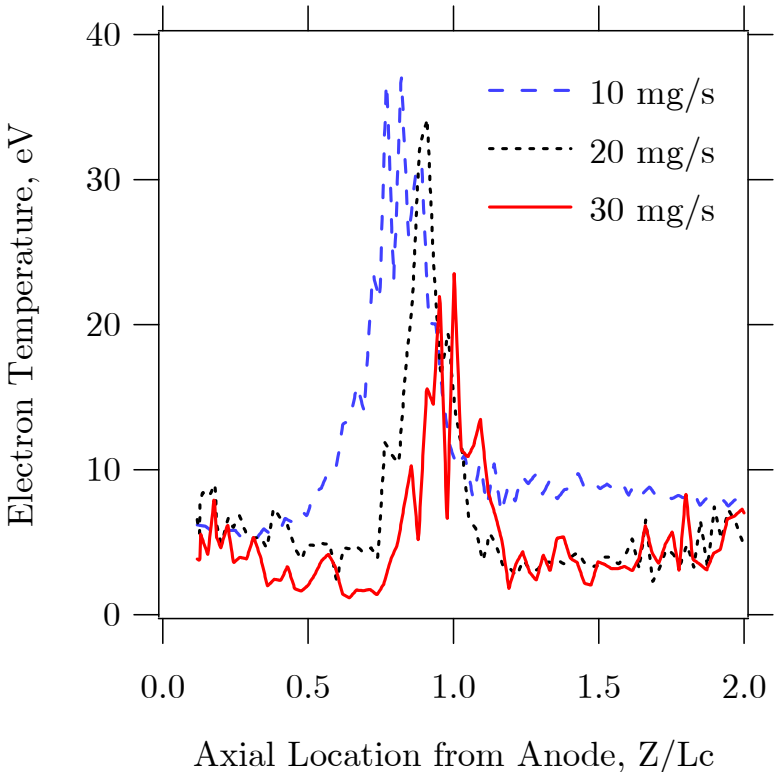

Figure 7-6. Comparison of electron temperature calculated by the Langmuir probe on channel centerline for thruster operating conditions of 300 V and 10, 20, and 30 mg/s.

7.2.4 Ion Number Density

The ion density was separately calculated for thin sheath and OML assumptions and combined into a "blended" ion density based on the recommendation of Chen [111] that analysis techniques be chosen based on the value of R_p/λ_D; for $R_p/\lambda_D < 3$, the OML analysis was chosen and for $R_p/\lambda_D > 10$, the thin sheath analysis was chosen. In between these two bounds an R_p/λ_D weighted average was implemented. The blended ion density is used throughout the remainder of the text unless otherwise stated.

The calculated R_p/λ_D for 300 V and 10, 20, and 30 mg/s are shown in Figure 7-7 at all radial locations as a function of distance from the anode. At 10 mg/s, R_p/λ_D ranged from 2 to 6, indicating probe operation in the OML and transitional regime between OML and thin sheath. At 20 mg/s, R_p/λ_D ranged from 4 to 12, indicating probe operation primarily in the transitional regime. At 30 mg/s, R_p/λ_D ranged from 5 to 22, indicating thin sheath dominated probe operation.

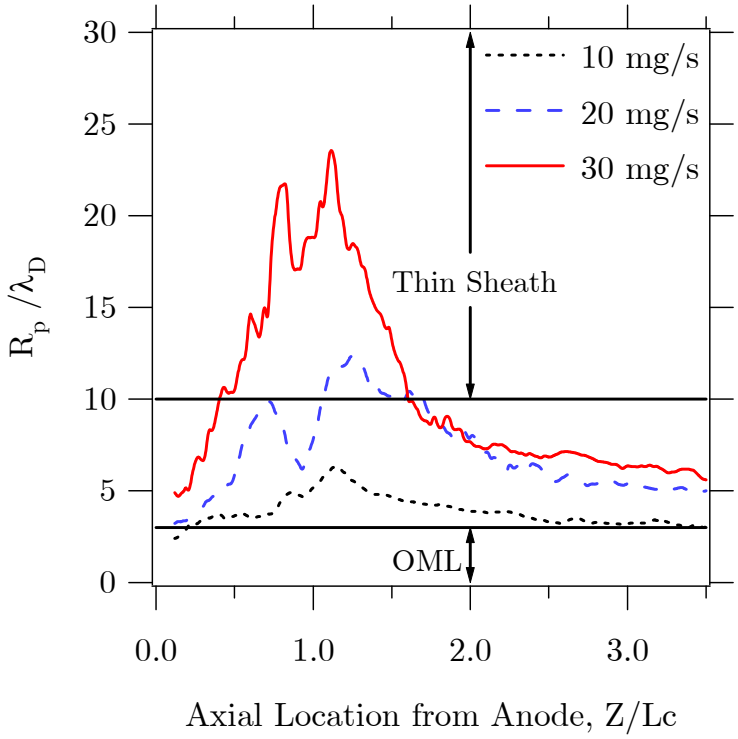

Figure 7-7. R_p/λ_D for thruster operation at 300 V and 10, 20, and 30 mg/s.

The thin sheath, OML, and blended ion densities are shown separately throughout the measurement domain at each operating condition in Figure 7-8, Figure 7-9, and Figure 7-10, respectively. The OML ion number density was highly symmetric about channel centerline, peaking at approximately 2, 4, and 9×10^{18} m^{-3} at 300 V and 10, 20, and 30 mg/s, respectively. The thin sheath density exhibited more non-uniformity throughout the domain due to the non-uniform electron temperature. The thin sheath ion density peaked at approximately 1, 4, and 15×10^{18} m^{-3}, exhibiting reasonable agreement with the peak OML ion density considering the $>$ 50% estimated uncertainty for each calculation. The blended number density peaked at approximately 2, 4, and 15×10^{18} m^{-3} at 300 V and 10, 20, and 30 mg/s.

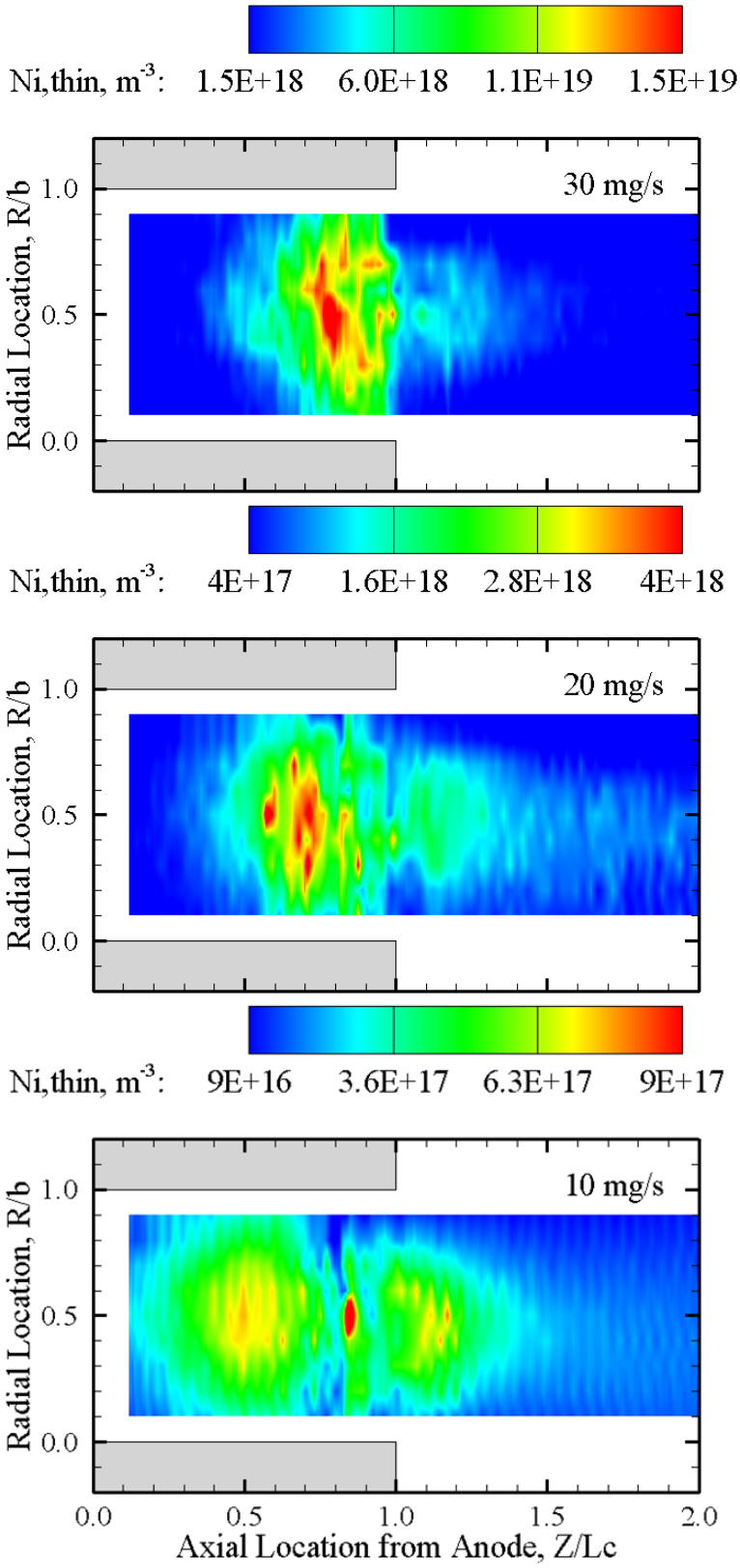

Figure 7-8. Thin sheath ion density measured by the Langmuir probe for thruster operation at 300 V and 10, 20, and 30 mg/s.

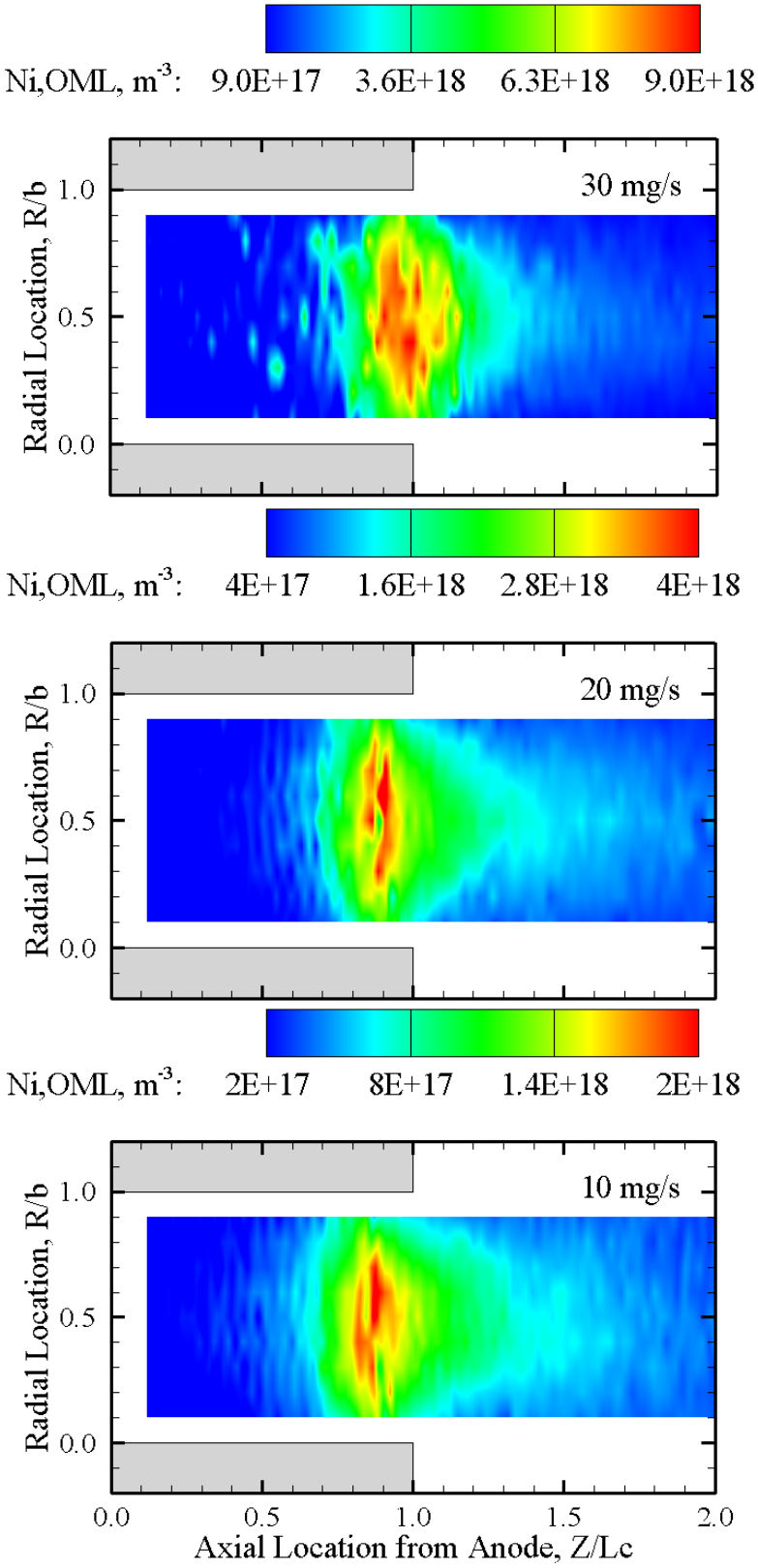

Figure 7-9. OML ion density measured by the Langmuir probe for thruster operation at 300 V and 10, 20, and 30 mg/s.

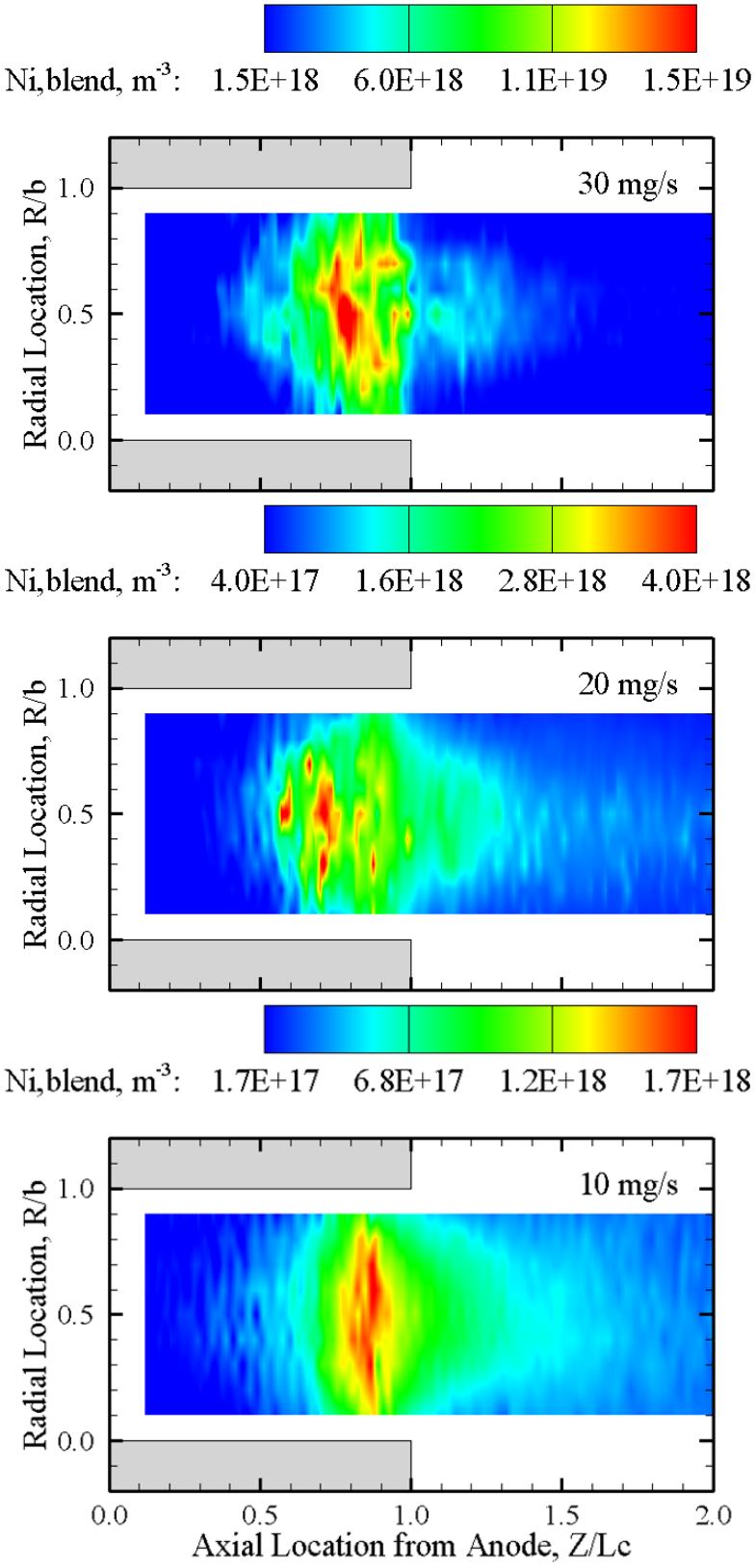

Figure 7-10. Blended ion density measured by the Langmuir probe for thruster operation at 300 V and 10, 20, and 30 mg/s.

The peak ion density magnitude at 10 mg/s was compared with two similar size thrusters operating at 300 V and 10 mg/s. These measurements indicated peak ion densities of 3×10^{18} m^{-3} [51] and 1×10^{18} m^{-3} [109], which were well-correlated with the present peak density of 2×10^{18} m^{-3}. In general, the ion density was expected to be directly proportional to the anode mass flow rate. Using the ion density at 10 mg/s as a starting point, linear scaling with flow rate produces ion densities that are expected to be approximately 2-4 and 3-6$\times10^{18}$ m^{-3} at 20 and 30 mg/s, respectively. The data at 20 mg/s agreed well with this linear scaling; however, the peak density at 30 mg/s was a factor of two to three greater than expected. This deviation from the linear relationship could indicate increased production of ions (higher propellant utilization), increased thermionic emission of electrons that leads to artificially high ion saturation currents (in magnitude), or some other unknown source of uncertainty. Considering the ion flux produced by the product of ion density and ion velocity (taken from plasma potential) a 1-D current continuity analysis indicated that the ion density may have been overpredicted by as much as 2-300% (see Section 8.2.1). The potential inaccuracy due to thermionic emission is considered in Section 7.4 and does not appear to be a major contribution. Another contribution to the deviation from the linear relationship with flow rate may have been due to a more compact ionization region. By creating ions over a smaller axial or radial domain, the peak density increased accordingly. This hypothesis was loosely supported by the

results in Section 7.4.1.1 that indicated that the ionization region became more compact in the axial direction as flow rate was increased.

A comparison of thin sheath, OML, and blended ion densities on channel centerline is shown in Figure 7-11, Figure 7-12, and Figure 7-13 for thruster operation at 300 V and 10, 20, and 30 mg/s. The data were somewhat irregular, but the trend of increased peak ion density with increased mass flow rate was apparent for all three ion density calculations. The OML and thin sheath ion densities both exhibited a clear downstream displacement of the peak density with increased flow rate. The OML peak ion density was located at 87, 92, and 100% L_c at 10, 20, and 30 mg/s, respectively. The thin sheath peak ion density was located at 52, 72, and 73% L_c at 10, 20, and 30 mg/s, respectively. This trend was not as pronounced with blended data, likely due to the offset of approximately 15-20% L_c between the OML and thin sheath densities that are combined to produce the blended density. The blended peak ion density was located at 74, 74, and 87% L_c at 10, 20, and 30 mg/s, respectively.

The OML and thin sheath ion density analysis techniques were reasonably well correlated in terms of shape and peak magnitude, especially at lower flow rates. The biggest difference between the two analysis methods was the peak density location. The OML density peaked approximately 2% L_c upstream of the peak electron temperature, whereas the thin-sheath density peaked at an average of 15% L_c upstream.

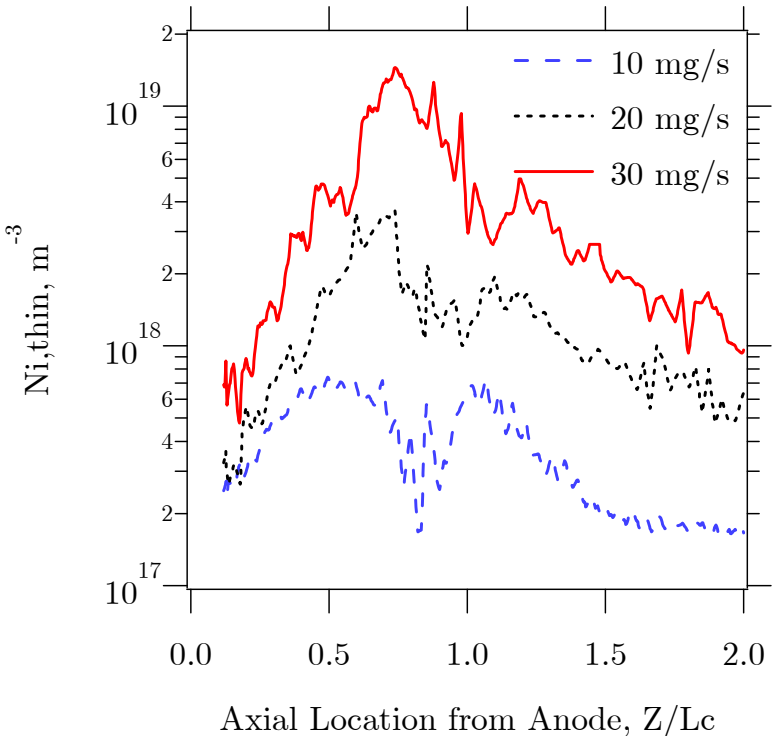

Figure 7-11. Centerline comparison of ion number density for thin sheath analysis at 300 V and 10, 20, and 30 mg/s.

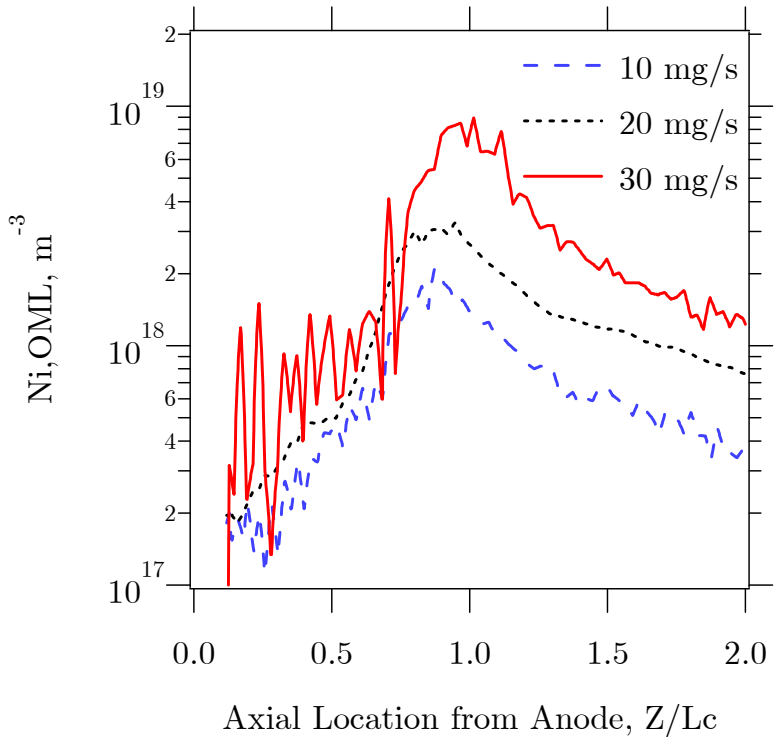

Figure 7-12. Centerline comparison of ion number density for OML analysis at 300 V and 10, 20, and 30 mg/s.

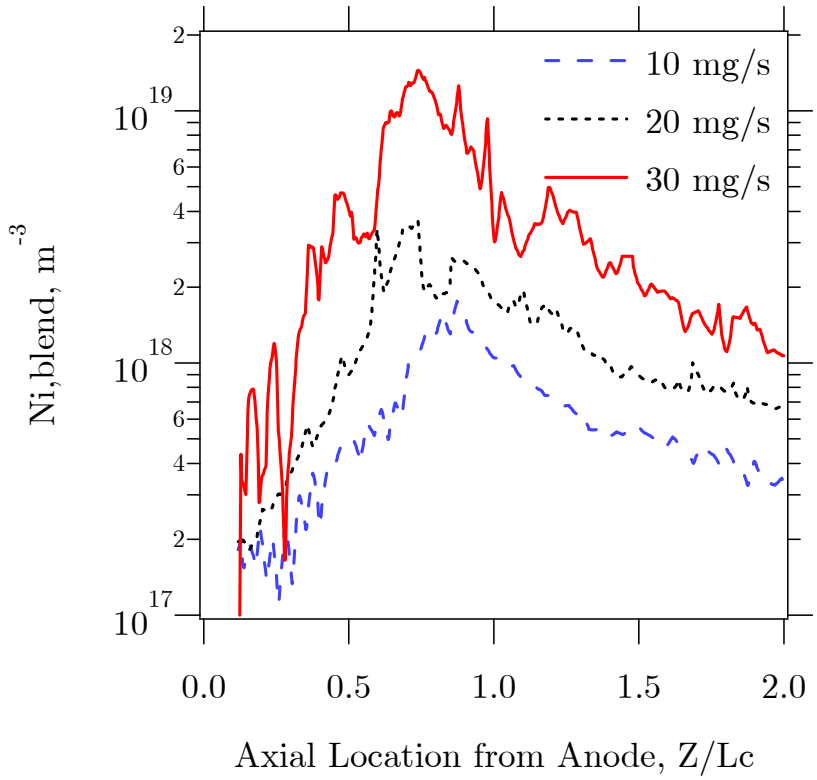

Figure 7-13. Centerline comparison of ion number density for blended analysis at 300 V and 10, 20, and 30 mg/s.

7.3 Floating Emissive Probe Results

The emissive probe used in this study was described in Section 4.9.3. The primary goal of the emissive probe measurements was to determine the plasma potential throughout the measurement domain so that the ion acceleration process could be investigated. The electron temperature was also calculated using the floating potential results from Section 7.2.2.

Due to the intense probe heating at the 300 V and 30 mg/s operating condition (~10 kW), the probe filament was unable to survive repeated sweeps into the thruster. The only available set of data was collected at thruster centerline. Although plasma potential data were not available across the entire

channel at 30 mg/s, the electron temperature was still calculated based on the difference between the centerline plasma potential and the floating potential across the channel. All plasma potential measurements were referenced to cathode potential.

7.3.1 Electron Temperature

The electron temperature was calculated by using the potential difference between the plasma and floating potentials given by Eq. 4-22. This calculation required knowledge of the plasma potential from the floating emissive probe and the floating potential, which was taken from the Langmuir probe measurements of Section 7.2. Since the floating potential is geometry dependent, there can be appreciable uncertainty introduced by combining the results from the Langmuir and emissive probes (which have drastically different geometry, see Sections 4.9.2.1 and 4.9.3.1). Any uncertainty associated with the geometry was deemed acceptable in this situation since the electron temperature calculation from the emissive probe is typically considered a gross estimate. Similar comparisons between Langmuir probe and emissive probe electron temperatures have been performed in previous studies [51, 156].

The electron temperature measured throughout the measurement domain with the emissive probe is shown in Figure 7-14. When compared with the Langmuir probe results, the emissive probe electron temperature was much more uniform across the channel, more widespread along the channel, and increased in

peak value with increased mass flow rate. The uniformity across the channel can be a strong indicator of isothermal electrons. The trend of increased electron temperature measured by the emissive probe opposed that of the Langmuir probe results; however, less credence is placed with the emissive probe trend based on the assumptions and large uncertainty in the calculations. The centerline electron temperature determined by the emissive probe is shown in Figure 7-15 for thruster operation at 300 V and 10, 20, and 30 mg/s. The emissive probe electron temperature peaked at approximately 28, 38, and 42 eV at 10, 20, and 30 mg/s, respectively. Similar to the Langmuir probe, the peak electron temperature location moved downstream with each addition of anode flow rate. The peak electron temperature occurred at 79, 90, and 93% L_c at 10, 20, and 30 mg/s, respectively. These locations were consistent with the Langmuir probe measurements at 10 and 20 mg/s (81 and 90% L_c, respectively), but the Langmuir probe peak electron temperature location (100% L_c) was 7% L_c downstream of the emissive probe peak electron temperature location.

The emissive probe peak electron temperature was relatively high and since the analysis did not account for the effects of high-energy ions, may be less reliable, especially at higher ion densities. Furthermore, less credence was placed in the emissive probe electron temperature since it was derived from two data points rather than the 10's of points used in Langmuir probe analysis. For these

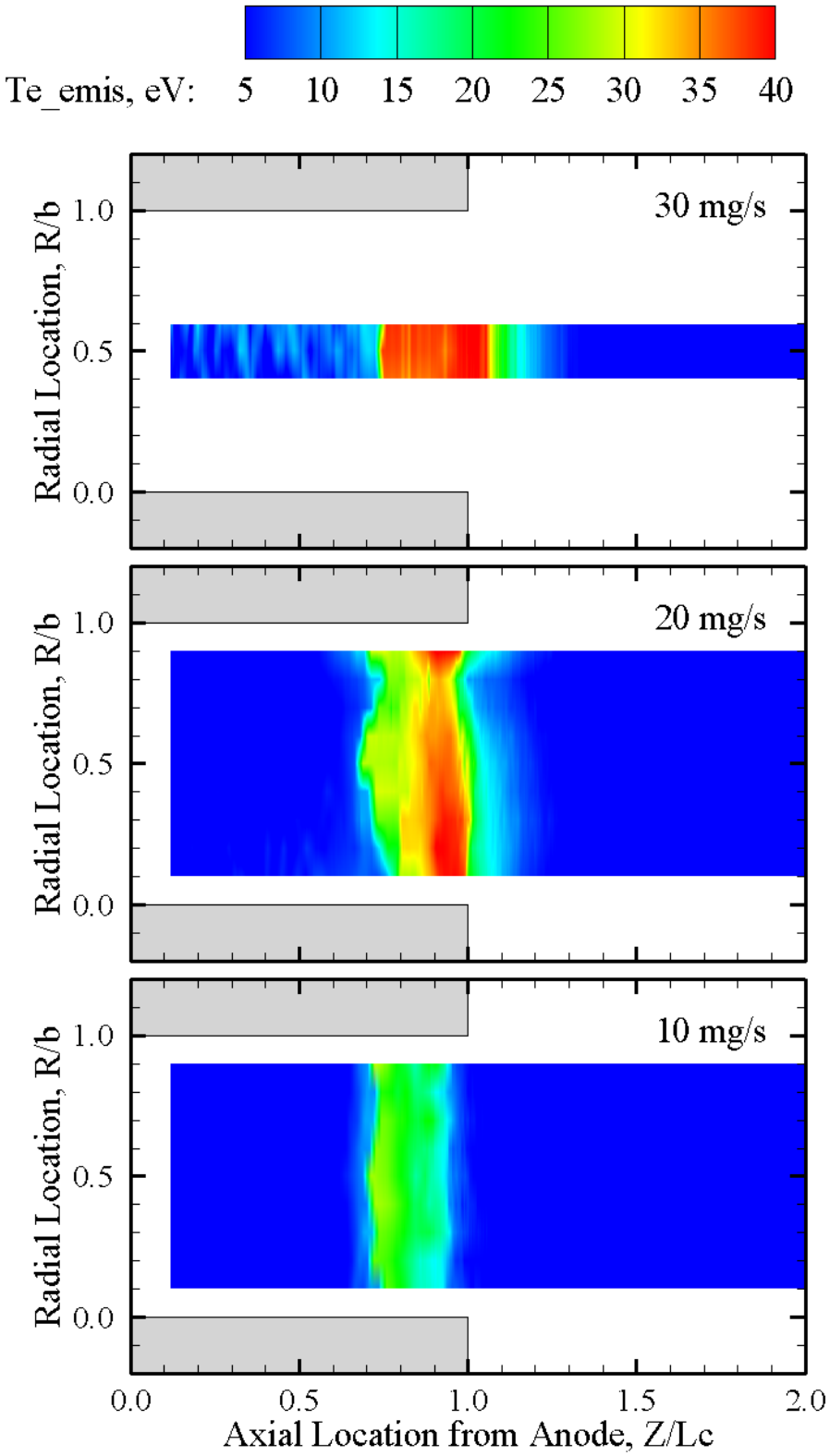

Figure 7-14. Electron temperature from emissive probe for thruster operation at 300 V and 10, 20, and 30 mg/s.

reasons, the electron temperature derived from emissive probe measurements will not be used in further analyses.

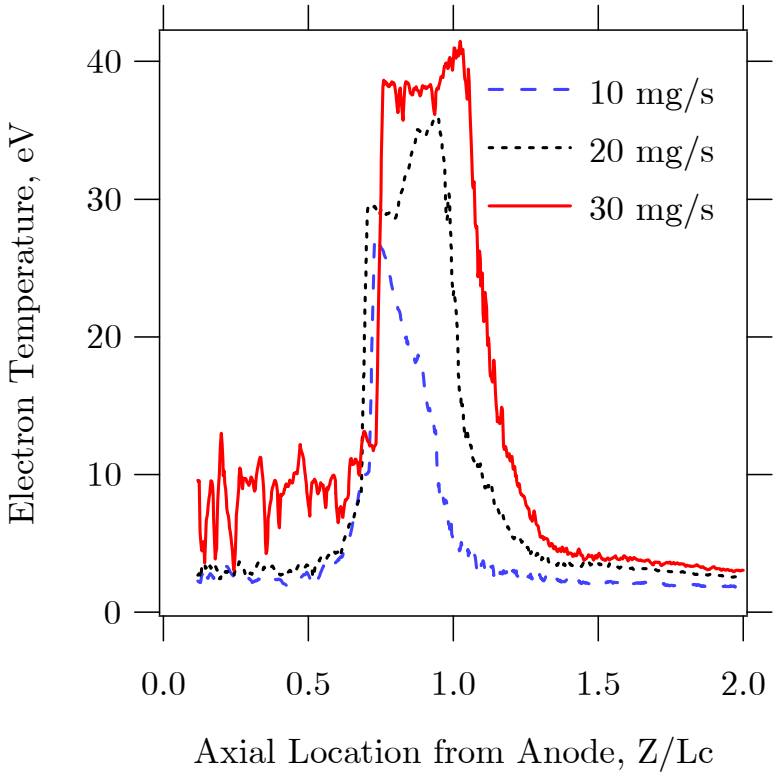

Figure 7-15. Emissive probe electron temperature on channel centerline at 300 V and 10, 20, and 30 mg/s.

7.3.2 Plasma Potential Fluctuations

Since emissive probe measurements of the plasma potential were collected at 83 kHz, fluctuations in the plasma potential were correlated to the discharge current oscillations which ranged from 15 to 25 kHz (see Section 6.2). The distinct correlation between peak plasma potential (with respect to cathode) and peak discharge current is shown in Figure 7-16 for thruster operation at 300 V and 10 mg/s. The probe was located on channel centerline at approximately 10% L_c from the anode. The plasma potential displayed a phase delay of 30-40 μs,

likely due to the ion transit time, sampling delays, or cable length that were not explicitly accounted for in these measurements. Another lower frequency discharge oscillation (1-5 kHz), which is attributed to the "spoke mode instability" [30], was observed in the discharge current and plasma potential measurements. Although instantaneous plasma potential measurements were recorded, the time-averaged results were used throughout this dissertation (except where noted).

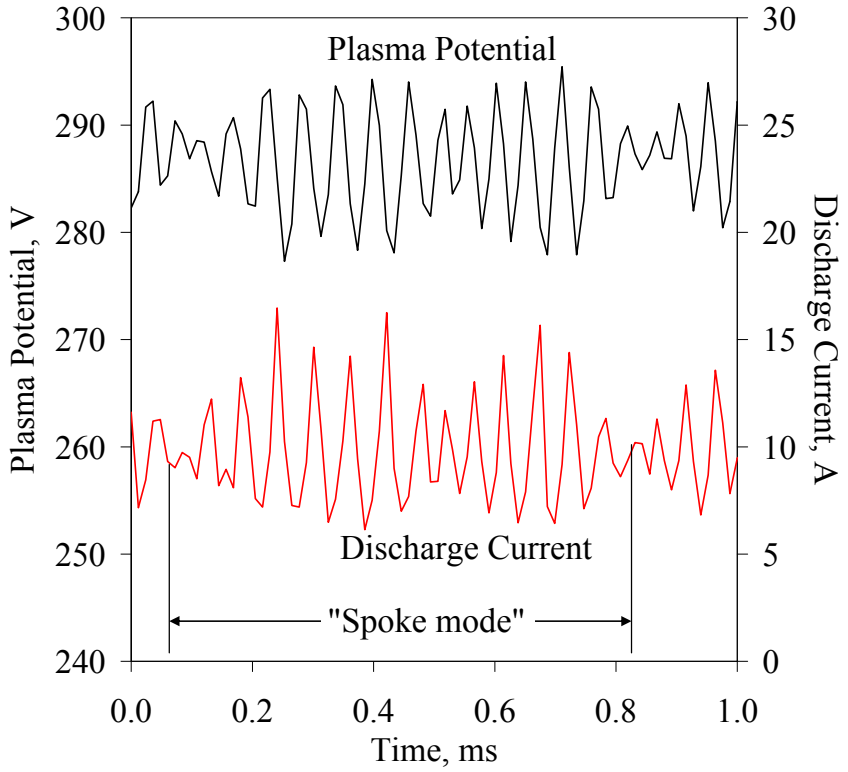

Figure 7-16. Time-dependent correlation between plasma potential and discharge current oscillations on channel centerline and 10% L_c from the anode during thruster operation at 300 V and 10 mg/s.

Plasma potential oscillations were measured at each point throughout the measurement domain and these data are shown in Figure 7-17. The plasma potential oscillations, reported as the amplitude about the mean, peaked

downstream of the exit plane in the same location as the peak discharge oscillation that was shown in Figure 7-2. The two oscillations were dependent upon each other and were caused by shorting of the plasma between the filament electrode in regions of high electric field. The dependence of the discharge current and plasma potential oscillations on the electric field was discussed in more detail in Ref. [109]. The peak plasma potential fluctuation was lower for 10 mg/s than for 20 and 30 mg/s, a result that was consistent with the magnitude of discharge current fluctuations during probe insertion.

A portion of the large potential oscillation near the exit plane is due to the inherent axial movement of the acceleration region. Movement on the order of 1 mm can cause plasma potential fluctuations on the order of a few tens of volts (see profile in Figure 7-20). Since the results presented here are time-averaged, oscillation of the acceleration region would be identified as an increase in plasma potential oscillation.

The displacement current produced by the fluctuation in plasma potential and hence, electric field was estimated using Ampere's law that states

$$\mu^{-1} \nabla \times \vec{B} = \vec{j} + \varepsilon \frac{\partial \vec{E}}{\partial t} \tag{7-1}$$

where μ is the permeability, ε is the permittivity, and j is the ion current density. The second term on the RHS of Eq. 7-1 (dielectric current density) can be estimated as 10^{-6} mA/cm^2 by assuming an oscillation frequency of 20 kHz ($dt =$

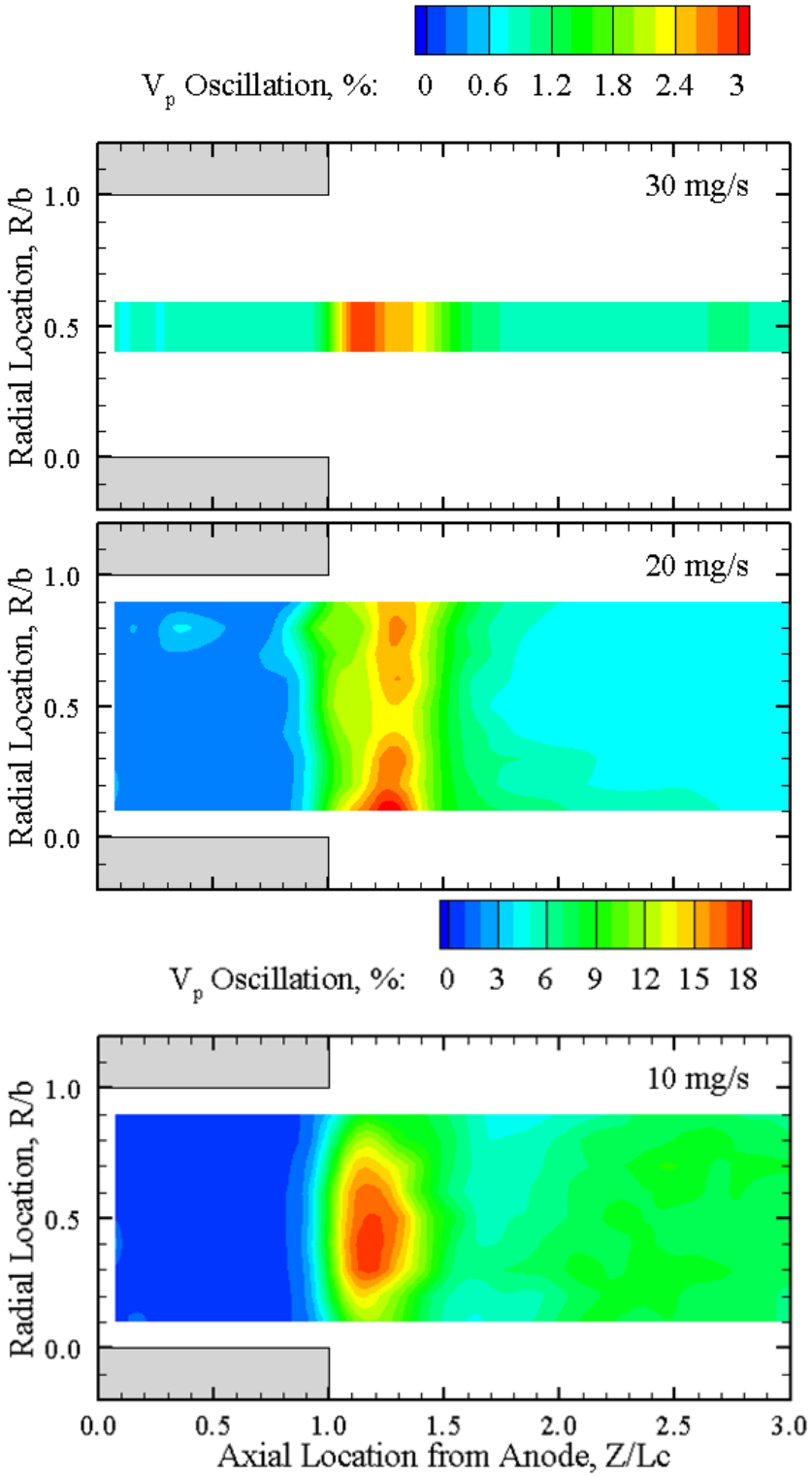

Figure 7-17. Plasma potential percent oscillation throughout the measurement domain for thruster operation at 300 V and 10, 20, and 30 mg/s.

5×10^{-5} s, see Section 6.2) and worst-case change in electric field of 100 V/mm. The first term on the RHS of Eq. 7-1 (ion current density) is on the order of 10^2 mA/cm^2 for most operating conditions. This comparison indicates that the dielectric current is several orders of magnitude smaller than the total ion current, a result that was noted in previous experimental and numerical reports [27, 157, 158].

7.3.3 Plasma Potential

Plasma potential measurements were corrected using Eq. 4-21 and the electron temperature from Langmuir probe measurements since it is more trusted and widely accepted than the emissive probe calculation. The corrected plasma potential with respect to cathode is shown in Figure 7-18 throughout the measurement domain for thruster operation at 300 V and 10, 20, and 30 mg/s. The plasma potential was highly uniform across the channel at all three operating conditions.

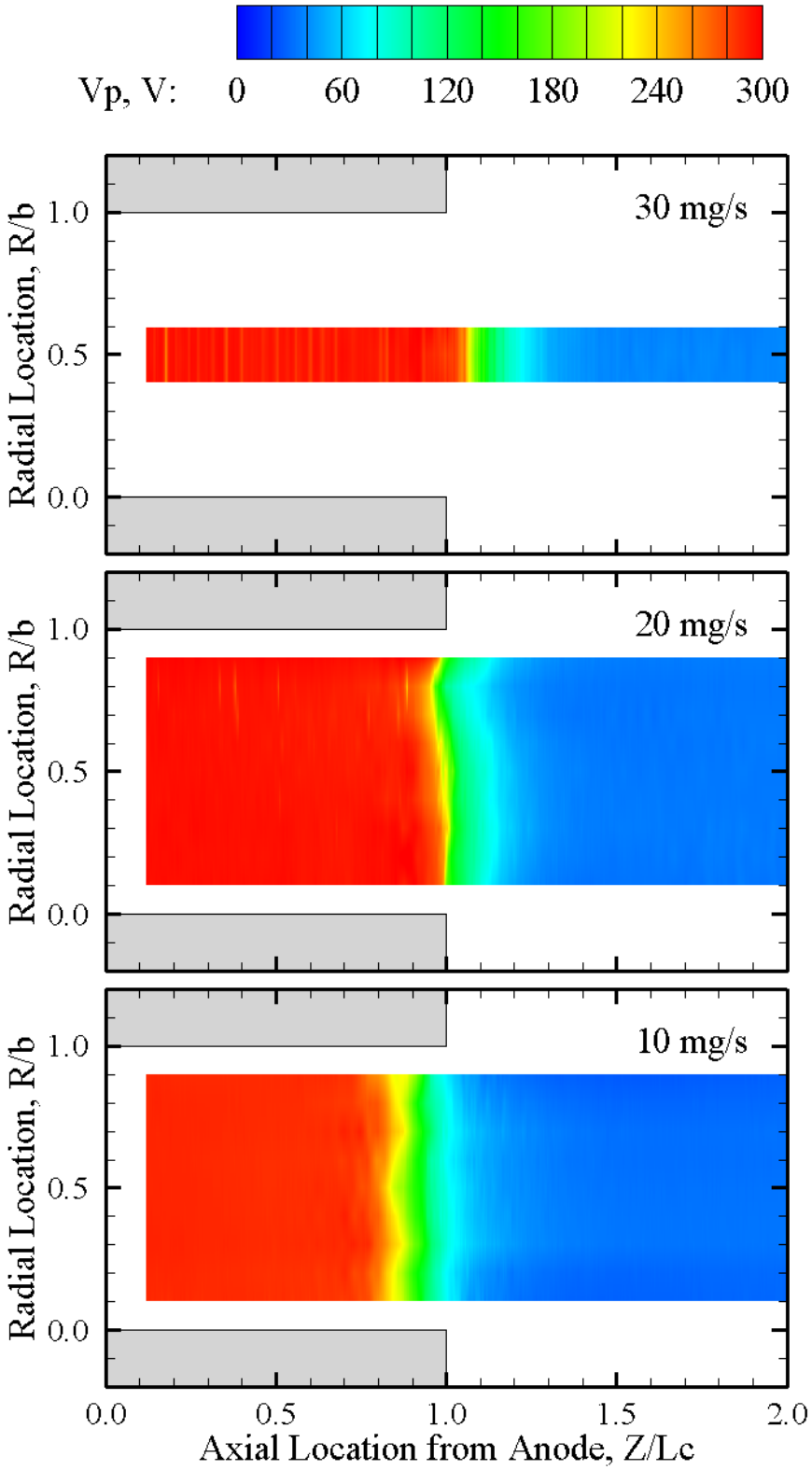

Figure 7-18. Plasma potential contours for thruster operation at 300 V and 10, 20, and 30 mg/s.

The centerline electron temperature and plasma potential before and after correction by the electron temperature are shown in Figure 7-19 for thruster operation at 300 V and 10 mg/s. The electron temperature correction did not have a drastic impact on the profile of the plasma potential; however, the correction tends to reduce the amount of electric field that persists into the channel. This artifact could account for some of the discrepancy between experimental plasma potential profiles and those produced by simulations (see Ref. [61] and Figure 7-26). Although the uncorrected experimental plasma potential profiles show better agreement with simulated profiles, there is sound theoretical basis for the plasma potential correction. The minor differences between the corrected experimental profiles and simulated profiles indicate that the code is not fully capturing some of the plasma physics or that the measurements and/or analysis are flawed in some way. This topic deserves additional attention in future work.

The corrected plasma potential is compared on channel centerline in Figure 7-20 for thruster operation at 300 V and 10, 20, and 30 mg/s. This comparison indicated an increase in the axial electric field (plasma potential slope), and the peak location moved downstream as flow rate was increased.

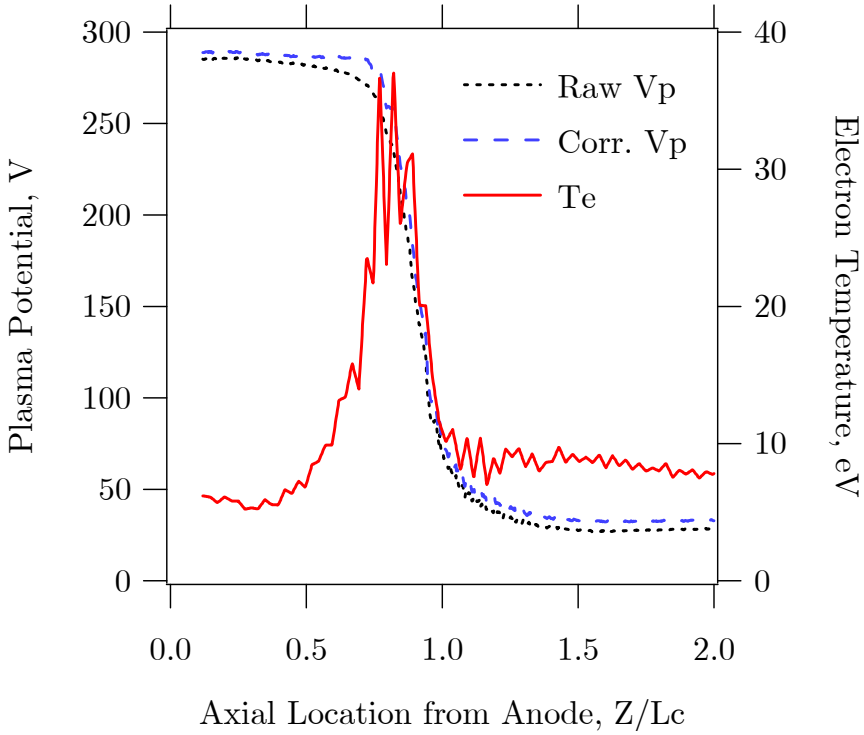

Figure 7-19. Comparison of pre- and post-corrected plasma potentials, including electron temperature at 300 V and 10 mg/s.

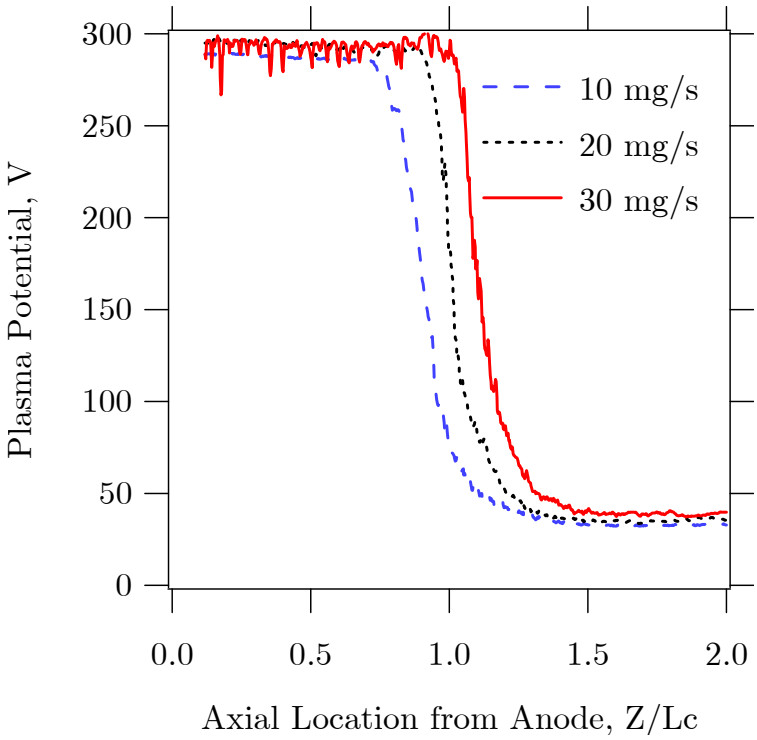

Figure 7-20. Comparison of plasma potential on channel centerline at 300 V and 10, 20, and 30 mg/s.

7.3.4 Axial Electric Field

The axial electric field, E_z was computed from the first derivative of the corrected plasma potential in the axial direction. The results are shown throughout the measurement domain for thruster operation at 300 V and 10, 20, and 30 mg/s in Figure 7-21 (300 V and 30 mg/s has single sweep). As flow rate was increased, the peak electric field increased and the region of elevated electric field became more compact. To highlight these trends the axial electric field is compared on channel centerline in Figure 7-22 for all three operating conditions. The peak axial electric field moved downstream with each addition of anode flow rate, occurring at 95, 100, and 102% L_c for 10, 20, and 30 mg/s, respectively. The centerline peak electric field was approximately 37, 50, and 60 V/mm at 10, 20, and 30 mg/s, respectively.

As Hall thrusters get more advanced, the axial electric field strength tends to increase. This is approximately followed with the advancement achieved from the UM/AFRL P5, NASA-173Mv1, and the 6-kW Hall thrusters, which achieved peak axial fields of approximately 25, 40, and 45 V/mm, respectively. To make the comparison valid, the larger size of the 6-kW Hall thruster was accounted for by estimating the electric field between 15 mg/s using linear interpolation.

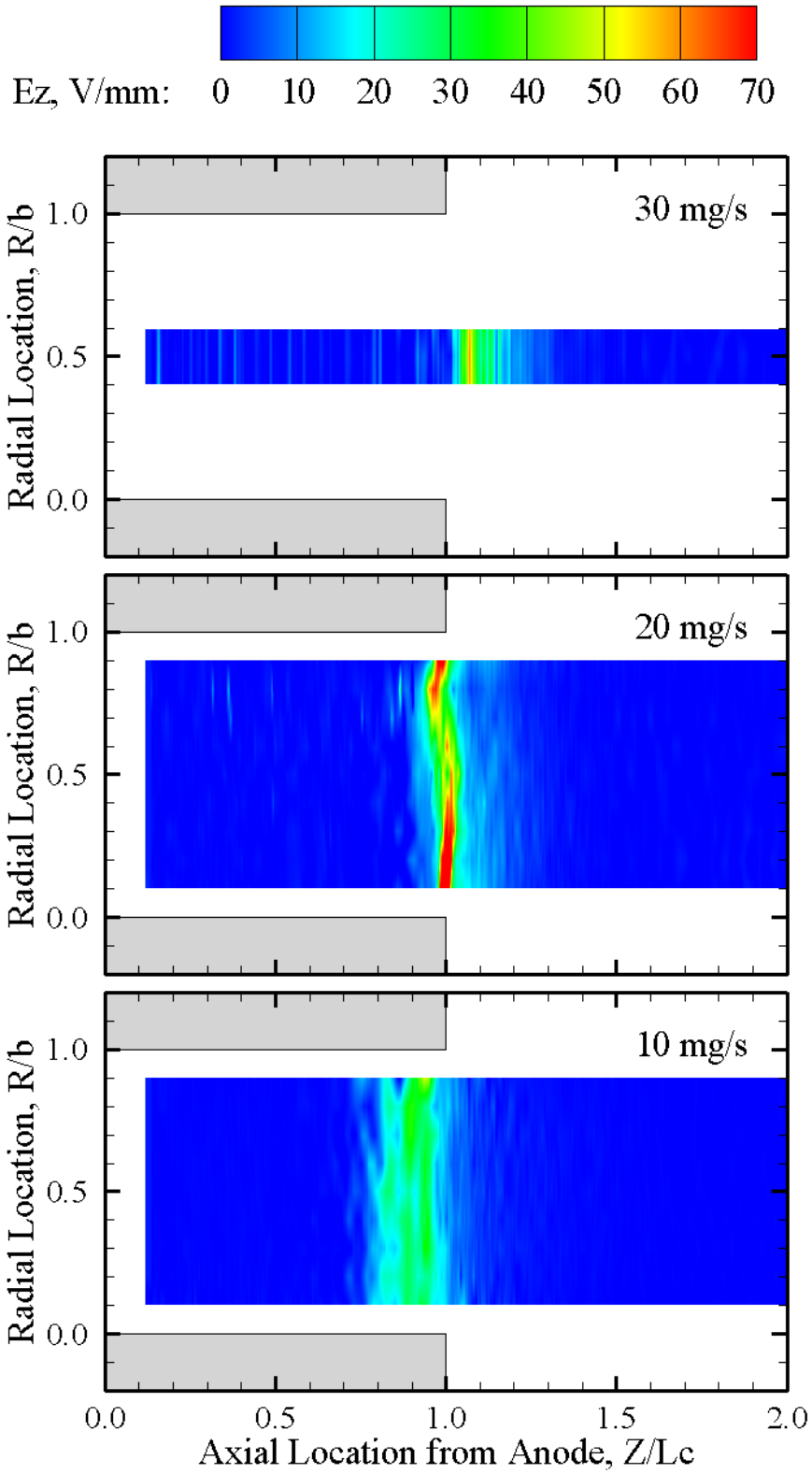

Figure 7-21. Axial electric field contours for thruster operation at 300 V and 10, 20, and 30 mg/s.

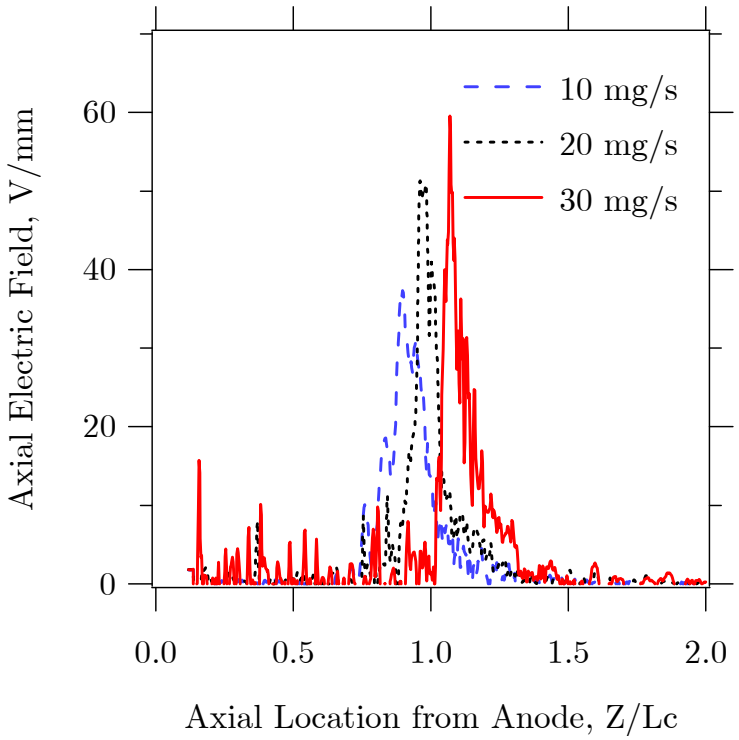

Figure 7-22. Comparison of axial electric field on channel centerline at 300 V and 10, 20, and 30 mg/s.

7.3.5 Radial Electric Field

The radial electric field was computed from the first derivative of the plasma potential in the radial direction. The magnitude of the radial electric field remained below a few V/mm and the structure did not exhibit much cohesion that would lead to useful conclusions. This result was in direct opposition to the strong ion focusing (~15 V/mm at 300 V and 10 mg/s) that was measured by Linnell [51]. The primary reason for the lack of radial electric field is that the ionization and acceleration occurred closer to the exit plane than in the NASA-173Mv1. The magnetic field lines were primarily radial at this location, and since they serve as an estimate of the equipotential lines [9], the plasma potential was highly uniform across the channel. The plasma potential uniformity resulted in

very little radial electric field and hence, negligible radial focusing of ions toward channel centerline.

7.4 Discussion

The Langmuir and emissive probe measurements indicated that the peak locations for the electron temperature, ion density, and electric field moved downstream as flow rate was increased. To further elucidate these trends, the peak location and width of the primary ionization, high electron temperature, and acceleration regions are considered. A discussion of the mechanisms that contributed to the trends in these data is included in Section 8.6.

Experimental measurements of plasma potential, electron temperature, and ion density are compared to HPHALL-2 simulations at each operating condition. At this point, these comparisons were intended to provide mutual validation of the simulations and experimental data. In Chapter 8, a more in-depth analysis provides valuable insight into the mechanisms that produce the trends discussed in this chapter. In this context, the simulations were used as a tool to investigate experimental trends.

7.4.1 Hall Thruster Regions

Although the ionization and acceleration regions were schematically represented as distinct zones in Figure 2-3, in practice, each of these processes is continuous. Ionization occurs directly downstream of the anode and once ions are created, they are immediately accelerated by the electric field. Although these

regions can not be rigorously separated or their locations definitively defined, it is useful to consider the "primary" regions of intense ionization and acceleration.

The primary ionization and acceleration regions were defined as the locations of 15 and 50% of the peak on either side of the ion density and electric field peak, respectively. These values were similar to those used by Linnell [51]. Although the cutoff criteria are somewhat arbitrary, using a consistent value across all operating conditions provides useful comparisons. In addition to the ionization and acceleration regions, the high electron temperature region was also considered and was defined as the location where the electron temperature dropped below the first ionization potential of xenon at 12 eV.

7.4.1.1 Ionization Region

The upstream and downstream boundaries of the ionization region are shown with the peak ion density location in Figure 7-23 (shown for blended density). As noted in Section 7.2, the peak ion density moved downstream 5-7% L_c with each addition of 10 mg/s. The length of the ionization region decreased by more than 50% from 10 to 20 mg/s and 30% from 20 to 30 mg/s, indicating that the ionization region became more compact as flow rate was increased. The average length of the ionization region at each operating condition is summarized in Table 7-4.

7.4.1.2 Acceleration Region

The upstream and downstream boundaries of the acceleration region are shown with the peak electric field location in Figure 7-24. As noted in Section 7.3, the acceleration region moved downstream 5-7% L_c with each addition of flow rate. As the acceleration region moved downstream, the corresponding electric field increased (see Table 7-2). In addition, the acceleration length decreased by approximately 40% from 10 mg/s to 20 mg/s. It was unclear if the acceleration region continued to get more compact at 30 mg/s due to the single measurement that was available. However, based on this single measurement the acceleration length increased by 20% from the 20 mg/s results (25% decrease from 10 mg/s). The average length of the acceleration region at each operating condition is summarized in Table 7-4, and further discussion on the acceleration region trends can be found in Section 8.3.

7.4.1.3 High T_e Region

The upstream and downstream boundaries of the high electron temperature region are shown with the peak electron temperature in Figure 7-25. As noted in Section 7.2, the high electron temperature region moved downstream 5-7% L_c with each addition of flow rate. In addition, the length of the high electron temperature region decreased by 45% from 10 to 20 mg/s and another 23% from 20 to 30 mg/s. The average length of the high electron temperature region at each operating condition is summarized in Table 7-4 and further

discussion on the high electron temperature region trends can be found in Section 8.3.

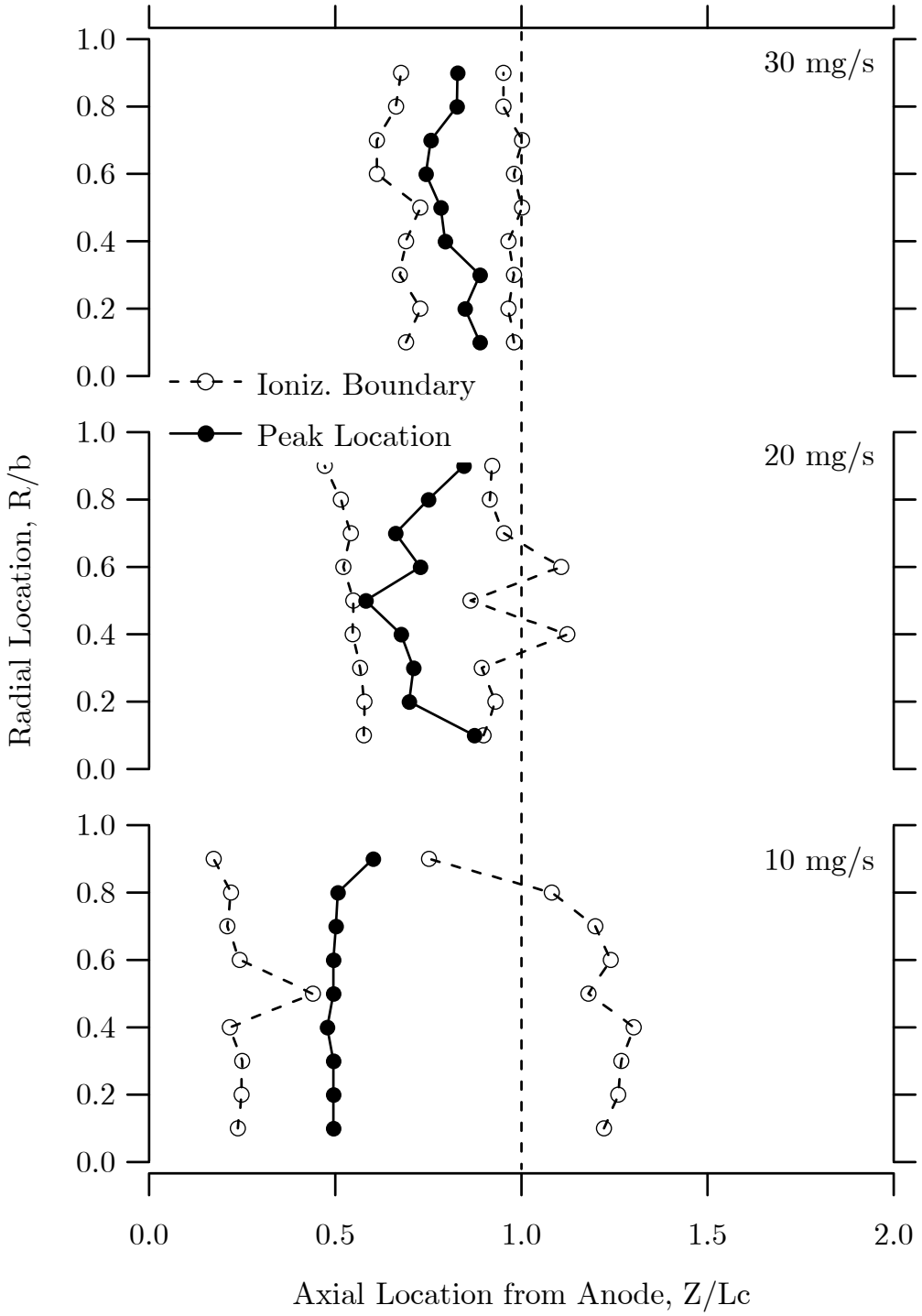

Figure 7-23. Location of upstream and downstream boundaries of ionization region for thruster operation at 300 V and 10, 20, and 30 mg/s.

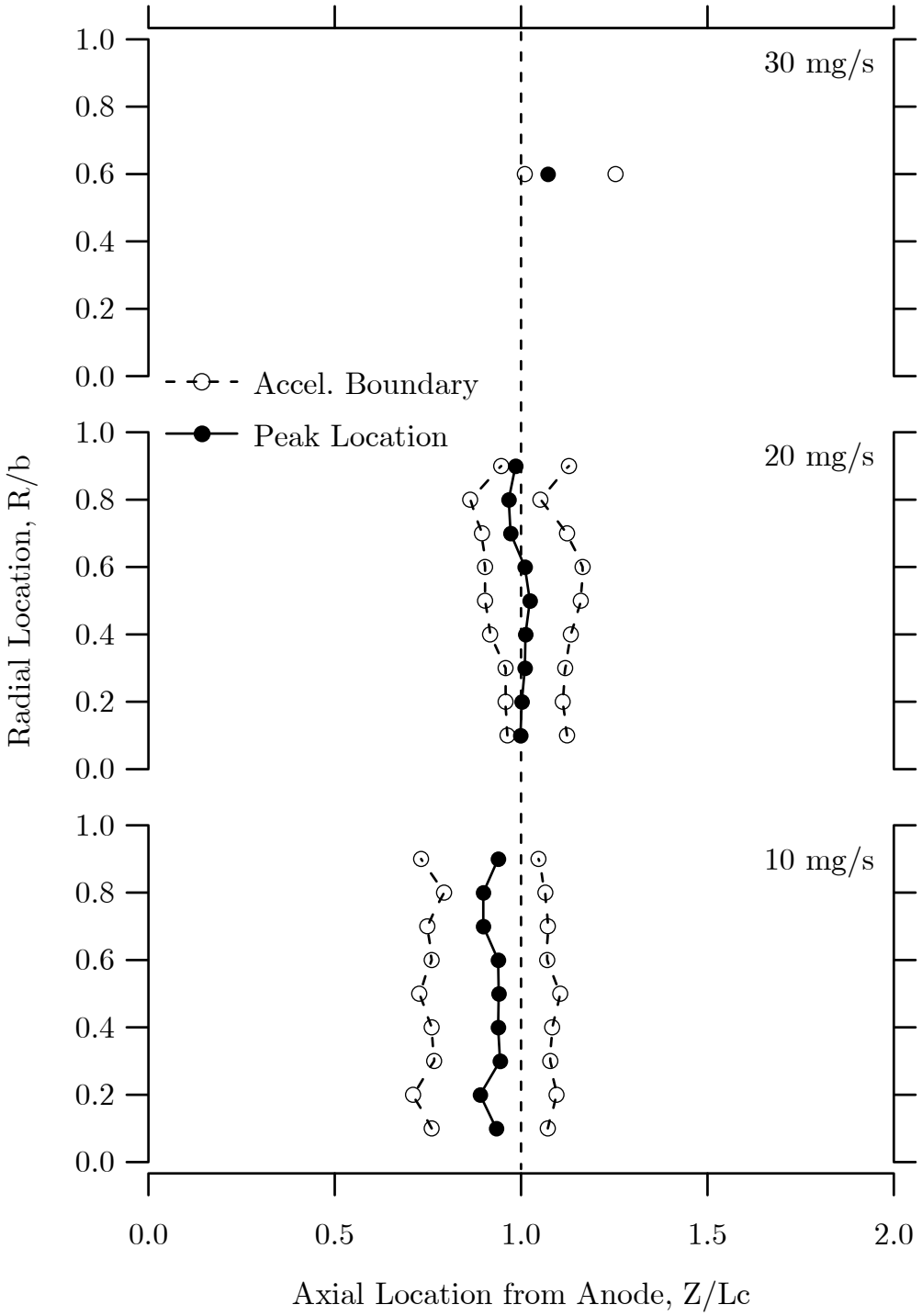

Figure 7-24. Location of upstream and downstream boundaries of acceleration region for thruster operation at 300 V and 10, 20, and 30 mg/s.

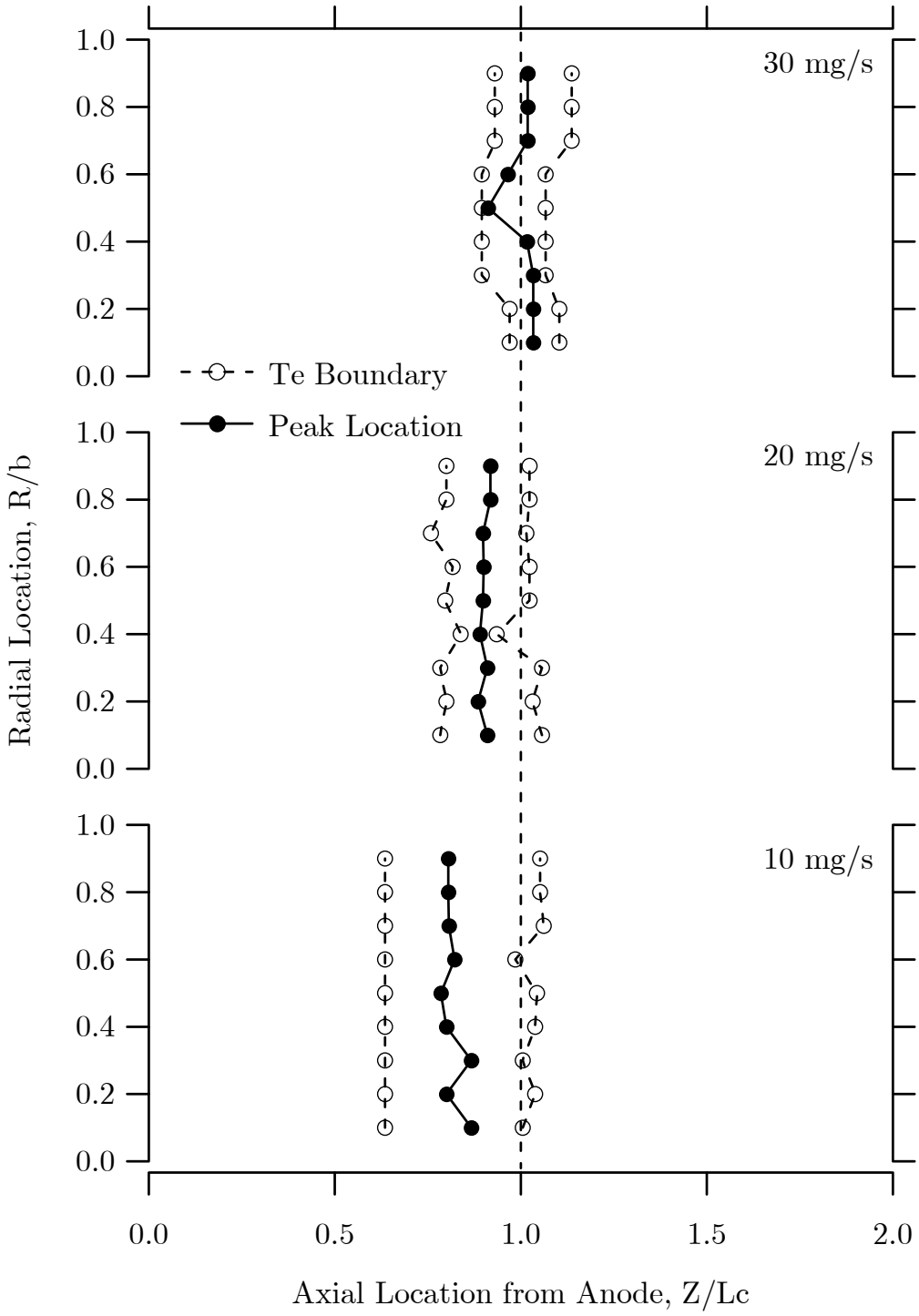

Figure 7-25. Location of upstream and downstream boundaries of high electron temperature region for thruster operation at 300 V and 10, 20, and 30 mg/s.

7.4.2 Comparisons with HPHALL-2 Simulations

HPHALL-2 is a hybrid-PIC computer code that has been under development for a number of years [28, 57-62]. A brief discussion of the code and results for plasma-off simulations can be found in Section 3.3.3. It should be noted that HPHALL-2 is not currently regarded as a predictive simulation. Instead, simulation results are adjusted to match global parameters such as discharge current and thrust. The results are then compared with experimental results to further investigate trends and microscopic properties such as collision frequency and localized wall losses.

It is important to highlight the number of free parameters associated with obtaining a solution in HPHALL-2 so that the results can be put into perspective. Before discussing the free parameters, several inputs that are based on operating conditions are necessary as boundary conditions. The primary inputs are discharge voltage, cathode potential, anode mass flow rate, and magnetic field. Consistent with experiment, the magnetic field shape was held constant between operating conditions so that the peak magnetic field value was the only variable. Other secondary boundary conditions included anode and channel temperature and injector Mach number. The channel temperature varied with discharge power using the results of Mazouffre *et al.* [49], and the anode temperature was input at 100 K below the channel temperature. The injector Mach number was taken from FLUENT results in Section 3.7.3. The boundary conditions used in these HPHALL-2 simulations are summarized in Table 7-1.

Table 7-1: Summary of inputs used for HPHALL-2 simulations.

300 V	10 mg/s	20 mg/s	30 mg/s
Cathode Potential, V	-13	-12	-11
Channel Temperature, K	780	940	1060
Anode Temperature, K	680	840	960
Injector Mach number, -	0.26	0.38	0.48

After imposing the boundary conditions, which are dependent on the operating condition, several free parameters remain. The primary free parameters are grouped into three categories: 1) location and size of the three mobility regions, 2) intensity of the turbulence within each of the three mobility regions, and 3) the level of electron temperature anisotropy. The first category is all but eliminated from these simulations since the geometry of the mobility region was held constant for simplicity. To preserve consistency with experimental results, the entire mobility structure was then translated downstream by 5% L_c for each 10 mg/s increment in mass flow rate. The second category would suggest three additional free parameters since each mobility region has a distinct turbulence intensity associated with it. The regions are: region I: near the anode, region II: near-channel-exit, and region III: outside the channel (plume). However, the plume mobility was held constant at 10 times the Bohm value based on the recommendation in Ref. [61]. These simplifications reduce the number of free parameters to three: 1) turbulence intensity in the near-anode region, 2) turbulence intensity in the near-channel-exit region, and 3) electron temperature

anisotropy ratio. These three variables were adjusted until the discharge current and thrust were within 2-3% of the experimental values.

The simulated plasma potential and electron temperature are compared to experimental data in Figure 7-26 and a comparison of the simulation ion density is compared to the three experimental ion densities (thin sheath, OML, and blend) in Figure 7-27. Overall, the simulations showed good agreement with experimental measurements on channel centerline.

The electron temperature shape and peak location showed excellent agreement at all three flow rates. At 10 and 20 mg/s the simulated peak electron temperature was within 3% (~1 eV) of the measured value; however, the simulated peak electron temperature was more than 50% greater than the measured value at 30 mg/s (outside the experimental uncertainty).

The plasma potential shape showed good agreement at all three flow rates. The agreement between the experimental and simulated plasma potential shape and location at 10 mg/s was exceptional. At 20 and 30 mg/s, the shape of the profiles were in good agreement, however the simulated profile was shifted approximately 5% L_c upstream of the measured value. As briefly discussed in Section 7.3.3, some of the differences between the experimental and simulated profiles may be due to the plasma potential correction for electron temperature that is applied to experimental measurements. Since there is a sound theoretical

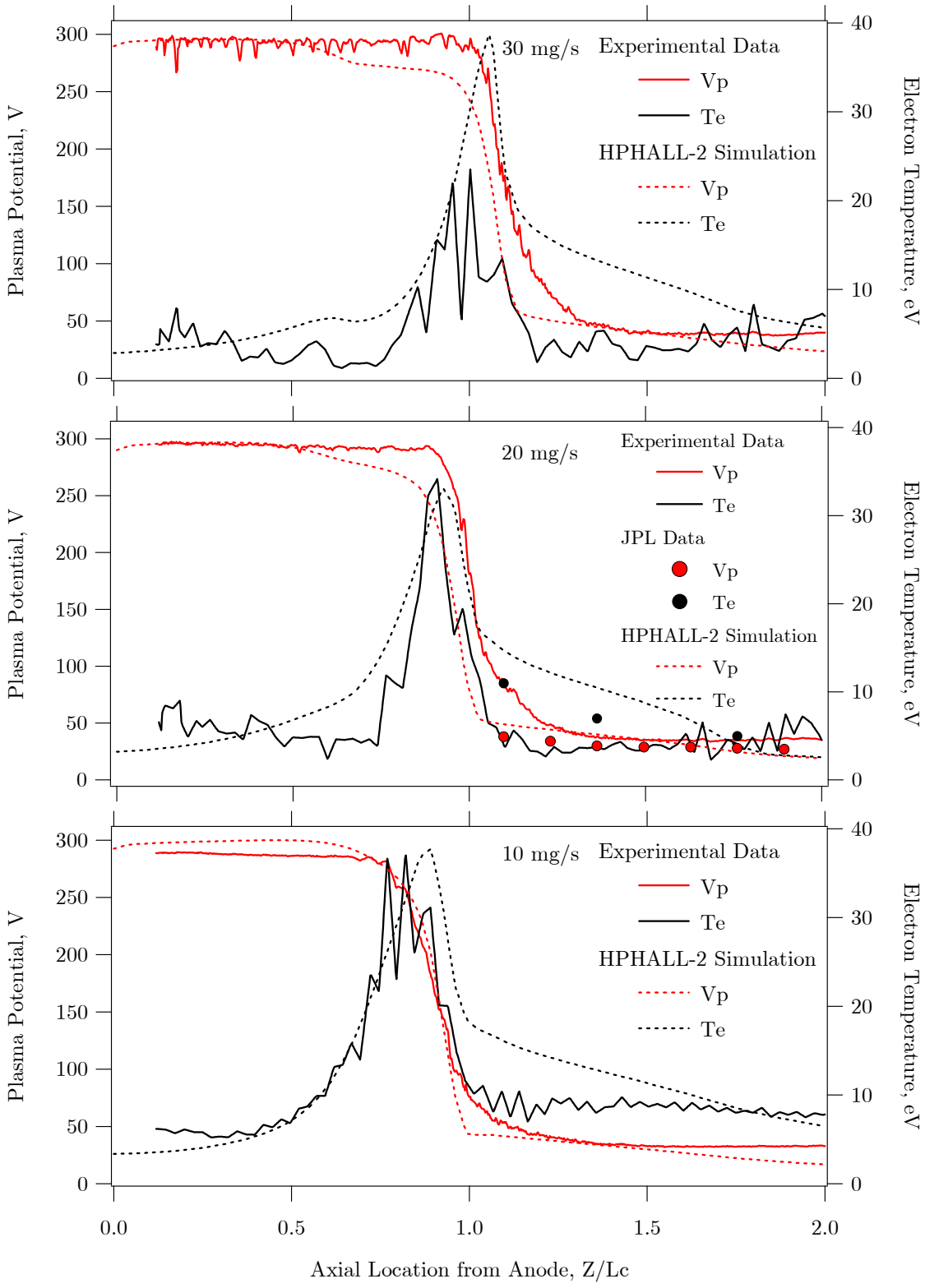

Figure 7-26. Comparison of plasma potential and electron temperature for HPHALL-2 simulations and experimental results on channel centerline at 300 V and 10, 20, and 30 mg/s.

basis for the correction to the experimental measurements, the discrepancy indicates that the code is not fully capturing some of the plasma physics or that the measurements and/or analysis are flawed in some way. This topic deserves additional attention in future work.

Data taken at JPL [106] are included at 20 mg/s and they displayed excellent agreement with the simulated plasma potential and electron temperature. The difference between the two experimental sets of data (UM and JPL) may indicate differences in thruster operation, facility effects, or uncertainty bounds that were larger than expected. The thruster used at JPL was fabricated to be identical to the one at UM; however, the JPL thruster required approximately 5% additional anode mass flow to produce the same discharge current. This additional flow may have increased the neutral density in the near-field plume, causing increased near-field electron mobility into the channel. This effect would tend to diminish the presence of the electric field in the near-field plume that was measured at UM.

The simulated ion density is compared with all three experimentally calculated ion densities in Figure 7-27. The profiles of the simulated and experimental ion density were qualitatively similar to each other and the peak magnitudes were within 50% each other at all flow rates. The best agreement occurred at 20 mg/s with a 20% difference between the simulated and

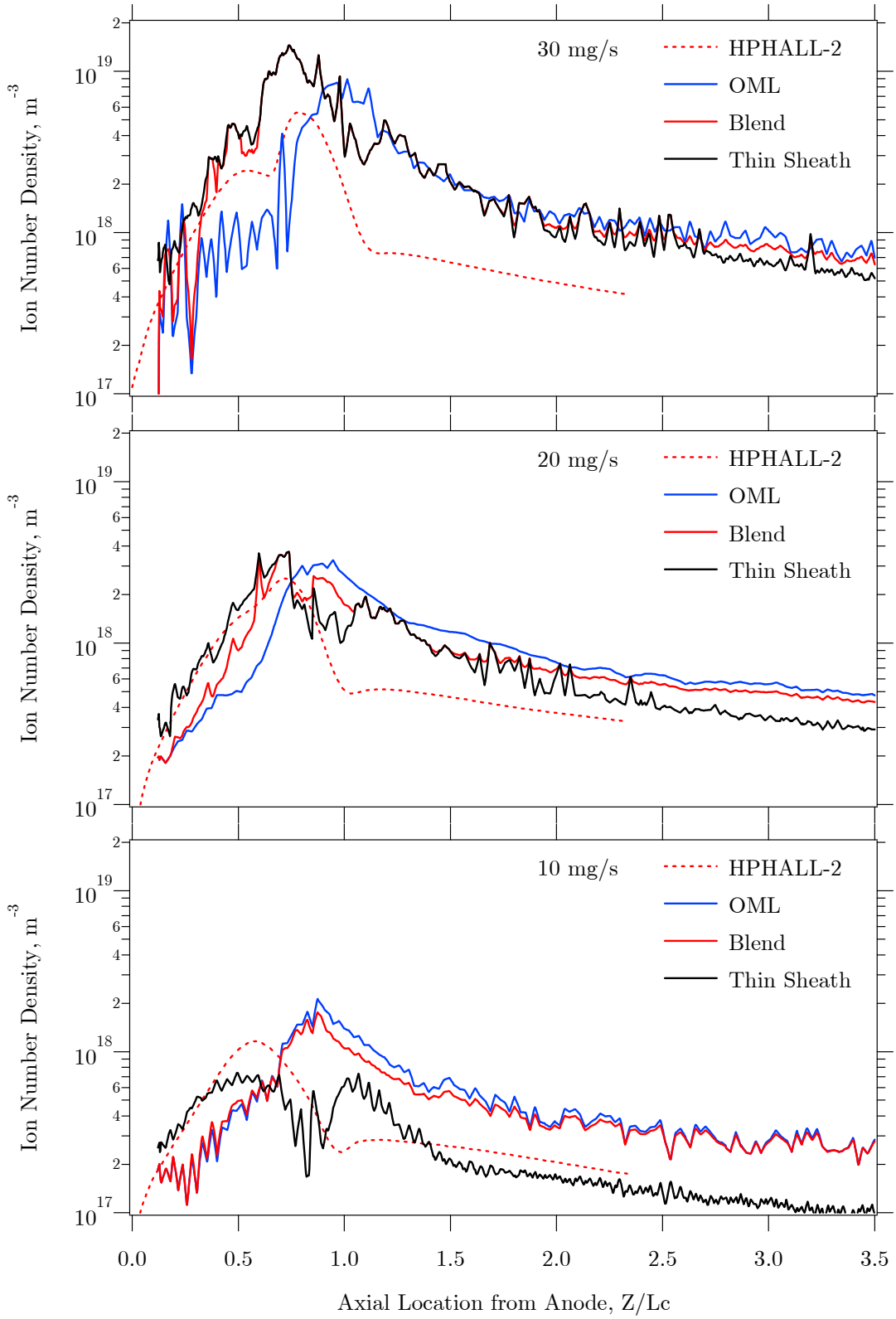

Figure 7-27. Comparison of ion density for HPHALL-2 simulations and experimental results on channel centerline at 300 V and 10, 20, and 30 mg/s.

experimental ion densities. The simulated ion density consistently lined up with the thin sheath ion density. This is consistent with the results of Section 7.2.4 that indicated most of the data were either in the transition between thin sheath and OML or fully thin sheath.

7.4.3 Plasma Potential Consistency

Plasma potential measurements from the floating emissive probe are compared to ion energy measurements from an RPA and the discharge voltage in Figure 7-28 for 300 V and 10, 20, and 30 mg/s. The ion voltage distribution was measured with the RPA positioned 2 m from the exit plane. The raw RPA potential increased by 1-2 V for each addition of 10 mg/s and the RPA potential corrected by the local plasma potential remained constant to within 0.5%. The corrected RPA potential with respect to cathode was within 10% of the discharge voltage at all operating conditions, indicating nearly constant voltage utilization efficiency ($\eta_v = V_{accel}/V_D$). The plasma potential at the peak ion density location measured by the emissive probe was within 3.8, 1.4, and 2.0% of the anode potential at 10, 20, and 30 mg/s, respectively. The estimated uncertainty in the plasma potential near the anode was ± 10 V (± 5 V for voltage drop across the filament and approximately ± 5 V for 0.9 T_e uncertainty). Considering the all of the sources of uncertainty, the plasma potential at each operating condition was consistent with the discharge voltage and RPA measurements.

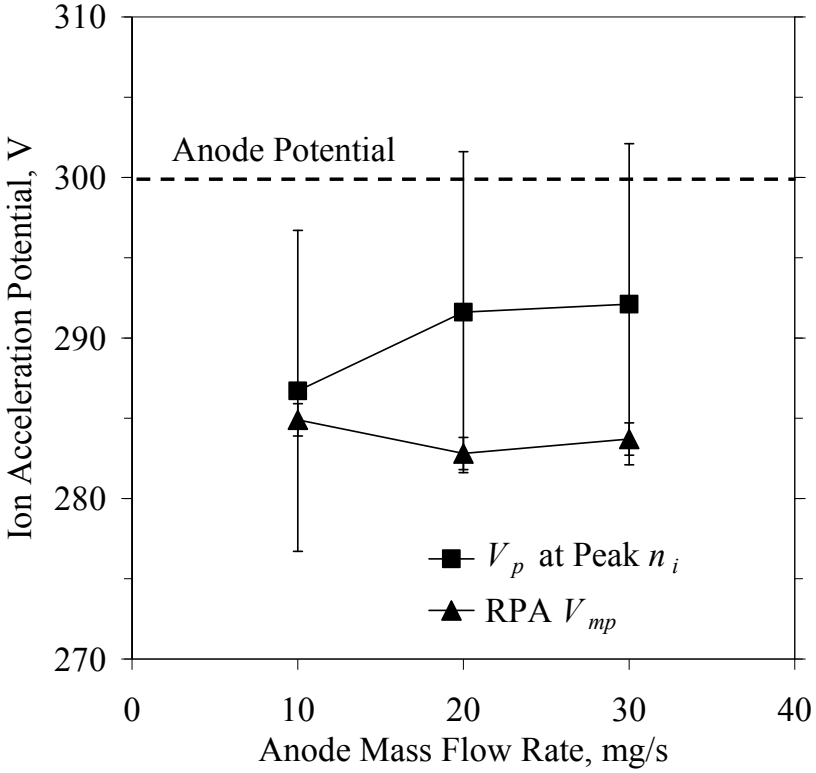

Figure 7-28. Comparison of RPA most probable voltage and plasma potential at peak ion density measured by the emissive probe for thruster operation at 300 V and 10, 20, and 30 mg/s.

7.5 Summary of Internal Measurements

The methods used to perform the measurements contained in this chapter were based on the work of Haas [109] and Linnell [51]. The single Langmuir probe measurement technique was improved by allowing the probe voltage to oscillate about the floating potential using a programmable function generator rather than approximating it as a square wave. This improvement decreased the need for multiple sweeps into the thruster, thereby increasing probe life and streamlining the data analysis procedure. The fidelity of emissive probe measurements was increased by acquiring data at high speed (83 kHz) and monitoring the probe voltage drop throughout the entire data collection cycle.

This technique allowed fluctuations in the plasma potential to be correlated to discharge oscillations and it offered a quantitative method to evaluate probe saturation as the probe was swept into the thruster.

As anode mass flow rate was increased, the peak ion density, electron temperature, and electric field moved downstream on the order of 5-7% L_c (see Table 7-3). The average peak ion density increased somewhat linearly with flow rate, but results at 30 mg/s were a factor of 2-3 too high. The average peak electric field increased by nearly 100% from 10 to 20 mg/s and decreased by 20% from 20 to 30 mg/s (increase of 50% from 10 mg/s). The validity of this trend at 30 mg/s was suspect due to the single available measurement (due to probe failure at high power). The average peak electron temperature decreased by approximately 25% for each addition of 10 mg/s from 10 to 30 mg/s. The primary electron energy loss mechanism was due to wall losses, which is discussed in Chapter 8.

Overall, the internal Langmuir and emissive probe measurements in this chapter provided evidence that the neutral flow rate had a strong influence on the location, intensity, and profile of the ionization, acceleration, and high electron temperature regions. The location of these regions affects thruster performance, lifetime, stability, and thermal margin.

Table 7-2: Summary of peak ion number density, axial electric field, and electron temperature (averaged across channel).

Peak Property Magnitude	10 mg/s	20 mg/s	30 mg/s
Peak n_i (blended), m^{-3}	2×10^{18}	4×10^{18}	15×10^{18}
Peak n_i (thin sheath), m^{-3}	1×10^{18}	4×10^{18}	15×10^{18}
Peak n_i (OML), m^{-3}	2×10^{18}	3×10^{18}	9×10^{18}
Peak E_z, V/mm	33	63	49
Peak T_e, eV	38	27	17

Table 7-3: Summary of peak location for ion number density, axial electric field, and electron temperature (averaged across channel).

Peak Property Location, % L_c	10 mg/s	20 mg/s	30 mg/s
Peak n_i location (blended)	74	74	87
Peak n_i location (thin sheath)	52	72	73
Peak n_i location (OML)	86	88	98
Peak E_z location	93	100	107
Peak T_e location	81	90	100

Table 7-4: Summary of region length for ionization, acceleration, and high electron temperature regions (averaged across channel).

Region Length, % L_c	10 mg/s	20 mg/s	30 mg/s
Ionization Length	92	42	30
Acceleration Length	33	20	24
High T_e Length	39	22	18

Chapter 8

Internal Analysis

The electron energy and momentum equations are introduced in order to discuss the results and trends presented in Chapter 7. Experimental results were combined with analytical analysis to investigate the electron mobility in the discharge channel by considering the electron Hall parameter. To properly account for all of the contributions to electron mobility, the ion and neutral number density were required. The ion density was measured directly by the Langmuir probe and the neutral density was calculated using a 1-D mass continuity analysis. In a similar fashion, the electron current at each axial location was calculated from a 1-D current continuity analysis with the ion flux. Examining the electron Hall parameter and electron physics in the channel allowed the contribution of neutral flow rate to the ionization and acceleration processes to be rigorously identified. The electron power balance was evaluated through HPHALL-2 simulations so that the major contributions to electron energy loss could be identified.

8.1 Electron Equations

To evaluate the contributions to electron physics in the channel and near-field plume, the energy equation and momentum equations are described. These equations are then used to evaluate electron collisions with ions, neutrals, and walls so that the Hall parameter and electron mobility can be investigated.

8.1.1 Electron Energy Equation

Following the formulation used in HPHALL-2 simulations, the electron energy equation can be written as [28, 61]

$$\frac{\partial}{\partial t}\left(\frac{3}{2}n_e k_B T_e\right)+\nabla\cdot\left(\frac{5}{2}n_e k_B T_e \vec{u}_e+\vec{q}_e\right)+\dot{E}_w=\vec{j}_e\cdot\vec{E}+S_i\,, \tag{8-1}$$

where $\vec{q}_e$ is the thermal conduction vector, $\dot{E}_w$ is the wall energy loss term, and the inelastic loss term accounting for each ionization event is given by

$$S_i=\left(\dot{n}_i^{1+}\varphi E_i\right)^{0\to1}+\left(\dot{n}_i^{2+}\varphi E_i\right)^{1\to2}+\left(\dot{n}_i^{2+}\varphi E_i\right)^{0\to2}, \tag{8-2}$$

where E_i is the ionization energy. Since the experimental data in Chapter 7 do not differentiate between ion species, and the contribution from doubly-charged ions is much smaller than singly-charged ions, the inelastic loss term reduces to

$$S_i=\left(\dot{n}_i^{1+}\varphi E_i\right), \tag{8-3}$$

where φ is Dugan's ionization cost factor [28, 159]

$$\varphi\left(T_e/E_i\right)=2+0.254\exp\left(0.677E_i/T_e\right), \tag{8-4}$$

which accounts for ionization and excitation of the ground state (excitation of singly- and doubly-charged ions is neglected) and $\dot{n}_i$ is the ion production rate [28]

$$\dot{n}_i = n_i n_n \varsigma\left(T_e\right), \tag{8-5}$$

where

$$\varsigma\left(T_e\right) = Q\beta_1 \frac{I\left(\theta\right)}{\theta^{3/2}}. \tag{8-6}$$

Here Q is 4.13×10^{-13} m^3/s, β_1 is 1.00, $\theta = k_B T_e / E_i$ and

$$I\left(\theta\right) = \int_1^\infty e^{-\frac{u}{\theta}} \frac{\left(u-1\right)}{u} \ln\left(1.25\beta_2 u\right) du, \tag{8-7}$$

where $u = E / E_i$ and β_2 is 0.80. Q, β_1, and β_2 are constants specific to xenon that were based on fits to the Drawin ionization model assuming Maxwellian electrons [28, 160]. Further detail regarding the derivation of the energy equation can be found in Refs. [28, 58, 61].

By introducing the electron energy equation, we can evaluate the primary contributions to the electron energy as the anode mass flow rate was increased. The equation indicates that there are four main constituents: 1) convection and conduction, 2) wall losses, 3) Ohmic heating, and 4) ionization/excitation (inelastic losses).

8.1.2 Electron Momentum Equation

To further understand the mechanisms that affect Hall thruster operation, the electron physics were considered by using the electron momentum equation that is written as

$$m_e n_e \left(\frac{d\vec{u}_e}{dt} + (\vec{u}_e \cdot \nabla)\vec{u}_e \right) = -en_e \left(\vec{E} + \vec{u}_e \times \vec{B} \right) - \nabla P_e - m_e n_e \vec{u}_e \nu_{e,tot}, \qquad (8\text{-}8)$$

where $\nu_{e,tot}$ is the total electron collision frequency and the remaining variables have their usual meaning. To simplify the analysis of the momentum equation, the coordinate system was transformed to be relative to the magnetic field lines. The transformation was accomplished by a coordinate rotation defined by

$$\tan\phi = \frac{B_z}{B_r}, \qquad (8\text{-}9)$$

and shown graphically in Figure 8-1.

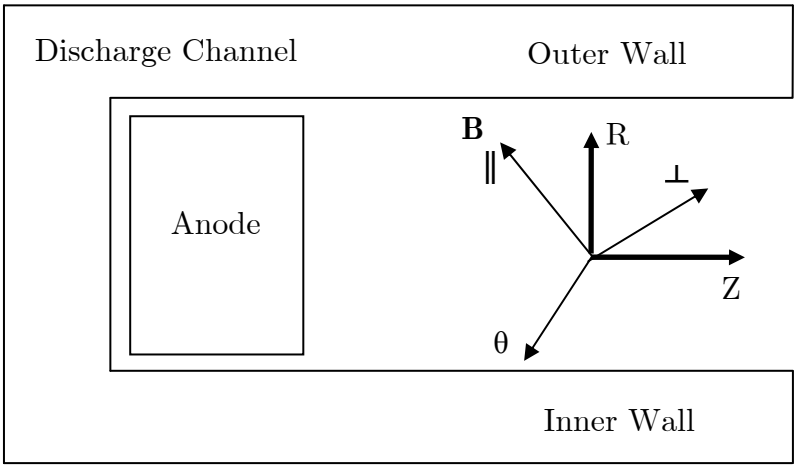

Figure 8-1. Schematic of coordinate transformation used in electron analysis.

The transformation equations are

$$\begin{pmatrix} \hat{e}_{\perp} \\ \hat{e}_{\parallel} \\ \hat{e}_{\theta} \end{pmatrix} = \begin{bmatrix} \cos\phi & \sin\phi & 0 \\ -\sin\phi & \cos\phi & 0 \\ 0 & 0 & 1 \end{bmatrix} \begin{pmatrix} \hat{e}_{z} \\ \hat{e}_{r} \\ \hat{e}_{\theta} \end{pmatrix}. \tag{8-10}$$

Using these transformations, the electron momentum equation was rewritten and separated into each of its three components as

$$0 = -en_e E_{\perp} + en_e u_{e\perp} B - \frac{\partial P_e}{\partial \perp} - m_e n_e u_{e\perp} \nu_{e,tot}, \tag{8-11}$$

$$0 = -en_e E_{\parallel} - \frac{\partial P_e}{\partial \parallel} - m_e n_e u_{e\parallel} \nu_{e,tot} - \frac{n_e k_B T_e}{B} \frac{\partial B}{\partial \parallel}, \tag{8-12}$$

$$0 = -en_e u_{e\theta} B - m_e n_e u_{e\theta} \nu_{e,tot}. \tag{8-13}$$

In this set of equations, the inertial term was neglected, the plasma was assumed to be steady-state, axisymmetric (no θ variation), and the azimuthal component of the magnetic field was neglected (very good approximations).

For convenience, several additional parameters are introduced, including the classical electron mobility

$$\mu = \frac{e}{\nu_{e,tot} m_e}, \tag{8-14}$$

electron Hall parameter

$$\Omega_{e,class} = \frac{\omega_c}{\nu_{e,tot}} = \mu B, \tag{8-15}$$

and diffusivity

$$D = \frac{k_B T_e}{\nu_{e,tot} m_e}. \tag{8-16}$$

The cross-field electron mobility is written as

$$\mu_{e\perp} = \frac{e}{\nu_e m_e}\left(\frac{1}{1+\Omega_e^2}\right). \tag{8-17}$$

Using these definitions and the assumption that electrons are isothermal along the magnetic field lines, the electron velocity in each direction can be written as

$$u_{e\perp} = -\frac{1}{1+\Omega_e^2}\left[\mu E_\perp + \frac{D}{T_e}\frac{\partial T_e}{\partial \perp} + \frac{D}{n_e}\frac{\partial n_e}{\partial \perp}\right], \tag{8-18}$$

$$u_{e\|} = -\left[\mu E_\| + \frac{D}{n_e}\frac{\partial n_e}{\partial \|} + \frac{D}{B}\frac{\partial B}{\partial \|}\right], \tag{8-19}$$

$$u_{e\theta} = \frac{\Omega_e}{1+\Omega_e^2}\left[\mu E_\perp + \frac{D}{T_e}\frac{\partial T_e}{\partial \perp} + \frac{D}{n_e}\frac{\partial n_e}{\partial \perp}\right]. \tag{8-20}$$

The perpendicular velocity was strongly affected by the Hall parameter. This characteristic enabled discussions about the electron mobility to benefit from considering the Hall parameter. Other contributions to the perpendicular velocity were electric field and electron pressure gradient (second and third term on RHS of Eq. 8-18). The parallel velocity was not directly dependent on the Hall parameter and the azimuthal velocity was only weakly affected by it, especially for Hall parameters that were much greater than unity. The parallel velocity was instead controlled by a balance between the electric field, pressure forces, and the magnetic mirror force. With the exception of the magnetic mirror force term (third term on the RHS of Eq. 8-19), Eq. 8-19 is the classic form for unmagnetized electrons. The azimuthal velocity was composed of the E×B drift (first term on the RHS of Eq. 8-20) and diamagnetic drift (second two terms on the RHS of Eq. 8-20).

8.1.3 Collisions

The Hall parameter given by Eq. 8-15 was inversely proportional to the total collision frequency that was a combination of classical and Bohm collision frequencies:

$$\nu_{e,tot} = \nu_{classical} + \nu_{Bohm} . \tag{8-21}$$

The classical collision frequency was modeled as

$$\nu_{classical} = \nu_{en} + \nu_{ei} + \nu_{ew} . \tag{8-22}$$

The electron-neutral collision frequency is modeled as

$$\nu_{en} = n_n Q_{en} \sqrt{\frac{8 k_B T_e}{\pi m_e}} , \tag{8-23}$$

where Q_{en} is the energy-dependent cross-section given by

$$Q_{en} = \begin{cases} 33.9581 \times 10^{-20} & T_e < 5\ eV \\ \left(11.3596 + 28.0985 \times e^{-0.043349 T_e}\right) \times 10^{-20} & T_e \geq 5\ eV \end{cases} . \tag{8-24}$$

The electron-neutral cross-section was derived from a Maxwellian average of measured cross-sections by Nickel *et al.* [161]. This is the same form used in HPHALL-2 simulations and is qualitatively similar to that used by Haas [109] and Linnell [51].

The electron-ion collision frequency was modeled as [62, 162]

$$\nu_{ei} = 2.91 \times 10^{-12} n_e T_e^{-3/2} \ln \Lambda , \tag{8-25}$$

where the electron temperature is in eV and the Coulomb logarithm is given by

$$\ln \Lambda = \begin{cases} 23 - \log\left(T_e^{-3/2} \sqrt{n_e \times 10^{-6}}\right) & T_e < 10\ eV \\ 24 - \log\left(T_e^{-1} \sqrt{n_e \times 10^{-6}}\right) & T_e \geq 10\ eV \end{cases} . \tag{8-26}$$

The electron-wall collision frequency was modeled as [18, 61, 163, 164]

$$\nu_{ew} = \chi \frac{2\delta_w}{h\left(1-\delta_w\right)} \sqrt{\frac{k_B T_e}{m_{xe}}}, \tag{8-27}$$

where χ is a correction factor accounting for the radial plasma density gradient between the bulk plasma and the wall (taken as 0.2, which is consistent with the value used in HPHALL-2 and simulations of Garrigues *et al.* [163]), h is the magnetic field line length, and the yield of secondary electrons from the discharge channel walls is [62]

$$\delta_w\left(T_e\right) = \delta_o + \left(1-\delta_o\right)\frac{2T_e}{E_1}, \tag{8-28}$$

where $\delta_o = 0.54$ and $E_1 = 40.0$ eV. Electron collisions with the discharge channel wall are responsible for additional cross-field electron mobility. This enhanced mobility is referred to as wall mobility or near-wall conductivity [18, 50, 165, 166]. This source of mobility is enhanced by high SEE from the walls, particularly in the case of space-charge saturated wall sheaths [50, 122, 156].

The plasma density and electron temperature were taken from the Langmuir probe measurements (see Section 7.2) and the neutral density was taken from the 1-D continuity analysis or HPHALL-2 simulations (see Section 8.2.2).

Classical collisions allow electrons to move towards the anode with a step size on the order of a Larmor radius. Considering electron transport due to classical mobility alone does not provide good agreement with measured

transport trends, indicating the need for additional contributions to electron mobility. One such contribution is referred to as Bohm mobility or "anomalous mobility". Bohm mobility is often attributed to turbulent fluctuations in the electric field and plasma density, a situation that is analogous to the observation of enhanced diffusion due to turbulence in hydrodynamic fluids. Bohm mobility was observed experimentally [21] and is often used in computational models to improve agreement with experimental measurements. The Bohm collision frequency was modeled using

$$\nu_{Bohm} = \frac{1}{16}\alpha_B \omega_c \,, \tag{8-29}$$

where α_B is an adjustable coefficient that is typically matched to experiment so that the necessary amount of cross-field diffusion results. In the case of classical Bohm diffusion, α_B would have a value of unity, which over-predicts the mobility in the acceleration region. To account for this discrepancy, computational models vary the amount of anomalous mobility throughout the domain by changing α_B or by allowing several distinct values through a two- or three-region mobility model [28, 61, 167].

8.1.4 Total Hall Parameter

Physically, the Hall parameter characterizes the number of azimuthal orbits that an electron completes prior to experiencing a particle collision that enables cross-field migration towards the anode. In this way, the Hall parameter can be estimated as the ratio of the azimuthal electron current to axial electron

current. The Hall parameter can be written in these physical terms as the ratio between the azimuthal and perpendicular electron velocities by solving Eqs. 8-18 and 8-20 for the Hall parameter. The result is

$$\Omega_e = -\frac{u_{e\theta}}{u_{e\perp}}. \tag{8-30}$$

The negative sign can be omitted since the perpendicular electron velocity, $u_{e\perp}$ is directed towards the anode (negative axial direction).

The azimuthal electron velocity, $u_{e\theta}$ is calculated from Eq. 8-20, and the perpendicular velocity is calculated from the axial electron current, which was calculated from a 1-D current continuity (see Eq. 8-32 in Section 8.2.1). The Hall parameter calculated with Eq. 8-30 is referred to as the total Hall parameter since it is expected to account for all contributions to electron mobility. This quantity is sometimes referred to as the "experimental Hall parameter" since it is calculated from directly measured quantities including electric field, magnetic field, and plasma density.

8.2 Continuity Analysis

A 1-D mass and current continuity was performed to determine the ion current, electron current, and neutral number density throughout the measurement domain. These properties were needed to calculate the electron Hall parameter, which describes the electron mobility. The ion current (charge flux) was calculated using the OML ion density measured by the Langmuir probe and

the ion velocity derived from the plasma potential measured by the emissive probe using

$$u_{iz}(z) = u_{iz}(0) + \sqrt{\frac{2e}{m_{xe}}\left(V_p(z) - V_{p,0}\right)}, \tag{8-31}$$

where $V_p(z)$ is the local plasma potential, $V_{p,0}$ is the plasma potential near the anode, and $u_{iz}(0)$ is the initial ion velocity that is taken as 0.1 eV, which is consistent with values used in Hall thruster models [168]. This simple model was appropriate in this context since ions were considered unmagnetized and collisionless.

The beam current calculated from the ion flux had a relatively large uncertainty associated with it, stemming from the uncertainty in ion density and to a lesser degree ion velocity. The velocity was derived from the plasma potential, which was accurate to 5-10% and the terminal velocity was confirmed by RPA (see Section 5.3) and LIF [134] measurements. Therefore, any over prediction of the beam current indicated that the measured ion number density was too high. Several factors that may have contributed to the overprediction of ion density were considered and determined to be negligible [110]. However, it was difficult to accurately gauge the effect of thermionic emission due to electrode heating if it was present. Probe I-V characteristics were compared for the insertion and removal cycles during data collection, displaying excellent agreement. If thermionic emission were present, the two cycles would produce different measurements. The good agreement between the two cycles was

considered as conclusive evidence that thermionic emission was not present during data collection.

The ion flux was grossly overpredicted by each of the measured ion densities (thin sheath, OML, and blended). The ion density was decreased until the peak flux was consistent with the measured beam current reported in Chapter 5. This analysis indicated that the ion density was overpredicted by as much as 2-300%, which was well outside the uncertainty bounds of typical Langmuir probe analysis. The effects of tip collection were accounted for and thermionic emission was not expected to affect the results. However, if the size of the sheath was not properly accounted for or if tip collection was underestimated, then the calculated ion density would be too high. Another potential contribution to the overprediction may have been a DC offset in the Langmuir probe measurement circuit. Although detailed circuit calibrations were performed at vacuum, an anomalous offset in the circuit may have existed when the plasma discharge was present. Although the magnitude of the density was decreased significantly, the relative uncertainty between each point in the domain was expected to be relatively small.

The electron fluid description allowed the electron current to be solved inside the channel through a 1-D current continuity with the ion flux. All quantities in Eqs. 8-18 to 8-20 were known from experimental data; however, one additional assumption was introduced in order to close the equations: the electron

current density was assumed uniform across the channel at each axial location. Although this assumption is not strictly valid since it does not account for near-wall conductivity, it will suffice for the current application. Using the known values of discharge current and ion density and velocity (flux) the axial electron current at each axial location was calculated using

$$I_{ez}(z) = I_D - \int_{A_{ch}} en_i u_{iz} dA \,, \tag{8-32}$$

where I_{ez} is the axial electron current, u_{iz} is the axial ion velocity, and the other values have their usual meaning.

8.2.1 Ion and Electron Current

The ion and electron currents produced by the 1-D continuity analysis are shown in Figure 8-2 for thruster operation at 300 V and 10, 20, and 30 mg/s. The results produced an unphysical profile outside the thruster where the ion current peaked then decreased with increased axial location. This result was due to the loss of current through the radial boundaries of the measurement domain past the exit plane.

Consistent with the internal region results, the location of maximum ion flux moved downstream with flow rate, occurring at 93, 103, and 111% L_c. The only mechanism that contributed to this trend of increased flux downstream as flow rate was increased was additional ionization outside the thruster. This was consistent with the results in Section 7.2.3 that indicated the peak electron

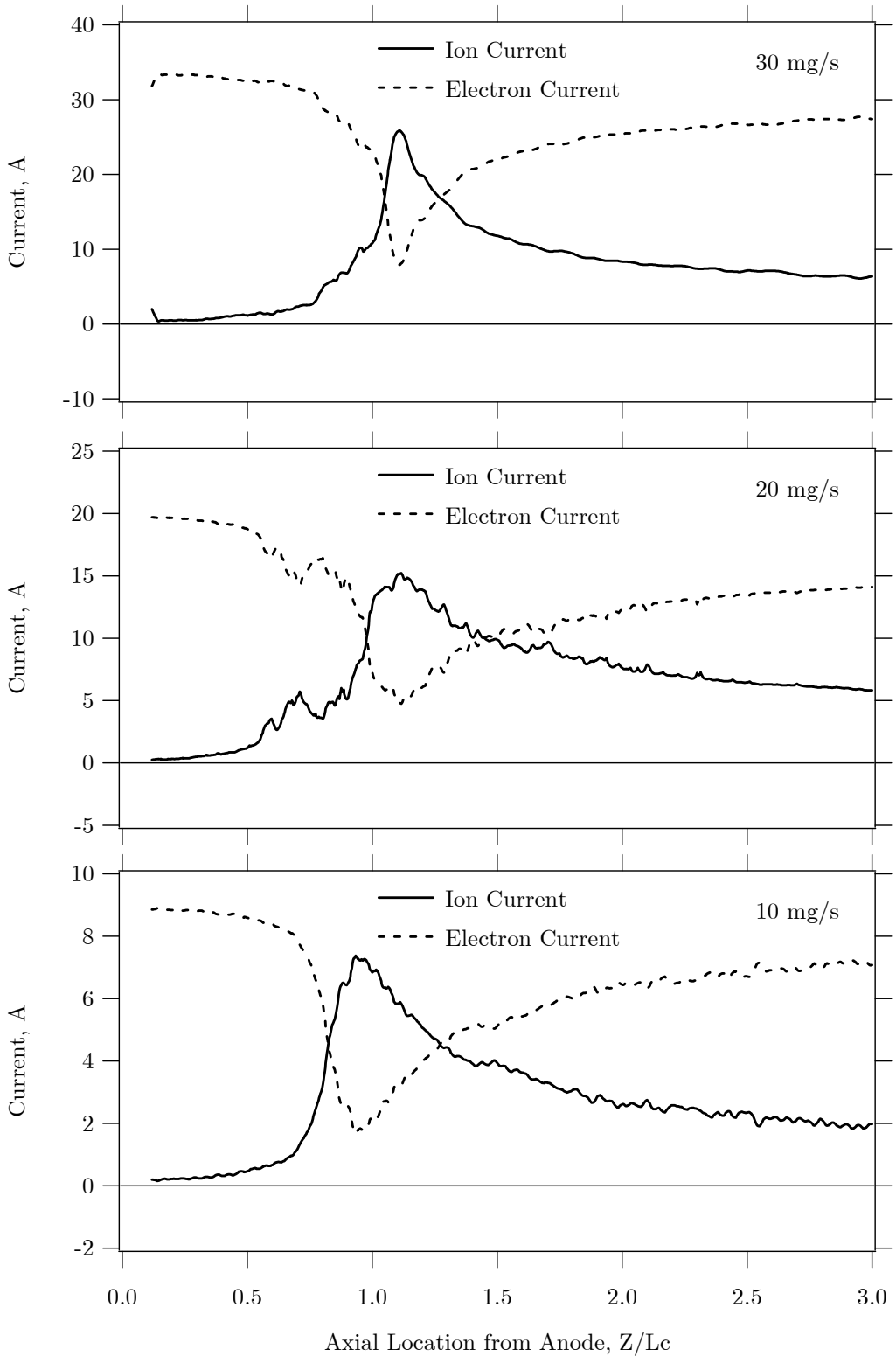

Figure 8-2. Experimental ion and electron currents at each axial location for operation at 300 V and 10, 20, and 30 mg/s.

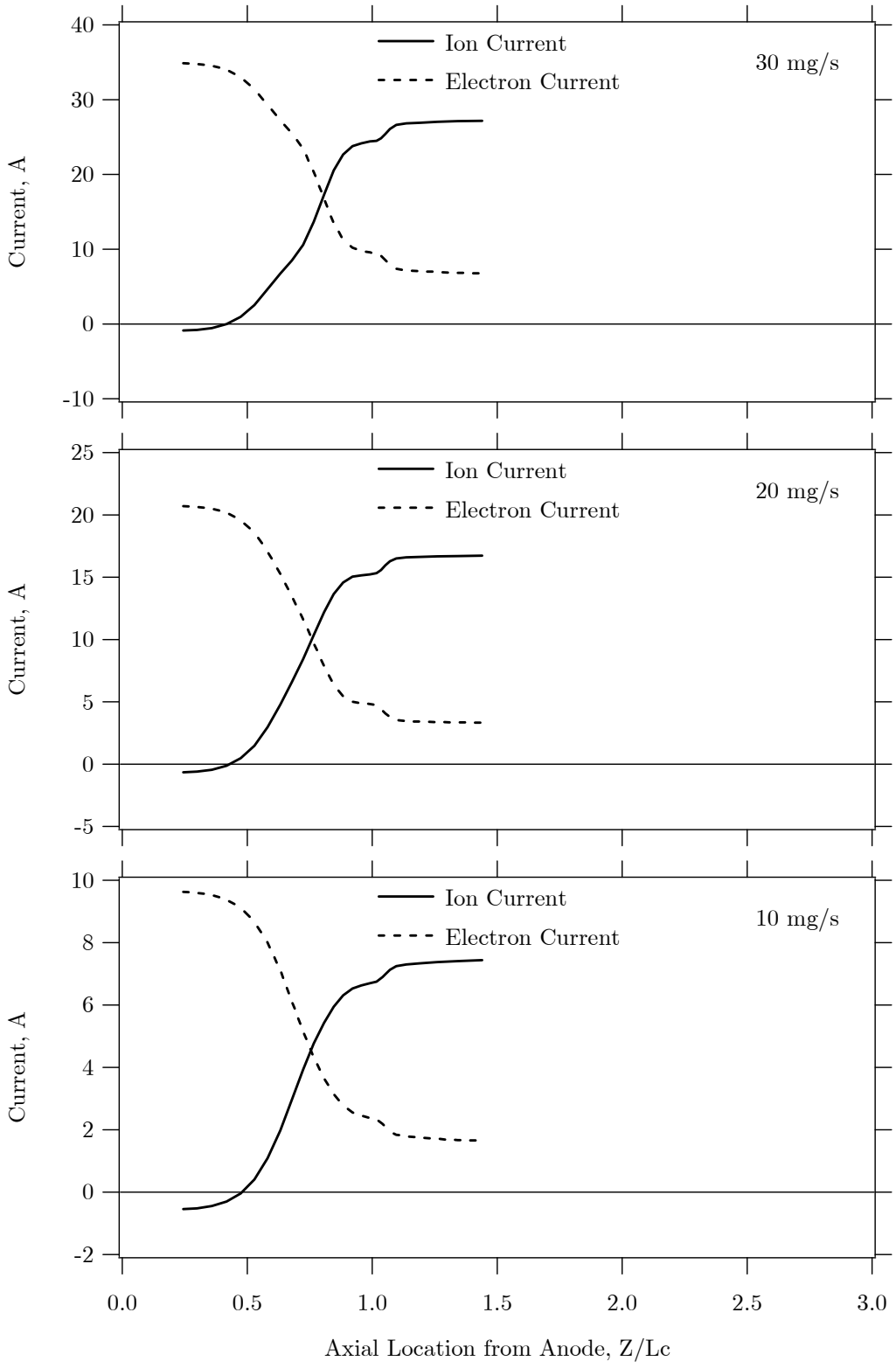

Figure 8-3. Simulated ion and electron currents at each axial location for operation at 300 V and 10, 20, and 30 mg/s.

temperature location occurred further downstream with increased flow rate. At 30 mg/s, this region of high electron temperature was almost entirely outside the thruster.

HPHall-2 simulations of ion and electron current are shown in Figure 8-3. The results showed a monotonic increase in ion current with increasing axial distance that saturated at approximately 120% L_c. This profile was more physical than the experimental ion flux that showed ion current decreasing outside the channel.

8.2.2 Neutral Density

The neutral density was calculated by using a 1-D heavy particle (ions and neutrals) mass continuity

$$\nabla \cdot \left(n_n \vec{u}_n \right) = -n_i n_n \varsigma \left(T_e \right), \tag{8-33}$$

$$\nabla \cdot \left(n_i \vec{u}_i \right) = n_i n_n \varsigma \left(T_e \right). \tag{8-34}$$

Combining these equations and discretizing:

$$\left(n_n u_n + n_i u_i \right)\Big|_z = \left(n_n u_n + n_i u_i \right)\Big|_{z-1}. \tag{8-35}$$

The flux calculation was initiated at the anode ($z = 0$) and the combined heavy flux was maintained at the injected mass flux from the anode ($\dot{m}_a / A_{ch}$).

The neutral number density calculated on channel centerline from Eq. 8-35 is shown in Figure 8-4 for thruster operation at 300 V and 10, 20, and 30 mg/s. The density was approximately constant inside the channel and dropped drastically near the exit plane. This decrease in neutral density was due to the

intense ionization that occurred in this region. Beyond the channel exit, the density drastically increased, reaching a significant fraction of its near-anode value. This shape was unphysical and simulations indicated that the density should continue to decrease outside the thruster. The results from simulations at 300 V and 10, 20, and 30 mg/s are shown in Figure 8-5. These results were highly correlated with the 1-D analysis within the thruster, but they diverged outside the thruster.

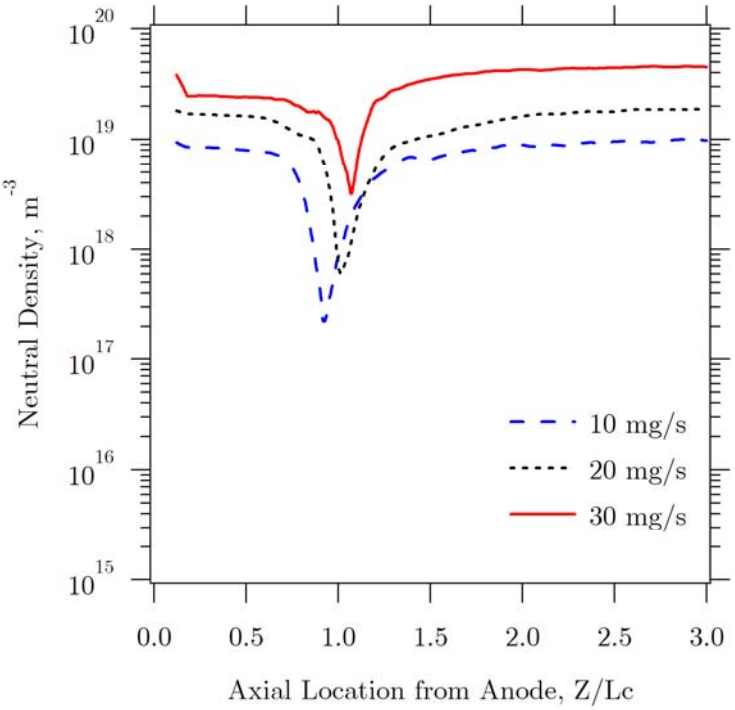

Figure 8-4. Centerline neutral density calculated from 1-D analysis for thruster operation at 300 V and 10, 20, and 30 mg/s (uncorrected).

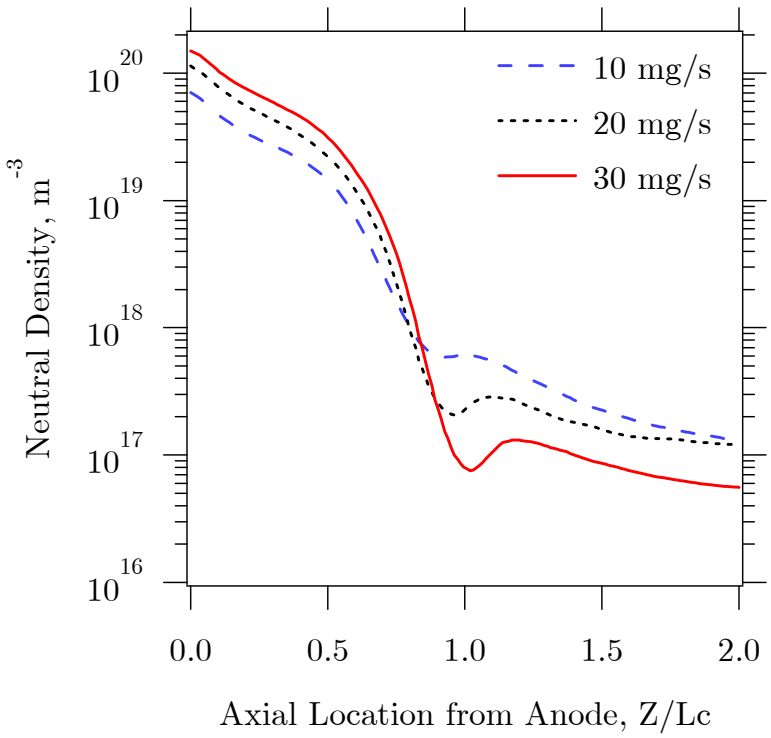

Figure 8-5. HPHALL-2 simulated neutral density on thruster centerline during thruster operation at 300 V and 10, 20, and 30 mg/s.

The drastic increase in density that was calculated by the 1-D continuity analysis beyond the exit plane was suggested to be influenced by recombination [51]; however, this effect is due to the loss of mass from diverging ions and expansion of neutrals through the boundary of the measurement domain. By using the measurement domain as a strict mass continuity boundary, the neutral density was unnaturally forced to compensate for mass lost through the domain boundary outside the channel. The unphysical increase in neutral density was corrected by accounting for the loss of mass from the domain, which was primarily due to the expansion of neutrals since ions had very large axial velocities. Although the velocity distribution of neutrals exiting the channel was skewed towards the positive axial direction (acceleration of neutrals was

discussed in Section 3.8), their collective behavior was reasonably approximated as a thermal distribution (as discussed below). In this case, neutrals exit the channel with a random orientation resulting in an effective exhaust area that takes the shape of a toroid. Using this assumption, the mass within the domain decreased with axial location since the neutral flow exiting the thruster was assumed to be distributed over a larger surface area with increased distance from the channel exit.

An illustration of the discrepancy in area definitions is shown in Figure 8-6. Inside the channel the area was taken as the annular thruster exit area and outside the channel the area was taken as a toroid having a radius equal to the axial distance from the channel exit. To facilitate a smooth transition near the exit plane, the first half channel width (0.5 b) downstream of the exit plane was populated with a linear interpolation between the two area definitions. To account for the axial velocity of neutrals (i.e., departure from random thermal motion assumption), a coefficient having a value of approximately 0.3 was used to reduce the effect of the toroidal area correction. The coefficient was adjusted until the neutral density in the plume matched the neutral density produced by HPHALL-2 simulations.

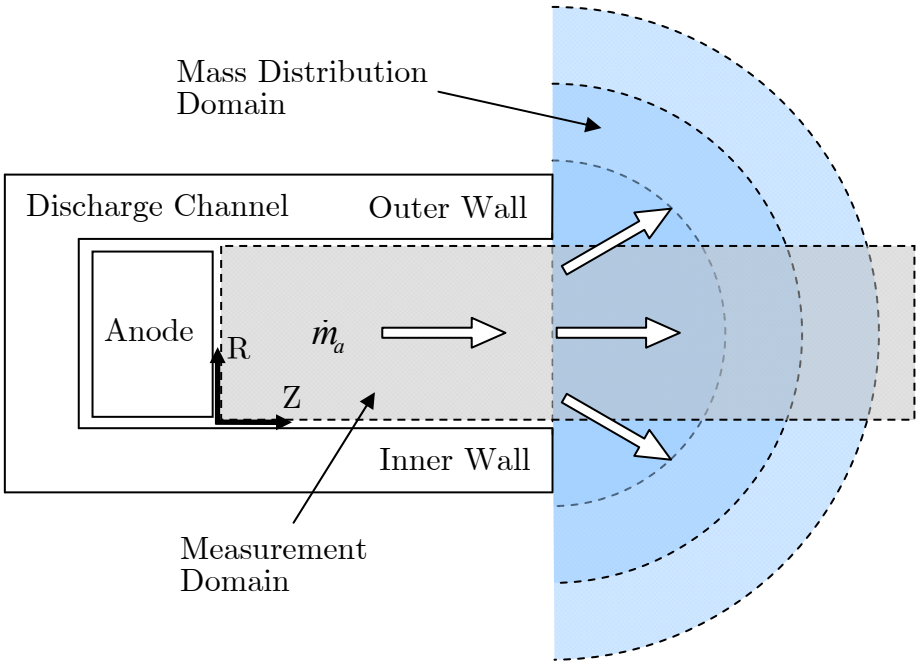

Figure 8-6. Schematic of the geometric area definitions used in the mass correction for the 1-D mass continuity analysis.

The validity of the toroidal area correction technique was supported by HPHALL-2 simulations that confirmed the decrease of mass flux within the experimental measurement domain downstream of the exit plane. The decrease in mass flux was dominated by loss of neutral flux through the radial boundaries. The toroidal area assumption produced a correction that linearly increased with distance from the thruster, which was consistent with the linear decrease in total mass flux calculated from HPHALL-2 simulation results shown in Figure 8-7. The initial drop in simulated mass flow was due to the radial expansion of neutrals exhausted by the anode, which leave the experimental measurement domain and occupy the region near the wall. Further downstream, the neutrals were accelerated towards the channel exit and channel center, increasing the total mass flow within the domain near the exit plane. Beyond the exit plane, ions and

especially neutrals expanded into the plume, effectively reducing the amount of mass flow contained within the measurement domain.

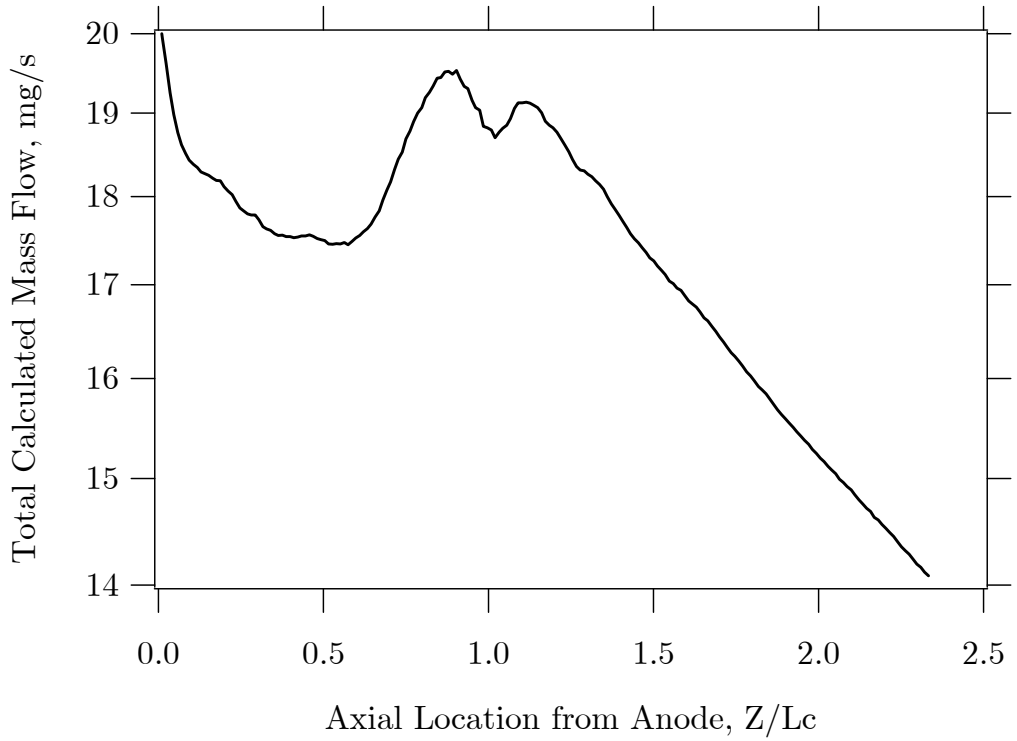

Figure 8-7. HPHALL-2 simulation results for the mass flux within the experimental measurement domain at 300 V and 20 mg/s.

The validity of the toroidal area correction technique was also supported by results of an analytical calculation of the neutral density within the plume. The calculation was derived by Katz (unpublished), and it uses view factors to determine the decrease in density with axial distance of a disk of particles exhausted into vacuum. The decay of neutral density closely resembled that produced by HPHALL-2 simulations and the toroidal area correction that was applied to experimental results.

The neutral density calculated by the 1-D analysis using the toroidal area correction is shown in Figure 8-8. The results displayed a density decrease outside the channel that resembled the HPHALL-2 simulated profile shape and magnitude. 2-D contours of the neutral density calculated from the 1-D analysis are shown in Figure 8-9 using an exponential scale for thruster operation at 300 V at 10, 20, and 30 mg/s.

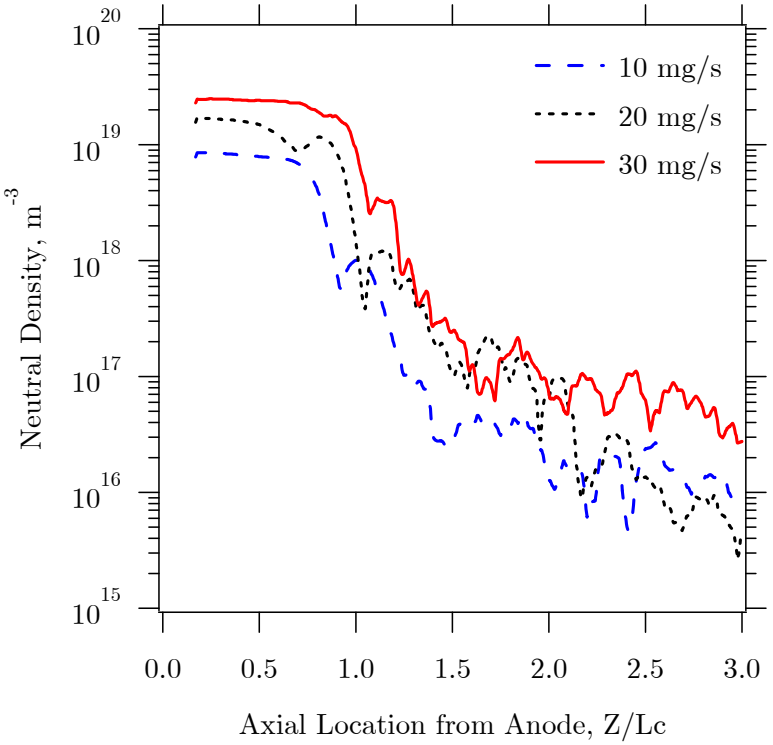

Figure 8-8. Centerline neutral density calculated from 1-D analysis for thruster operation at 300 V and 10, 20, and 30 mg/s (corrected).

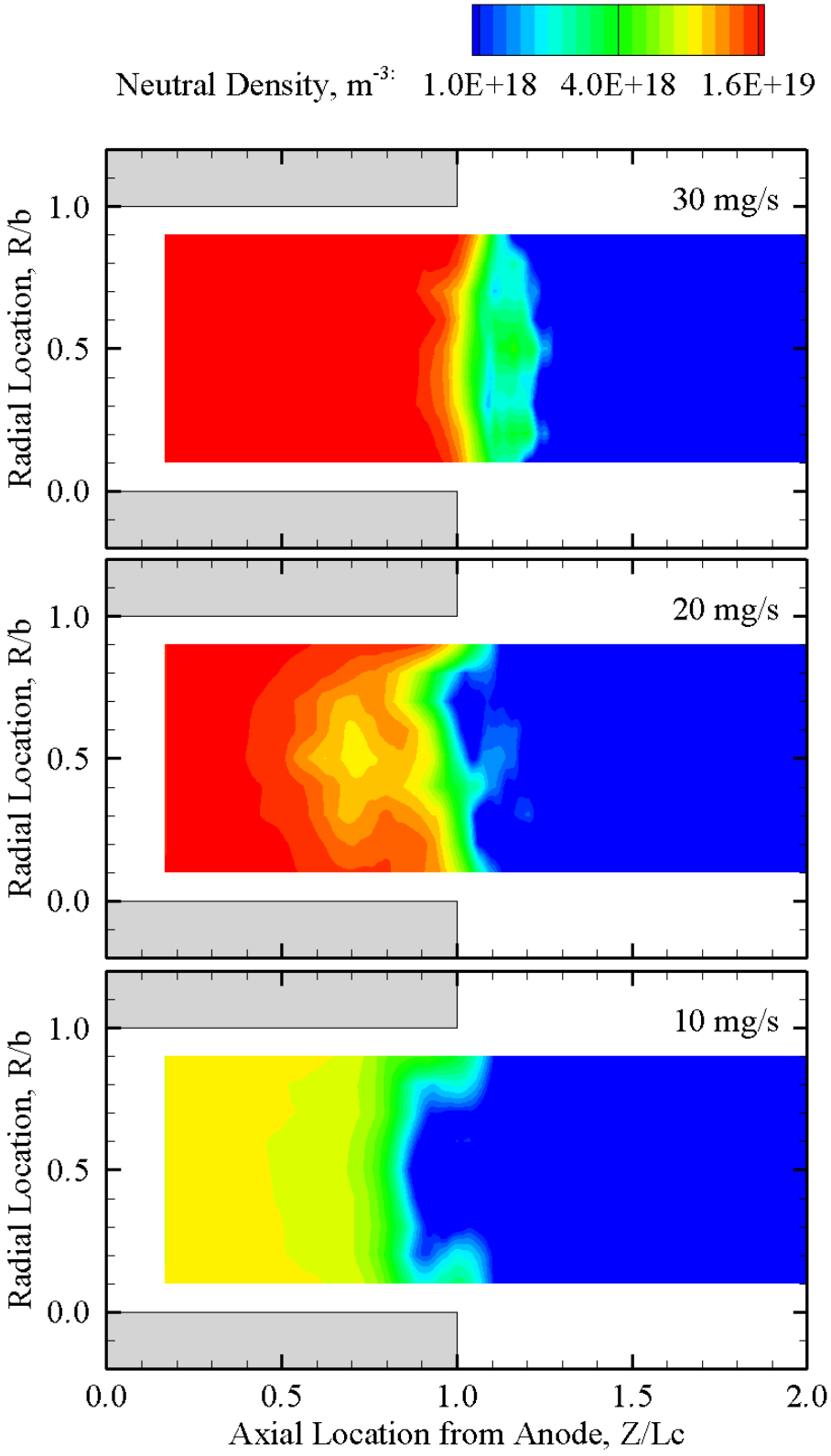

Figure 8-9. Contours of experimental neutral density during thruster operation at 300 V and 10, 20, and 30 mg/s (corrected).

As a comparison with the corrected experimental neutral density, the HPHALL-2 simulated neutral density is shown in Figure 8-10 at 300 V and 20 mg/s. The 2-D contours are represented with exponential spacing. Unlike the radially uniform results from the 1-D neutral analysis, the results from HPHALL-2 simulations showed a distinct plume that issued from the channel. Of particular importance was the boundary at the channel inner and outer radii that were correlated with the regions of increased fluctuations noted in the near-field Faraday probe measurements in Section 5.5.3. The shape of this boundary was controlled by neutral depletion near channel center due to the ionization process. This boundary also confirmed that a significant fraction of the neutral gas exhausted by the thruster expanded radially beyond the measurement domain used during internal plasma characterization.

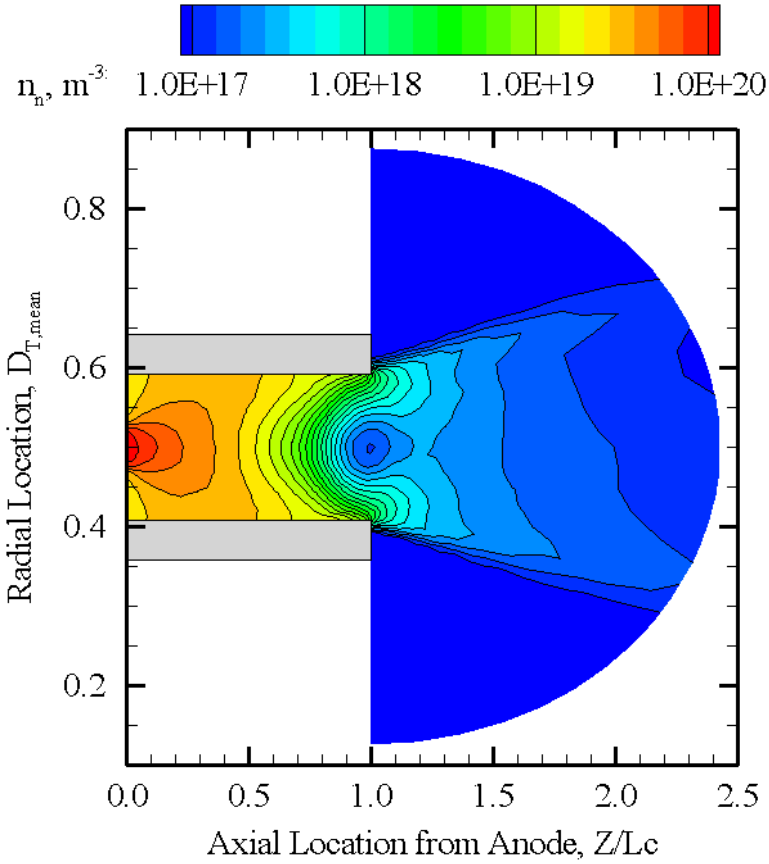

Figure 8-10. Contours of simulated neutral density for thruster conditions of 300 V and 20 mg/s.

8.3 Collision Frequency

The collision frequency is a critical parameter to consider when attempting to evaluate electron motion in Hall thruster plasmas. The collision frequency was calculated using experimental measurements and these results are compared to the simulated collision frequency from HPHALL-2.

8.3.1 Experimental Collisions

The electron collision frequency was calculated by combining ion density measurements and neutral density calculations. The classical collision frequency (Eq. 8-22) is composed of the electron-ion, electron-neutral collisions, and

electron-wall collisions. Results for the individual collision frequencies are shown in Figure 8-11 for thruster operation at 300 V and 10, 20, and 30 mg/s. The classical collision frequency was expected to exhibit a region of suppressed collision rate near the channel exit that corresponded to the location of the Hall current. In this region of low collision rate (i.e., low mobility), electrons were heated by the electric field and trapped in E×B motion resulting in ionization of the neutral population. Once ions were created, they were immediately accelerated through the electric field. Since the neutrals were depleted by ionization and the ions were lost to acceleration into the plume, the classical electron collision frequency was expected to drop in this region due to the significant decrease in ion and neutral density. However, the calculated neutral density remained high, preventing the total collision frequency from decreasing in a measureable amount. Outside the channel, the classical electron collision frequency monotonically decreased as the neutral and ion densities decreased.

The wall collision frequency peaked near the exit plane at all operating conditions. At 10 mg/s the electron-wall collision frequency exceeded the electron-neutral collision frequency near the channel exit. At 20 and 30 mg/s the electron-wall collision frequency was lower than (but on same order as) the electron-neutral collision frequency. This result indicates that the wall collisions played a greater role at lower flow rates. This conclusion is consistent with the downstream movement of the ionization region that was presented in Chapter 7.

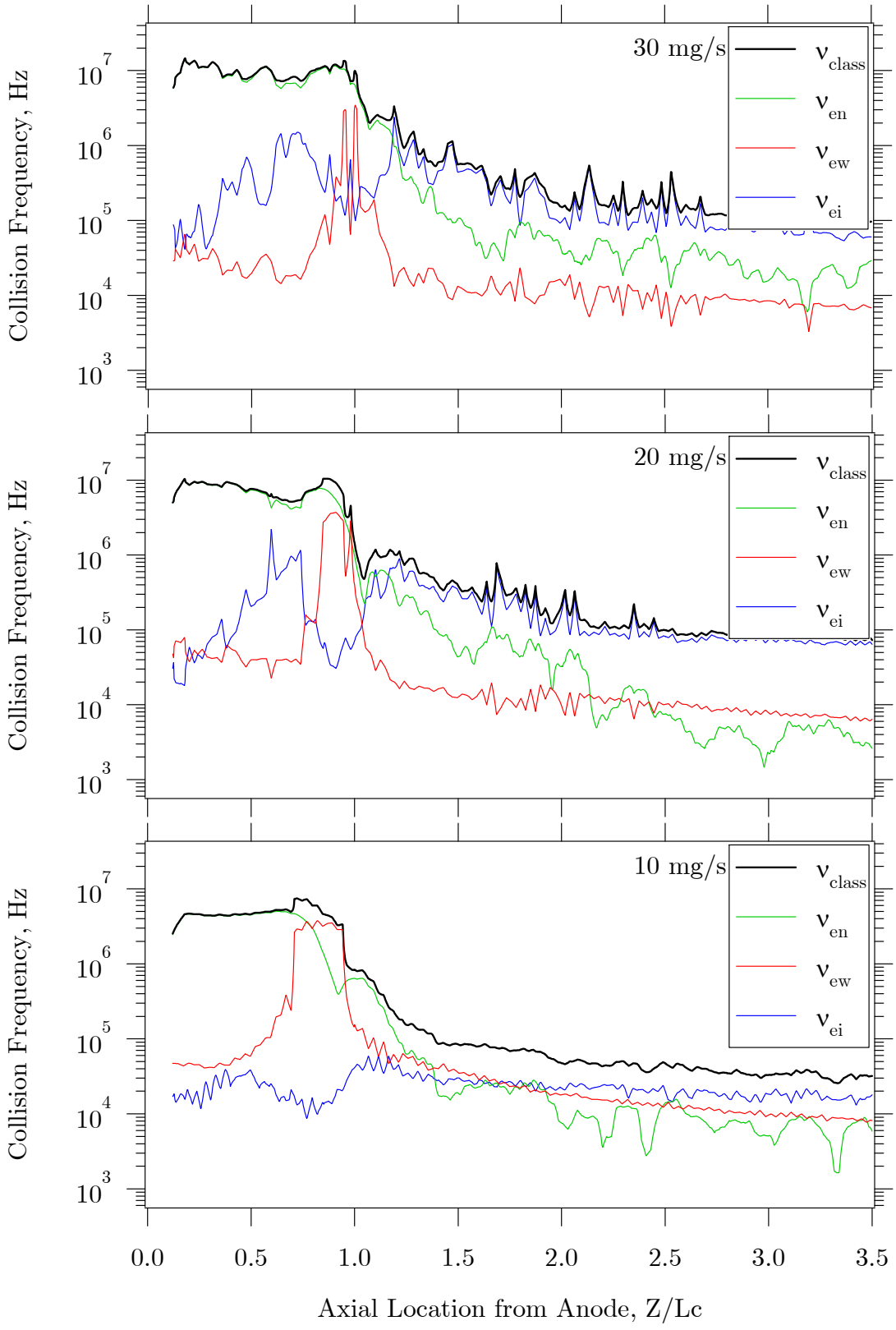

Figure 8-11. Electron collision frequencies for thruster operation at 300 V and 10, 20, and 30 mg/s.

Since ionization occurred further downstream, the neutral density decreased further downstream. Hence, the electron-neutral collision rate remained higher for more of the channel length as flow rate increased, allowing neutral collisions to account for a larger fraction of the total collision rate.

The large neutral collision rate throughout most of the channel is consistent with the previous claim that neutrals control the location of the ionization, high electron temperature, and acceleration regions. This topic is discussed further in Section 8.6.1. In addition, the diminishing impact of wall collisions with flow rate provides evidence that electron-neutral collisions may have contributed to the electron temperature cooling measured with the Langmuir probe. This topic is discussed further in Section 8.6.2

8.3.2 HPHALL-2 Simulations

Electron collision frequencies from HPHALL-2 simulations are shown in Figure 8-12 for nominal thruster settings of 300 V and 20 mg/s. These results were representative of results at 10 and 30 mg/s. Unlike the experimental collision frequency, the total simulated collision frequency exhibited a region of suppressed collisions near the channel exit in the expected location of E×B electron drift. This region occurred because the simulated neutral density decreased well upstream of the experimental calculations. The reason for the discrepancy in neutral density is not well understood.

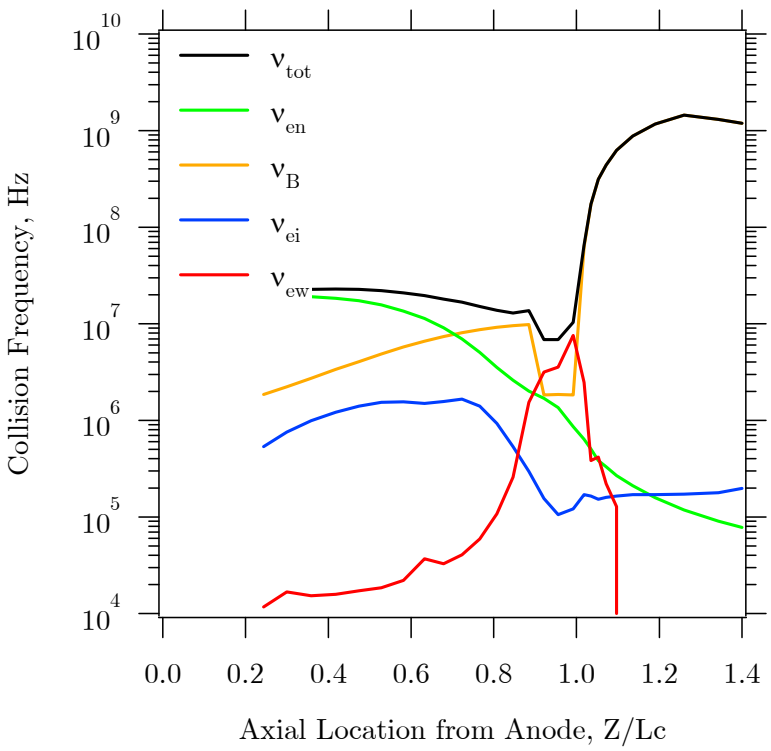

Figure 8-12. HPHALL-2 simulated collision frequencies 300 V and 20 mg/s. Values are volume-weighted averages over magnetic field lines.

Although the total simulated collision frequency had a different profile than the experimental data, the magnitudes were in good agreement. Similar to the experimental data, the electron-wall collision frequency exceeded the electron-neutral and Bohm values near the exit plane. This indicates that the channel wall plays a significant role in cross-field electron diffusion within HPHALL-2.

8.4 Hall Parameter

The Hall parameter is a critical quantity to consider when evaluating electron mobility in the channel. The Hall parameter is essentially the inverse of the total cross-field mobility. The Hall parameter is calculated by the two methods described in the preceding discussions allowing comparisons between the

so-called classical and total Hall parameters. The Hall parameter from HPHALL-2 simulations is also discussed and compared to the experimentally derived values. Finally, the turbulent collision frequency is estimated by calculating the collision frequency that is necessary to account for the observed differences between the two Hall parameter calculations (classical and experimental).

8.4.1 Classical Hall Parameter

Using the electron-neutral, electron-ion, and electron-wall collision frequency results in Figure 8-11, the classical Hall parameter (Eq. 8-15) was calculated and the results are shown in Figure 8-13 for thruster operation at 300 V and 10, 20, and 30 mg/s. The Bohm value of 16 is highlighted in black for reference. The Bohm value was reached at approximately 50% L_c for all three flow rates, indicating electron mobility that is dominated by classical collisions near the anode. Outside the channel, the Hall parameter increases drastically, obtaining a value of greater than 1,000. This result is not physical since it would suggest that electrons are highly trapped far from the thruster, which can not occur since the electric field is negligible. The unphysical high Hall parameter outside the thruster indicates that the classical analysis is not accounting for all of the electron transport mechanisms.

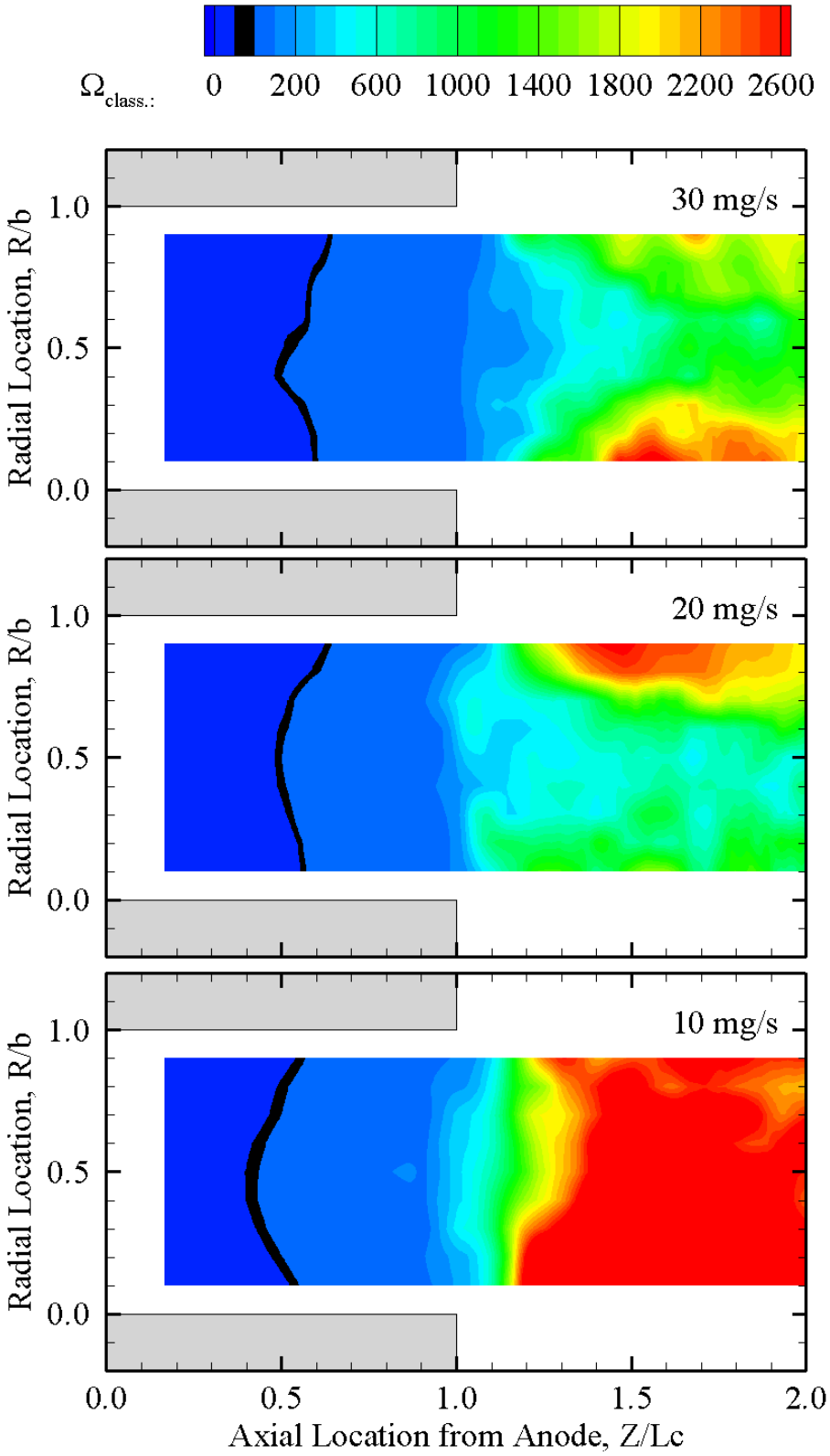

Figure 8-13. Classical Hall parameter contours for thruster operation at 300 V and 10, 20, and 30 mg/s.

The classical Hall parameters at 10, 20, and 30 mg/s are compared in Figure 8-14, where the Bohm value of 16 is included as a horizontal line for reference. The classical Hall parameter remained well above the Bohm value outside the thruster. The Hall parameter slowly decreased due to the magnetic field structure and lack of neutral or ion collisions with electrons.

The classical Hall parameter reached a global maximum at approximately 150% L_c for all three flow rates, which is well downstream of the expected location of the Hall current. Since the Hall current is composed of electrons in E×B motion, the Hall current was expected to occur at the location of maximum electric field, which was near the exit plane for all three operating conditions (see Section 7.3.4). The global peak occurring at 150% L_c is an unphysical result that was dominated by the electron-wall collision frequency. The wall collision frequency peaked near the exit plane, and the large magnitude decreased the Hall parameter near the exit and completely removed the peak that would have corresponded to the expected location of the Hall current.

The unphysical shape can be significantly improved by removing the wall collisions from the classical analysis. In doing so, the classical Hall parameter produced an initial peak near the thruster exit plane. The secondary peak was still present since the calculated collision rate from electrons and neutrals were not high enough in the near-field plume.

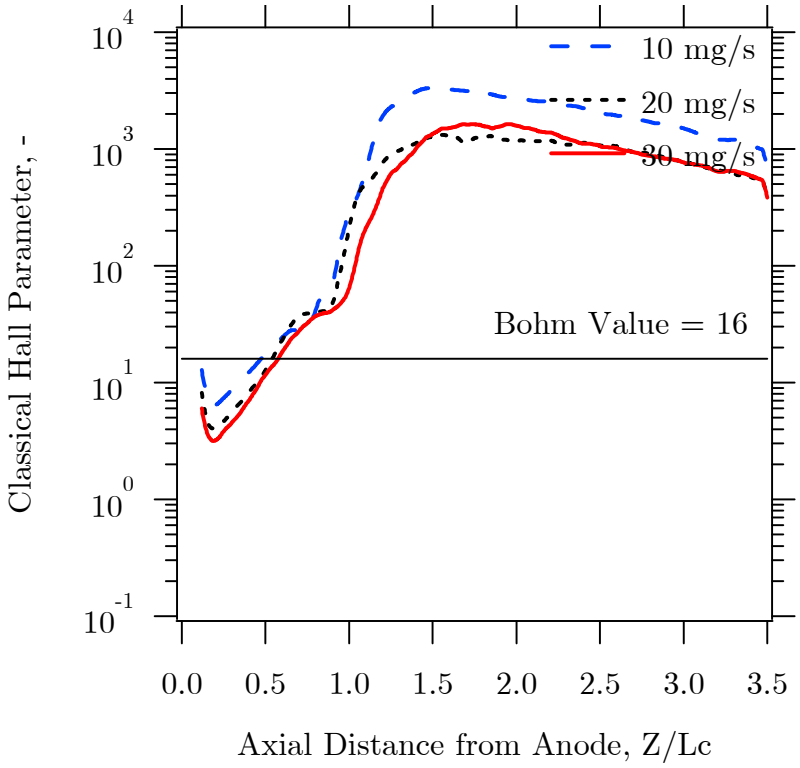

Figure 8-14. Radially-averaged classical Hall parameter (including wall collisions) downstream of the anode for thruster operation at 300 V and 10, 20, and 30 mg/s.

Another way to view these results is by comparing the Hall parameter to the plasma potential as shown in Figure 8-15. Since these comparisons removed the spatial dependence of the Hall parameter, the exit plane location was highlighted for each flow rate. These results indicated that the Hall parameter was primarily independent of the plasma potential since the profiles are approximately constant from 50 to 250 V. This also highlighted the fact that the ion acceleration occurred over a relatively short distance that was coincident with the region of highest Hall parameter.

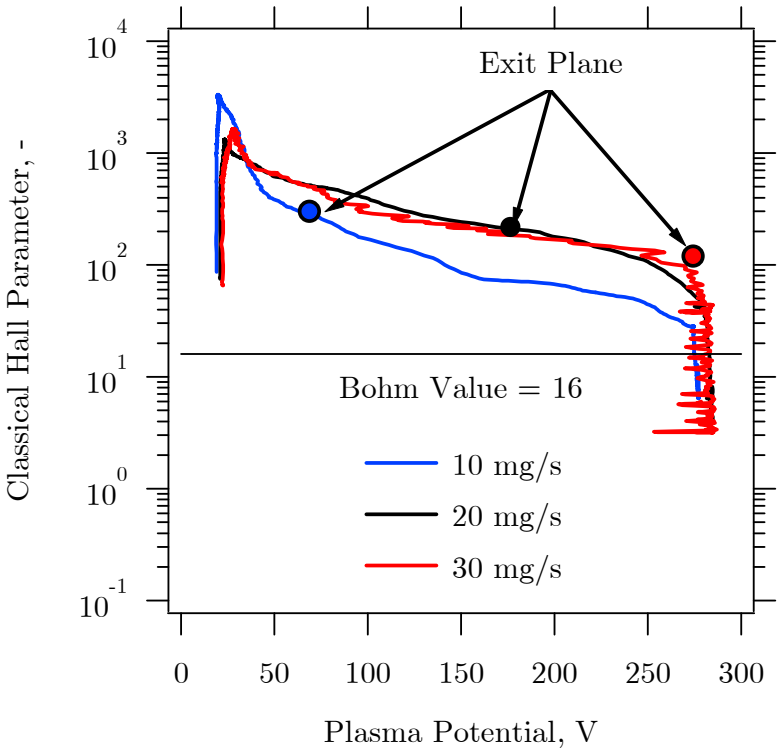

Figure 8-15. Radially-averaged classical Hall parameter as a function of plasma potential for thruster operation at 300 V and 10, 20, and 30 mg/s.

8.4.2 Total Hall Parameter

The total Hall parameter was calculated from Eq. 8-30 and the results are shown in Figure 8-16. The Bohm value of 16 is highlighted in black for reference. The total Hall parameter peaked near the thruster exit plane at all three flows and moved downstream with each increase in flow rate, consistent with the classical Hall parameter results. The total Hall parameter indirectly accounts for all sources of electron transport, producing a profile that better represents the mobility in the near-field plume. As such, the total Hall parameter is more useful than the classical Hall parameter.

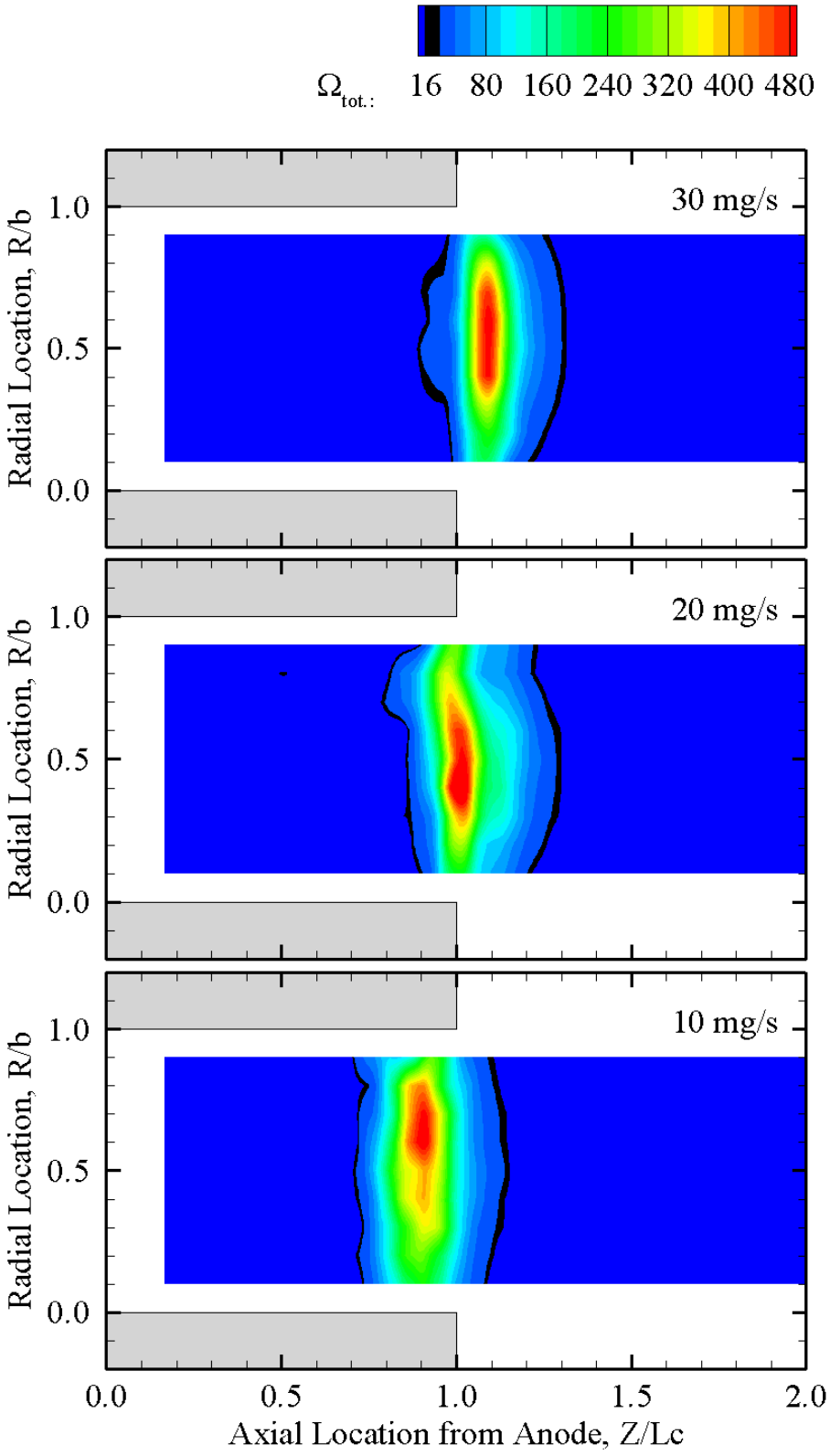

Figure 8-16. Total Hall parameter contours for thruster operation at 300 V and 10, 20, and 30 mg/s.

The total Hall parameters at 10, 20, and 30 mg/s are compared in Figure 8-17, where the Bohm value of 16 is included as a horizontal line for reference. The total Hall parameter peaked at 92, 101, and 109% L_c for 10, 20, and 30 mg/s, respectively. These results indicated that the location of the Hall current moved downstream approximately 9% L_c with each increase in flow rate (consistent with results in Chapter 7). The peak locations for the total Hall parameters were very similar to the peak electric field locations of 93, 100, and 107% L_c (see Table 7-3). This consistency was expected since the total Hall parameter was calculated using the azimuthal electron velocity, which is dominated by the E×B velocity (~E/B).

The magnitude of the total Hall parameter decreased linearly with increased flow rate, having values of 625, 555, and 470 at 10, 20, and 30 mg/s, respectively. These values were consistent with those reported by Haas [109] and Linnell [51], as were the low values outside the channel (approximately unity). Although the Hall parameter decreased by approximately 10-15% with each addition of 10 mg/s, the results still indicate that there is a finite bandwidth of Hall parameter values that allow efficient operation of Hall thrusters. The Hall parameter is expected to fall within a value of several hundred to maintain efficient operation [88].

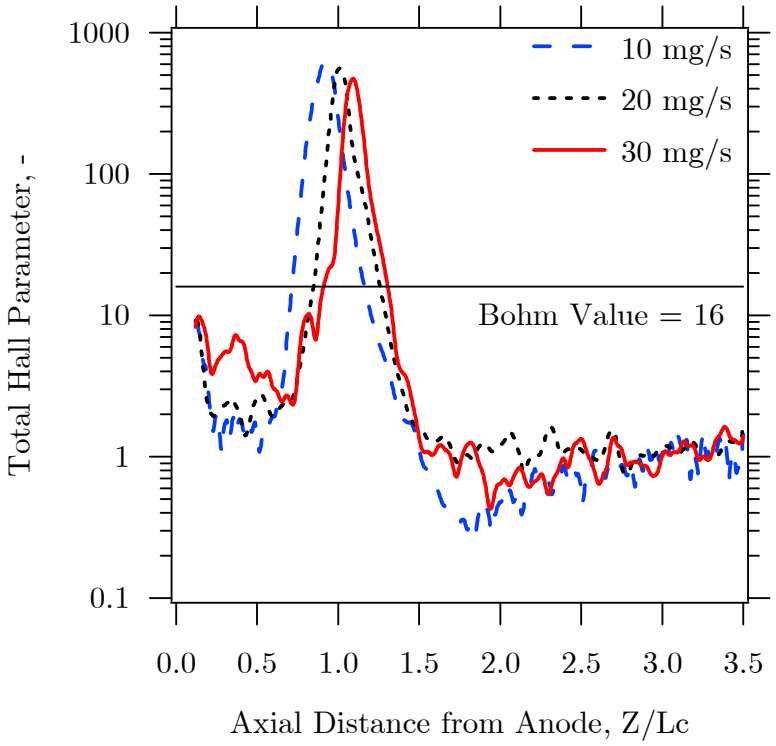

Figure 8-17. Radially-averaged total Hall parameter downstream of the anode for thruster operation at 300 V and 10, 20, and 30 mg/s.

Consistent with the comparison for the classical Hall parameter, the total Hall parameter is shown as a function of the plasma potential in Figure 8-18. Since these comparisons removed the spatial dependence of the Hall parameter, the exit plane location was highlighted for each flow rate. The independence of the Hall parameter from the plasma potential is more pronounced in the experimental results than the classical results, highlighting the intense ion acceleration that occurs near the channel exit.

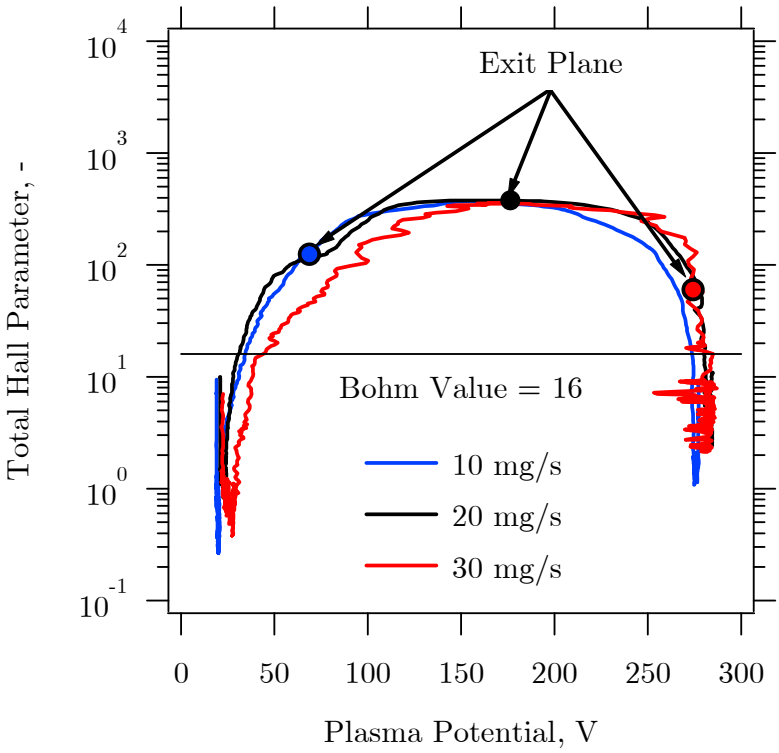

Figure 8-18. Radially-averaged total Hall parameter as a function of plasma potential for thruster operation at 300 V and 10, 20, and 30 mg/s.

The total Hall parameter results support the discussion in Section 8.6.1, which identifies the electron-neutral collision frequency as the primary mechanism for the ionization and acceleration regions occurring further downstream with increased flow rate. Hall parameter results showed that as flow rate increased the collision rate in the channel increased, and remained high over more of the channel, which led to a decrease in Hall parameter (increased electron mobility).

8.4.3 HPHALL-2 Simulations

The HPHALL-2 simulated classical Hall parameter is shown in Figure 8-19 on channel centerline for thruster operation at 300 V and 10, 20, and 30 mg/s.

The simulated classical Hall parameter exhibited the same shape as the experimental classical Hall parameter, having a peak upstream of the exit plane and another downstream of the exit plane.

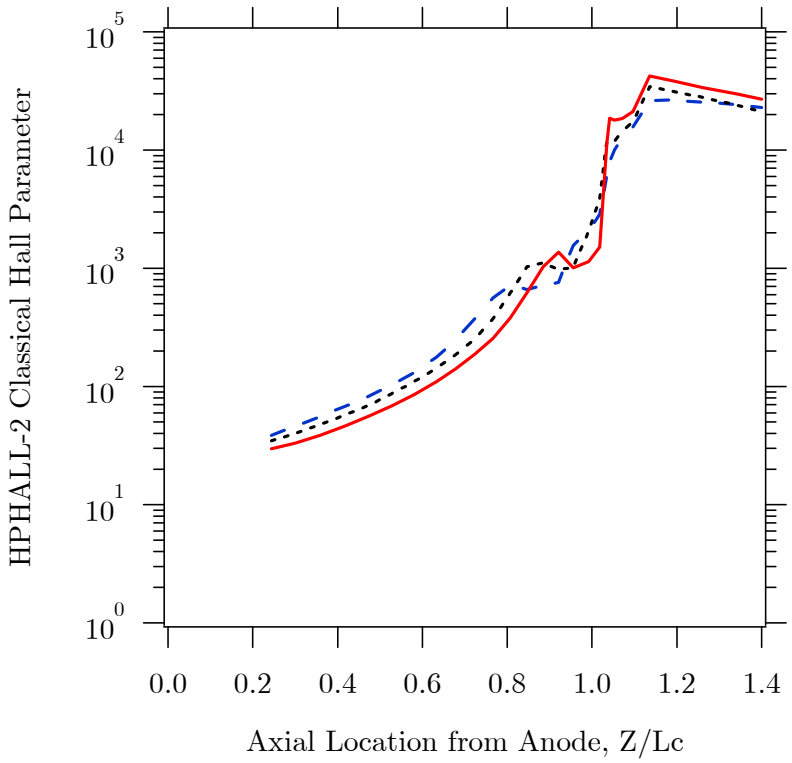

Figure 8-19. Simulated classical Hall parameter on channel centerline for thruster operating conditions of 300 V and 10, 20, and 30 mg/s.

The HPHALL-2 simulated total Hall parameter is shown in Figure 8-20 on channel centerline for thruster operation at 300 V and 10, 20, and 30 mg/s. The simulated total Hall parameter was analogous to the total Hall parameter calculated in previous sections with experimental data. The simulated total Hall parameter peaked at a value of 890, 745, and 690 at 96, 99, and 104% L_c for thruster conditions of 300 V and 10, 20, and 30 mg/s respectively. The peak

locations and magnitudes were in good agreement with the experimentally observed values.

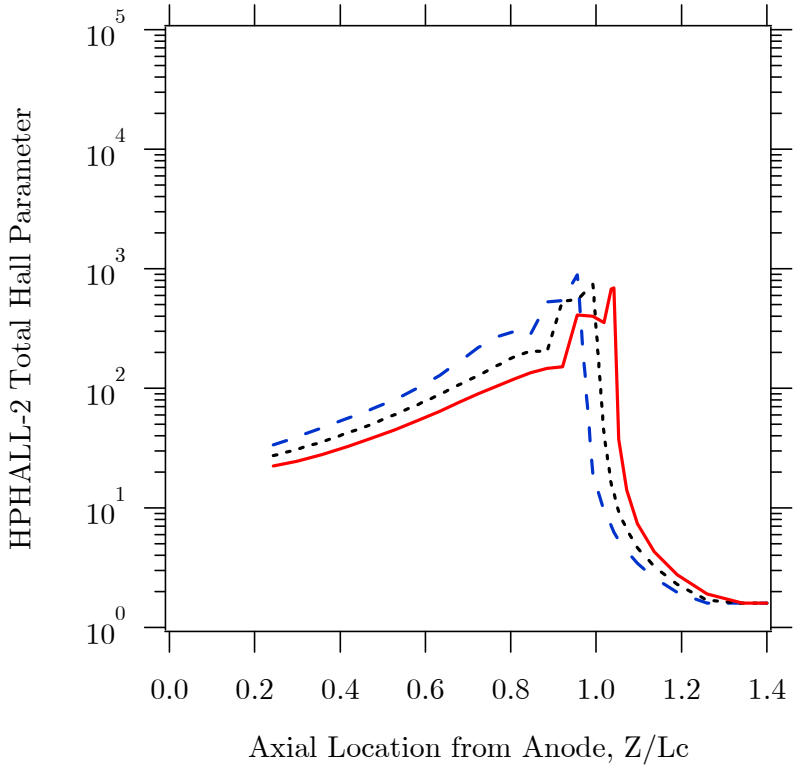

Figure 8-20. Simulated total Hall parameter on channel centerline for thruster operating conditions of 300 V and 10, 20, and 30 mg/s.

The simulated Hall parameter results exhibited the same discrepancy between the classical and total Hall parameters outside the thruster. The discrepancy was due to the relatively high Bohm mobility that was imposed in the plume to increase the simulation's correlation with experimental data [61]. The physical mechanisms that contribute to this high level of anomalous electron diffusion deserves further attention in future investigations.

8.4.4 Discrepancy in the Near-field Plume

The results in Figure 8-14 and Figure 8-17 indicated good agreement between the classical and total Hall parameter calculations at each flow rate inside the thruster. However, there was significant discrepancy in the near-field plume, continuing the widely-observed result of classical analyses severely underpredicting the experimentally observed electron mobility. The classical Hall parameter was more than an order of magnitude higher than the experimental value in the near-field plume. This discrepancy indicated that the classical analysis improperly accounted for the electron mobility by only considering contributions from electron-ion, electron-neutral, and electron-wall collisions. These collisions can not be the only mechanism for electron mobility since the ion and neutral densities decreased rapidly outside the thruster and the magnetic field remained on the order of 10 G at 1 $D_{T,mean}$ downstream.

The large discrepancy between the classical and total Hall parameters in the near-field plume indicates some type of anomalous transport mechanism, which is likely attributed to turbulence. It should be noted that the mechanism for sustaining turbulence in the near-field plume is not immediately clear since the electric field and electron temperature are low. For now, we assume that turbulence is the determining factor for the discrepancy between the two Hall parameter calculations.

The total Hall parameter can be converted to the total collision frequency, using

$$\nu_{tot} = \frac{e\,B}{m_e\,\Omega_{tot}}. \tag{8-36}$$

The total collision frequency considers all transport, whereas the classical collision frequency only accounts for electron-neutral, electron-ion, and electron-wall collisions:

$$\begin{aligned} \nu_{tot} &= \nu_{en} + \nu_{ei} + \nu_{ew} + \nu_{turb} \\ \nu_{class} &= \nu_{en} + \nu_{ei} + \nu_{ew} \end{aligned}. \tag{8-37}$$

Using this relationship, the turbulent collision frequency can be calculated as the difference between the classical and total collision frequencies. The turbulent collision frequency is then simply the collision frequency that is necessary to account for the difference between the classical and total Hall parameters. The calculated turbulent collision frequency is divided by the Bohm value to create a turbulence intensity ratio that allows the amount of turbulence to be discussed in terms relative to the Bohm collision frequency. It should be noted that the turbulence intensity ratio is the inverse of the Bohm coefficient in Eq. 8-29.

Results for the turbulence intensity ratio are shown in Figure 8-20. The results confirm the existence of at least three distinct regions where the turbulent collision frequency has a unique value. As a reminder, the three regions were: region I: near-anode, region II: near exit plane, and region III: near-field plume as discussed in Sections 3.3.3 and 7.4.2 and Ref. [61]. The three regions are approximately bounded by the location where the turbulence intensity ratio

passes through unity, demarcating the point where the necessary turbulence is below the Bohm value (turbulence suppression).

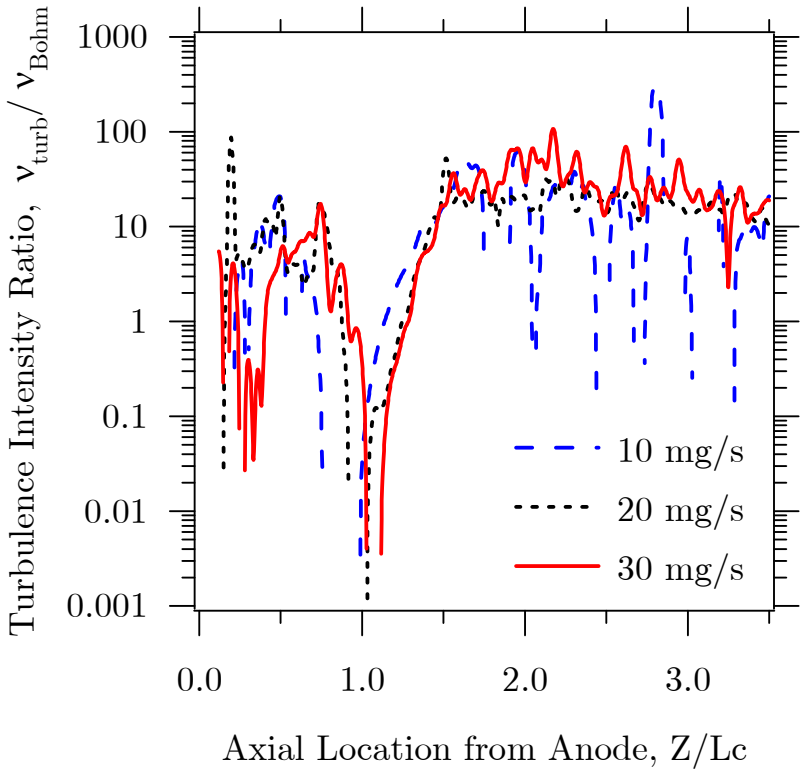

Figure 8-21. Turbulence intensity ratio along channel centerline for thruster operation at 300 V and 10, 20, and 30 mg/s.

In region I, the turbulence required to account for the difference between the classical and total Hall parameter was on the order of 1-10 times greater than the Bohm value. This result was somewhat unexpected since the electron mobility inside the channel is typically closely-approximated by classical collisions alone. These results indicate that there may be additional turbulent transport inside the channel. In region II, the required turbulence was suppressed, which is consistent with the result that the Hall current exists in the location of lowest mobility. In region III, the turbulence must be on the order of 10-100

times greater than the Bohm value. This is consistent with the Bohm coefficient of 10 that was used in the near-field plume during HPHALL-2 simulations [61]. The large turbulence intensity ratio outside the channel was also noted in simulations in Refs. [28] and [164]. Those simulations were implemented with turbulence intensity ratios of approximately 100 to produce results that were in good agreement with experiments.

8.5 Hall Current

The total Hall-current density was calculated from the azimuthal velocity using

$$j_{Hall} = en_i \frac{\Omega_e}{1+\Omega_e^2}\left[\mu E_\perp + \frac{D}{T_e}\frac{\partial T_e}{\partial \perp} + \frac{D}{n_e}\frac{\partial n_e}{\partial \perp}\right], \tag{8-38}$$

which is simply Eq. 8-20 multiplied by the ion density and elementary charge. As a reminder, the first term in the bracket on the RHS is the E×B velocity component, and the remaining two terms represent the diamagnetic contribution. Although not shown separately, the diamagnetic component of the Hall-current density was always approximately an order of magnitude smaller than the E×B component.

The Hall-current density is shown in Figure 8-22 for thruster operation at 300 V and 10, 20, and 30 mg/s. The location of the Hall current moved downstream with increased flow rate in a manner consistent with ion density, electron temperature, and electric field results that were presented in Chapter 7.

It should be noted that the Hall-current density is dominated by the electric field, so minor changes in the ion density peak location due to selection of thin sheath, OML, or blended analysis have little effect on these results. At 30 mg/s, the Hall current was almost entirely outside the discharge channel. Although no erosion measurements have been recorded, moving the Hall current downstream should lead to increased thruster lifetime since ions will have a lower probability of impacting the channel walls.

The magnitude of the Hall-current density was proportional to the flow rate in a manner that was consistent with the increase in ion density. The "total Hall current" was calculated from these data by integrating the Hall-current density, producing azimuthal currents of approximately 25, 45, and 72 A at 300 V and 10, 20, and 30 mg/s, respectively. These integrated azimuthal currents were approximately 2-3 times higher than the discharge current. These results were consistent with the results of Hass [109] and Linnell [51] that indicated Hall currents that were 2-3 and 3-4 times larger than the discharge current, respectively.

The location of the Hall current at 20 mg/s was highly correlated with the location of probe failure in the early stages of data collection at 20 mg/s. On several occasions, the alumina probe shaft melted and broke at the thruster exit. It was believed that interaction from the intense Hall current was responsible and these results support that hypothesis.

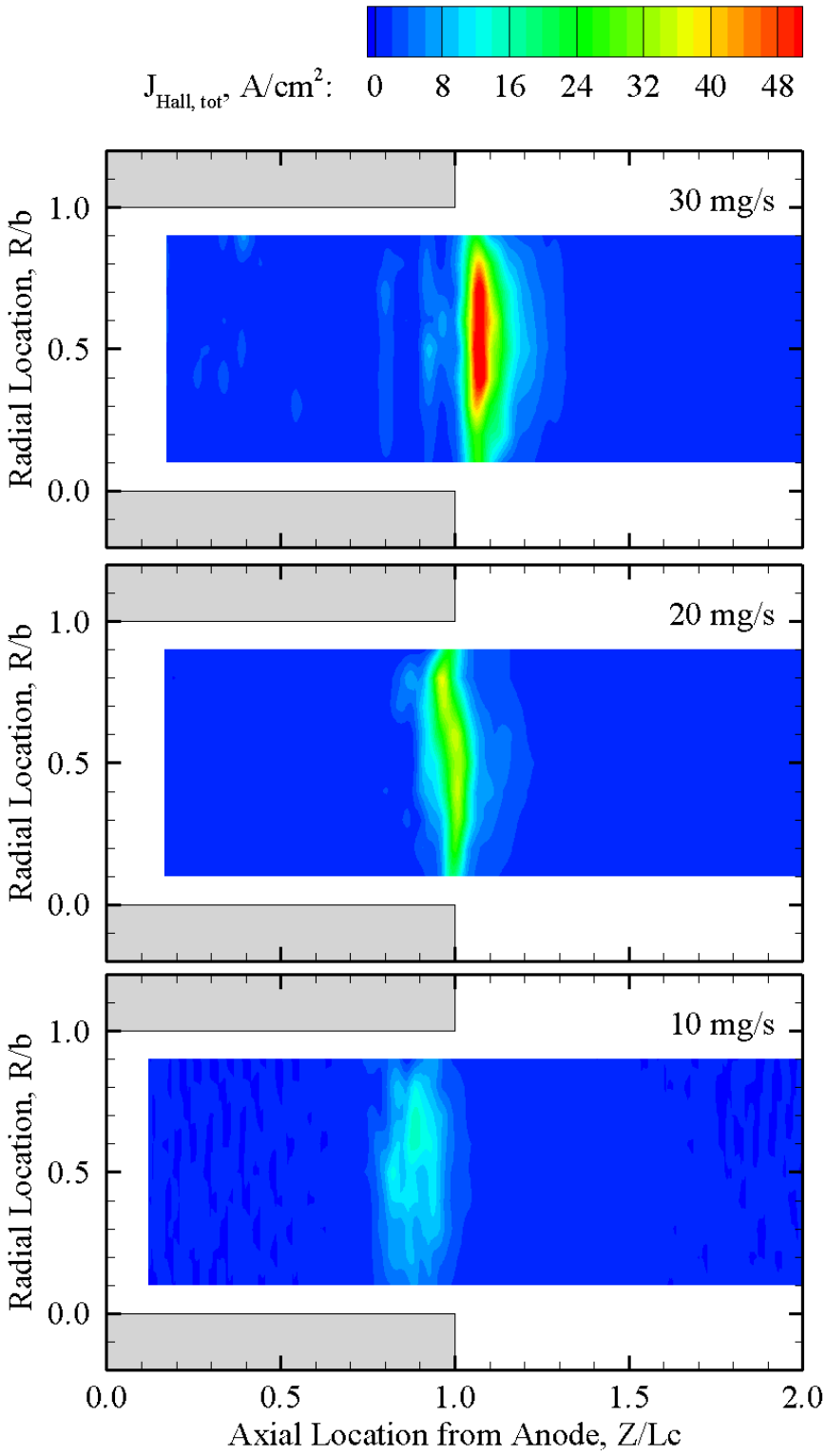

Figure 8-22. Hall current contour plots for thruster operation at 300 V and 10, 20, and 30 mg/s.

8.6 Trends with Flow Rate

The measurements in Chapter 7 showed that the ionization, high electron temperature, and acceleration regions moved downstream with flow rate and that the electron temperature decreased with flow rate. This section provides additional discussion on the mechanisms that contributed to these trends.

8.6.1 Internal Regions

As flow rate increased, the ionization, high electron temperature, and acceleration regions moved downstream by 5-7% L_c. Although details of the magnetic field can not be discussed (due to ITAR), it is worth noting that the downstream location of ionization and acceleration regions occurred beyond the peak radial magnetic field. The downstream boundary remained approximately stationary as flow rate increased; however, the upstream boundary moved further downstream (see Section 7.4.1 for addition details).

Within the discharge channel, neutrals played a significant role in augmenting the electron mobility through electron-neutral collisions. Again, the electron-neutral collision rate is directly proportional to the neutral density (see Eq. 8-23), which is directly proportional to the mass flow rate (see Section 3.7.3); thus, increasing the mass flow rate is equivalent to increasing the electron-neutral collision rate within the channel.

As neutral flow rate increased, the peak electron temperature moved downstream, primarily due to the increased electron-neutral collision rate in the

channel. The downstream motion of the high electron temperature region is illustrated in Figure 8-23, where the region of high neutral density is shown near the anode and the region of high electron temperature is shown near the exit plane. The ions are not included in this diagram since they have much less influence over the electron mobility than neutrals (see collision rates in Section 8.3). As Figure 8-23 shows, the region of high neutral density persisted further downstream as flow rate was increased, causing the region of hot electrons to move downstream. This qualitative explanation was consistent with the collision frequency analysis in Section 8.3 that indicated the electron-neutral collision frequency shifted downstream by 5-7% L_c for each 10 mg/s increment (same movement as ionization, acceleration, and high electron temperature regions). Since the collision frequency remained higher over a larger portion of the channel, the electron mobility remained high near the anode, eroding the upstream boundary of the high electron temperature region, and forcing the peak location to move downstream. Again, this qualitative explanation is consistent with experimental measurements of the electron current, which indicated a larger electron recycle fraction as flow rate increased (see Section 6.4).

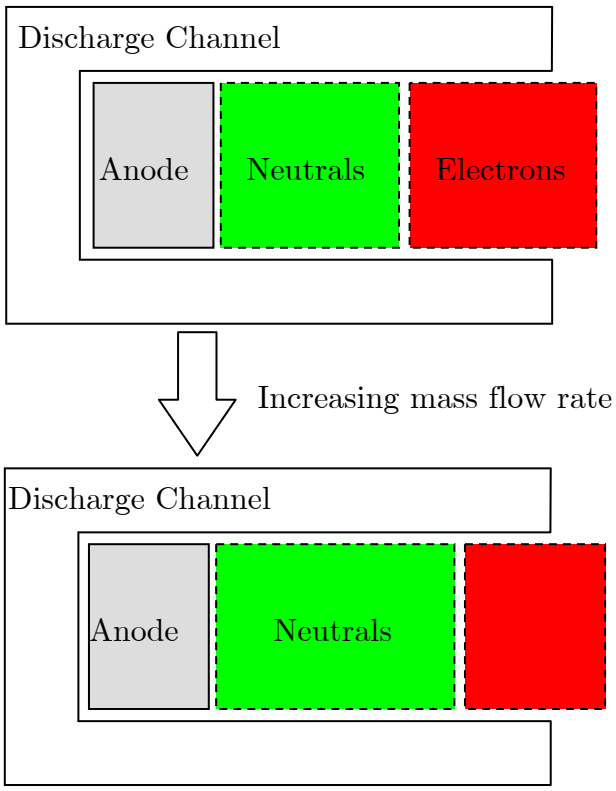

Figure 8-23. Schematic showing the downstream displacement of the high electron temperature region with increased flow rate.

Internal measurements showed that as the high electron temperature region moved downstream it became more compact in the axial direction. This occurred because the upstream side of the high electron temperature region was pushed downstream by neutral collisions, but the downstream side remained approximately stationary since it was bound to the stationary magnetic field at approximately 90% of the maximum radial magnetic field (also illustrated in Figure 8-23).

As the peak electron temperature moved downstream, the ionization region was forced to move downstream since it relies heavily on the presence of high-temperature electrons (ion production controlled by electron-impact

ionization). The heavy reliance on high-temperature electrons for ionization also led to the result that the ionization region became more compact since the upstream boundary moved downstream but the downstream boundary remained stationary (based on electron temperature downstream boundary).

Since the ionization process occurred further downstream, the acceleration process was forced to move downstream for two reasons: 1) ion acceleration can not occur prior to ionization; hence, when ionization occurs further downstream, ion acceleration must also occur further downstream, and 2) the electric field arises in order to maintain a self-consistent current continuity; hence, when ionization occurs further downstream, the electron current must also be created further downstream to maintain ion-electron current continuity.

As the acceleration region moved downstream, the cathode plane likely remained stationary (cathode position, flow fraction, and floating potential all remained constant). Since the voltage utilization was approximately constant, the total voltage drop in the acceleration region remained constant (see Section 6.4). Since the upstream boundary of the acceleration region was pushed downstream and the downstream boundary remained approximately stationary, the peak electric field was forced to increase. This conclusion was supported by plasma potential measurements (see electric field profiles in Section 7.3.4) and LIF measurements [74] that indicated that the acceleration process ended at approximately the same location, regardless of flow rate.

The preceding discussion indicated that increased mass flow rate caused the entire plasma to shift downstream. This result occurred since electron-neutral collisions controlled the location of the high electron temperature region, which in turn controlled the ionization and acceleration regions. This general result was also observed in cathode plasmas [169]. Simulations and experiments found that the cathode flow rate (neutral collision frequency) controlled the cathode potential, the plasma attachment area, and the transition of the cathode operation from "spot mode" to "plume mode." The result that was relevant to the discussion of Hall thruster regions was that the plasma attachment area decreased with increased flow rate. This occurred because the higher collision frequency caused the plasma to shift downstream.

8.6.2 Electron Temperature

The electron temperature was shown to decrease with flow rate in Chapter 7. The reasons for this trend are quantified by examining individual contributions to the bulk electron temperature from the electron energy equation (Eq. 8-1). Although an analytical formulation is tractable for the inelastic, convective, and conductive losses, the wall losses are not easily obtained with the available data. In lieu of a direct analytical description combined with experimental results, the electron power balance from HPHALL-2 simulations is considered. These results should be representative of the experimental results based on the very good

agreement between electron temperature, plasma potential, and ion density (see Section 7.4.2).

The electron power balance from HPHALL-2 simulations is shown in Figure 8-24 for thruster conditions of 300 V and 10, 20, and 30 mg/s. Joule heating was the dominant electron gain mechanism at all three operating conditions, and its contribution to electron energy peaked near the exit plane, which was consistent with the peak electric field location. The primary energy loss mechanism throughout most of the channel was due to inelastic losses. This was consistent with the large electron-neutral collision frequency that existed inside the channel. Outside the channel, the dominant loss mechanism was not readily identified since the amount of Ohmic heating was negligible. The most important region to consider in terms of controlling the electron temperature is the near-exit region. This region was dominated by wall, convective, and conductive losses. These results suggest that the inelastic losses played only a minor role in the trend of decreased electron temperature with increased flow rate. Instead, the wall losses increased near the exit since electrons with sufficient energy to overcome the wall sheath can impact the wall. Wall collisions effectively reduce the bulk electron temperature by depleting the high-energy electrons of the distribution. As flow rate increased, the Hall current density increased, causing the wall collision rate to increase (increased loss of high-energy electrons) and hence, electron temperature decreased.

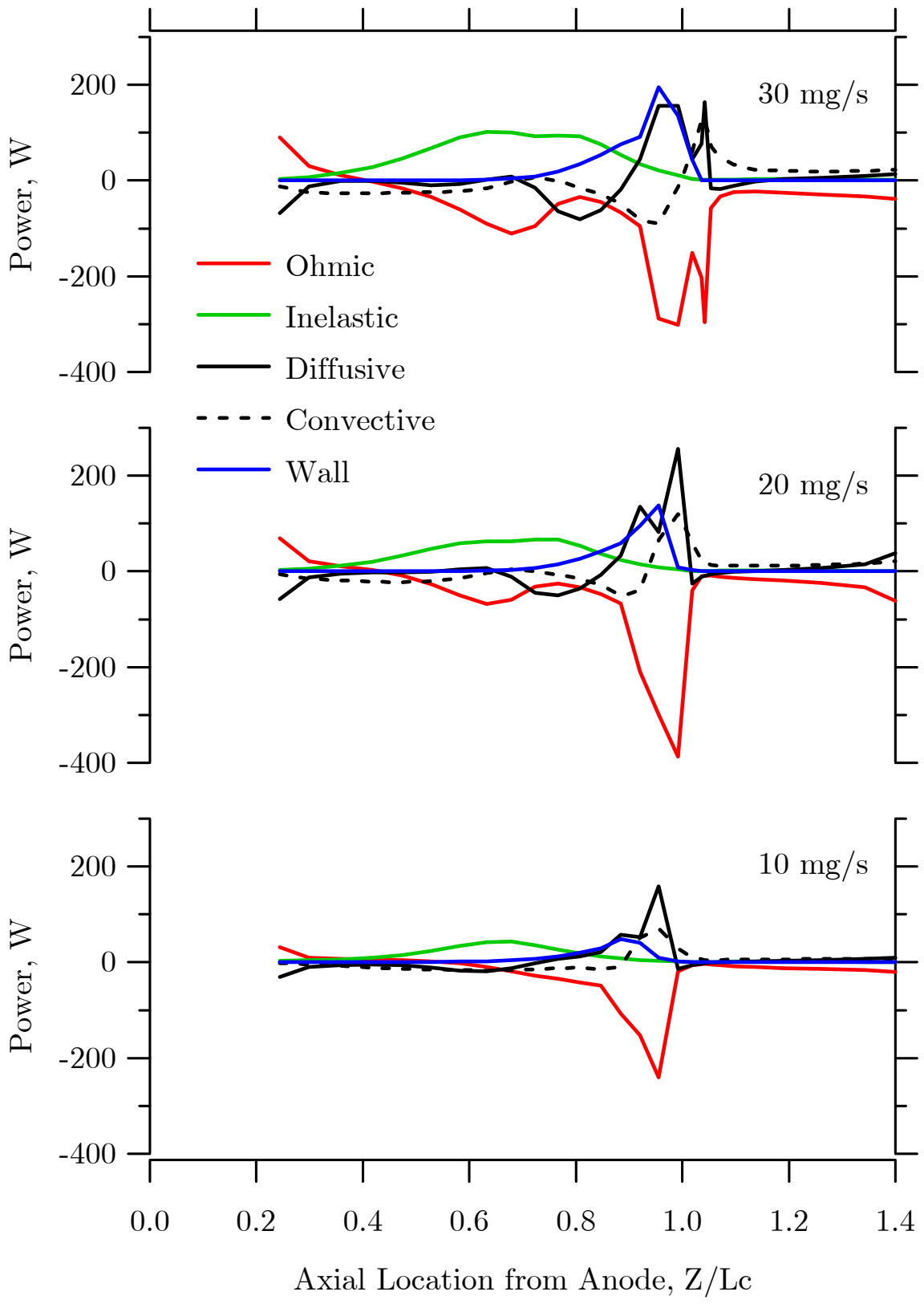

Figure 8-24. HPHALL-2 simulated contributions to the electron energy equation for thruster conditions of 300 V and 10, 20, and 30 mg/s.

The preceding discussion regarding contributions to the energy equation is supported by the results from the collision frequency discussion in Section 8.3.1, which indicated the electron-wall collision frequency was greater than or equal to the electron-neutral collision frequency near the channel exit at all mass flow rates. Although the inelastic losses are not expected to control the peak electron temperature, they do contribute, and the importance of neutrals within the channel should not be underestimated. The total power loss due to inelastic losses was approximately twice as large as any other loss mechanism. In addition, the collision frequency analysis confirmed that electron-neutral collisions controlled the locations of ionization, high electron temperature, and acceleration regions. The individual loss mechanisms in the electron energy equation are very sensitive to the locations of these three regions, in particular the high electron temperature region.

8.7 Summary of Internal Analysis

The analysis contained in this chapter relied heavily on the extensive work of Haas [109] and Linnell [51], who conducted similar experiments. Several incremental improvements in the analysis increased the consistency with simulations in HPHALL-2. In particular, the neutral density calculated by a 1-D mass continuity analysis for ions and neutrals that was corrected for the loss of mass from the measurement domain using an area correction. This correction

eliminated the unphysical neutral density increase that occurred in the near-field plume.

The Hall parameter was calculated using two methods; classical collisions and ratio of azimuthal-to-axial electron currents. Comparing the two methods confirmed the existence of at least three regions of distinct turbulence intensity: region I: near-anode, region II: near exit plane, and region III: near-field plume (see Section 7.4.2 and Ref. [61] for more). In region I, the turbulence was approximately 1-10 times greater than the Bohm value, indicating that the mobility in region I was approximated by classical collisions. Region II was characterized as a region of turbulence suppression, where the difference between classical and total Hall parameter was relatively small. In region III, the turbulence intensity was approximately 10-100 times greater than the Bohm value, indicating a large contribution from anomalous mobility. The order of the turbulence intensity was consistent with the mobility model used in HPHALL-2.

The major contribution of this chapter, and indeed this entire dissertation, was the discussion of the internal plasma trends with flow rate. Results in Chapter 7 indicated that the ionization, high electron temperature, and acceleration regions moved downstream by 5-7% L_c for each addition of 10 mg/s from 10 to 30 mg/s. At the same time, the electron temperature decreased by 5-10 eV for each addition of flow rate. The downstream trend of the internal regions with flow was found to be controlled by neutral density within the

discharge channel. As the flow rate increased, the density increased and caused the electron-neutral collision frequency to increase. This caused the location of the high electron temperature electrons to be pushed downstream. Since the electrons control ionization, the ionization region moved downstream and forced acceleration to occur further downstream. The electron temperature trend was controlled by wall losses near the channel exit, but inelastic losses played a minor role.

The location, size, and intensity of the internal regions affect thruster performance, lifetime, stability, and thermal margin. The combined effect of these regions moving downstream was that the Hall current moved downstream, eventually residing almost entirely outside the channel at 30 mg/s. Although no erosion measurements have been recorded, moving the Hall current further downstream should lead to increased thruster lifetime.

Chapter 9

Conclusions

The central aim of this dissertation was to improve the general understanding of neutral flow dynamics in the operation of Hall thrusters. Performance, plume, and internal measurements were taken at constant discharge voltage, magnetic field shape, and cathode flow fraction. In doing so, the anode flow rate was isolated as the independent variable. The performance and plume measurements were combined into an efficiency analysis that decomposed the anode efficiency into individual utilizations. To support the conclusions of this analysis, internal measurements were taken at the same operating conditions to understand the ionization and acceleration processes. These measurements identified a strong influence of neutral flow rate on the location, size, and intensity of these regions. These findings are relevant to future thruster design efforts and indicate that neutral flow dynamics and anode configuration should be considered with as much attention as the magnetic circuit, cathode, and discharge channel designs. These results are also relevant to ongoing and future research related to electron mobility and cathode physics.

The remainder of this chapter summarizes the major conclusions of this dissertation, followed by suggestions for future work.

9.1 Neutral Flow Dynamics

The importance of achieving highly symmetric neutral flows was highlighted by a review of prior research that indicated a link between neutral flow properties and thruster efficiency, stability, thermal margin, and lifetime. The major conclusion was that improving neutral symmetry improved thruster performance by increasing the current utilization.

9.2 Influence of Neutral Flow Rate

Experiments were performed using a methodology that isolated the anode flow rate as the single independent variable as the thruster was throttled from ± 50% of the nominal flow rate of 20 mg/s. As flow rate increased, there were four major conclusions that were drawn from performance and plasma measurements:

1) **Current utilization decreased**. The current utilization was the primary efficiency loss mechanism, and it decreased with flow rate due to increased ionization losses and electron-wall losses.
2) **Divergence utilization increased**. As flow rate increased, the ionization and acceleration occurred over a smaller axial region and the ion density became more concentrated towards channel centerline. These

effects allowed a larger fraction of ions to be accelerated along channel centerline.

3) **Plasma moved downstream**. The ionization, high electron temperature, and acceleration regions were pushed downstream as flow rate was increased. Electron collision analysis and electron Hall parameter showed that the primary reason for this movement was increased electron-neutral collision frequency that persisted over more of the channel as flow rate increased.

4) **Electron temperature decreased**. For most of the channel, the electron-neutral collisions were the primary contributor to electron energy loss and cross-field mobility. However, near the channel exit, electron-wall collisions increased and became the primary contributor to the measured decrease in electron temperature with increased flow rate.

9.3 Three-region Mobility

The existence of three distinct mobility regions was confirmed by considering the classical and total electron Hall parameter. As implemented in the hybrid-PIC Hall thruster simulation code HPHALL-2 [61], the three regions were near anode, channel exit, and plume. Near the anode, the turbulence was approximated by the Bohm value. Near the channel exit, the turbulence was suppressed and electrons were most effectively trapped by the Hall current in this region. In the plume, the turbulence was an order of magnitude greater than the

Bohm value, indicating large contributions to electron transport from turbulence or a currently unaccounted for anomalous transport mechanism.

9.4 Comparisons with HPHALL-2

HPHALL-2 simulations were compared with results from electrostatic probe measurements, showing relatively good agreement at all operating conditions (300 V and 10, 20, and 30 mg/s). The good agreement provided confidence in the trends and conclusions that were drawn from the experimental results and provided confidence in the ability of the code to accurately model Hall thruster physics. Simulations were used to determine that the measured decrease in electron temperature with increased flow rate was primarily due to increased wall losses.

9.5 Suggestions for Future Work

The research contained in this dissertation established a solid foundation from which future neutral flow dynamics investigations may proceed. However, some additional topics that deserve added attention include, at least:

1) **High-speed measurements of plasma properties within the discharge channel**. Emissive probe measurements in this dissertation were acquired at > 80 kHz, showing promising results; however, high-speed Langmuir probe measurements were not achieved due to DAQ limitations. Recent advancements in commercially-available DAQ systems offer the ability to obtain high-frequency Langmuir and probe

measurements within the discharge channel. These measurements may offer additional insight into the ion, electron, and neutral dynamics in the channel. High-speed internal measurements would be instrumental in examining the azimuthal, radial, and axial evolution of the Hall current. Furthermore, high-speed internal plasma potential measurements (MHz-GHz) could provide critical insight to the influence of plasma turbulence.

2) **Near-field neutral density measurements**. An optical survey of the near-field neutral density and LIF survey of the neutral velocity would provide invaluable information that could be used to understand the centerline spike, near-field CEX, and electron transport from the cathode to the discharge channel. These measurements would benefit from simulations of the complex neutral field that is produced by the intersection of neutrals that are exhausted from the annular discharge channel and cathode orifice. The Hall parameter analyses of Chapter 8 indicated that enhanced mobility outside the thruster could be linked to elevated neutral density, "ion reflux," or other anomalous transport mechanisms.

3) **Additional near-field measurements**. Plasma measurements should be taken over a wide range of cathode flow rates at fixed discharge voltage and anode mass flow rates to understand electron mobility.

Changing the cathode flow rate directly influences the near-field neutral density that is believed to augment electron mobility to the discharge channel. These measurements should be linked with near-field neutral measurements and additional internal measurements. To complement the near-field Faraday probe measurements in this dissertation, plasma potential and Langmuir probe measurements should be taken to identify the presence of radial electric fields and density gradients that may contribute to the formation of the centerline "spike".

4) **Additional internal measurements**. Based on the radially symmetric plasma properties within the channel presented in Chapter 7, a detailed survey is not always necessary. A single measurement on channel centerline will reduce data collection time and increase probe life, while capturing the majority of the relevant physics. The suggested measurements include: a) measurements at 300 V and flow rates from 5 to 40 mg/s in increments of 5 mg/s to determine the point of transition to poor thruster performance and the mechanism that is responsible for the transition; b) measurements at constant operating condition and varied cathode flow fraction to investigate the mechanisms that allow electrons to reach the discharge channel; c) measurements at a constant operating condition and varied

background pressure to complement the LIF work of Nakles *et al.* [170]; and d) measurements with a modified anode to investigate the physics that caused increased electron current and plume asymmetry in the work of Hofer [26].

Appendix A

Summary of Performance Data

Table A-1. 6-kW Hall thruster performance data taken at PEPL after approximately 220 hours of operation.

V_D, V	V_k, V	I_D, A	P_D, W	$\dot{m}_a$, mg/s	$\dot{m}_c$, mg/s	IM, A	OM, A	ITC, A	P_{mag}, W	Thrust, mN	T/P_{tot}, mN/kW	$I_{sp,a}$, s	$I_{sp,tot}$, s	η_a	η_{tot}	Pressure, torr-xe
150	-12.3	8.995	1349	10	0.7	2.10	1.88	-0.40	13	109	80	1100	1050	0.44	0.41	7.1E-06
150	-11.2	9.196	1379	10	0.7	2.10	1.88	0.00	13	109	78	1100	1050	0.43	0.40	7.1E-06
150	-9.4	21.38	3207	20	1.4	2.60	2.31	-0.45	19	252	78	1300	1200	0.50	0.46	1.4E-05
150	-9.4	21.40	3210	20	1.4	2.60	2.32	0.00	20	248	77	1250	1200	0.48	0.45	1.4E-05
150	-8.5	35.56	5334	30	2.1	2.80	2.51	0.00	25	400	75	1350	1250	0.50	0.47	1.9E-05
300	-19.8	3.953	1186	5	1.4	2.70	2.41	0.00	21	77	63	1550	1200	0.49	0.38	4.0E-06
300	-12.7	9.056	2717	10	0.7	2.40	2.13	0.00	13	187	68	1900	1800	0.64	0.60	7.3E-06
300	-14.1	8.709	2613	10	0.7	2.40	2.14	-0.50	14	184	70	1900	1750	0.65	0.61	7.1E-06
300	-11.4	19.94	5982	20	1.3	3.51	3.13	-1.10	42	398	66	2050	1900	0.66	0.62	1.4E-05
300	-11.3	19.99	5997	20	1.3	3.13	3.50	-1.10	41	401	66	2050	1900	0.67	0.62	1.4E-05
300	-11.7	19.94	5982	20	1.3	3.50	3.13	-1.10	36	395	66	2000	1900	0.65	0.61	1.4E-05
300	-11.8	19.94	5982	20	1.3	3.50	3.13	-1.10	37	393	65	2000	1900	0.64	0.60	1.4E-05
300	-10.6	20.33	6099	20	1.4	3.00	2.68	0.00	31	397	65	2000	1900	0.65	0.60	1.4E-05
300	-11.5	32.50	9750	30	2.1	3.70	1.96	-0.61	33	605	62	2050	1900	0.63	0.58	1.5E-04
300	-10.3	33.26	9978	30	2.1	3.20	2.85	-0.40	39	625	62	2100	2000	0.65	0.61	1.9E-05
300	-10.1	33.79	10137	30	2.1	2.86	3.31	0.00	41	627	62	2150	2000	0.65	0.60	1.9E-05
300	-10.0	32.83	9849	30	2.1	3.20	2.85	-0.40	38	620	63	2100	1950	0.65	0.61	1.9E-05
600	-20.1	3.867	2320	5	1.4	2.70	2.40	0.00	20	117	50	2400	1850	0.59	0.46	4.1E-06
600	-13.9	9.499	5699	10	0.7	4.70	4.20	0.00	79	283	49	2900	2700	0.70	0.65	7.3E-06
600	-14.0	9.186	5512	10	0.7	4.60	4.12	-0.60	74	277	50	2850	2650	0.70	0.64	7.3E-06

Table A-2: 6-kW Hall thruster performance data taken at PEPL after approximately 40 hours of operation.

V_D, V	V_k, V	I_D, A	P_D, W	$\dot{m}_a$, mg/s	$\dot{m}_c$, mg/s	IM, A	OM, A	ITC, A	P_{mag}, W	Thrust, mN	T/P_{tot}, mN/kW	$I_{sp,a}$, s	$I_{sp,tot}$, s	η_a	η_{tot}	Pressure, torr-xe
150	-10.2	22.48	3379	20.0	1.4	2.5	2.23	0.3	13	268	79	1370	1280	0.53	0.50	2.1E-05
200	-11.3	21.36	4276	20.0	1.4	3.0	2.67	0.4	20	324	76	1660	1550	0.62	0.57	2.1E-05
300	-12.4	20.00	6000	20.0	1.4	3.5	3.13	1.1	34	409	68	2090	1950	0.70	0.65	2.1E-05
300	-12.4	20.36	6108	20.3	1.4	3.5	3.13	1.1	34	416	68	2090	1960	0.70	0.65	2.1E-05
300	-12.4	20.72	6218	20.6	1.4	3.5	3.13	1.1	34	423	68	2090	1960	0.70	0.65	2.1E-05
400	-11.4	20.28	8112	20.0	1.4	3.5	3.13	1.1	38	486	60	2480	2320	0.73	0.68	2.1E-05
400	-11.4	20.64	8256	20.3	1.4	3.5	3.13	1.1	38	495	60	2480	2330	0.73	0.68	2.1E-05
400	-11.4	21.04	8416	20.6	1.4	3.5	3.13	1.1	38	501	60	2470	2320	0.72	0.67	2.1E-05

Table A-3: 6-kW Hall thruster performance data taken at AFRL after approximately 40 hours of operation.

V_D, V	V_k, V	I_D, A	P_D, W	$\dot{m}_a$, mg/s	$\dot{m}_c$, mg/s	IM, A	OM, A	ITC, A	P_{mag}, W	Thrust, mN	T/P_{tot}, mN/kW	$I_{sp,a}$, s	$I_{sp,tot}$, s	η_a	η_{tot}	Pressure, torr-xe
150	-9.27	22.20	3328	20.0	1.4	2.50	2.23	0.3	19	266	80	2200	2060	0.53	0.49	1.4E-05
200	-7.47	29.97	5997	10.0	0.7	3.80	3.39	1.2	50	463	77	2950	2760	0.67	0.62	2.0E-05
200	-7.54	34.52	6914	30.0	2.1	3.80	3.39	1.2	50	552	80	1880	1760	0.73	0.68	2.2E-05
201	-10.5	21.39	4290	40.0	2.7	3.00	2.68	0.4	27	328	76	1620	1520	0.62	0.58	1.4E-05
301	-11.8	20.01	6015	20.0	1.4	3.50	3.13	1.1	40	433	72	2570	2400	0.78	0.72	1.2E-05
400	-11.0	20.18	8080	10.3	1.4	3.50	3.13	0.9	42	504	62	3020	2670	0.79	0.73	1.2E-05
401	-13.6	15.07	6042	15.6	1.1	4.25	3.80	1.0	62	372	62	2430	2270	0.73	0.68	9.7E-06
600	-16.6	9.56	5738	26.7	2.0	7.00	6.25	1.1	167	289	50	1770	1650	0.73	0.66	7.3E-06
601	-12.7	10.10	6065	10.0	0.7	7.00	6.25	1.0	169	304	50	1100	1030	0.74	0.64	8.0E-06

Appendix B

The Effect of Facility Neutrals on Performance and Plume Measurements

B.1 Performance Measurements

To quantify the impact that facility effects had on Hall thruster performance measurements, the facility pressure was varied while recording thrust and discharge current. Measurements were recorded at facility pressures of 1.2, 1.4, 1.6, and 1.9×10^{-5} torr-xe. The facility pressure was regulated by injecting xenon gas 2 m below the thruster so that it impacted the underside of the thrust stand mounting structure and diffusely scattered in all directions. The injection location was an average of 2 m from the cryopump surfaces and 4 m from the ionization gauges.

After performance measurements were recorded as a function of facility pressure, a linear extrapolation to vacuum pressure was performed. A similar extrapolation method was briefly mentioned in Ref. [67], treated with more rigor in Ref. [171], and an analytical analysis of the effect of elevated facility pressure

was treated in Ref. [91]. To summarize these findings, the change in performance with facility pressure was primarily due to the random incident flux of facility neutrals into the discharge channel. Once neutrals reached the thruster channel they were ionized and accelerated. This process artificially increased the total thruster mass flow rate, which is linearly proportional to discharge current and thrust.

B.1.1 6-kW, 300 V Thruster Operation

The thruster was operated at the nominal condition of 300 V and 20 mg/s. Thrust measurements at the various facility pressures were taken continuously, without shutting the thruster off for zero measurements. A calibration was performed before and after the entire set of measurements and the instantaneous zero position of the thrust stand was inferred by linear interpolation. The results for thrust and discharge current are shown in Figure B-1. The resulting extrapolations to zero pressure indicated that the vacuum thrust and discharge current were 400 ± 2 mN and 19.6 ± 0.1 A, respectively. These represented a 2.2 and 3.4% deviation from the nominal background pressure measurements of 409 ± 2 mN and 20.3 ± 0.1 A, respectively. The vacuum values of thrust and discharge current combined to reduce total efficiency from the nominal value of 64 ± 2% to 61 ± 2%.

B.1.2 8-kW, 400 V Thruster Operation

The same procedure was used for 8-kW thruster operation at 400 V and 20 mg/s. The results for thrust and discharge current are shown in Figure B-2. The resulting extrapolations to zero pressure indicated that the vacuum thrust and discharge current were 476 ± 2 mN and 19.9 ± 0.1 A, respectively. These represented a 2.1 and 3.4% deviation from the nominal facility pressure measurements of 486 ± 2 mN and 20.6 ± 0.1 A, respectively. These deviations were nearly identical to the 6-kW operating condition and the variations combined to reduce total efficiency at 8 kW from 67 ± 2% to 64 ± 2% at vacuum.

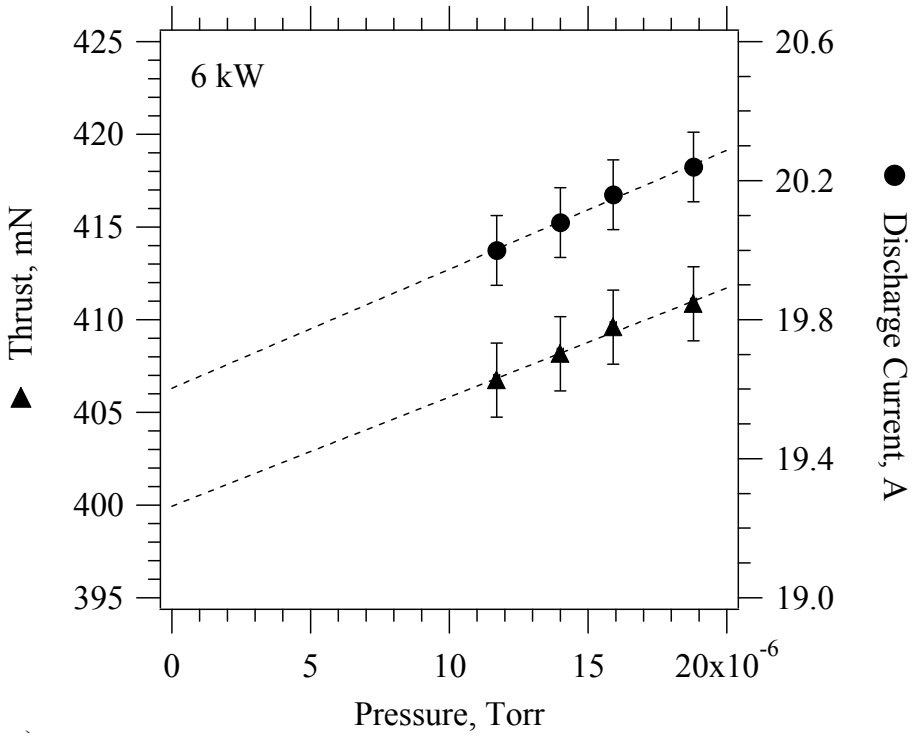

Figure B-1. Thrust and discharge current variations with facility backpressure at 6 kW thruster power (300 V and 20 mg/s).

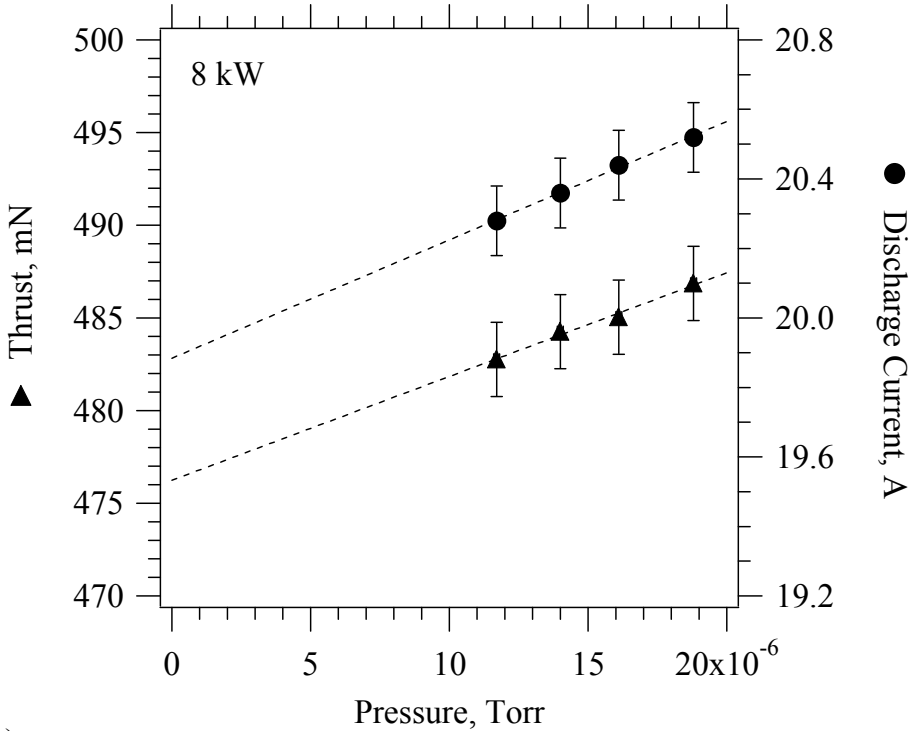

Figure B-2. Thrust and discharge current variations with facility backpressure at 8 kW thruster power (400 V and 20 mg/s).

B.2 Analytical Method to Quantify Facility Effects on Performance Measurements

An improved calculation of the entrained flow was necessary to account for the discrepancy between the predicted entrained flow and the measured increment in discharge current and thrust. Walker [172] made a similar attempt to rectify the discrepancy in measured and predicted entrained flow by considering the increment in current as a function of facility pressure. In the present treatment, the discharge current and thrust were corrected to their vacuum values by removing the contribution from facility neutrals by introducing a hemispherical entrainment area with a radius equivalent to the discharge channel outer radius. Correcting with this entrainment definition produced good

agreement with experimental data that was extrapolated to zero background pressure.

B.2.1 Entrained Neutral Gas

To evaluate the effect that higher facility pressure had on thruster performance, the effect of entrained flow due to facility neutral gas needed to be quantified. Using a derivation similar to Ref. [91], the entrained mass flow, $\dot{m}_{en}$ was calculated by integrating the random thermal mass flux of facility neutrals across a surface (usually the discharge channel exit plane) using the kinetic approximation

$$\dot{m}_{en} = A_{en} \frac{n_n m_{xe}}{4} \left(\frac{8 k_B T}{\pi m_{xe}} \right)^{1/2} = A_{en} P \left(\frac{m_{xe}}{2 \pi k_B T} \right)^{1/2}, \tag{B-1}$$

where A_{en} is the area over which the entrainment occurs, T is the temperature of the facility neutrals, and P is the facility pressure. The entrained mass flow was converted to entrained discharge current by

$$I_{en} = \dot{m}_{en} \frac{e}{m_{xe}}, \tag{B-2}$$

where the neutrals were assumed to be singly ionized. For the simple model in Eq. B-1, the entrained mass flow was primarily dependent on the facility pressure and selection of entrainment area. The uncertainty in the facility pressure reading was approximately ± 20% and the facility pressure reading was assumed to be representative of the neutral density near the thruster due to facility neutrals.

It was reasonable to assume that the entrained mass flow should be integrated over a larger area than the discharge channel cross section since the electron temperature in the first few centimeters downstream of the channel exit plane remained high enough to ionize neutral gas (see Section 7.2.3). A logical selection of area was a hemisphere that had a diameter equivalent to the outer diameter of the thruster channel. This boundary accounted for the regions of high electron temperature that extended beyond the confines of the discharge channel and increased the entrainment area by an order of magnitude. The hemispherical entrainment area was used to correct discharge current and thrust measurements to their vacuum values, and the results were compared to the traditional channel exit area definition.

B.2.2 Discharge Current Correction

Considering Eqs. B-1 and B-2 indicates a linear relationship between discharge current due to entrained flow and facility pressure, confirming the observed linear relationship of discharge current with pressure as shown in Figure B-1 and Figure B-2. Using the entrained current, the measured discharge current was reduced to represent the corrected vacuum value by

$$I_{corr} = I_D - I_{en} . \tag{B-3}$$

Assuming a background neutral temperature of 300 K and using the channel exit as the entrainment area, this analysis predicted a contribution of 0.03 A between 1.2×10^{-5} and 1.9×10^{-5} torr, nearly an order of magnitude lower than the 0.24 A

measured at both 6 and 8 kW. Additional neutral mass flow was proposed to be introduced by the cathode flow [173]; however, this contribution remains nearly constant with facility pressure, and would still be present at vacuum. The goal of the present analysis is to account for facility effects by correcting thrust and discharge current to their vacuum values. By using the proposed hemispherical entrainment area, the analysis predicted a contribution of 0.23 A between 1.2×10^{-5} and 1.9×10^{-5} torr, which was in excellent agreement with the measured increment in discharge current of 0.24 A. The corrected discharge current at 6 kW was 19.60 ± 0.01 A at *all* facility pressures investigated, closely matching the linearly extrapolated value of 19.6 ± 0.1 A. Similarly, at 8 kW the corrected discharge current was 19.88 ± 0.01 A at *all* facility pressures, closely matching the linearly extrapolated value of 19.9 ± 0.1 A.

B.2.3 Thrust Correction

In a similar fashion to the discharge current correction, the thrust measurements can be corrected to remove the contribution from entrained mass flow by using

$$T_{corr} = T\left(1-\zeta_{en}\frac{\dot{m}_{en}}{\dot{m}_a+\dot{m}_{en}}\right), \tag{B-4}$$

where T_{corr} is the vacuum corrected thrust, T is the measured thrust, and ζ_{en} is the entrainment utilization. ζ_{en} was introduced to account for ingested neutrals that were ionized yet did not contribute to useful thrust due to large divergence or ions that did not achieve full acceleration since they were produced outside the

channel, beyond the primary acceleration region. When ζ_{en} is unity, the contribution from all of the entrained flow that contributed to discharge current is removed from the measured thrust. When ζ_{en} is zero, the thrust is uncorrected. For $\zeta_{en} = 1$, the corrected thrust varied with facility pressure from 394 to 396 mN at 6 kW, and 466 to 470 mN at 8 kW. Both of these values were approximately 2% lower than the linearly extrapolated values of 400 and 476 mN for 6 and 8 kW, respectively. Since the corrected thrust still varied with pressure, the selection of unity for the correction factor was not appropriate. The values of ζ_{en} that produced consistent results at all pressures were 0.6 and 0.5 at 6 and 8 kW, respectively. At 6 kW using $\zeta_{en} = 0.6$ produced a corrected thrust of 400.0 ± 0.4 mN for all pressures investigated, closely matching the extrapolated value of 400 ± 2 mN. Similarly, at 8 kW using $\zeta_{\text{en}} = 0.5$ produced a corrected thrust of 476.1 ± 0.2 mN at all pressures, closely matching the extrapolated value of 476 ± 2 mN. These results indicated that approximately 50% of the ingested neutrals that were ionized and contributed to higher discharge current did not contribute to useful thrust. This result was consistent with the suggestion that many of the ingested facility neutrals were ionized outside the thruster and experienced little axial acceleration; hence, the introduction of the hemispherical entrainment area is justified. The presence of highly divergent ions may have a direct impact on the increased current density in the wings that was observed at higher flow rates.

B.2.4 Pressure Criterion

To obtain reliable performance measurements, the facility pressure should be kept below a threshold that maintains the fraction of entrained mass flow below 3% of the anode mass flow. This threshold ensures that the uncertainty introduced by facility effects is within the uncertainty of the performance measurement, which was primarily due to mass flow rate measurement uncertainty. To calculate the maximum acceptable facility pressure, Eq. B-1 can be rearranged into

$$P = \left(\frac{\dot{m}_{en}}{\dot{m}_a} \right) \frac{\dot{m}_a}{A_{en}} \left(\frac{2\pi k_B T}{m_{xe}} \right)^{1/2}, \tag{B-5}$$

where $\dot{m}_{en} / \dot{m}_a$ is the entrainment fraction. From Eq. B-5 it is apparent that the maximum acceptable facility pressure to maintain the fraction of entrained mass flow below 3% increases with increased anode mass flow rate. Using Eq. B-5, the facility pressure should not exceed 3.3×10^{-6}, 6.5×10^{-6}, 1.3×10^{-5}, and 2.6×10^{-5} torr for anode mass flow rates of 5, 10, 20, and 40 mg/s, respectively. These pressure restrictions rely on the assumption that the entrainment area for the 6-kW thruster used in this investigation was approximately constant over a large range of anode mass flow rates, which is a good assumption based on the performance and plume measurements in the main body of this dissertation.

The analysis of the preceding sections indicates that the entrainment area based on the discharge channel exit area is an order of magnitude too low. Using the updated entrainment area definition, and the relation in Eq. B-5 provides a

more accurate description of the effects of facility gas entrainment than the one provided in Ref. [91].

B.3 Faraday Probe Measurements

Far-field faraday probe measurements were recorded at facility pressures ranging from 1.3 to 2.0×10^{-5} torr-xe. These measurements are shown in Figure B-3 and exhibit a clear trend of increased current density in the wings. The central portion of the plume remained mainly unaffected as pressure was changed. A similar set of measurements were performed by Manzella [104] showing the same trend of increased current density in the wings with increased facility pressure.

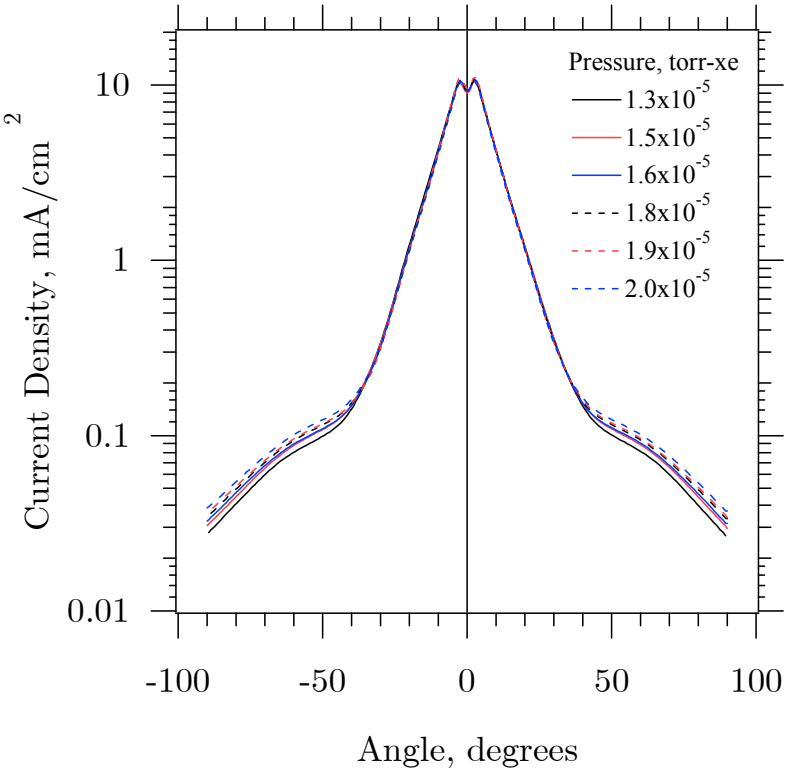

Figure B-3. Ion current density measurements at facility pressures ranging from 1.5 to 2.0×10^{-5} torr-xe.

The increase in current density in the wings followed a distinct linear trend with facility pressure that is shown in Figure B-4 for locations from 50-90°. This relationship allowed the current density to be extrapolated to zero facility pressure, offering an approximation of the true vacuum current density distribution. The linear relationship shown in Figure B-4 persisted at all locations throughout the plume; however, the relationship was less distinct at angles below ± 30°.

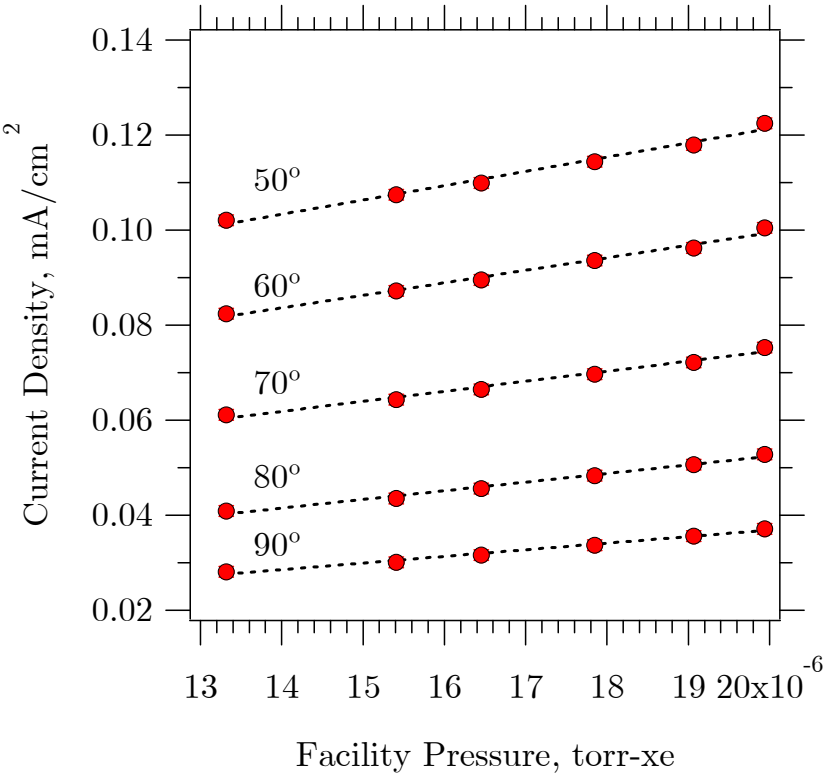

Figure B-4. Linear relationship of ion current density with facility pressure at several angular locations.

The vacuum extrapolation method was insensitive to a precise measurement of facility pressure. This was an important characteristic since most facilities employ typical Bayard-Alpert ion gauges, which have absolute pressure

uncertainties of at least ± 20%. During analysis, changes of ± 50% in the pressure reading (for all pressures) resulted in an imperceptible change in the extrapolated current density shape, total current, and plume divergence. However, the same features were heavily dependent on the slope of the pressure reading, which was dependent on the gauge type and accuracy of the linear fit. In this study, two independent pressure readings were recorded and averaged to obtain the reported facility pressure.

The effectiveness of the vacuum extrapolation method was evaluated by comparing the vacuum current density profile to several separate probe measurements including: 1) current density measurements taken with a forward- and rear-facing faraday probe, 2) exponential extrapolation of the current density from the central core ($|\theta| < 30^{o}$) to the wings ($|\theta| > 30^{o}$), and 3) gridded Faraday probe.

The current density measured by the forward and rear-facing Faraday probes ("CEX-removed" in the figure) reduced the current in the wings, but did not offer a significant change in the profile. The profile of the exponential extrapolation matched the other measurement techniques in the core, but provided overcorrection in the wings. This overcorrection completely removed the characteristic wings and the corresponding contribution from thruster-induced CEX. Even at vacuum conditions, the wings were expected to remain intact due to thruster-induced CEX [174]. The current density profile produced by the

vacuum extrapolation method agreed extremely well with the gridded Faraday probe. These measurements indicated that a gridded Faraday probe produced the most reliable current density profile in the plume of a Hall thruster.

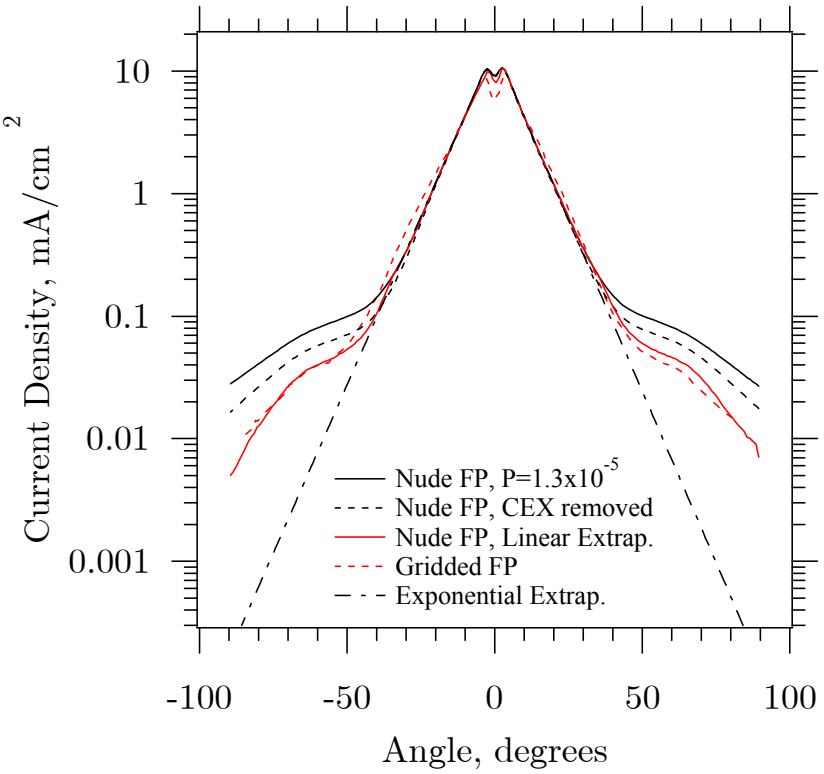

Figure B-5. Comparison of ion current density profiles for uncorrected forward-facing, rear-facing corrected by reverse-facing, linear extrapolation correction, and gridded Faraday probe.

B.4 Summary of Facility Effects

Thrust and discharge current exhibited a linear relationship with facility backpressure at both 6- and 8-kW thruster-operating conditions. Using the linear relationship, vacuum values of thrust and discharge current decreased from their nominal values by approximately 2.1 and 3.4%, respectively. The combined effect caused the total vacuum efficiency to drop by less than 3% (absolute) for both power levels. The relative changes in thrust, discharge current, and total

efficiency were nearly identical at 6 and 8 kW (same mass flow rate and discharge current), which indicated that the correction method was independent of the discharge voltage.

In addition to the linear relationship of thrust and discharge current with pressure, a second method to correct thrust and discharge current was suggested based on entrained facility neutrals. Entrainment was found to occur over an effective area defined by a hemisphere with a radius equal to the discharge channel outer radius, which contrasts the previously suggested discharge channel exit area, which was an order of magnitude smaller than the suggested hemispherical area definition [91]. The hemispherical area correction fully accounted for the entrained flow that contributed to discharge current. The corrections for thrust and discharge current due to entrained flow were consistent since they returned the same value at each pressure investigated and agreed extremely well with the linear extrapolation results.

A linear relationship was found between current density in the wings and facility pressure. Using this distinct relationship, an extrapolation to vacuum conditions was performed and the results showed remarkable agreement with a gridded Faraday probe. These results indicated that a gridded Faraday probe produced the most reliable current density measurement for determining vacuum properties.

Appendix C

Low Discharge Voltage Measurements

Plume and internal plasma measurements were performed at 150 V and 10, 20, and 30 mg/s. The results presented here are analogous to those presented in the main body of this dissertation.

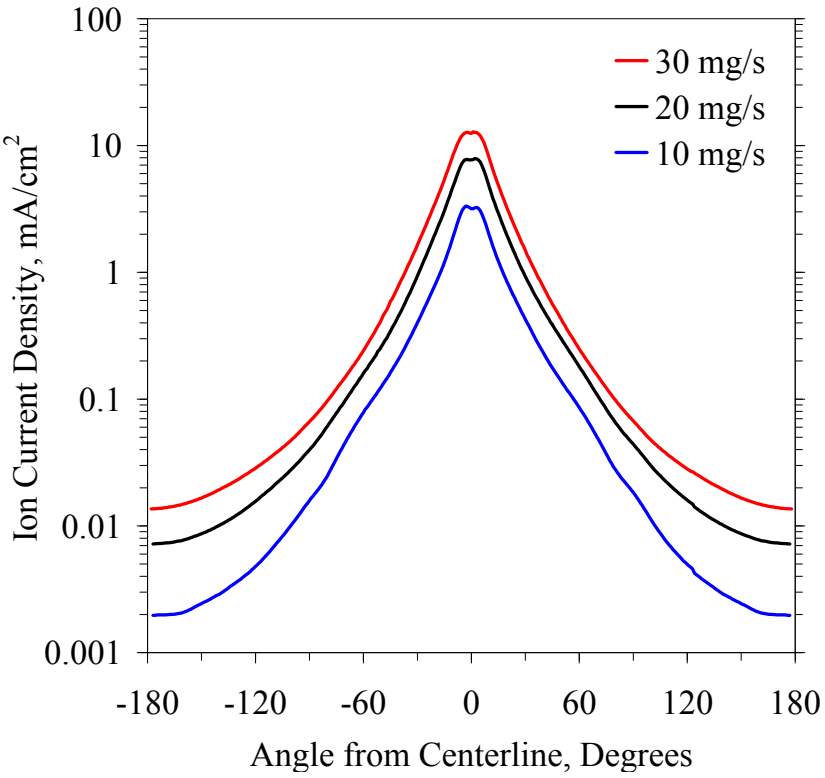

Figure C-1. Far-field Faraday probe measurements at 150 V and 10, 20, and 30 mg/s.

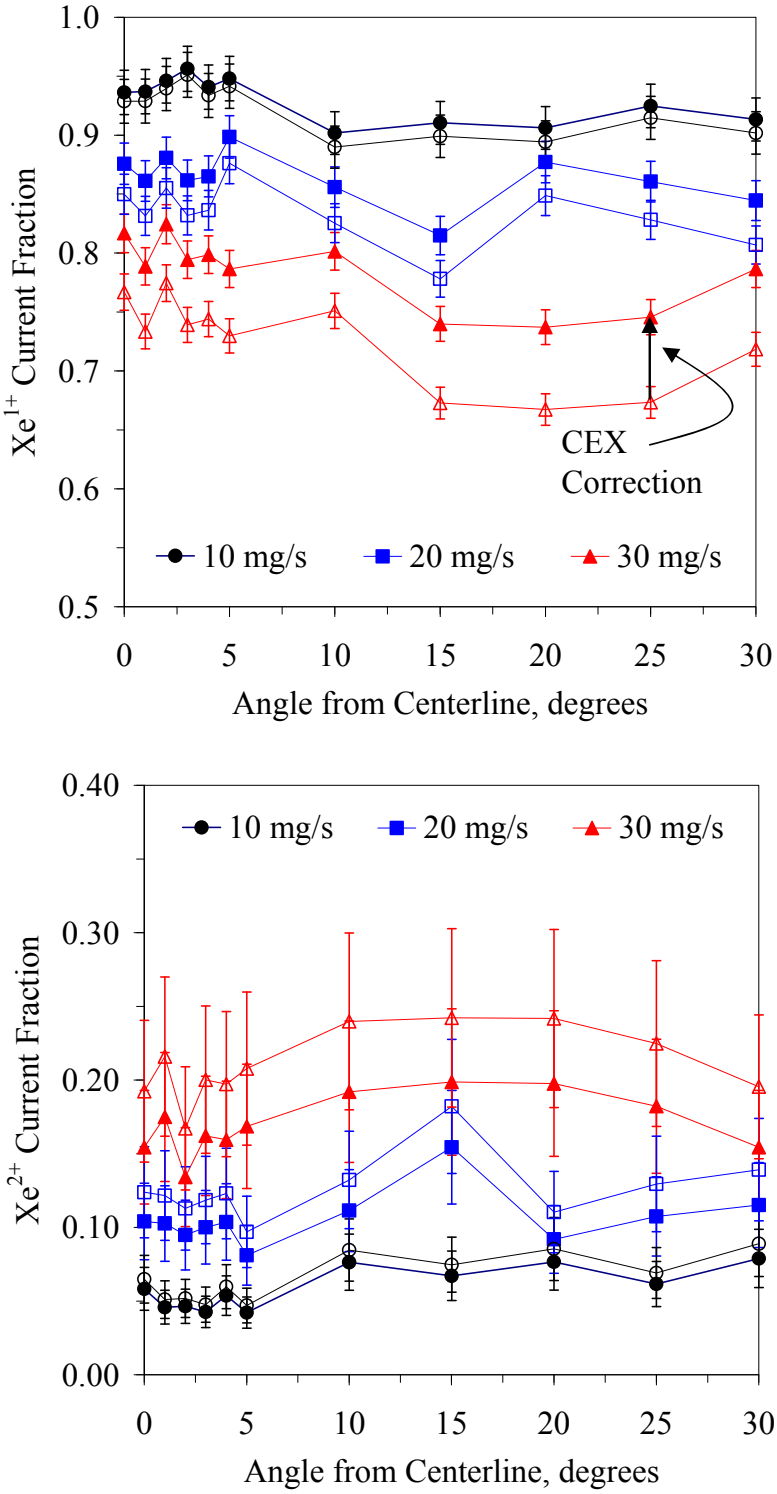

Figure C-2. **Xe^{1+} and Xe^{2+} ion current fractions for thruster operation at 150 V and 10, 20, and 30 mg/s ($z = 9\ D_{T,mean}$). Open markers are uncorrected data, solid markers have been corrected for CEX.**

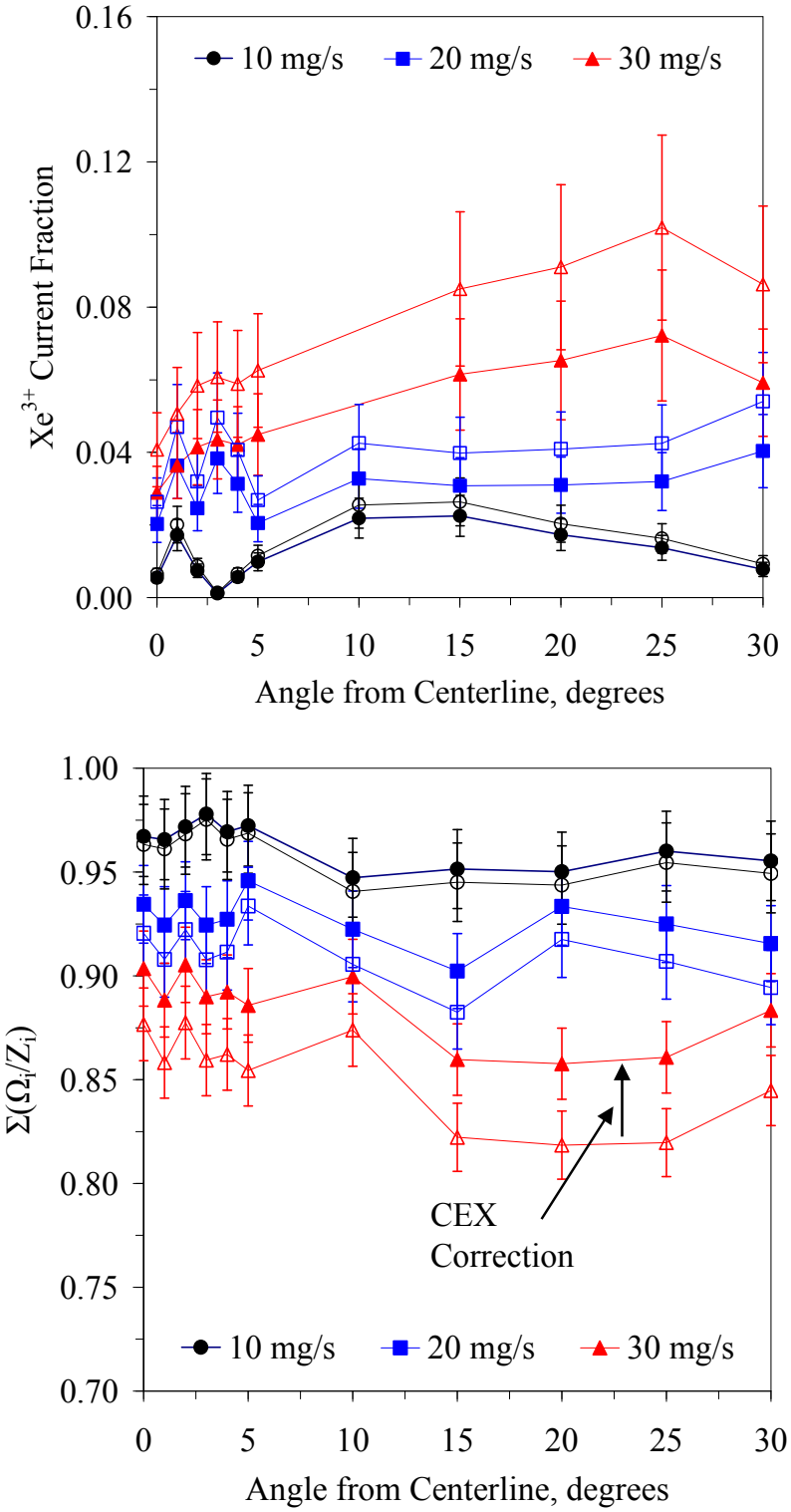

Figure C-3. Xe^{3+} ion current fraction and $\Sigma(\Omega_i/Z_i)$ for thruster operation at 150 V and 10, 20, and 30 mg/s ($z = 9\ D_{T,mean}$). Open markers are uncorrected data, solid markers have been corrected for CEX.

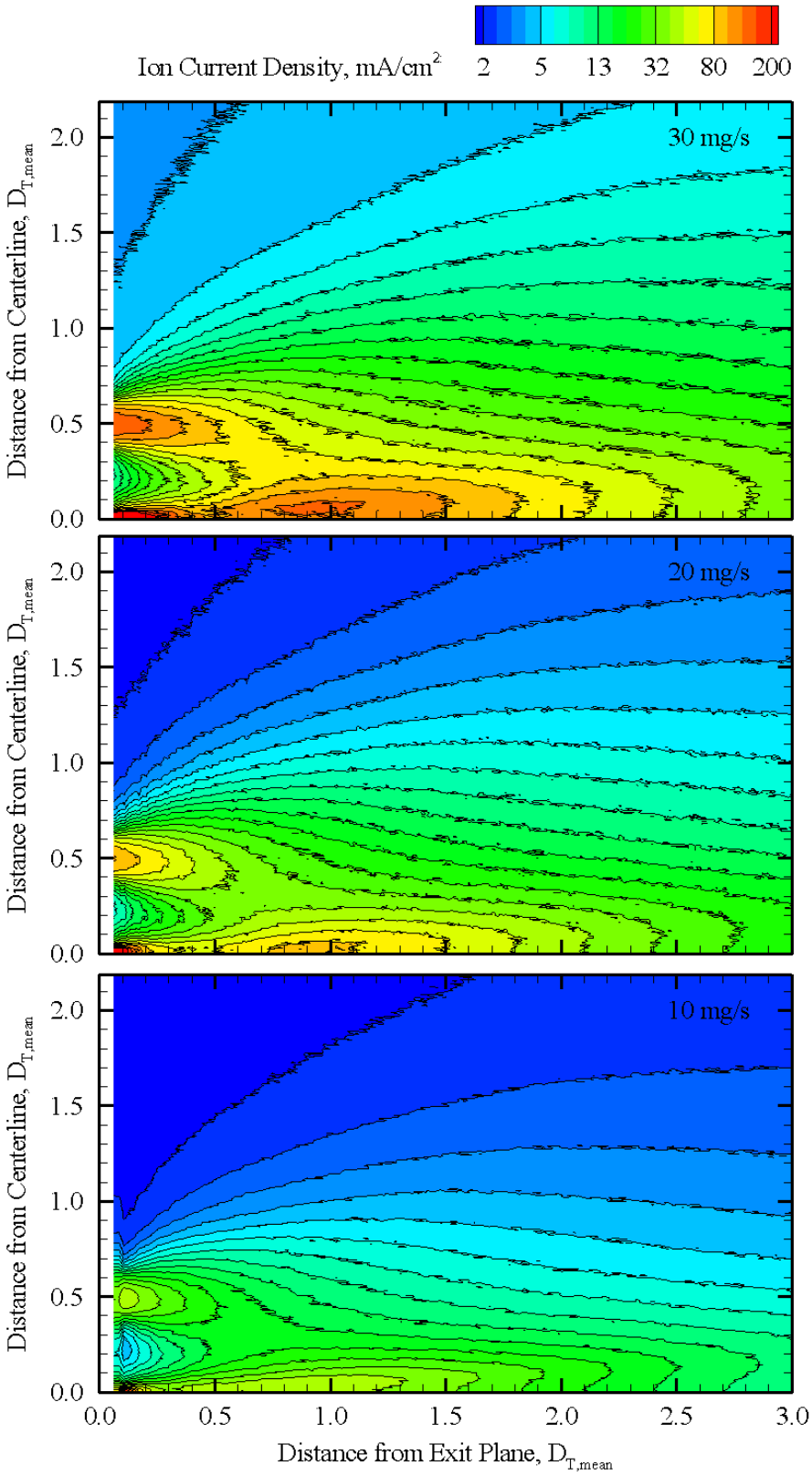

Figure C-4. Near-field Faraday probe measurements at 150 V and 10, 20, and 30 mg/s.

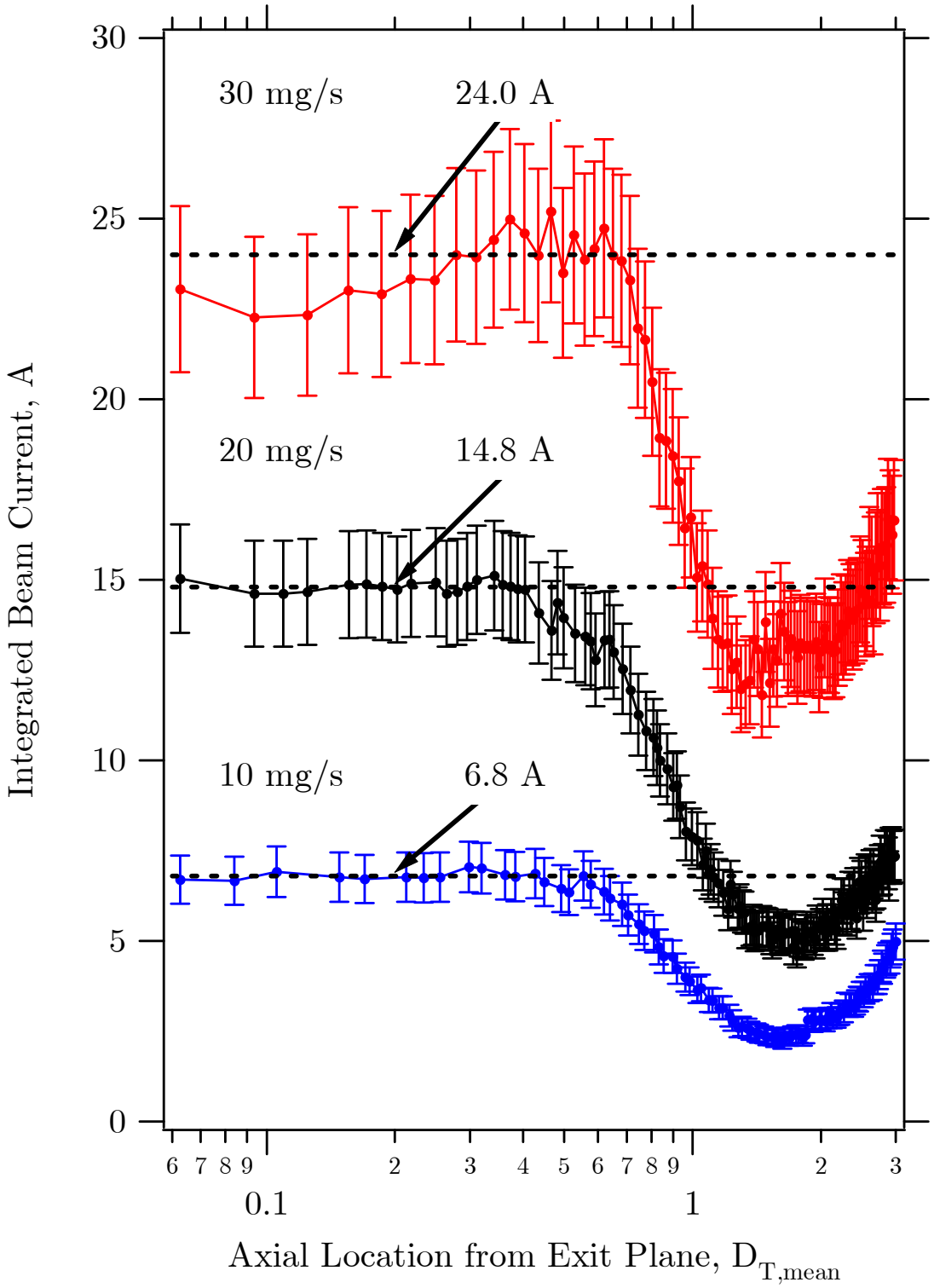

Figure C-5. Integrated beam current for thruster operation at 150 V and 10, 20, and 30 mg/s.

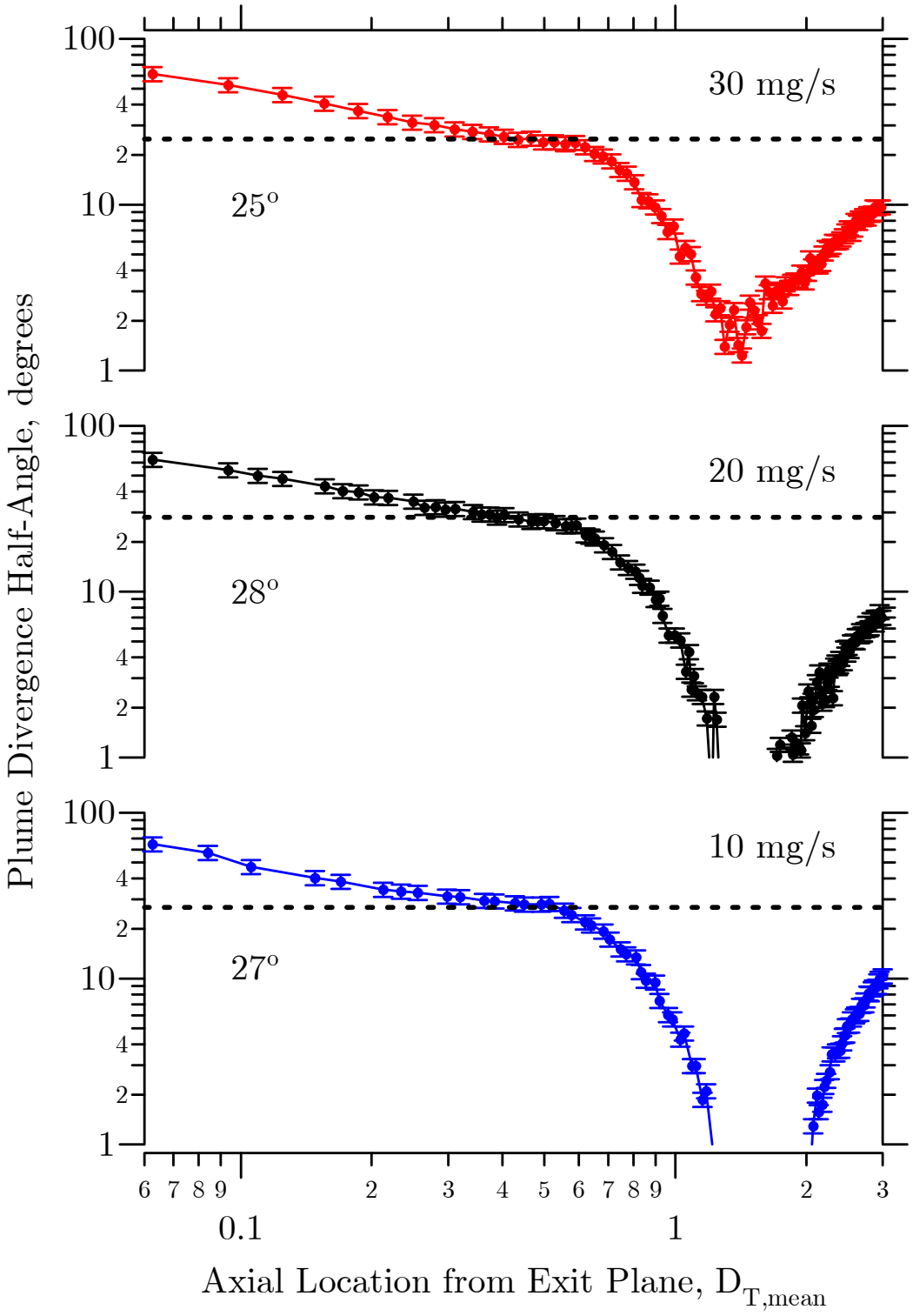

Figure C-6. Plume divergence half-angle for thruster operation at 150 V and 10, 20, and 30 mg/s.

Table C-1: Results from plume measurements for operation at 150 V.

150 V	10 mg/s	20 mg/s	30 mg/s
Xe^{1+} Current Fraction, Ω_1	0.916	0.855	0.765
Xe^{2+} Current Fraction, Ω_2	0.067	0.113	0.186
Xe^{3+} Current Fraction, Ω_3	0.017	0.031	0.049
RPA V_{mp}, V	135	131	130
RPA FWHM, V	22	30	52
RPA $V_{p,loc}$, V	11	11	10
Far-field Plume Div., θ	55	54	53
Far-field Beam Current, A	7.2	17.0	28.2
Near-field Plume Div., θ	25	28	27
Near-field Beam Current, A	6.8	14.8	24.0

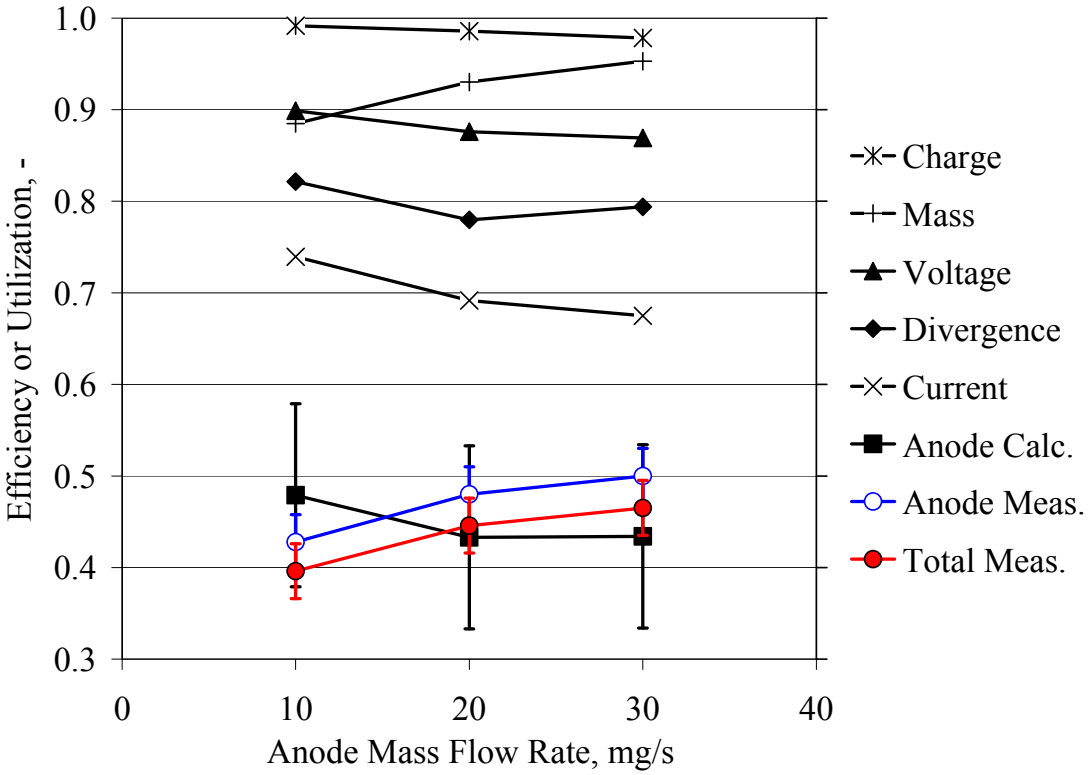

Figure C-7. Measured and computed thruster efficiency and individual utilization efficiencies for thruster operation at 150 V and 10, 20, and 30 mg/s.

Table C-2: Results from efficiency analysis for operation at 150 V.

150 V	10 mg/s	20 mg/s	30 mg/s
Charge Utilization	0.992	0.986	0.978
Voltage Utilization	0.899	0.876	0.869
Divergence Utilization	0.821	0.780	0.794
Current Utilization	0.739	0.692	0.675
Mass Utilization	0.885	0.930	0.953
Anode Efficiency – Calculated	0.479	0.433	0.434
Anode Efficiency – Measured	0.428	0.480	0.500
Total Efficiency – Measured	0.396	0.446	0.465

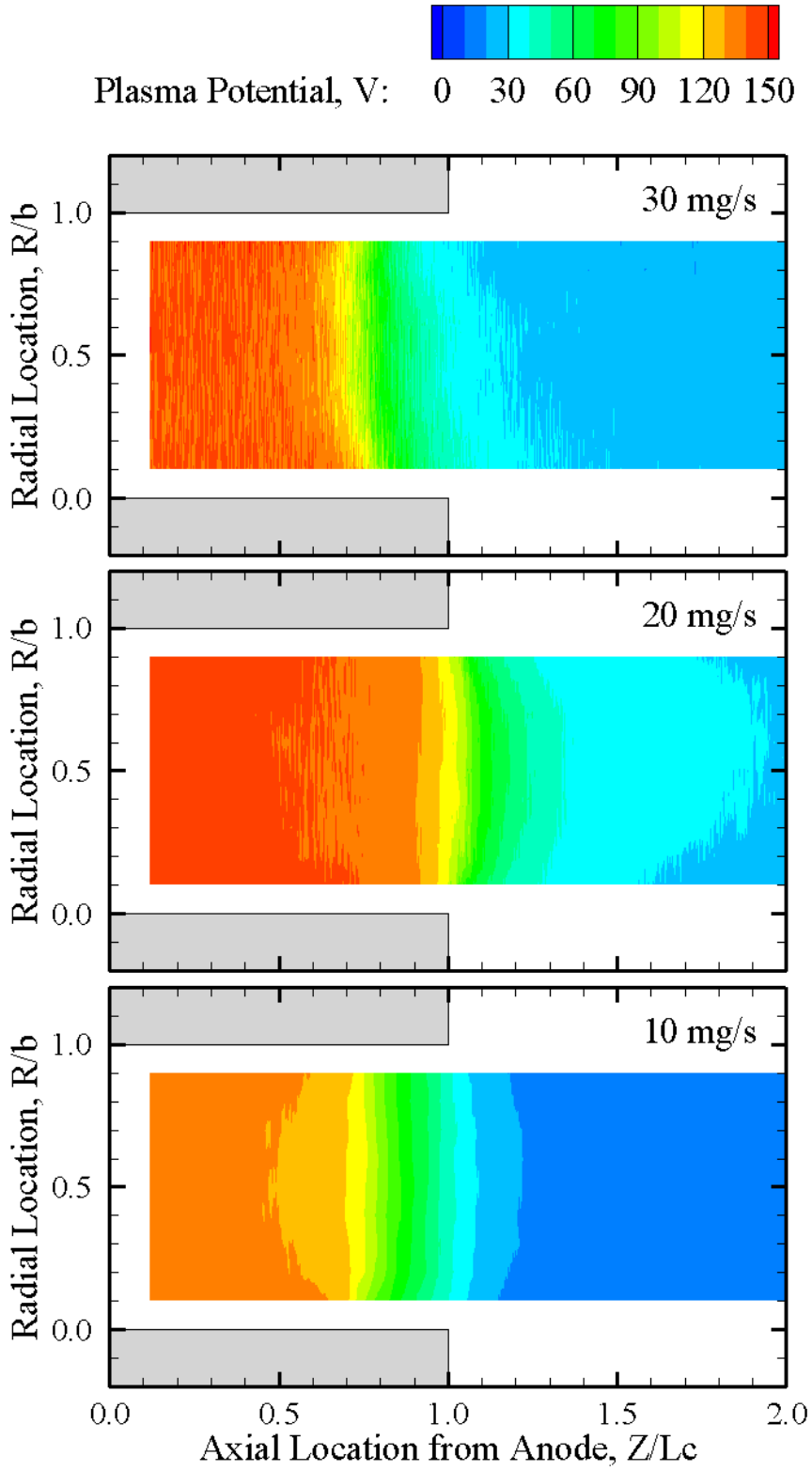

Figure C-8. Plasma potential contours for thruster operation at 150 V and 10, 20, and 30 mg/s.

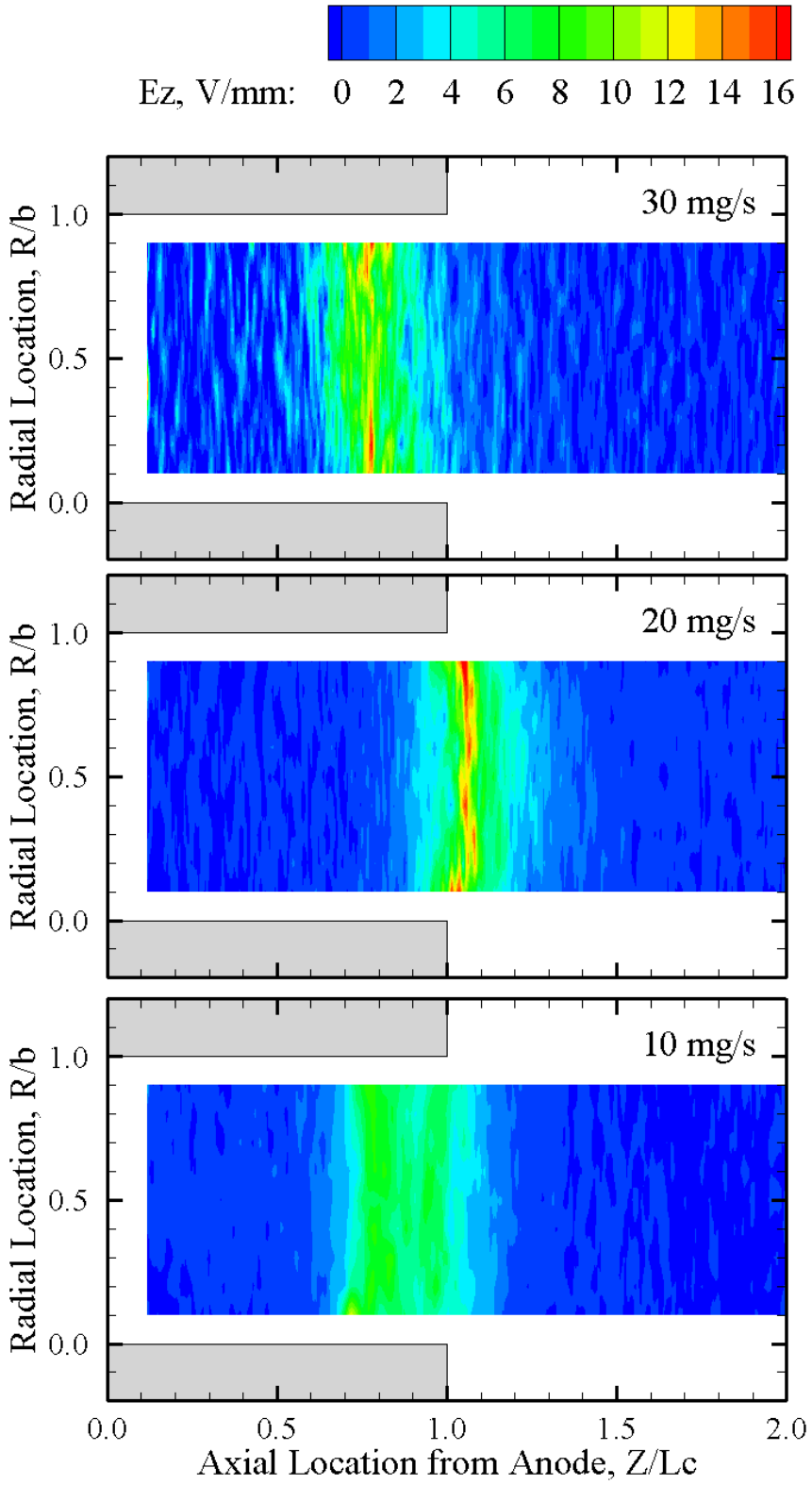

Figure C-9. Axial electric field contours for thruster operation at 150 V and 10, 20, and 30 mg/s.

Appendix D

Near-field Faraday Probe Measurements for the NASA-173M Hall Thruster

Near-field Faraday probe measurements were taken with the NASA-173M operating at 300 V and 7, 10, and 15 mg/s. The current density results are in the entire measurement domain, and the integrated beam current and plume divergence are shown at each axial location.

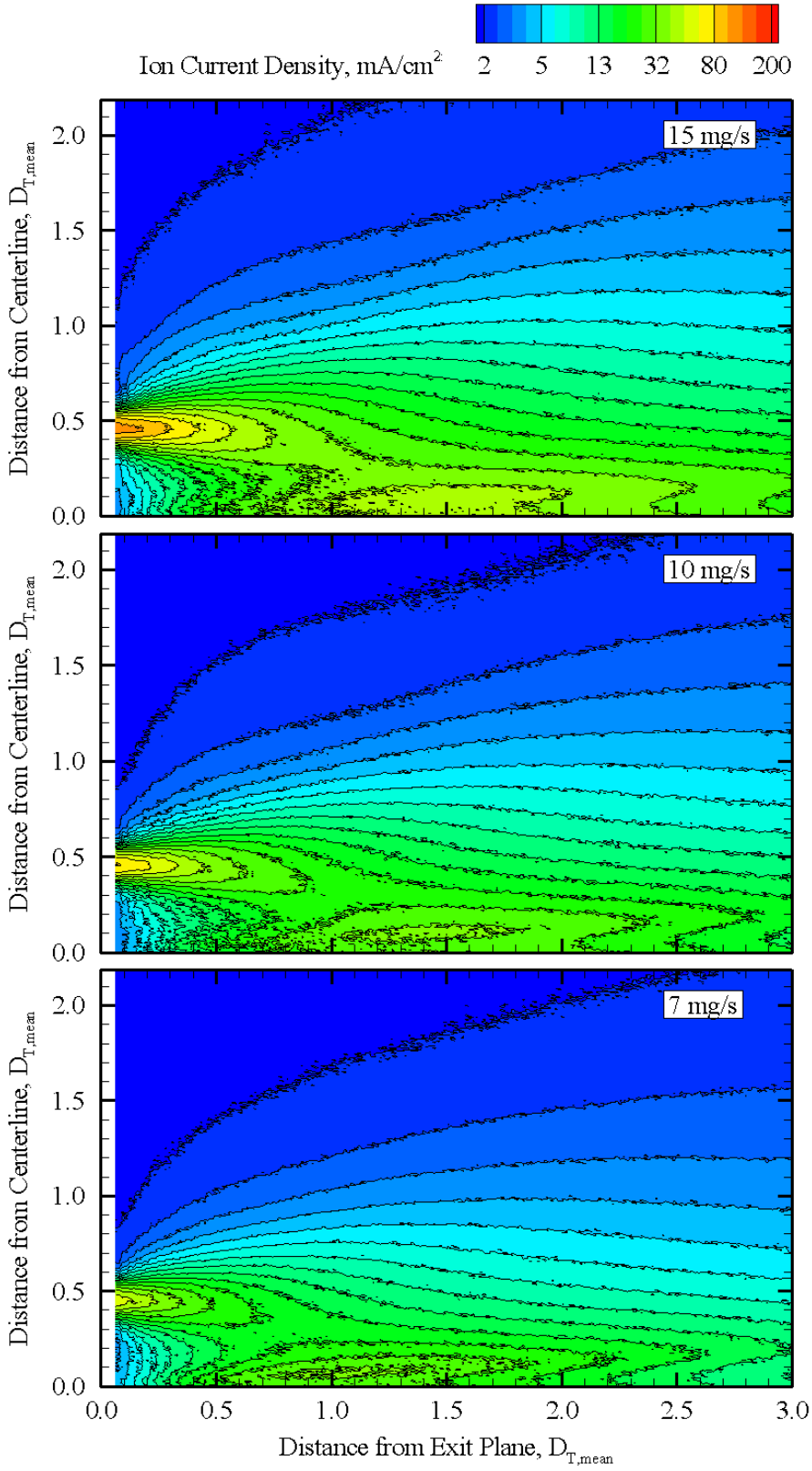

Figure D-1. Near-field Faraday probe measurements with the NASA-173M Hall thruster operating at 300 V and 7, 10, and 15 mg/s.

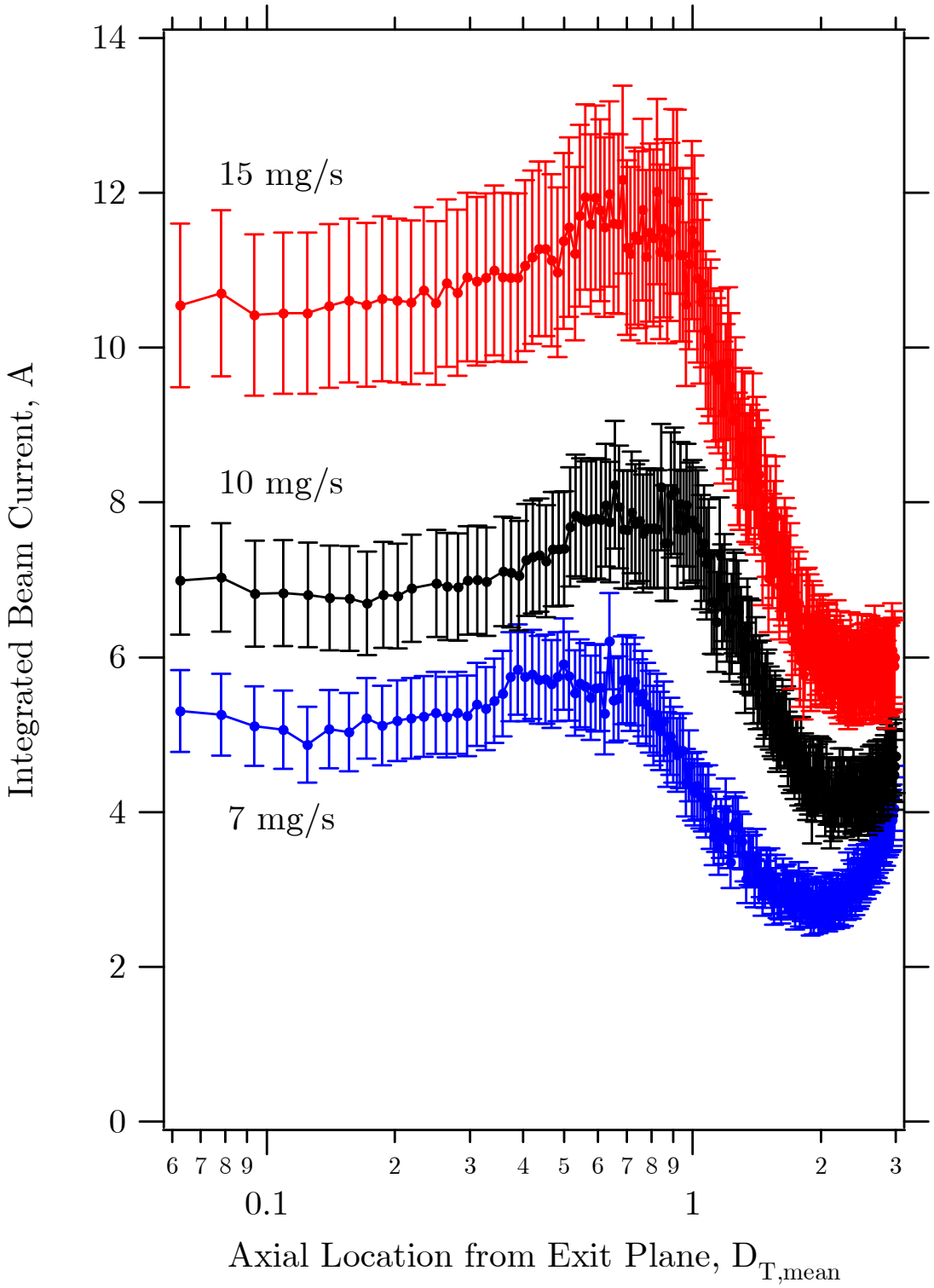

Figure D-2. Integrated beam current at each axial location for the NASA-173M Hall thruster operating at 300 V and 7, 10, and 15 mg/s.

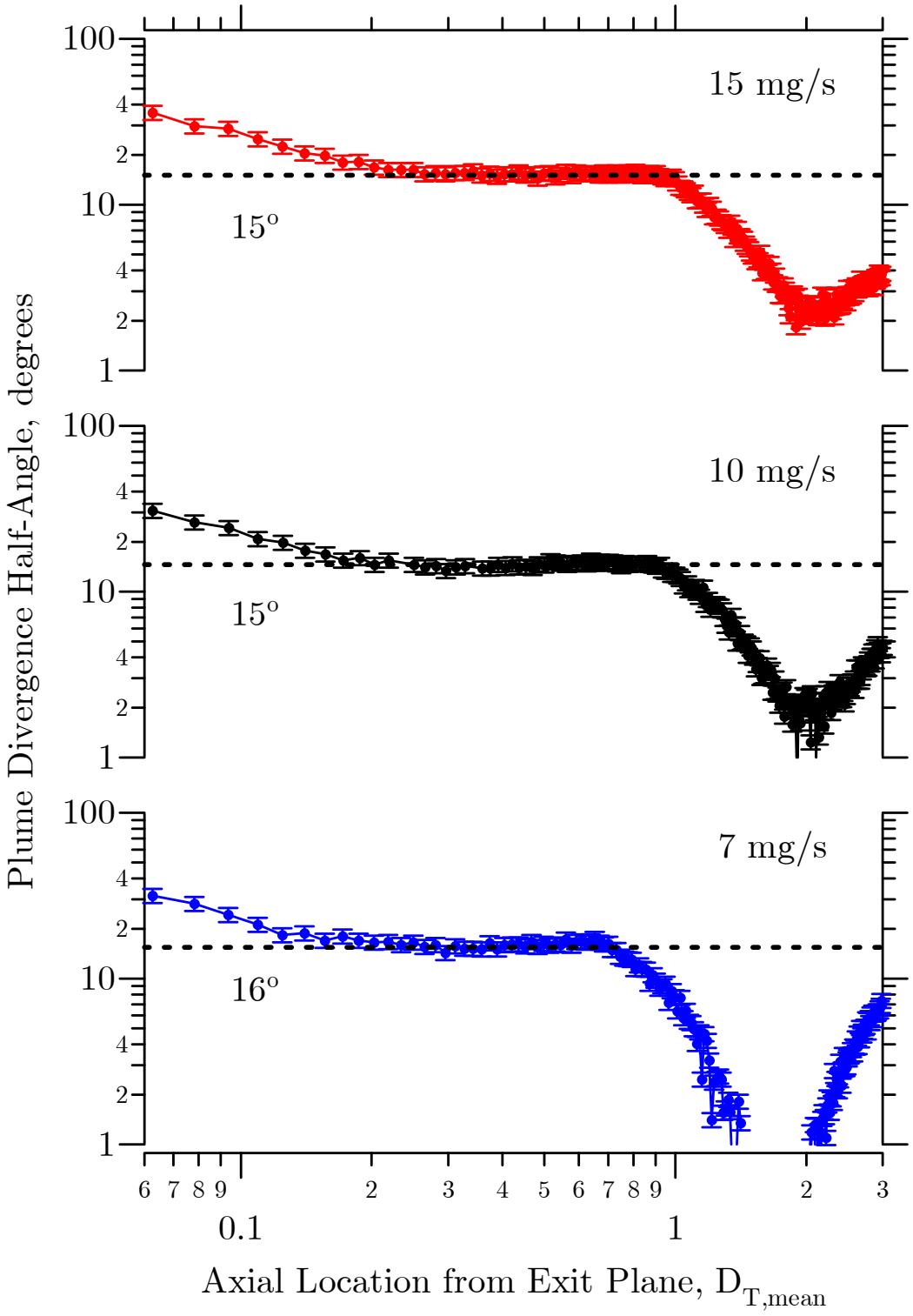

Figure D-3. Plume divergence half-angle at each axial location for the NASA-173M Hall thruster operating at 300 V and 7, 10, and 15 mg/s.

Bibliography

[1] Brophy, J., "NASA's Deep Space 1 Ion Engine (Plenary)," Review of Scientific Instruments, **73**, 2, 2002.

[2] Koppel, C. R. and Estublier, D., "The SMART-1 Hall Effect Thruster around the Moon: In Flight Experience," *29th International Electric Propulsion Conference*, IEPC-2005-119, Princeton, NJ, Oct. 31-Nov. 4, 2005.

[3] Brophy, J., Marcucci, M. G., Ganapathi, G. B., Gates, J., Garner, C., et al., "Implementation of the Dawn Ion Propulsion System," *41st AIAA/ASME/SAE/ASEE Joint Propulsion Conference*, AIAA-2005-4071, Tucson, AZ, July 10-30, 2005.

[4] Sutton, G. P. and Biblarz, O., *Rocket Propulsion Elements*, 7th Ed., John Wiley & Sons, Inc., New York, NY, 2001.

[5] Jahn, R. G., *Physics of Electric Propulsion*, McGraw-Hill Book Company, New York, 1968.

[6] Stuhlinger, E., *Ion Propulsion for Space Flight*, 1st ed. Ed., McGraw-Hill, New York, 1964.

[7] Choueiri, E. Y., "A Critical History of Electric Propulsion: The First 50 Years (1906-1956)," Journal of Propulsion and Power, **20**, 2, 193-203, 2004.

[8] Martinez-Sanchez, M. and Pollard, J. E., "Spacecraft Electric Propulsion - an Overview," Journal of Propulsion and Power, **14**, 5, 688-699, 1998.

[9] Zhurin, V. V., Kaufman, H. R. and Robinson, R. S., "Physics of Closed Drift Thrusters," Plasma Sources Science and Technology, **8**, 1, R1-R20, 1999.

[10] Kim, V., "Main Physical Features and Processes Determining the Performance of Stationary Plasma Thrusters," Journal of Propulsion and Power, **14**, 5, 736-743, 1998.

[11] Reid, B. M., Gallimore, A. D., Hofer, R. R., Li, Y. and Haas, J. M., "Anode Design and Verification for a 6-kW Hall Thruster," JANNAF Journal of Propulsion and Energetics, **2**, 1, 2009.

[12] Reid, B. M., Gallimore, A. D., Hofer, R. R., Li, Y. and Haas, J. M., "Anode Design and Verification for the ## Hall Thruster," *Presented at the 54th JANNAF Propulsion Meeting*, Denver, CO, May 14-17, 2007.

[13] Haas, J. M., Hofer, R. R., Brown, D. L., Reid, B. M. and Gallimore, A. D., "Design of the ## Hall Thruster for High Thrust/Power Investigation," *54th JANNAF Propulsion Meeting*, Denver, CO, May 14-17, 2007.

[14] Manzella, D. H., Jankovsky, R. and Hofer, R. R., "Laboratory Model 50 kW Hall Thruster," *38th AIAA/ASME/SAE/ASEE Joint Propulsion Conference*, AIAA-2002-3676, Indianapolis, IN, Jul. 7-10, 2002.

[15] Pote, B., Hruby, V. and Monheiser, J., "Performance of an 8 kW Hall Thruster," *26th International Electric Propulsion Conference*, IEPC-1999-080, Kitakyushu, Japan, Oct. 17-21, 1999.

[16] Dunaevsky, A., Raitses, Y. and Fisch, N. J., "Secondary Electron Emission from Dielectric Materials of a Hall Thruster with Segmented Electrodes," Physics of Plasmas, **10**, 6, 2574-2577, 2003.

[17] Choueiri, E. Y., "Fundamental Difference between the Two Hall Thruster Variants," Physics of Plasmas, **8**, 11, 5025-5033, 2001.

[18] Barral, S., Makowski, K., Peradzyski, Z., Gascon, N. and Dudeck, M., "Wall Material Effects in Stationary Plasma Thrusters. II. Near-Wall and in-Wall Conductivity," Physics of Plasmas, **10**, 10, 4137-4152, 2003.

[19] Raitses, Y., Staack, D., Dorf, L. and Fisch, N. J., "Experimental Study of Acceleration Region in a 2 kW Hall Thruster," *39th Joint Propulsion Conference*, IEPC-2003-5153, Huntsville, Alabama, July 2003.

[20] Haas, J. M. and Gallimore, A. D., "Considerations on the Role of the Hall Current in a Laboratory-Model Thruster," IEEE Transactions on Plasma Science, **30**, 2, 687- 697, 2002.

[21] Meezan, N. B., Hargus, W. A. and Cappelli, M. A., "Anomalous Electron Mobility in a Coaxial Hall Discharge Plasma," Physical Review E, **63**, 026410, 2001.

[22] Gascon, N., Crawford, W. S., Corey, R. L. and Cappelli, M. A., "Coaxial Hall Thruster with Diamond Inner Channel Wall," *42nd AIAA/ASME/SAE/ASEE Joint Propulsion Conference*, AIAA-2006-4995, Sacramento, CA,

[23] Meezan, N. B., Gascon, N. and Cappelli, M. A., "Linear Geometry Hall Thruster with Boron Nitride and Diamond Walls," *27th International Electric Propulsion Conference*, IEPC-2001-039, Pasadena, CA,

[24] Gascon, N., Dudeck, M. and Barral, S., "Wall Material Effects in Stationary Plasma Thrusters. I. Parametric Studies of an SPT-100," Physics of Plasmas, **10**, 10, 4123, 2003.

[25] Peterson, P. Y. and Manzella, D. H., "Investigation of the Erosion Characteristics of a Laboratory Hall Thruster," *39th AIAA/ASME/SAE/ASEE Joint Propulsion Conference*, AIAA-2003-5005, Huntsville, AL, Nov. 2003.

[26] Hofer, R. R., "Development and Characterization of High-Efficiency, High-Specific Impulse Xenon Hall Thrusters," Ph.D. Dissertation, Dept. of Aerospace Engineering, University of Michigan, Ann Arbor, MI, 2004.

[27] Boeuf, J. P. and Garrigues, L., "Low Frequency Oscillations in a Stationary Plasma Thruster," Journal of Applied Physics, **84**, 7, 3541-3554, 1998.

[28] Fife, J. M., "Hybrid-PIC Modeling and Electrostatic Probe Survey of Hall Thrusters," Ph.D. Dissertation, Dept. of Aeronautics and Astronautics, Massachusetts Institute of Technology, Cambridge, MA, 1998.

[29] Fife, J. M., Martinez-Sanchez, M. and Szabo, J., "A Numerical Study of Low-Frequency Discharge Oscillations in Hall Thrusters," *33rd AIAA/ASME/SAE/ASEE Joint Propulsion Conference*, AIAA-1997-3052, Seattle, WA, Jul. 6-9, 1997.

[30] Choueiri, E. Y., "Plasma Oscillations in Hall Thrusters," Physics of Plasmas, **8**, 4, 1411-1426, 2001.

[31] Reid, B. M. and Gallimore, A. D., "Review of Hall Thruster Neutral Flow Dynamics," *30th International Electric Propulsion Conference*, IEPC-2007-038, Florence, Italy, Sept. 17-20, 2007.

[32] Gulczinski, F. S., "Examination of the Structure and Evolution of Ion Energy Properties of a 5 kW Class Laboratory Hall Effect Thruster at Various Operational Conditions," Ph.D. Dissertation, Dept. of Aerospace Engineering, University of Michigan, Ann Arbor, MI, 1999.

[33] Pote, B. and Tedrake, R., "Performance of a High Specific Impulse Hall Thruster," *27th International Electric Propulsion Conferecne*, IEPC-2001-035, Pasadena, CA, Oct. 15-19, 2001.

[34] Reid, B. M., Gallimore, A. D., Hofer, R. R., Li, Y. and Haas, J. M., "Anode Design and Verification for the ## Hall Thruster," *54th JANNAF Propulsion Meeting*, Denver, CO, May 14-17, 2007.

[35] Dorf, L., Raitses, Y. and Fisch, N. J., "Experimental Studies of Anode Sheath Phenomena in a Hall Thruster," Journal of Applied Physics, **97**, 103309, 2005.

[36] Kim, V., "Investigation of the Anode Configuration Influence on the PPS-1350 Laboratory Model Plume Divergence," *34th AIAA/ASME/SAE/ASEE Joint Propulsion Conference*, AIAA-1998-3787, Cleveland, OH, Jul. 13-15, 1998.

[37] Vial, V., Lazurenko, A., Laure, C. and Bouchoule, A., "Xenon Gas Injection in SPT Thrusters," *28th International Electric Propulsion Conference*, IEPC-2003-221, Toulouse, France, Mar. 2003.

[38] Garrigues, L., Hagelaar, G. J. M., Boniface, C. and Boeuf, J. P., "Optimized Atom Injection in a Hall Effect Thruster," Applied Physics Letters, **85**, 22, 5460-5462, 2004.

[39] Miyasaka, T., Furukawa, T., Soga, T., Nakayama, E., Kitagawa, T., et al., "Influence of Propellant-Inlet Condition on Hall Thruster Performance," *28th International Electric Propulsion Conference*, IEPC-2003-091, Toulouse, France, Mar. 2003.

[40] Raitses, Y., Ashkenazy, J. and Guelman, M., "Propellant Utilization in Hall Thrusters," Journal of Propulsion and Power, **14**, 2, 247-253, 1998.

[41] Loyan, A. V. and Oghienko, S. A., "Investigation of Possibility to Increase the Thruster Efficiency, Discharge Efficiency, and the SPT Life-Time by Influence of the Speed of the Neutral Propellant Gas Stream," *26th International Electric Propulsion Conference*, IEPC-1999-17, Kitakyushu, Japan, Oct. 1999.

[42] Anderson, J. D., *Modern Compressible Flow: With Historical Perspective*, 2nd Ed., McGraw-Hill Publishing, 1990.

[43] Taslim, M. E. and Ugarte, S., "Discharge Coefficient Measurements for Flow through Compound-Angle Conical Holes with Cross-Flow," International Journal of Rotating Machinery, **10**, 145-153, 2004.

[44] Hill, P. and Peterson, C., *Mechanics and Thermodynamics of Propulsion*, Second Edition Ed., Addison-Welsley Publishing Company, 1992.

[45] King, B. and Gallimore, A. D., "Gridded Retarding Pressure Sensor for Ion and Neutral Particle Analysis in Flowing Plasmas," Review of Scientific Instruments, **68**, 2, 1997.

[46] Arkhipov, B. A., Krochak, L. Z. and Maslennikov, N. A., "Thermal Design of the Electric Propulsion System Components: Numerical Analysis and Testing at Fakel," *34th AIAA/ASME/SAE/ASEE Joint Propulsion Conference*, AIAA-1998-3489, Cleveland, OH, Jul. 13-15, 1998.

[47] Arkhipov, B. A., Krochak, L. Z., Kudriacev, S. S., Murashko, V. M. and Randolph, T., "Investigation of the Stationary Plasma Thruster (SPT-100) Characteristics and Thermal Maps at the Raised Discharge Power," *34th AIAA/ASME/SAE/ASEE Joint Propulsion Conference*, AIAA-1998-3791, Jul. 13-15, 1998.

[48] Jacobson, D. T., Manzella, D. H., Hofer, R. R. and Peterson, P. Y., "NASA's 2004 Hall Thruster Program," *40th AIAA/ASME/SAE/ASEE Joint Propulsion Conference*, AIAA-2004-3600, Fort Lauderdale, FL, Oct. 2004.

[49] Mazouffre, S., Echegut, P. and Dudeck, M., "A Calibrated Infrared Imaging Study on the Steady State Thermal Behaviour of Hall Effect Thrusters," Plasma Sources Science and Technology, **16**, 13-22, 2007.

[50] Ivanov, A. A., Jr., A. A. I. and Bacal, M., "Effect of Plasma–Wall Recombination on the Conductivity in Hall Thrusters," Plasma Physics and Controlled Fusion, **44**, 8, 1463-1470, 2002.

[51] Linnell, J. A., "An Evaluation of Krypton Propellant in Hall Thrusters," Ph.D. Dissertation, Dept. of Aerospace Engineering, University of Michigan, Ann Arbor, 2007.

[52] Janes, G. S. and Lowder, R. S., "Anomalous Electron Diffusion and Ion Acceleration in a Low-Density Plasma," The Physics of Fluids, **9**, 6, 1116-1123, 1966.

[53] Baranov, V., Nazarenko, Y. and Petrosov, V., "Azimuthal Non-Uniformities in Accelerators with Closed Electron Drift," *27th International Electric Propulsion Conference*, IEPC-2001-018, Pasadena, CA, Oct. 14-19, 2001.

[54] "Fluent." Release 6.2.16, ed.^eds., Fluent Incorporated, Lebanon, NH. 2005.

[55] Walker, M. L. R., Gallimore, A. D., Boyd, I. D. and Cai, C., "Vacuum Chamber Pressure Maps of a Hall Thruster Cold-Flow Expansion," Journal of Propulsion and Power, **20**, 6, 1127-1131, 2004.

[56] Boyd, I. D., VanGilder, D. B. and Liu, X., "Monte Carlo Simulation of Neutral Xenon Flows of Electric Propulsion Devices," *25th International Electric Propulsion Conference*, IEPC-1997-020, Cleveland, OH, Oct. 1997.

[57] Gamero-Castano, M. and Katz, I., "Estimation of Hall Thruster Erosion Using Hphall," *29th International Electric Propulsion Conference*, IEPC-2005-303, Princeton, NJ, Oct. 31-Nov. 4, 2005.

[58] Parra, F. I., Ahedo, E., Fife, J. M. and Martinez-Sanchez, M., "A Two-Dimensional Hybrid Model of the Hall Thruser Discharge," Journal of Applied Physics, **100**, 023304, 2006.

[59] Hofer, R. R., Katz, I., Mikellides, I. and Gamero-Castano, M., "Heavy Particle Velocity and Electron Mobility Modeling in Hybrid-PIC Hall Thruster Simulations," *42nd AIAA/ASME/SAE/ASEE Joint Propulsion Conference*, AIAA-2006-4658, Sacramento, CA, July 9-12, 2006.

[60] Hofer, R. R., Mikellides, I., Katz, I. and Goebel, D. M., "Wall Sheath and Electron Mobility Modeling in Hybrid-PIC Hall Thruster Simulations," *43rd AIAA/ASME/SAE/ASEE Joint Propulsion Conference*, AIAA-2007-5267, Cincinnati, OH, July 8-11, 2007.

[61] Hofer, R. R., Katz, I., Mikellides, I. G., Goebel, D. M., Jameson, K. K., et al., "Efficacy of Electron Mobility Models in Hybrid-PIC Hall Thruster Simulations," *AIAA/ASME/SAE/ASEE Joint Propulsion Conference*, AIAA-2008-4924, Hartford, CT, Jul. 20-23, 2008.

[62] Hofer, R. R., Mikellides, I., Katz, I. and Goebel, D. M., "BPT-4000 Hall Thruster Discharge Chamber Erosion Model Comparison with Qualification Life Test Data," *30th International Electric Propulsion Conference*, IEPC-2007-267, Florence, Italy, Sept. 17-20, 2007.

[63] Oghienko, S. A. and Oranskiy, A. I., "The Gear of a Working Gas Flow in the SPT Discharge Chamber," *28th International Electric Propulsion Conference*, IEPC-2003-024, Toulouse, France, Mar. 2003.

[64] Masouffre, S., Pagnon, D., Lasgorceix, P. and Touzeau, M., "Temperature of Xenon Atoms in a Stationary Plasma Thruster," *28th International Electric Propulsion Conf.*, IEPC-03-283, Mar. 2003.

[65] Bonnet, J., "LIF-Doppler Velocity Measurement of Xenon Atoms in a SPT-50," *28th International Electric Propulsion Conference*, IEPC-2003-300, Toulouse, France, Mar. 2003.

[66] Stephenson, W. B., "Use of Pitot Tubes in Very Low Density Flows," AEDC-TR-81-11, Arnold Engineering Development Center, Arnold AFS, TN, Oct. 1981.

[67] de Grys, K. H., Meckel, N., Callis, G., Greisen, D., Hoskins, A., et al., "Development and Testing of a 4500 Watt Flight Type Hall Thruster and Cathode," *27th International Electric Propulsion Conference*, IEPC-2001-011, Oct. 2001.

[68] Boyd, I. D., "Experimental and Numerical Investigations of Low-Density Nozzle and Plume Flows of Nitrogen," AIAA Journal, **30**, 10, 2453-2461, 1992.

[69] King, L. B., Gallimore, A. D. and Marrese, C. M., "Transport-Property Measurements in the Plume of an SPT-100 Hall Thruster," Journal of Propulsion and Power, **14**, 3, 327-335, 1998.

[70] Arhipov, B. A., Krochak, L. Z. and Maslennikov, N. A., "Thermal Design of the Electric Propulsion System Components: Numerical Analysis and Testing at Fakel," *34th AIAA/ASME/SAE/ASEE Joint Propulsion Conference*, AIAA-1998-3489, Cleveland, OH, Jul. 13-15, 1998.

[71] Arhipov, B. A., Krochak, L. Z., Kudriacev, S. S., Murashko, V. M. and Randolph, T., "Investigation of the Stationary Plasma Thruster (SPT-100) Characteristics and Thermal Maps at the Raised Discharge Power," *34th AIAA/ASME/SAE/ASEE Joint Propulsion Conference*, AIAA-1998-3791, Jul. 13-15, 1998.

[72] Smith, T. B., Huang, D., Reid, B. M. and Gallimore, A. D., "Near-Field Laser-Induced Fluorescence Velocimetry of Neutral Xenon in a 6-kW Hall Thruster Plume," *30th International Electric Propulsion Conference*, IEPC-2007-252, Florence, Italy, Sept. 17-20, 2007.

[73] Hargus, W. A., "Laser-Induced Fluorescence of Neutral Xenon in the near Field of a 200 W Hall Thruster," *41st AIAA/ASME/SAE/ASEE Joint Propulsion Conference*, AIAA-2005-4400, Tucson, AZ, Jul. 10-13, 2005.

[74] Hargus, W. A. and Cappelli, M. A., "Laser-Induced Fluorescence Measurements of Velocity within a Hall Discharge," Applied Physics B, **72**, 961-969, 2001.

[75] Hargus, W. A. and Cappelli, M. A., "Interior and Exterior Laser-Induced Fluoresence and Plasma Measurements with a Hall Thruster," Journal of Propulsion and Power, **18**, 1, 159-168, 2002.

[76] Cedolin, R. J., Hargus, W. A., Storm, P. V., Hanson, R. K. and Cappelli, M. A., "Laser-Induced Fluorescence Study of a Xenon Hall Thruster," Applied Physics B, **65**, 459-469, 1997.

[77] Dushman, S., *Scientific Foundations of Vacuum Technique*, Vol. 4, Wiley, New York, 1958.

[78] Reid, B. M., Gallimore, A. D., Hofer, R. R., Li, Y. and Haas, J. M., "Anode Design and Verification for a 6-kW Hall Thruster," JANNAF Journal, Accepted, 2008.

[79] Brown, D. L., Reid, B. M., Gallimore, A. D., Hofer, R. R., Haas, J. M., et al., "Performance Characterization and Design Verification of the ## Laboratory Model Hall Thruster," *54th JANNAF Propulsion Meeting*, Denver, CO, May 14-17, 2007.

[80] Hofer, R. R., Goebel, D. M. and Watkins, R. M., "Compact LaB6 Hollow Cathode for the ## Hall Thruster," *54th JANNAF Propulsion Meeting*, Denver, CO, May 14-17, 2007.

[81] Dymond, J. H. and Smith, E. B., *The Virial Coefficients of Pure Gases and Mixtures, a Critical Compilation*, Oxford University Press, New York, 1980.

[82] Haas, J. M., Gallimore, A. D., McFall, K. and Spanjers, G., "Development of a High-Speed, Reciprocating Electrostatic Probe System for Hall Thruster Interrogation," Review of Scientific Instruments, **71**, 11, 4131-4138, 2000.

[83] Haag, T. W., "Design of a Thrust Stand for High Power Electric Propulsion Devices," *25th AIAA/ASME/SAE/ASEE Joint Propulsion Conference*, AIAA-1989-2829, Monterey, CA, Jul. 10-13, 1989.

[84] Kim, S. W., "Experimental Investigations of Plasma Parameters and Species-Dependent Ion Energy Distribution in the Plasma Exhaust Plume of a Hall Thruster," Ph. D. Dissertation, Dept. of Aerospace Engineering, University of Michigan, Ann Arbor, 1999.

[85] Kim, S. W. and Gallimore, A. D., "Plume Study of a 1.35 kW SPT-100 Using an ExB Probe," *35th AIAA/ASME/SAE/ASEE Joint Propulsion Conference*, AIAA-1999-2423, Los Angeles, CA., Jun. 20-24, 1999.

[86] Hofer, R. R. and Gallimore, A. D., "Ion Species Fractions in the Far-Field Plume of a High-Specific Impulse Hall Thruster," *39th AIAA/ASME/SAE/ASEE Joint Propulsion Conference*, AIAA 2003-5001, Huntsville, AL, Jul. 20-23, 2003.

[87] Reid, B. M., Shastry, R., Gallimore, A. D. and Hofer, R. R., "Angularly-Resolved ExB Probe Spectra in the Plume of a 6-kW Hall Thruster," *44th AIAA/ASME/SAE/ASEE Joint Propulsion Conference*, AIAA-2008-5287, Hartford, CT, Jul. 20-23, 2008.

[88] Hofer, R. R., Jankovsky, R. S. and Gallimore, A. D., "High-Specific Impulse Hall Thrusters, Part 2: Efficiency Analysis," Journal of Propulsion and Power, **22**, 4, 732-740, 2006.

[89] Ekholm, J. M. and Hargus, W. A., "ExB Measurements of a 200 W Xenon Hall Thruster," *41st AIAA/ASME/SAE/ASEE Joint Propulsion Conference*, AIAA-2005-4405, Tucson, AZ, Jul. 10-13, 2005.

[90] Shastry, R., Hofer, R. R., Reid, B. M. and Gallimore, A. D., "Method for Analyzing ExB Probe Spectra from Hall Thruster Plumes," *44th AIAA/ASME/SAE/ASEE Joint Propulsion Conference*, AIAA-2008-4647, Hartford, CT, Jul. 20-23, 2008.

[91] Randolph, T., Kim, V., Kaufman, H. R., Kozubsky, K., Zhurin, V. V., et al., "Facility Effects on Stationary Plasma Thruster Testing," *23rd International Electric Propulsion Conference*, Seattle, WA, Sept. 13-16, 1993.

[92] Hutchinson, I. H., *Principles of Plasma Diagnostics*, Second Ed., Cambridge University Press, Cambridge, 2002.

[93] Hofer, R. R., Haas, J. M. and Gallimore, A. D., "Ion Voltage Diagnostics in the Far-Field Plume of a High-Specific Impulse Hall Thruster," *39th AIAA/ASME/SAE/ASEE Joint Propulsion Conference*, AIAA-2003-4556, Huntsville, AL, Jul. 20-23, 2003.

[94] Linnell, J. A. and Gallimore, A. D., "Efficiency Analysis of a Hall Thruster Operating with Krypton and Xenon," Journal of Propulsion and Power, **22**, 6, 2006.

[95] King, L. B., "Transport-Property and Mass Spectral Measurements in the Plasma Exhaust Plume of a Hall-Effect Space Propulsion System," Ph.D. Dissertation, Dept. of Aerospace Engineering, University of Michigan, Ann Arbor, 1998.

[96] Beal, B. E. and Gallimore, A. D., "Energy Analysis of a Hall Thruster Cluster," *28th International Electric Propulsion Conference*, IEPC-2003-035, Toulouse, France, Mar. 17-21, 2003.

[97] Rovey, J. L., Walker, M. L. R., Gallimore, A. D. and Peterson, P. Y., "Magnetically Filtered Faraday Probe for Measuring the Ion Current Density Profile of a Hall Thruster," Review of Scientific Instruments, **77**, 013503, 2006.

[98] Beal, B. E., "Clustering of Hall Effect Thrusters for High-Power Electric Propulsion Applications," Ph.D. Dissertation, Dept. of Aerospace Engineering, University of Michigan, Ann Arbor, MI, 2004.

[99] Azziz, Y., Martinez-Sanchez, M. and Szabo, J., "Determination of in-Orbit Plume Characteristics from Laboratory Measurements," *42nd AIAA/ASME/SAE/ASEE Joint Propulsion Conference*, AIAA-2006-4484, Sacramento, CA, Jul. 9-12, 2006.

[100] de Grys, K. H., Tilley, D. L. and Aadland, R. S., "BPT Hall Thruster Plume Characteristics," *35th AIAA/ASME/SAE/ASEE Joint Propulsion Conference*, AIAA-1999-2283, Los Angeles, CA, Jun. 20-24, 1999.

[101] Hofer, R. R., Walker, M. L. R. and Gallimore, A. D., "A Comparison of Nude and Collimated Faraday Probes for Use with Hall Thrusters," *27th International Electric Propulsion Conference*, IEPC-2001-020, Pasadena, CA, Oct. 15-19, 2001.

[102] Walker, M. L. R., Victor, A. L., Hofer, R. R. and Gallimore, A. D., "Effect of Backpressure on Ion Current Density Measurements in Hall Thruster Plumes," Journal of Propulsion and Power, **21**, 3, 408-415, 2005.

[103] Goebel, D. M. and Katz, I., *Fundamentals of Electric Propulsion: Ion and Hall Thrusters*, Jet Propulsion Laboratory, 2008.

[104] Manzella, D. H., "Hall Thruster Ion Beam Characterization," *31st AIAA/ASME/SAE/ASEE Joint Propulsion Conference*, AIAA-1995-2927, San Diego, CA, Jul. 10-12, 1995.

[105] Hofer, R. R. and Gallimore, A. D., "Recent Results from Internal and Very-near-Field Plasma Diagnostics of a High Specific Impulse Hall Thruster," *28th International Electric Propulsion Conference*, IEPC-2003-037, Toulouse, France, Mar. 17-21, 2003.

[106] Jameson, K. K., Goebel, D. M., Hofer, R. R. and Watkins, R. M., "Cathode Coupling in Hall Thrusters," *30th International Electric Propulsion Conference*, IEPC-2007-278, Florence, Italy,

[107] Lieberman, M. A. and Lichtenberg, A. J., *Principles of Plasma Discharges and Materials Processing*, John Wiley & Sons, Inc., New York, 1994.

[108] Chen, F. F., *Introduction to Plasma Physics and Controlled Fusion*, Vol. 1: Plasma Physics, Plenum Press, New York, 1984.

[109] Haas, J. M., "Low-Perturbation Interrogation of the Internal and near-Field Plasma Structure of a Hall Thruster Using a High-Speed Probe Positioning System," Ph.D. Dissertation, Dept. of Aerospace Engineering, University of Michigan, 2001.

[110] Reid, B. M. and Gallimore, A. D., "Langmuir Probe Measurements in the Discharge Channel of a 6-kW Hall Thruster," *44th AIAA/ASME/SAE/ASEE Joint Propulsion Conference*, AIAA-2008-4920, Hartford, CT, Jul. 20-23, 2008.

[111] Chen, F. F. "Electric Probes." Plasma Diagnostic Techniques, R. H. Huddlestone and S. L. Leonard, ed.^eds., Academic Press, New York. 1965.

[112] Hershkowitz, N. "How Langmuir Probes Work." Plasma Diagnostics, O. Auciello and D. L. Flamm, ed.^eds., Academic Press, Inc., Boston, 113-184. 1989.

[113] Cherrington, B. E., "The Use of Electrostatic Probes for Plasma Diagnostics - a Review," Plasma Chemistry and Plasma Processing, **2**, 2, 113-140, 1982.

[114] Reid, B. M. and Gallimore, A. D., "Plasma Potential Measurements in the Discharge Channel of a 6-kW Hall Thruster," *44th AIAA/ASME/SAE/ASEE Joint Propulsion Conference*, AIAA-2008-5185, Hartford, CT, Jul. 20-23, 2008.

[115] Shastry, R., Gallimore, A. D. and Hofer, R. R., "Interpretation of Wall-Mounted Probe Characteristics in Hall Thrusters," *44th AIAA/ASME/SAE/ASEE Joint Propulsion Conference*, AIAA-2008-4723, Hartford, CT, Jul. 21-23, 2008.

[116] Aikawa, H., "The Measurement of the Anisotropy of Electron Distribution Function of a Magnetized Plasma," Journal of the Physical Society of Japan, **40**, 6, 1741-1749, 1976.

[117] Laframboise, J. G., "Theory of Spherical and Cylindrical Langmuir Probes in a Collisionless, Maxwellian Plasma at Rest," UTIAS Report No. 100, Institute for Aerospace Studies, University of Toronto, Toronto, Canada, Jun. 1966.

[118] Steinbruchel, C., "A New Method for Analyzing Langmuir Probe Data and the Determination of Ion Densities and Etch Yields in an Etching Plasma," Journal of Vacuum Science and Technology A, **8**, 3, 1663-1667, 1990.

[119] Mausbach, M., "Parametrization of the Laframboise Theory for Cylindrical Langmuir Probe Analysis," Journal of Vacuum Science and Technology A, **15**, 6, 2923-2929, 1997.

[120] Narasimhan, G. and Steinbrüchel, C., "Parametrization of Laframboise'S Results for Spherical and Cylindrical Langmuir Probes," Journal of Vacuum Science and Technology A, **19**, 1, 376-378, 1999.

[121] Narasimhan, G. and Steinbruchel, C., "Analysis of Langmuir Probe Data: Analytical Parametrization, and the Importance of the End Effect," Journal of Vacuum Science and Technology A, **19**, 1, 376-378, 2001.

[122] Raitses, Y., Staack, D., Smirnov, A. and Fisch, N. J., "Space Charge Saturated Sheath Regime and Electron Temperature Saturation in Hall Thrusters," Physics of Plasmas, **12**, 073507, 2005.

[123] Raitses, Y., Staack, D. and Fisch, N. J., "Plasma Characterization of Hall Thruster with Active and Passive Segmented Electrodes," AIAA Journal, **2002-3954**, 2002.

[124] Haas, J. M. and Gallimore, A. D., "Internal Plasma Potential Profiles in a Laboratory-Model Hall Thruster," Physics of Plasmas, **8**, 2, 652-660, 2001.

[125] Hobbs, G. D. and Wesson, J. A., "Heat Flow through a Langmuir Sheath in the Presence of Electron Emission," Plasma Physics, **9**, 1, 85-87, 1967.

[126] Schwager, L. A., Hsu, W. L. and Tung, D. M., "Effects of Cold Electron Emission on the Plasma Sheath," Physics of Fluids B: Plasma Physics, **5**, 2, 621-630, 1993.

[127] Linnell, J. A. and Gallimore, A. D., "Internal Plasma Potential Measurements of a Hall Thruster Using Plasma Lens Focusing," Physics of Plasmas, **13**, 103504, 2006.

[128] Linnell, J. A. and Gallimore, A. D., "Internal Plasma Potential Measurements of a Hall Thruster Using Xenon and Krypton Propellant," Physics of Plasmas, **13**, 093502, 2006.

[129] Kim, V., Grdlichko, D., Kozlov, V., Lazurenko, A., Popkov, G. B., et al., "Local Plasma Parameter Measurements by Nearwall Probes inside the SPT Accelerating Channel under Thruster Operation with Kr," *38th AIAA/ASME/SAE/ASEE Joint Propulsion Conference*, AIAA-2002-4108, Indianapolis, IN, Jul. 7-10, 2002.

[130] Staack, D., Raitses, Y. and Fisch, N. J., "Temperature Gradient in Hall Thrusters," Applied Physics Letters, **84**, 16, 3028-3030, 2004.

[131] Katz, I., Hofer, R. R. and Goebel, D. M., "Ion Current in Hall Thrusters," IEEE Journal, 2008.

[132] Walker, M. L. R., Hofer, R. R. and Gallimore, A. D., "The Effects of Nude Faraday Probe Design and Vacuum Facility Backpressure on the Measured Ion Current Density Profile of Hall Thruster Plumes," *38th AIAA/ASME/SAE/ASEE Joint Propulsion Conference*, AIAA-2002-4253, Indianapolis, IN, Jul. 7-10, 2002.

[133] Smith, T. B., "Deconvolution of Ion Velocity Distributions from Laser-Induced Fluorescence Spectra of Xenon Electrostatic Thruster Plumes," Doctoral, Dept. of Aerospace Engineering, University of Michigan, Ann Arbor, MI, 2003.

[134] Huang, D., Reid, B. M., Smith, T. B. and Gallimore, A. D., "Laser-Induced Fluorescence of Singly-Charged Xenon in a 6-kW Hall Thruster Plume," *44th AIAA/ASME/SAE/ASEE Joint Propulsion Conference*, AIAA-2008-5102, Hartford, CT, Jul. 20-23, 2008.

[135] Pacros, A., "Instruments Design and Testing for a Hall Thruster Plume Experiment on the Space Shuttle," M.S., Dept. of Aeronautics and Astronautics, Massachusetts Institute of Technology, 2002.

[136] Hargus, W. A. and Charles, C. S., "Near Plume Laser Induced Fluorescence Velocity Measurements of a 600 W Hall Thruster," *44th AIAA/ASME/SAE/ASEE Joint Propulsion Conference*, AIAA-2008-5004, Hartford, CT, Jul. 21-23, 2008.

[137] Hruby, V., Monheiser, J., Pote, B., Rostler, P., Kolencik, J., et al., "Development of Low Power Hall Thrusters," *30th Plasmadynamics and Lasers Conference*, AIAA-1999-3534, Norfolk, VA, Jun. 28-Jul.1, 1999.

[138] Hofer, R. R., Peterson, P. Y. and Gallimore, A. D., "A High Specific Impulse Two-Stage Hall Thruster with Plasma Lens Focusing," *27th International Electric Propulsion Conference*, IEPC-2001-036, Pasadena, CA, Oct. 15-19, 2001.

[139] Williams, G. J., Smith, T. B., Gulczinski, F. S., Beal, B. E., Gallimore, A. D., et al., "Laser Induced Fluorescence Measurements of Ion Velocities in the Plume of a Hal Effect Thruster," *35th AIAA/ASME/SAE/ASEE Joint Propulsion Conference*, AIAA-1999-2424, Los Angeles, CA,

[140] Hofer, R. R., Johnson, L. K., Goebel, D. M. and Wirz, R. E., "Effects of Internally-Mounted Cathodes on Hall Thruster Plume Properties," IEEE Journal, 2008.

[141] Jameson, K. K., "Investigation of Hollow Cathode Effects on Total Thruster Efficiency in a 6 kW Hall Thruster," Dept. of Aerospace Engineering, University of California Los Angeles, Los Angeles, 2008.

[142] Beal, B. E., Gallimore, A. D. and Hargus, W. A., "Preliminary Plume Characterization of a Low-Power Hall Thruster Cluster," *38th AIAA/ASME/SAE/ASEE Joint Propulsion Conference*, AIAA-2002-4251, Indianapolis, IN, Jul. 7-10, 2002.

[143] Raitses, Y., Granstedt, E., Smirnov, A., Merino, E. and Fisch, N. J., "Effects of Cathode Electron Emission on Hall Thruster Discharge," *44th AIAA/ASME/SAE/ASEE Joint Propulsion Conference*, AIAA-2008-5188, Hartford, CT, Jul. 21-23, 2008.

[144] Larson, C. W., Brown, D. L. and Hargus, W. A., "Performance Mapping for Hall Thrusters," *54th JANNAF Propulsion Meeting*, Denver, CO, May 14-17, 2007.

[145] Larson, C. W., Brown, D. L. and Hargus, W. A., "Thrust Efficiency, Energy Efficiency and the Role of VDF in Hall Thruster Performance Analysis," *43rd AIAA/ASME/SAE/ASEE Joint Propulsion Conference*, AIAA-2007-5270, Cincinnati, OH, Jul. 8-11, 2007.

[146] Brown, D. L., Larson, C. W., Haas, J. M. and Gallimore, A. D., "Analytical Extraction of Plasma Properties Using a Hall Thruster Efficiency Architecture," *30th International Electric Propulsion Conference*, IEPC-2008-188, Florence, Italy,

[147] Peterson, P. Y., Jacobson, D. T., Manzella, D. H. and John, J. W., "The Performance and Wear Characterization of a High-Power High-Isp NASA Hall Thruster," *41st AIAA/ASME/SAE/ASEE Joint Propulsion Conference*, AIAA-2005-4243, Tucson, AZ, Jul. 10-13, 2005.

[148] Day, M., Maslennikov, N. A., Randolph, T. and Rogers, W., "SPT-100 Subsystem Qualification Status," *AIAA/ASME/SAE/ASEE Joint Propulsion Conference*, AIAA-1996-2713, Buena Vista, FL, July 1-3, 1996.

[149] Peterson, P. Y., Kamhawi, H., Manzella, D. H. and Jacobson, D. T., "Hall Thruster Technology for NASA Science Missions: Hivac Status Update," *43rd AIAA/ASME/SAE/ASEE Joint Propulsion Conference*, AIAA-2007-5236, Cincinnati, OH, July 8-11, 2007.

[150] Manzella, D. H., Jacobson, D. T. and Jankovsky, R. S., "High Voltage SPT Performance," *37th AIAA/ASME/SAE/ASEE Joint Propulsion Conference*, AIAA-2001-3774, Salt Lake City, UT, Jul. 8-11, 2001.

[151] Arhipov, B. A., Vinogradov, V. N., Kozubsky, K., Kudriavtsev, S. S., Maslennikov, N. A., et al., "Development and Application of Electric Thrusters at EDB "Fakel"," *25th International Electric Propulsion Conference*, IEPC-1997-004, Cleveland, OH, Aug. 24-28, 1997.

[152] Hofer, R. R., Jankovsky, R. S. and Gallimore, A. D., "High-Specific Impulse Hall Thrusters, Part 1: Influence of Current Density and Magnetic Field," Journal of Propulsion and Power, **22**, 4, 721-731, 2006.

[153] Jacobson, D. T. and Manzella, D. H., "50 kW Class Krypton Hall Thruster Performance," *39th AIAA/ASME/SAE/ASEE Joint Propulsion Conference*, AIAA-2003-4550, Huntsville, AL, Jul. 20-23, 2003.

[154] Reid, B. M., Brown, D. L. and Haas, J. M., "Performance Measurements of a 3-cm Cylindrical Hall Thruster," JANNAF Journal of Propulsion and Energetics, **2**, 1, 2009.

[155] Staack, D., Raitses, Y. and Fisch, N. J., "Shielded Electrostatic Probe for Nonperturbing Plasma Measurements in Hall Thrusters," Review of Scientific Instruments, **75**, 2, 393-399, 2004.

[156] Raitses, Y., Staack, D., Keidar, M. and Fisch, N. J., "Electron-Wall Interaction in Hall Thrusters," Physics of Plasmas, **12**, 057104, 2005.

[157] Lazurenko, A., Dudok de Wit, T., Cavoit, C., Krasnoselskikh, V., Bouchoule, A., et al., "Determiniation of the Electron Anomalous Mobility through Measurements of Turbulent Magnetic Field in Hall Thrusters," Physics of Plasmas, **14**, 033504, 11, 2007.

[158] Dorval, N., Bonnet, J., Marque, J. P., Rosencher, E., Chable, S., et al., "Determination of the Ionization and Acceleration Zones in a Stationary Plasma Thruster by Optical Spectroscopy Study: Experiments and Model," Journal of Applied Physics, **91**, 8, 2002.

[159] Dugan, J. V. and Sovie, R. J., "Volume Ion Production Costs in Tenuous Plasmas," NASA TN D-4150, NASA Lewis Research Center, Cleveland, OH, Sep. 1967.

[160] Mitchner, M. and Kruger, C. H., *Partially Ionized Gases*, John Wiley & Sons, 1973.

[161] Nickel, J. C., Imre, K., Register, D. F. and Trajmar, S., "Total Electron Scattering Cross Sections: I. He, Ne, Ar, Xe," Journal of Physics B: Atomic, Molecular and Optical Physics, **18**, 125-133, 1985.

[162] Huba, J. D., *NRL Plasma Formulary*, Naval Research Laboratory, Washington, DC, 2002.

[163] Garrigues, L., Hagelaar, G. J. M., Boniface, C. and Boeuf, J. P., "Anomalous Conductivity and Secondary Electron Emission in Hall Effect Thrusters," Journal of Applied Physics, **100**, 123301, 2006.

[164] Ahedo, E., Gallardo, J. M. and Martinez-Sanchez, M., "Effects of the Radial Plasma-Wall Interaction on the Hall Thruster Discharge," Physics of Plasmas, **10**, 8, 3397-3409, 2003.

[165] Morozov, A. I., "Conditions for Efficient Current Transport by near-Wall Conduction," Sov.Phys. Tech.Phys., **32**, 8, 901-904, 1987.

[166] Morozov, A. I. and Savel'ev, V. V., "Theory of the near-Wall Conductivity," Plasma Physics Reports, **27**, 7, 570, 2001.

[167] Ahedo, E., "Radial Macroscopic Model of a Plasma Flowing Along Annual Dielectric Walls," Physics of Plasmas, **9**, 7, 3178-3186, 2002.

[168] Yim, J. T., Keidar, M. and Boyd, I. D., "An Investigation of Factors Involved in Hall Thruster Wall Erosion Modeling," *42nd AIAA/ASME/SAE/ASEE Joint Propulsion Conference*, AIAA-2006-4657, Sacramento, CA, Jul. 9-12, 2006.

[169] Downey, R. T., "Theoretical and Experimental Investigation into High Current Hollow Cathode Arc Attachment," Ph.D. Dissertation, Dept. of Astronautical Engineering, University of Southern California, 2008.

[170] Nakles, M. R. and Hargus, W. A., "Background Pressure Effects on Internal and near-Field Ion Velocity Distribution of the BHT-600 Hall Thruster," *44th AIAA/ASME/SAE/ASEE Joint Propulsion Conference*, AIAA-2008-5101, Hartford, CT, Jul. 21-23, 2008.

[171] Hofer, R. R., Peterson, P. Y. and Gallimore, A. D., "Characterizing Vacuum Facility Backpressure Effects on the Performance of a Hall Thruster," *27th International Electric Propulsion Conference*, IEPC-2001-045, Pasadena, CA, Oct. 15-19, 2001.

[172] Walker, M. L. R. and Gallimore, A. D., "Performance Characteristics of a Cluster of 5-kW Laboratory Hall Thrusters," Journal of Propulsion and Power, **23**, 1, 2007.

[173] Manzella, D. H., Hamley, J., Miller, J., Clauss, C., Kozubsky, K., et al., "Operational Characteristics of the SPT-140 Hall Thruster," *33rd AIAA/ASME/SAE/ASEE Joint Propulsion Conference*, AIAA-1997-2919, Seattle, WA, Jul. 6-9, 2007.

[174] Boyd, I. D., "Review of Hall Thruster Plume Modeling," Journal of Spacecraft and Rockets, **38**, 3, 381-387, 2001.

"A month in the laboratory can often save an hour in the library."

--F. H. Westheimer